# Aerodynamic design and production of the front wing for Formula Student vehicle

**MASTER OF ENGINEERING THESIS**

TURIN POLYTECHNIC
Department of Mechanical and Aerospace Engineering
MSc in Mechanical Engineering
Academic Year 2018-2019



SUPERVISOR:
Prof. Andrea Tonoli

CANDIDATE:
Ludovico Angelini

CO-SUPERVISOR:
Prof. Gaetano Iuso

STUDENT ID:
253726

*To my whole family*

# Contents

# List of Figures

# List of Tables

# Abstract

The purpose of this dissertation is the design and the production and validation of a front wing for the open-wheel (single-seater) car of the Turin Polytechnic, participating in the 2019 Formula Student season.
Having previously established the objectives through an analysis of the vehicle dynamics, correlated also to the other aerodynamic components, this work is mainly based on the following macro-topics:
*Aerofoils' choice*: the choice is made first by building the characteristic curves of each one using macros in Java and plotting on Matlab, subsequently optimizing the 2D configuration through Heeds MDO.
*Front wing*: optimization of the 3D configuration of the aerofoils, end-plates and strakes in order to generate the maximum downforce compatible with the car's balance, with the wake's size produced by the front wheels and the front wing itself, granting an air flow directed towards the undertray of the car. Using Catia V5 (CAD) to design it and Star CCM+ (CFD) to analyse it, taking into account mesh and physic issues.
*Construction and production process of the whole front wing*: the production process began with the elaboration of CAD files for the moulds and for the rohacell core; the second step was the raw preparation for milling and therefore the treatment of milled moulds; the third step was the carbon fiber lamination process and the carbon fiber cure; finally, after finishing the piece, the final step was the assembly of the front wing on the vehicle.
*Testing*: Preparation of clamps, dummy and stiff suspensions to effectively perform wind tunnel tests with moving ground and rolling wheels. The tests were performed with varying speeds, yaw, pitch, drag reduction system, so as to validate the CFD model, as well as to obtain additional data on the car. Finally, the streamlines were visualized thanks to the woolen thread method.

The presentation is organized as follows:
After a brief introduction on the history of aerodynamics in open-wheel cars, in the first part (Ch. 1) the main characteristics and peculiarities of the Formula Student are specified, so to give an idea on the framework where the job was done.
In the second part (Ch. 2-4), the presentation deals with the aeropack performance, focusing on the different possibilities of front wing's development in relation to the different design orientation that is to be pursued. The section include details on CFD methodology and procedure used and describe the overall aerodynamic package's design.
In the third part (Ch. 5-7) the front wing's design, the production and the validation tests are described in details.
Some conclusions and considerations about future developments follow in the last chapter.

# Introduction

Aerodynamics is a science that began to develop significantly in the early twentieth century, along with the first developments in the aviation field.

Figure 1: Maserati 4CLT - 1950-51

At that time, the tendency of designers to abandon the shapes of the carriage to develop more subtle forms was emphasized by the development of aerodynamic science for the study of the behaviour of air around moving bodies.
The indications coming from the first theories developed in the context of this new science, were initially used to pursue economic benefits by reducing the aerodynamic resistance and therefore containing the power needed to overcome this force, which at that time was equal to about $\frac{3}{4}$ of the power of a terrestrial vehicle.


Figure 2: Lotus 49B - April 1968

The real big turning point came in 1968, when it became clear that aerodynamic drag could be exploited to improve the performance of the vehicle, expecially racing cars. Later, when they faced the problem of high-speed lifting, they began to look for a force capable of counteracting this phenomenon in order to increase vehicle stability and handling. Efforts were directed towards improving tire grip even at the expense of greater aerodynamic drag, in addition to the use of the mechanical grip generated through the tires and the suspension system. Moreover, beyond enhancing cornering ability, aerodynamic downforce has enabled greater acceleration by allowing the tyres to transmit more thrust force without wheel spin.
Thus, the potential deriving from the use of downforce was understood and man, for the first time, orbited the moon in the Apollo 8 spacecraft, and, contemporaneously, first wings were fastened onto Formula One cars. On the one hand aerodynamics took men higher into space than they had ever been before, but, on the other hand, it also had the function to keep them closer to the ground. Graham Hill arrived at Monaco in May, 1968 with modest front wings and a very subtle rear spoiler on his Lotus 49B. This was the start of 'aero' in Formula 1.
The position of these wings was then increasingly raised because, to perform their function best, they needed to interact with clean air, that is not disturbed by vortices and air flows created by the car body. They were immediately followed by front wings and other aerodynamic elements which had the purpose of modifying the air flow around the car.


Figure 3: Lotus 72D - 1972

A stroke of genius by the great designer and founder of Lotus, Colin Chapman, in 1972 showed the way ahead for Formula 1. Chapman designed the Lotus 72 with a pointed 'shovel' nose and a nose-cone in the form of a wedge, with radiators fitted into sidepods. This also had the effect of moving the car's centre of gravity toward the rear. Thanks to its revolutionary aerodynamics, the Lotus drove 15 kph faster on the straights than its predecessor with the same engine power.

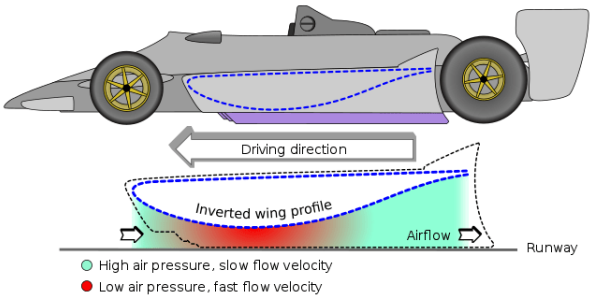


It was Colin Chapman again who introduced another design breakthrough in 1977/78. The Lotus 78 featured inverted wings which generated downforce, so naturally the car was soon dubbed the 'Wing Car'. The side-skirts on the side of the Lotus were virtually flush with the asphalt, this created a vacuum which pressed the car on to the track and allowed incredibly high cornering speeds. Therefore, downforce was increased not through additional surfaces, but through the advancement motion and the particular conformation of the car's undertray.

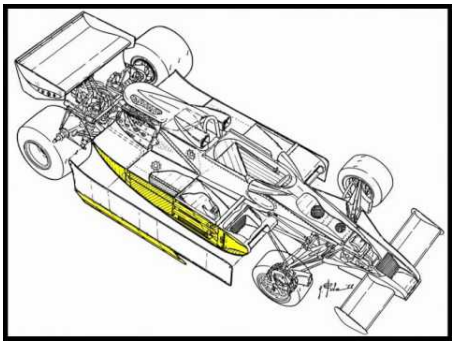


Figure 4: Ferrari 312T5 - 1980 (un example of wing car)

Nowadays, since the 1990s, aerodynamics has definitively become the central issue in the development of Formula 1.
At the beginning of the 2003 season, the occasional unconventional wing was first seen on the test tracks. However, given the current state of technology, it is unlikely that there will be new revolutionary developments like in the 1960s and 1970s. The aerodynamicists are now relying on steady evolution rather than revolution because they know that in Formula 1, finding just an extra hundredth of a second or two per lap might be enough to win.
It is a fact that a car's driving performance depends on its aerodynamic performance; it affects fuel consumption, top speed and, to a lesser extent, acceleration.

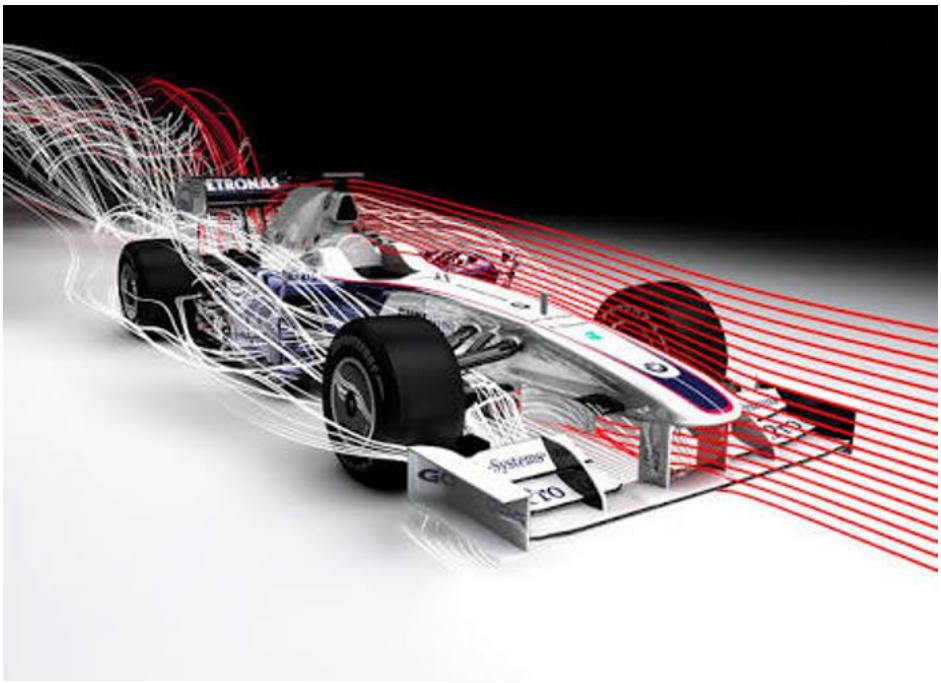

Figure 5: BMW-Sauber F1.09 - 2009

# Acknowledgements

I would like to remember all those who helped me in writing the dissertation with suggestions, criticisms and observations: my gratitude goes to them, even if I am responsible for every error in this thesis.

First of all, I thank Professor Andrea Tonoli, Supervisor, and Professor Gaetano Iuso, Co-Supervisor: without their support and wise guidance, this thesis would not exist.

I continue with all the colleagues from Squadra Corse, with whom I shared the entire design and production processes of this car, and with the staff of the FCA Prototypes plant and with that of CRF plant for their availability and their invaluable advices.

A special thanks goes to Leonardo Lenzi, Gabriele Ciullo and Giacomo Gentile who spent part of their time to discuss the development of the work with me; to Marco Rossini, for his work with the Lap Time Simulator; to Alessandro Boccini for facilitating my job; to Lorenzo Del Giudice for his help in preparation of wind tunnel tests; to Luca Bagattino, for the execution of the radiator experiment.

Finally, I would like to thank my loved ones: my friends and my family.

# Chapter 1

# Formula Student

## 1.1 History

Formula SAE is an international student competition established by the Society of Automotive Engineers (SAE) in 1981.


Figure 1.1: Formula SAE logo

The first European competition took place in the United Kingdom in 1998, since then the IMechE (Institution of Mechanical Engineers) decided to collaborate with SAE for the organization of European events. Since then, the competition has taken more and more importance taking the name of Formula Student [27].

Among the European races, the event in Italy is on the calendar from 2005. It is organized by the Associazione Tecnica dell'Automobile (ATA) and sees FCA and Dallara as its main sponsors. Indeed, the competition first took place on the Balocco FCA circuit, then on the Fiorano track owned by Ferrari and, finally, at the Riccardo Paletti racetrack at Varano de' Melegari, the Dallara

headquarters.

In 2007 Ross Brawn, former technical director of Ferrari, Brawn GP, Mercedes, and now, general manager and sports manager at Liberty Media for the Formula 1 project, became the patron of Formula Student.
From the dawn of this competition, technological progress has been remarkable also in the automotive sector, and accordingly even Formula SAE has not stopped evolving, introducing, for example, the full electric category in 2013.

## 1.2 Competition

The basic idea of Formula SAE is that a fictitious company would take on the team of students for the design, construction and testing of a racing car prototype.
This production is aimed at the market, with an expected demand of about 1000 units, of non-professional drivers called "weekend autocross racers", who want a car ready for use on the track.
The prototype, therefore, in addition to being performing, must be reliable, comfortable and, above all, have a low cost, suitable for mass production, and be safe [27].

The purpose of Formula SAE is to put teams composed by university students in competition to conceive, design, manufacture, and develop small formula-style racing cars and to to compete with each other in international competitions.
The competition is structured in such a way as to reward the team with the best relationship between performance, economy, manufacturability and saleability of their car. The key to success therefore lies in an efficient team work, based on team cohesion, individual skills and the ability to pool them, in order to optimize the design and construction phases.

There are four categories in race, so that each team can enroll in the most suitable one, for it, in terms of experience, potential and budget:

- Class 1: participation both in static and dynamic events with a totally new car in the following different categories:
  - 1E, electric: full electric vehicle;
  - 1C, combustion: vehicle with traction obtained only from the internal combustion engine;
  - 1D, driverless: self-driving vehicle
- Class 3: participation only in static events since the car has not yet been built

The participating teams come from all 5 continents and have a number of members that can vary from about thirty to more than a hundred people.
Events are also held at racetracks around the world, sometimes even in circuits rich in history and charm, for example: Silverstone, Hockenheim, Montmelò, Spielberg.

Often the judges come from the host country of the event and are important exponents of the main companies that orbit in the automotive world. Many of these are also among the most important sponsors of this event, such as:

- Car companies: FCA, Dallara, Ferrari, Abarth, Lamborghini, KTM, RedBull, Mercedes, BMW, Porsche, Audi, Volkswagen, Honda, Toyota, Ford, Skoda;
- Suppliers: Pirelli, SKF, Schaeffler, Hoosier, Shell, Loctite;
- Softwares: Solidworks, Altair, Siemens, Mathworks

Just to name a few.

## 1.3 Trials

### 1.3.1 Technical inspections


Figure 1.2: Rain test

In order to be able to take part in events that assign a score, the vehicle must necessarily be compliant with regulations and safety rules [8].
For this purpose, during each event, before competitions, the vehicle is required to pass the so-called technical checks:

- Tech & safety:
  - Visual inspection by the judges, who assess compliance with the regulation in all detail;
  - Pilot leakage test in less than 5 seconds;
  - Test of the main switch: check that the entire electrical system is turned off by it

- Tilt test: the vehicle is placed on a ramp and tilted at first by 45° , subsequently of another 15°, with judges checking that there are no leaks of liquids;
- Rain test: through simulated rain, judges verify that there are no infiltrations in the electrical part which might cause dangerous short circuits and put at risk pilot safety. This test is only required for the full electric category, while for the combustion category this test is replaced by the noise test;
- Brake test: once the car has reached sufficient speed, it must stop in a limited area, simultaneously blocking all four wheels to demonstrate that in the event of loss of control due to lack of grip during braking, the vehicle is capable to stop inside track's run-off areas

### 1.3.2 Static events


Figure 1.3: Design event

Static events are competitions that award points based on the quality and economic viability of the project [8]:

- Cost event (100 points): each team must present, before the competition, a written report concerning the car's design and production costs. The team that achieves the best cost-performance ratio receives 30 points, another 25 points are assigned based on the oral presentation by teams about the production process of two components chosen by the judges, and the last 20 points are given based on the real possibility of producing the vehicle;
- Business plan (75 points): the car is presented to a "Council" that has decision-making power over the "Formula Student" investment; the score is awarded based on the economic studies of budget, strategy and marketing carried out by the team, as well as their oral presentation;

- Design event (150 points): the score is assigned based on the efficiency of the design choices made and the ability of the different subsystems' managers to present and justify them and to answer the judges' questions. In particular, the most innovative technical solutions are rewarded, which at the same time are reliable and simple to implement

### 1.3.3 Dynamic events


Figure 1.4: Skidpad

The dynamic events are competitions that award points based on the actual performance of the car [8]:

- Acceleration (75 points): The test takes place on a straight line of 75 m, can be carried out by two different pilots, each one having two attempts at his disposal.
  The score is assigned based on the difference between the best and the worst time recorded by the different teams

$$Acceleration_{SCORE} = 71.5 * \frac{(\frac{5.8}{T_{your}}) - 1}{(\frac{5.8}{T_{min}}) - 1} + 3.5 \tag{1.1}$$

  Where 5,8 is the highest time (in seconds) taken into consideration by judges;

- Skidpad (50 points): the event, which can be performed by two different pilots (two attempts allowed each) for each team, takes place on an 8-shaped

course with two circles of 15.25 meters in diameter each, delimited by 16 pins internally and 16 externally.

$$Skidpad_{SCORE} = 47.5 * \frac{(\frac{6.184}{T_{your}})^2 - 1}{(\frac{6.184}{T_{min}})^2 - 1} + 2.5 \tag{1.2}$$

The aim is to evaluate the lateral vehicle dyanmics related to the development of lateral acceleration;

- Autocross (150 points): during the test, a qualifying lap has to be performed on a mixed circuit to evaluate the car's handling. The track is designed to obtain average speeds between 30 and 40 $\frac{\text{km}}{\text{h}}$ and includes short straight lines (no more than 60 metre), constant radius curves (from 23 to 45 metre in diameter), hairpin turns (external diameter minimum 9 metre), slaloms (cones at a distance between 25 and 40 metre), chicanes and variable radius curves.

$$Autocross_{SCORE} = 142.5 * \frac{(\frac{1.25 * T_{min}}{T_{your}}) - 1}{(\frac{1.25 * T_{min}}{T_{min}}) - 1} + 7.5 \tag{1.3}$$

This fast lap can be performed by two different drivers (two attempts allowed each) for each team;

- Endurance (300 points): this event takes place along a track similar to the Autocross one for a total of 22 km, the team members cannot intervene on the car and the driver change is scheduled at mid-race, during a three-minute break.

$$Endurance_{SCORE} = 250 * \frac{(\frac{1.45 * T_{min}}{T_{your}}) - 1}{(\frac{1.45 * T_{min}}{T_{min}}) - 1} + 50 \tag{1.4}$$

The score assigned takes into account the total time to complete the trial. There is only one possibility and the competition is considered concluded only at the end of the 22 km;

- Efficiency (100 points): during the Endurance it is not possible to recharge the vehicle's battery via external devices. At the end of the test a score is assigned based on the average energy consumption per kilometer, to reward the vehicle's efficiency and regeneration capacity:

$$Efficiency_{SCORE} = 100 * \frac{E_{min}}{E_{your}} \tag{1.5}$$

## 1.4 Rules

The competition regulation is updated every year and, although it imposes a high number of safety-oriented requirements, it leaves ample design freedom in all other fields in order to stimulate the students' inventiveness and to reward the best project, and the most brilliant designers.
While safety rules are very inflexible, technical ones are not stringent and make it possible to find cars with completely opposite design choices. t this regard, main macroscopic differences are shown in table 1.1.

| **Technical Area** | **Option 1** | **Option 2** |
|---|---|---|
| Wheels | 10" | 13" |
| Chassis | Tubular | Monocoque |
| Radiators | Positioning | Orientation |
| Aerodynamics Package | Advanced | Absent |

Table 1.1: Main different designing orientation

The main regulatory constraints from a technical (and not a safety) point of view are [8]:

- Formula-type car body: single-seater with open cockpit, and 4 not aligned open wheels;
- Wheelbase at least 1525 mm and free axles track, but with the minor at least 75 % of the largest;
- Vehicle conceived, designed and maintained by the students belonging to the team without the direct involvement of related professionals;
- The car can only be used for one year (starting from the first day of the first competition in which it participates). To be classified as new, the vehicle must have significant changes in the frame structure compared to the previous one;
- There can be no openings in the bodywork outside the cockpit, and those relating to the mounting of the suspensions and steering components;
- the minimum ground clearance for all components, except for the wheels, must be 30 mm;
- The TS (Tractive System, that is very part that is electrically connected to the motor(s) and TS accumulators) power at the outlet of the TS accumulator container must not exceed 80 kW.
- Maximum voltage allowed on an electrical connection is 600 V DC, while the control signals' voltage of the power electronic devices can reach 630 V DC;
- Molten salt, thermal batteries and fuel cells are forbidden

In addition to the aforementioned ones, there are many other, more precise and less influential, constraints for each technical area. In particular the definition of aerodynamics device is the following: *a specifically designed structure mounted on*

*the vehicle to guide the airflow around the vehicle, increasing the downforce acting on the vehicle and/or lowering its drag. The mounting of this structure is not regarded as an aerodynamic device, unless it is intentionally designed to be one* [8], the main rules for the aerodynamic division are the following:

- If aerodynamics devices are used in Formula SAE, their settings can be adjusted for the individual events, but wholesale removal or addition of components are not allowed;
- Vehicle's compliance with the type of open-wheel car, keeping the areas shown in the figure 1.5 unused;
- Vehicle's compliance with size and positioning limitations shown in the figure 1.6;
- It is not possible to use power devices to exploit the ground effect by removing air from the undertray;
- The following constraints on the stiffness and resistance of components must be fulfilled: 200 N distributed over 225 cm with an inflection of less than 10 mm; 50 N concentrated at any point with an inflection of no more than 25 mm; item Fitting radius of junction: 5 mm for vertical front edges, 3 for horizontal front edges;

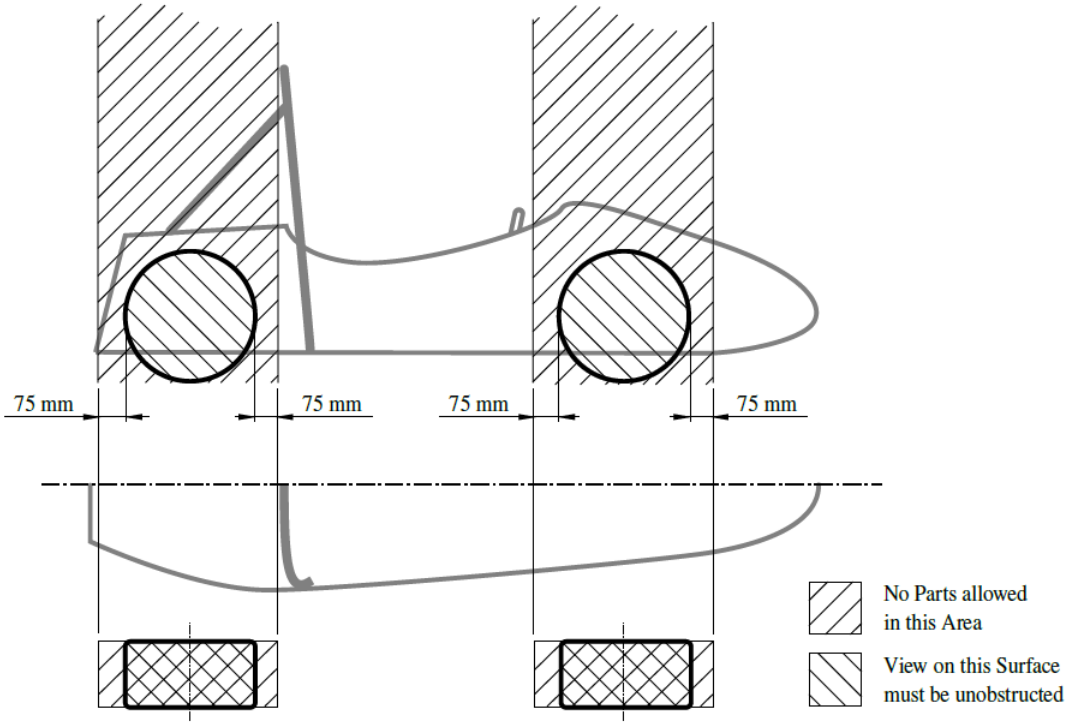


Figure 1.5: Unavailable areas

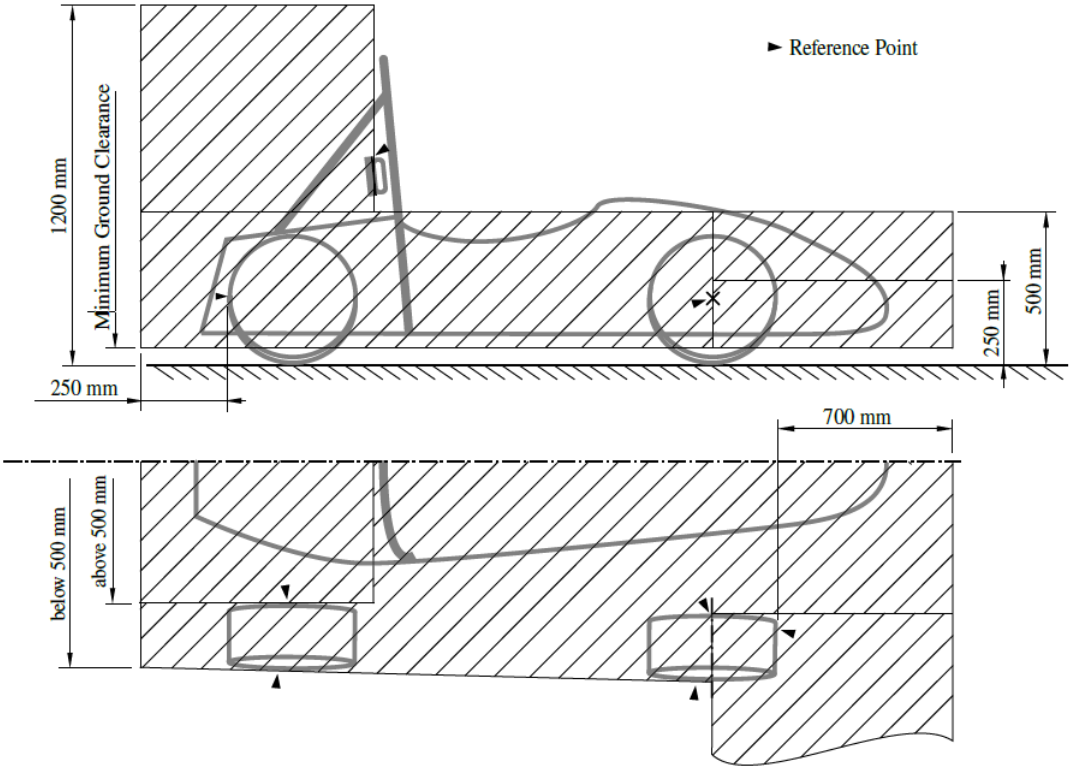


Figure 1.6: Available areas

## 1.5 Squadra Corse

### 1.5.1 History

The Squadra Corse of the Politecnico di Torino was born in october 2003 3 with the aim of competeing in the Formula SAE - Student world championship in the year 2005. The founders of the project are 9 Automotive Engineering students coordinated by the Faculty Advisor , Ing. Andrea Tonoli, who is still today the manager / coordinator of the racing team. The distinctive colors immediately were red, from the Italian automotive tradition, and black; while the chosen number was 46 in honor of Valentino Rossi.


As anticipated, the first car came to light in 2005 and was exactly called SC05. Its characteristic features were the tubular steel frame and the twin-cylinder Guzzi engine.
Later, following the indicated nomenclature, the SC06 and the SC07 were born. In the last one the traction was entrusted

to a four-cylinder Honda, while the leit motiv of the design remained the weight reduction constantly.

The first major breakthrough took place in 2008 with the SC08, that was important due to the introduction of laminated carbon fiber parts, the purchase of magnesium wheel rims and gear shift paddles mounted behind the steering wheel.


The subsequent cars saw a development of the components: indeed, after the SC09, the SCX was characterized by the introduction of a pneumatic clutch, and the SCXX was its evolution.

The most drastic and important turning point certainly took place with the SC12e in 2012, when Squadra Corse, the first team in Italy, moved from the combustion category to the development of a full electric vehicle.

Next car, the SCR, which competed both in 2013 and 2014, presented two fundamental innovations: the carbon fiber monocoque and the presence of an aerodynamic package.
Also SCXV (2015) represented a further technological development replacing the



two on-board electric motors, with 4 out-board electric motors including the respective transmissions. In 2016 it was thought to develop the SCXV by implementing a drag reduction system (DRS), thus obtaining SCXVevo.

From these experiences derived the following Squadra Corse cars: the SC17 and the SC18, up to the current SC19 (see section 1.5.3), which represents the crowning of the full electric route started in 2012: indeed, it was the first italian car to triumph in the 1E category, winning the Formula SAE Italy event (Formula ATA).

### 1.5.2 Team


Figure 1.7: Squadra Corse PoliTo 2019 team

The team is composed by 30 engineers and 4 pilots organized according to a hierarchical structure that allows to streamline the decision-making process without eliminating the dialogue, fundamental in a team work, between the single members. This structure estabilishes that the coordination of the entire team is entrusted to the team leader, from a management point of view, and to the technical director, from an engineering point of view, while the development of each technical area of the car is the task of a division, composed by engineers with specific technical skills related to each area and headed by a manager.
The technical areas and therefore the respective divisions are the following:

- Aerodynamics: aerodynamic package that increases the dynamic performance of the vehicle;
- Battery pack: electrical energy storage system, and relative cooling system, for powering both motor (HV) and other devices (LV);
- Chassis: monocoque which contains all sprung masses and must guarantee safety specifications as well as produce sufficient torsional stiffness to improve vehicle dynamics;
- Electric/Electronics: electronic control boards for all electrical appliances and wiring of all conductor cables;
- Management: relations with sponsors, promotion activities and travel organization;

- Powertrain: out-board transmission and motor and inverter cooling;
- Unsprung masses: uprights, suspension, wheel assembly, steering, anti-roll bar, pedals;
- Vehicle Dynamics: power controls and car setup

### 1.5.3 SC19


Figure 1.8: SC19

Based on the experience gained previously and analyzing the data collected both from the tests and from the simulations, the guidelines of the SC19 project were:

- Lightness: it affected the design of the battery, the choice of carbon fiber for almost all the components and the low-drag philosophy;
- Regeneration: it has determined an appropriate design of the brake pedal, as well as an adequate setting of the controls, based on the numerous tests carried out

The results were the following technical characteristics for each division:

- Aerodynamics: aerodynamic package weighing 10 kg, and performance, at the average speed of 60 $\frac{km}{h}$, about 560 kgf of downforce and 15 kgf of drag ($C_L = 3.82$ and $C_D = 0.87$);

- Battery pack: battery HV 600 DC (38 kg) and battery LV 12 DC, with a cooling system composed of 4 fans, all inside a carbon fiber safety container;
- Chassis: carbon fiber monocoque weighing 19.9 kg and torsional stiffness equal to 213000 $\frac{\mathrm{N\,m}}{\mathrm{rad}}$ ;
- Electric/Electronics: 4 torsional three-phase synchronous electric motors AMK with 32 kW each;
- Powertrain: planetary out-board transmission inside the wheel hub with a ratio of 14.5 and 0.8 mm module;
- Unsprung masses: aluminum uprights, titanium 3D printed fins, carbon arms with steel spare ones, carbon fiber steering wheel connected to a single cardan, brake pedal with regenerative braking and mechanical braking through the disks designed within the team, rims in magnesium and Pirelli tires of 13" radius;
- Vehicle Dynamics: Vehicle Dynamics: air damper with both stiffness and damping function, much lighter than the coil spring and hydraulic damper

Among these characteristics, several peculiarities can be identified compared to the majority of the other participating teams:

- Very efficient aerodynamic package;
- Carbon fiber battery pack;
- Brake disks, whose design was entirely developed within the team;
- Carbon fiber suspension arms and steering

The following performances were obtained:

| **Performance** | **Value** |
|---|---|
| Car weight | 180 kg |
| Max speed | 130 $\frac{\mathrm{km}}{\mathrm{h}}$ |
| 0 - 100 $\frac{\mathrm{km}}{\mathrm{h}}$ | 2.5 s |
| Max power (rule) | 80 kW |
| Max cornering speed (R=25 m) | 65.7 $\frac{\mathrm{km}}{\mathrm{h}}$ |
| Autonomy (without regeneration) | 22 km |

Table 1.2: SC19 main performances

# Chapter 2

# Aeropack performance

## 2.1 Vehicle dynamics

In order to understand benefits and problems related to the development of an aerodynamic package, it is necessary to introduce some fundamental concepts of vehicle dynamics.

### 2.1.1 Longitudinal dynamics

In order to transmit forces to the ground, the tire does not have a single point of contact, as in the case of the pure rolling physical model, but, due to its deformability, it has an elliptical area of contact with the ground, which, therefore, is at zero speed (adherence).
Because of this greater complexity of the phenomenon, more articulated models must be used to describe the ground-pneumatic interaction: one of the simplest and most understandable one is the brush model Which treats the tire as a series of separate bristles, which are allowed to deform independently and all marked out with the same stiffness.

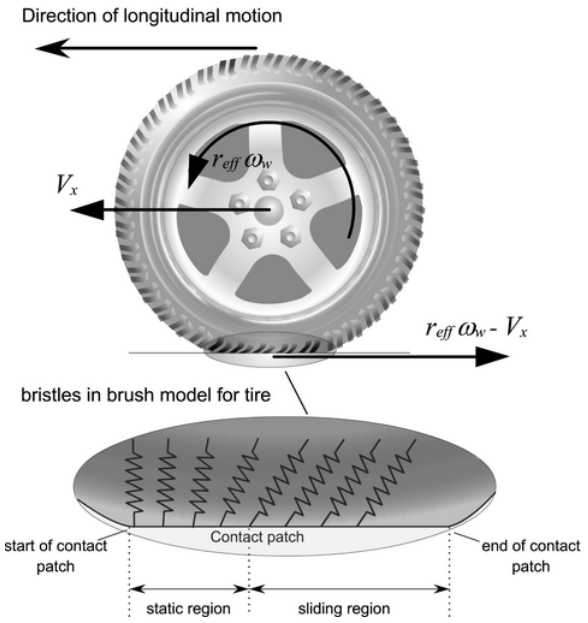


Figure 2.1: Longitudinal brush model

The deformations of these bristles, through the stress-strain law, cause stress which, integrated, turns out to be the force that the tire (the whole set of bristles) would like to exchange with the ground along the longitudinal direction. Indeed, it has been shown that the stress distribution along the longitudinal axis, due to the deformation of the bristles, is proportional to the slip ratio of the tire $\sigma$ (deformation measurement $u(\xi)$) and to the stiffness of the bristles $k_x$(tire's stiffness per unit length $C_\sigma$):

$$\sigma = \frac{v - \omega * R}{v} \tag{2.1}$$

$$C_\sigma = k_x = \frac{\tau_x}{u(\xi)} \tag{2.2}$$

$$\tau_x(\xi) = -C_\sigma * \sigma * \xi \tag{2.3}$$

where $\xi$ is the local longitudinal coordinate of the tire. This equation applies as long as the adherence condition is maintained.
Ideed, the static friction, multiplied by the normal force, indicates a maximum available tension and, therefore, as long as the one required by the deformation of the tire based on the equation 2.3 is lower, the static friction is able to satisfy it. However, if this condition should no longer be met, the adherence condition would be violated so that the tire would tend to slip and therefore the friction taken into consideration would be the dynamic one, which provides, multiplied by the normal force, a lower tension value, not only available, but effectively transmitted. In formulas:

$$\tau_x \leq \tau_x^{limite} = f_a * p(\xi) \tag{2.4}$$

$$\tau_x = \tau_x^{limite} = f_d * p(\xi) \tag{2.5}$$

where $p(\xi)$ it is the normal pressure distribution on the contact area of the tire and therefore represents the local definition of the normal force.
Assuming an elliptical pressure distribution, it can be seen how, as the deformation increases and so the required force, the slip ratio increases and therefore the required tension reaches the available tension value earlier, thus reducing the part of the tire in adherence and increasing the one in slip: this phenomenon results in the following trend (figure 2.2) of $F_x$ as a function of $\sigma$.
It also shows that the normal force $F_z$ is a parameter of this trend: in fact, with the same friction coefficients, increasing the $p(\xi)$ the adherence limit value will be reached, for the same slip ratio, for higher tension values, guaranteeing a maximum force on the ground. Furthermore, the vertical load, increasing the deformation of the tire, will increase the contact area giving a greater slip stiffness. With the same slip ratio the force and so, during braking, the deceleration is greater and, obviously, the braking distance will be smaller; or with equal braking distance and, therefore

equal force, the slip ratio will be lower guaranteeing less tire wear.
From both these considerations we get this graph:

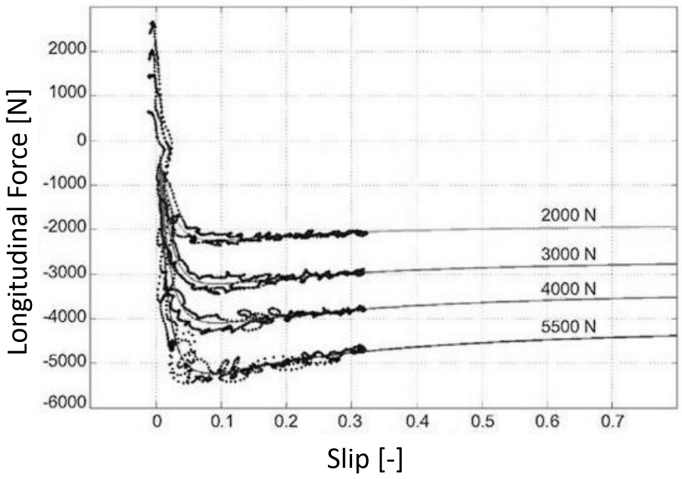


Figure 2.2: Longitudinal dynamics

### 2.1.2 Lateral dynamics

The lateral dynamics concerns the exchange of forces, and therefore of accelerations, which takes place along the transversal direction to the motion of the vehicle.

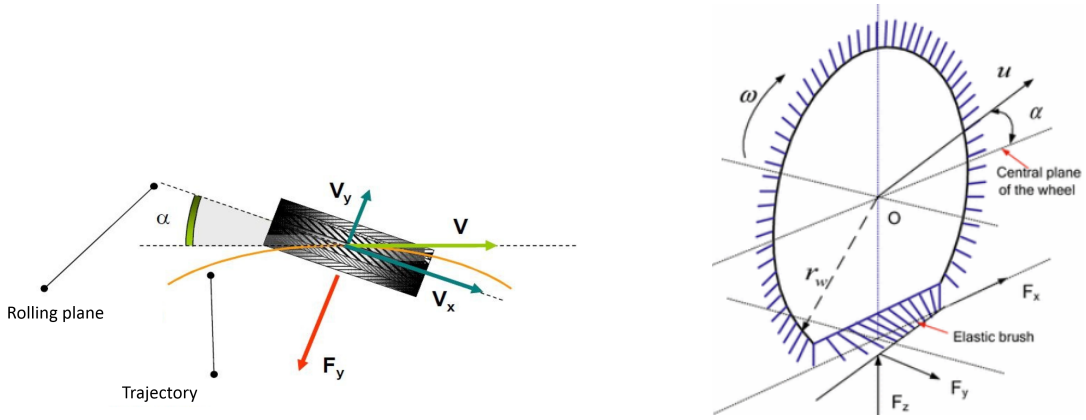


Figure 2.3: Lateral brush model

Since these are always forces exchanged between the tire and the ground, the treatise is similar to the previous one using the usual brush model.
Lateral deformation $w(\xi)$ is taken into account by slip angle $\alpha$, slip angle stiffness $C_\alpha$ and from the bristles' lateral stiffness $k_y$:

$$\alpha = -\frac{\partial w}{\partial \xi} \tag{2.6}$$

$$C_\alpha = k_y = \frac{\tau_y}{w(\xi)} \tag{2.7}$$

$$\tau_y(\xi) = -C_\alpha * \alpha * \xi \tag{2.8}$$

Making the same considerations on the friction coefficients and on the contact pressure, we have the following formulas:

$$\tau_y \leq \tau_y^{limite} = f_a * p(\xi) \tag{2.9}$$

$$\tau_y = \tau_y^{limite} = f_d * p(\xi) \tag{2.10}$$

The trend of $F_y$ is calculated as a function of $\alpha$ parametrized by $F_z$. It can be seen that at the same slip angle, the transmissible force, and therefore the cornering speed, are higher; or that at the same cornering speed the slip angle will be lower guaranteeing less tires' wear. Unlike the previous case, the lateral tension distribution on the contact area generates a moment around the steering axis of the wheels:

$$M_z = \int_0^a \tau_y(\xi) * (a - \xi) d\xi \tag{2.11}$$

These overall graphs are obtained:

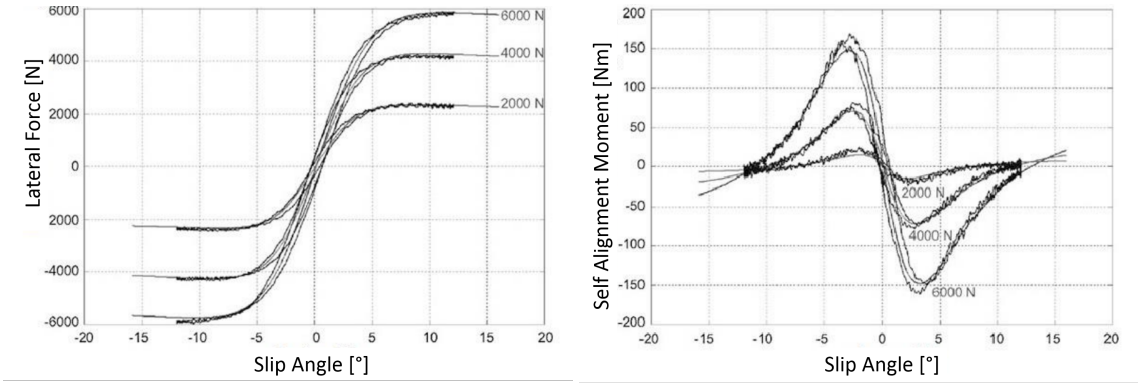


Figure 2.4: Lateral dynamics

### 2.1.3 Combined slip

Combining the two just seen dynamics we obtain the following trends:

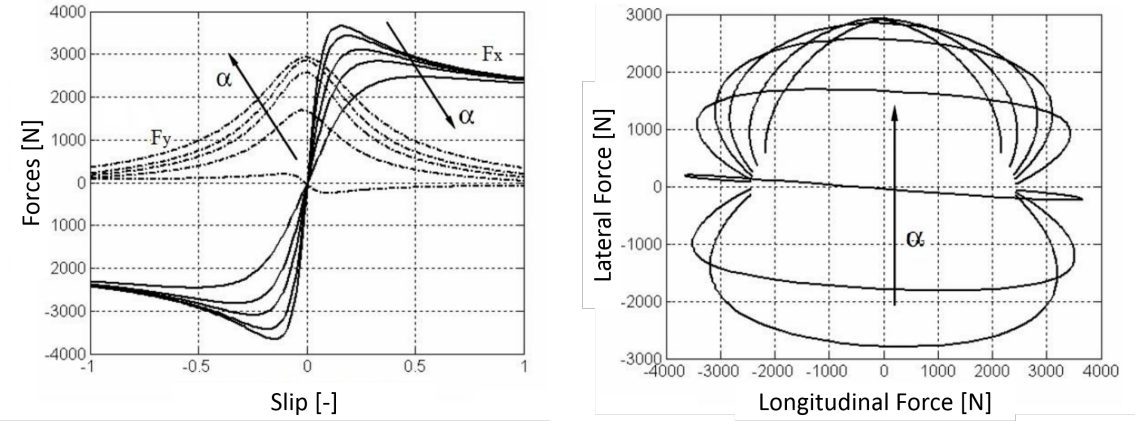


Figure 2.5: Combined dynamics

The trends clearly indicate that if the $F_x$ is high, the $F_y$ must be low and vice versa. This relationship can be plotted differently, obtaining the elliptic diagram, which does not represent the characteristic $F_y = f(F_x)$, but is plotted for points and indicates, fixed a force and then its deformation, which is the available deformation, and therefore the force, in the other direction.

## 2.2 Vehicle dynamics and aerodynamics

### 2.2.1 Qualitative analysis

From the dissertation just illustrated we can see how a greater vertical load only brings improvements from the vehicle dynamics' point of view, by increasing the contact pressure and the contact area, and therefore by ensuring greater ground-tire forces and greater fictitious rigidity.
This vertical load can be added by increasing the vehicle's mass, and so the weight, but nevertheless it would entail a considerable increase in inertia which would cause various problems:

- More difficult acceleration;
- Higher centrifugal force in curve, other conditions being equal;
- Worse car handling;
- Higher consumption due to the greater mass to be moved;
- More tire wear due to the increased force required, thus expanding the sliding zone

A more efficient and performing method of increasing vertical load is the introduction of an aerodynamic package. This solution has the advantages illustrated by the treatise of vehicle dynamics guaranteed by vertical load generation.
In particular, given that it is obtained by exploiting the aerodynamic forces and not the inertial forces (in fact the weight of the aerodynamic package is very limited and has little influence on the inertial mass of the vehicle) the problems described above can be deleted or reduced:

- Deleted:
  - Tires' wear: tires have to withstand lower forces and work in conditions of greater grip thanks to the vertical load. They also reach a more optimal temperature (however, a problem of overheating may arise);
  - Centrifugal force: the increase in inertial mass is negligible, therefore also the variation of centrifugal forces
- Reduced:
  - Acceleration and Consumption: the price for having the vertical load is the birth of an aerodynamic resistance which therefore causes a greater resisting force which both affects the acceleration and the consumption, but to a lesser extent than the weight increase;
  - Handling: on the one hand all the problems arising from weight gain are solved, but, on the other hand, various issues can arise:
    * Balancing: aerodynamic forces are applied at the center of pressure, which must therefore be as close as possible to the center of gravity to avoid the creation of moments that should be managed. However, these forces depend on the speed, but also on the side wind and on the pitching of the vehicle, which influences both the incidence and the ground effect (which is also affected by a different height from the ground), so it is very complex to succeed to find a neutral balance, or in any case to obtain such a distribution as to have the desired dynamic behaviour;
    * Center of gravity: mainly due to the height of the rear wing, the center of gravity is found to be in a higher position, complicating the dynamic performance of the vehicle;
    * Weight: possible increase in weight due to the larger size of the battery because of greater energy needed to win the drag

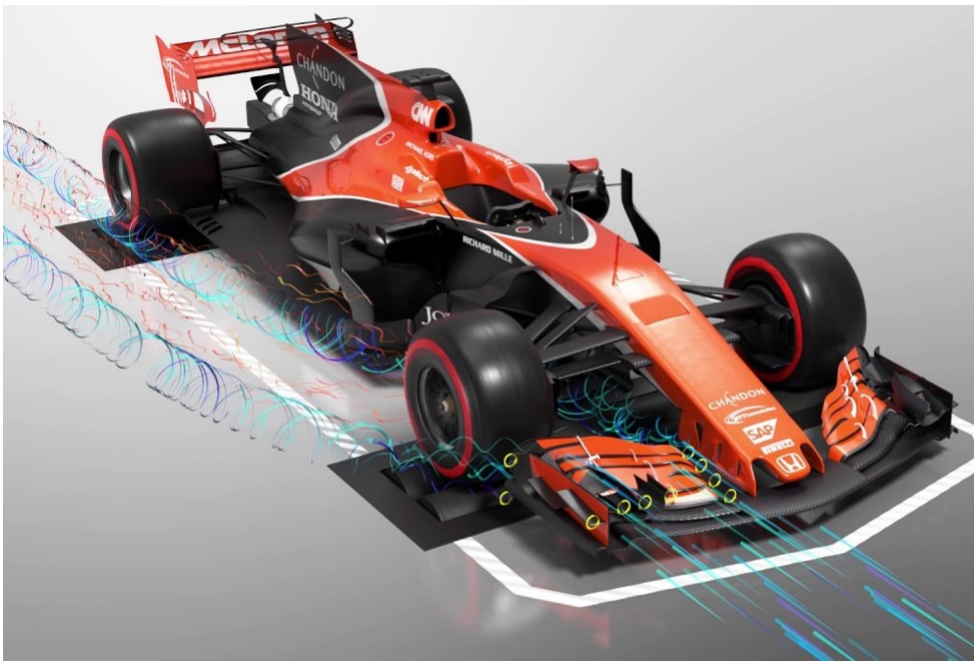


Figure 2.6: Outwash: McLaren MCL32 - 2017 (Motorsport.tv)

Other strengths, in addition to the vertical load, of the introduction of an aerodynamic package on a formula car are:

- Outwash: limitation of drag and lift produced by the wheels;
- Direction of flows at will: for example towards heat exchangers

In conclusion, the purpose of an aerodynamic package is to give the greatest possible downforce, with the right balance, with the minimum increase in aerodynamic drag, in order to increase vehicle performance.
However, in introducing an aerodynamci package, great attention has to be paid to the effects on the energy consumed, to the relationship with the tires, to the coexistence with the cooling system and to the influence on the position of the center of gravity.

### 2.2.2 Quantitative analysis

#### Lap time simulator

Once the qualitative analysis was carried out, we wanted to verify quantitatively the benefits deriving from the introduction of an aerodynamic package on the Formula Student car to justify its presence or not on the SC19. Once the advantages have been quantified, an in-depth analysis of their maximization has been conducted, thus establishing the aerodynamic targets for the 2019 season. For these simulations a half-car model was implemented in the Matlab and Simulink environment with the aim of obtaining the speed and energy data consumed during race on a selected track.
The half-car model is made up of the front and rear suspension modeled as spring/-damper systems. A more detailed model would include a tire model, and damper

nonlinearities such as velocity-dependent damping (with greater damping during rebound than compression). The vehicle body has pitch and bounce degrees of freedom. They are represented in the model by four states: vertical displacement, vertical velocity, pitch angular displacement, and pitch angular velocity. A full model with six degrees of freedom can be implemented using vector algebra blocks to perform axis transformations and force/displacement/velocity calculations.
Half-car model considers two wheels, one front and one rear wheel. In this type of models half of the weights of the entire car, including that of pilot, are considered for analysis purpose. The main advantages of this type of models are

- Vehicle pitch motions can be simulated;
- Front and rear dampers and spring characteristics can be modeled differently which are also different on the actual vehicle;
- Body motions and center of gravity effect can be simulated

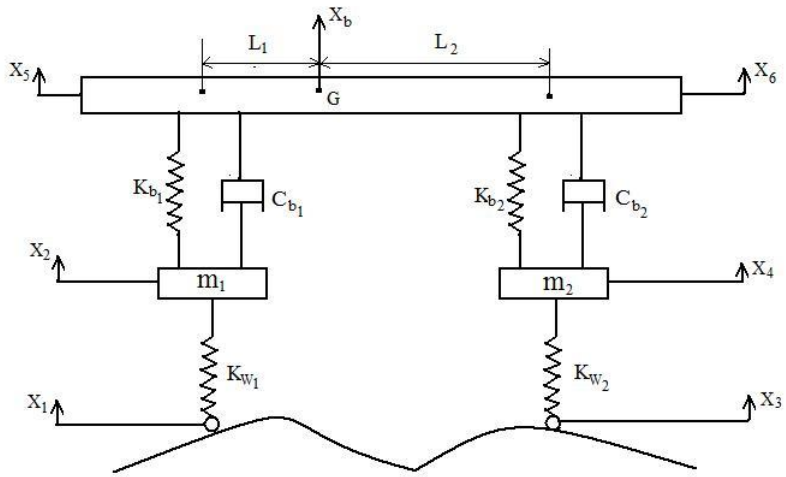


Figure 2.7: Half car model

As shown in the figure both the front wheel and back wheel supports half of the car weight by means of separate dampers attached to them. Model is again a two dimensional model which has a movement only on Z direction.

This model was validated by comparing the output of its simulations with the track data obtained during the Formula Student Spain 2018 event, in terms of lap time and energy consumed:

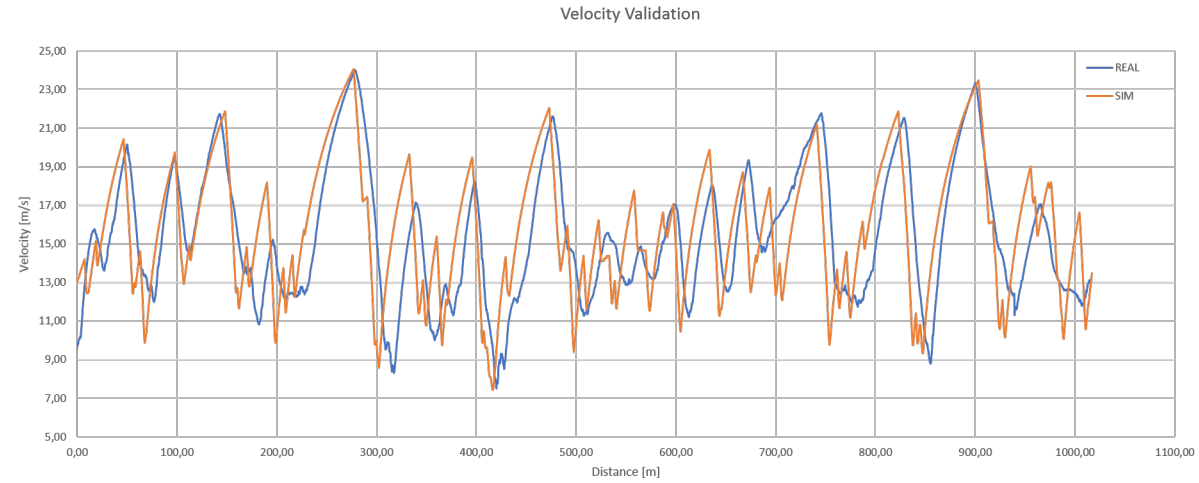


Figure 2.8: Velocity comparison

| | Simulazione [s] | FSS2018 [s] | errore [%] |
|---|---|---|---|
| Tempo sul giro | 72.07 | 72.46 | 1 |

Table 2.1: Velocity comparison

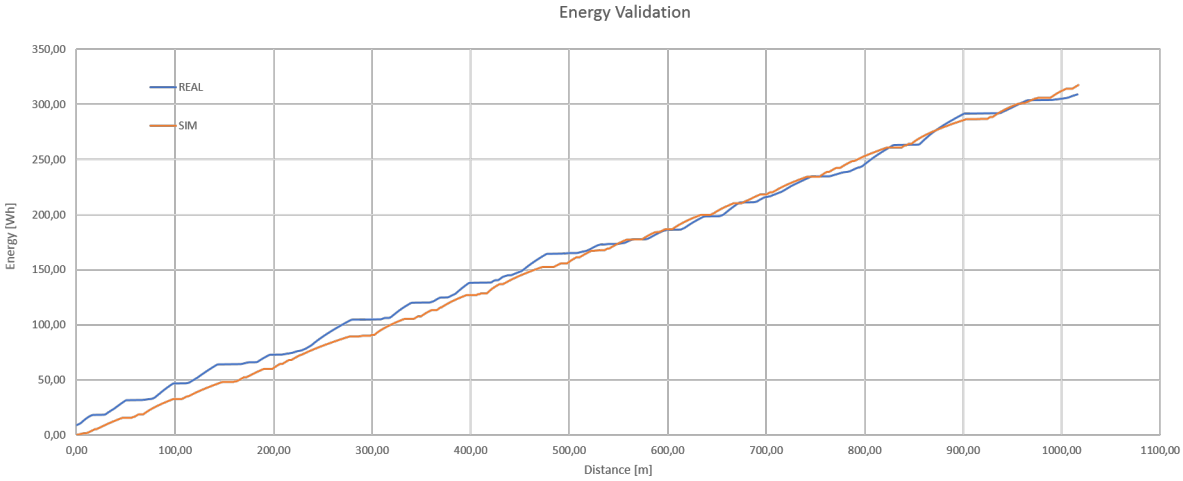


Figure 2.9: Energy comparison

| | Simulazione [W h] | FSS2018 [W h] | errore [%] |
|---|---|---|---|
| Energia | 318 | 309 | 3 |

Table 2.2: Energy comparison

The half-car model is a simplified model of car, indeed it has a two-dimensional nature and does not include the presence of suspensions. However, we note, through validation, how its accuracy, both in terms of lap time and energy (the two quantities

that assign score in Formula Student events), is sufficient for a preliminary analysis like the one described above, adopted for selecting a typology of aerodynamic configuration and to determine its objectives.

### Aerodynamics configurations

Simulating the progress of all five dynamic events, typical of a Formula Student race, employing cars equipped with 4 different aerodynamic packages illustrated below, the benefits deriving from the introduction of an aerodynamic package were verified quantitatively.
As previously seen the differences in behavior and, therefore, in the performance of the different half-car models, depend on the different values of the dynamic quantities that characterize them, ordered in the table 2.3: aerodynamic resistance, downforce, efficiency, overall mass, height of the center of gravity.

| | Complete Aeropack | No Rear Wing | No Wings | No Aeropack |
|---|---|---|---|---|
| Cx | 1.03 | 0.54 | 0.33 | 0.20 |
| Cz | 3.70 | 2.63 | 0.99 | 0.24 |
| E | 3.6 | 4.9 | 3.0 | 1.2 |
| Mass [kg] | 189 | 186 | 183 | 181 |
| $Z_{CG}$ [mm] | 242 | 237 | 233 | 234 |

Table 2.3: Aerodyanmics configurations

On the other hand, in this simulations we used the same values for:

- Energy: same power discharged in the same time;
- Power: electrical motors with the same performance;
- Percentage of regenerated energy: equal starting conditions in the efficiency competition

A higher energy level means a greater capacity of the battery so, with the same type of cells, a higher number of cells and therefore an increase in weight. To examine in depth the compromise between available energy and weight, all the events were carried out for two different fixed energy values. The first, greater, deriving from a heavier battery layout and, therefore, conferring worse dynamic performances; the second, smaller, resulting from a lighter battery layout and, therefore, giving better dynamic performance.

| Layout | Mass [kg] | Capacity [W h] |
|---|---|---|
| 5p130s | 42 | 7.0 |
| 4p140s | 35 | 6.1 |

Table 2.4: Battery-pack layout

To compare the results, each race's and total score were taken into consideration which would have been obtained during the FSS2018 event competing individually with the different types of aerodynamic package.

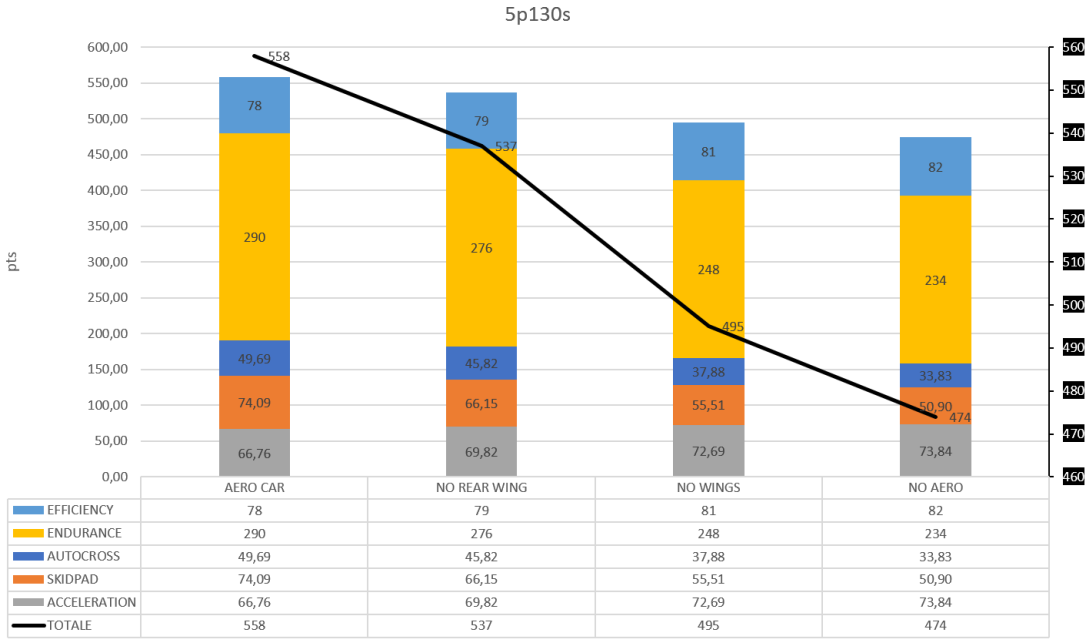


| | AERO CAR | NO REAR WING | NO WINGS | NO AERO |
|---|---|---|---|---|
| EFFICIENCY | 78 | 79 | 81 | 82 |
| ENDURANCE | 290 | 276 | 248 | 234 |
| AUTOCROSS | 49,69 | 45,82 | 37,88 | 33,83 |
| SKIDPAD | 74,09 | 66,15 | 55,51 | 50,90 |
| ACCELERATION | 66,76 | 69,82 | 72,69 | 73,84 |
| TOTALE | 558 | 537 | 495 | 474 |

Figure 2.10: Score with 5p130s layout

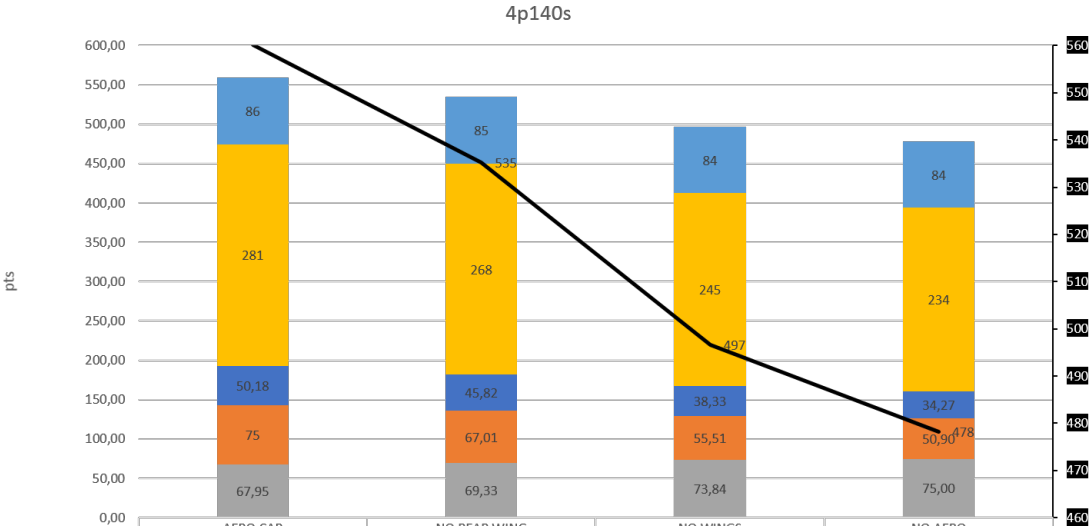


| | AERO CAR | NO REAR WING | NO WINGS | NO AERO |
|---|---|---|---|---|
| EFFICIENCY | 86 | 85 | 84 | 84 |
| ENDURANCE | 281 | 268 | 245 | 234 |
| AUTOCROSS | 50,18 | 45,82 | 38,33 | 34,27 |
| SKIDPAD | 75 | 67,01 | 55,51 | 50,90 |
| ACCELERATION | 67,95 | 69,33 | 73,84 | 75,00 |
| TOTALE | 560 | 535 | 497 | 478 |

Figure 2.11: Score with 4p140s layout

Results are congruent with the concepts expressed in the theoretical dissertation and with [22], and indicate that the complete aerodynamic package is the one that guarantees the best performance and the highest score, with both battery layouts.

Indeed, the complete configuration, in addition to provide the greatest vertical load, also allows a better balance with respect to the solution without rear wing (center of pressure too strongly located on the front axle) and that one without wings at all (center of pressure too much on the rear axle). Furthermore, the indicated configuration is also the one that has the greatest potential. Indeed, having more appendices, not only more components can be developed in order to obtain a greater level of downforce starting from the ones in the case under consideration, but also the load can be distributed more freely and the desired banlance obtained more easily. Finally, The analysis shows a pessimistic scenario because it is difficult not to increase the static events score, during a Formula Student competition, with a more detailed study [22].
This solution requires a definitely greater commitment in terms of costs, manufacturing complexity and production time, and also time's loss during the events to pass the techs, but it is by far the most efficient typology of aerodynamic package.
Finally, the solution with the lighter battery layout provides, albeit slightly, a higher score, despite obligate to limit the maximum power to 68 kW (to avoid consuming all the energy before the end of the Endurance 22 km, instead of 80 kW), thus raising the lap time and decreasing the score. This, therefore, is not only the currently best combination, but it is also the one with the greatest potential for the 2019 season: indeed the values of the dynamic quantities (table 2.3), used for these simulations, relate to the SC18, so designing the SC19 with reduced drag would increase the maximum power that could be supplied and therefore would improve performance and score even more.

### Objectives

From the study just concluded it is clear how the car's performance and therefore the score obtained are much more sensitive to downforce than to drag, so the goal should be to maximize downforce, at the expenses of aerodynamic drag. However, there are generally two conditions that limit the value of the drag:

- The desired maximum speed
- The expected consumption

The constraint imposed by the maximum speed is calculated through the power equation, where the driving power must equal the resistant one:

$$P_{mot} = P_d = P_d^{rot} + P_d^{\alpha} + P_d^{iner} + P_d^{aero} \tag{2.12}$$

Since these circuits are on average flat, the contribution due to the inclination of the ground is zero. Similarly, the inertial term is null because, once the maximum speed is reached, no more acceleration is possible. Furthermore, knowing that the maximum speed is greater than the critical speed, the power dissipated per rolling is negligible compared to that due to the aerodynamic resistance.
Therefore, the only possible contribution is the aerodynamic one so it is possible to derive the binding condition on the drag:

$$P_d^{aero} = \frac{1}{2} S C_x v^3 \tag{2.13}$$

- The air density is assumed to be 1.18 $\frac{\text{kg}}{\text{m}^3}$ (the same value as CFD simulations);
- It is estimated a frontal area equal to 1 $\text{m}^2$ considering the axle track, the height both equal to 1.2 m and with cavities within the wetted perimeter of frontal area;
- The regulation determines the maximum power that can be explained overall by the four electric motors, limited to 80 kW.
- In each Formula Student event, the average speed is around 60 $\frac{\text{km}}{\text{h}}$ and the maximum speed is 130 $\frac{\text{km}}{\text{h}}$, as the tracks are always
  - Maximum extension of straight lines $< 80$ m;
  - Curves' radius: 9 m $\div$ 50 m;
  - Slalom: 7.5 m $\div$ 62 m;
  - Track carriageway $> 3$ m;

Therefore, by using the aerodynamic resistance value of the chosen configuration and the light battery layout, by equaling the engine power to the aerodynamic power, we obtain:

$$v_{max}^{id} = \sqrt[3]{\frac{2 \cdot P_{mot}}{\rho S C_x}} = 183 \frac{km}{h} \tag{2.14}$$

It can be noted that the speed is much higher than that achievable on Formula Student tracks [29]. Indeed, imposing the maximum speed of 130 $\frac{km}{h}$:

$$C_x^{disp} = \frac{2 \cdot P_{mot}}{\rho S v^3} = 2.88 \tag{2.15}$$

Then, in order not to limit the maximum speed of the vehicle, the aerodynamic resistance can be increased, in favour of downforce, up to a (very high) value of 2.88. Ergo, the maximum speed for Formula Student cars does not impose a stringent constraint on the drag's value.

As already anticipated, consumption is important not only for the efficiency score, but also for the size, and therefore the weight, of the battery that will have an important influence on the dynamics and performance of the vehicle. For these reasons it is important to quantify the aerodynamic resistance limits imposed by the expected consumption.
Performing simulations with five values of $C_z$ and five values of $C_x$ paired in turn, shows that the same lap time, approximately, can be obtained with

- Higher downforce values and lower efficiency;
- Lower downforce values and greater efficiency

The second solution, with respect to the first one, has the advantage of guaranteeing more points to the Efficiency score having a lower energy consumption for a double reason:

- Greater efficiency, so lower values of aerodynamic resistance and therefore less $P_d^{aero}$ ;
- Less vertical load on the tires which then develop a $P_d^{rot}$ (it is no longer negligible as we were not at top speed)

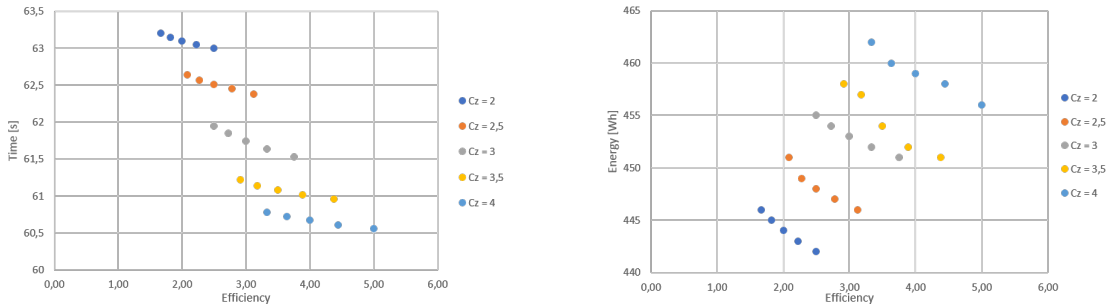


Figure 2.12: Downforce vs Efficiency

Taking into consideration the following aspects already debated at a qualitative level:

- Reduced lap time with increasing downforce;
- Decrease in battery weight as aerodynamic drag decreases;
- Rolling resistance decreases with decreasing downforce

quantitative simulations were performed to determine the optimal values of the SC19 aerodynamic package:

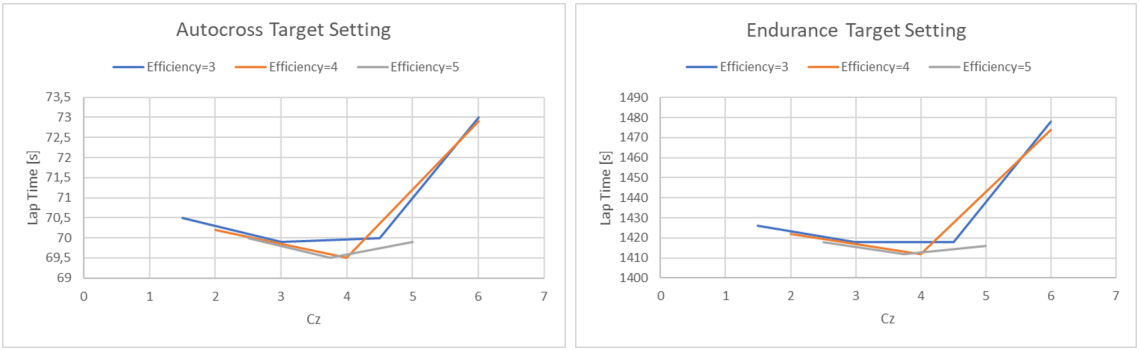


Figure 2.13: Target setting

It is clear that the dual condition of minimum lap time and minimum energy consumed occurs for:

$$C_z \approx 4 \qquad\qquad E \approx 4$$

These results indicate therefore, the target values to be reached in the 2019 season. Where the area value of 1 $m^2$ for the definition of the aerodynamic coefficients, has been chosen for two reasons:

- The reference area for motorsport is the frontal area of the vehicle, which in this case is approximately equal to 1 $m^2$;
- The arbitrariness in the choice of the reference surface can lead to remarkably different numerical values. For this reason, the chosen value does not introduce differences in terms of values between the quantities $C_z$ e $C_z$ and products $(C_z \cdot A)$ and $(C_x \cdot A)$ which instead are independent from the arbitrary choice of the reference area. This implies that the dissertation carried out can be interpreted both in specific terms and in absolute terms.

# Chapter 3

# CFD Methodology

## 3.1 Equations

In order to understand and to be able to perform and apply at best a post-processing, making it more similar to reality, the modelling of fluid behavior through a CFD software is necessary to know the equations that govern this phenomenon and the theory that determines them.

### 3.1.1 Definitions and physical quantities

#### Fluido

A fluid can be considered like a substance that deforms continuously (without therefore reaching an equilibrium configuration) when it is subjected to any shear tension (that is created by a force acting in a tangent direction to a surface).

The fluid is a dense molecular structure, but with weak chemical bonds: so the individual particles are free to move inside it.
The first necessary hypothesis, to avoid having to analyze the dynamics of each single microscopic particle is the theory of the continuous medium: treating the fluid as a continuous medium, the fluid particle can be equated to a point. The volume occupied by the particle must be large enough to statistically contain a significant number of molecules, but sufficiently small with respect to the characteristic size of the problem in question.
We can then hypothesize the fluid as a continuous medium if the Knudsen number is much smaller than 1:

$$Kn = \frac{l_{mfp}}{L} << 1 \tag{3.1}$$

In the case of air under standard conditions, the mean free path is $l_{mfp} \approx 10^{-8} m$
.
This hypothesis leads to consider, instead of the value of the single particle (microscopic), the average (macroscopic) value within a small volume, but which contains statistically a number of molecules sufficient to make the average a stable value.

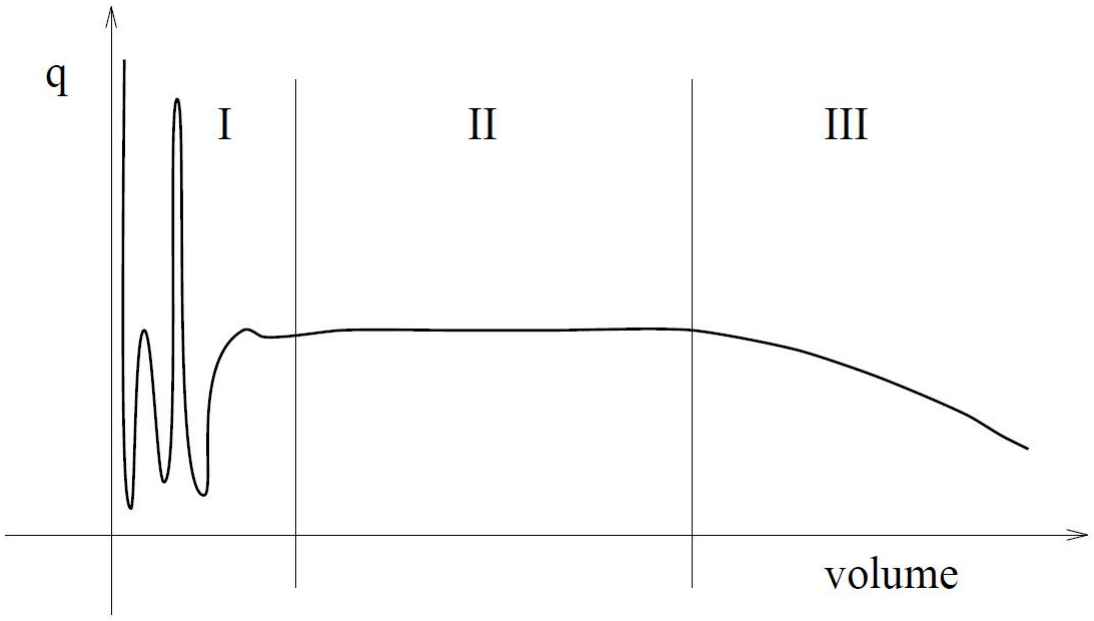


Figure 3.1: Variation of the measured value of a quantity q in relation to the dimensions of the measurement volume

**Density**

In this regard, we can define the density as the value of the mass of the particles contained within the unit of volume. In particular, the density of the gases is much lower than that of liquids due to the lower strength of the bonds and therefore to the greater rarefaction. Furthermore, the density of the gases varies strongly both with pressure and temperature, while that of liquids is almost totally independent from pressure (incompressibility).
Actually, the incompressibility of fluids is never total: indeed, each fluid has a compressibility modulus lower than infinite, and precisely this compressibility determines the finite speed with which a disturbance moves inside the medium. This speed is called the sound's speed and is linked to variations in density and pressure [9] :

$$a = \sqrt{(\frac{\partial p}{\partial \rho})_{isoentropica}} \tag{3.2}$$

where the hypothesis of constant entropy derives from the hypothesis of absence of friction and from the high speed of perturbation's propagation which makes the exchanged heat negligible.

**Viscosity**

In reality the friction inside a fluid exists (we will see later the importance it has): indeed, just like in a solid, if a tangential force is applied on the fluid's surface, shear tensions are born on the internal interfaces which tend to balance the external force. The birth of tensions implies the birth of deformations: sure enough, while the solid is deformed ($\beta$) until arriving to an equilibrium configuration in which the deformations are such as to generate sufficient tensions, the fluid, based on its

definition, will reach a speed of deformation ($\dot{\beta}$) such as to balance the system. Therefore $\tau \propto \dot{\beta} \propto \frac{\partial u}{\partial y}$:

$$\tau = \mu \cdot \frac{\partial u}{\partial y} \tag{3.3}$$

The proportionality coefficient is precisely the dynamic viscosity, whose value varies greatly depending on the fluid and the temperature variation [9] .
In liquids, viscosity decreases with increasing temperature due to weak bonds is more easily broken, whereas in gases, the opposite happens because of thermal agitation causes the particles to interact with each other in a more important way.
The Newtonian fluids are those fluids for which the viscosity does not depend on the speed and for which, therefore, the 3.3 holds.

#### Thermal conductivity

The interaction between the molecules of different fluid layers, through impacts, leads to exchange both momentum and kinetic energy, thus allowing their transmigration into the fluid. This kinetic energy migration coincides with the heat flow, or the amount of heat exchanged per unit of time and surface [9] :

$$q = -k \cdot \frac{\partial T}{\partial n} \tag{3.4}$$

### 3.1.2 Kinematics

#### Descriptions

There are two possible descriptions of the fluid's motion:

- Eulerian: the information on motion is expressed by what happens in fixed points of space while the fluid flows, therefore the properties are described as a function of time and spatial coordinates;
- Lagrangian: the information on motion is expressed by what happens on the "marked" particles following them as they move, therefore the properties are described as a function of time

The two descriptions are not independent but are related to each other through the vectorial law of motion, a scalar component of which will have the following expression [9] :

$$x_1^{eul} = x_1^{lag} + (a_{11} \cdot t)x_1^{lag} + (a_{12} \cdot t)x_2^{lag} + (a_{13} \cdot t)x_3^{lag} \tag{3.5}$$

Actually, as seen above, we are more interested in the velocities and their deformations, so it is of greater interest to express the link between the derivatives in the two descriptions:

$$\frac{D()}{D(t)} = \frac{\partial()}{\partial t} + (\vec{V} \cdot \vec{\nabla})() \tag{3.6}$$

Thus the Lagrangian derivative, also called material, has two contributions:

- Eulerian, also called local term, which represents the non-stationarity of motion;
- Spatial derivatives, also called convective term (advective), which represents the fact that the particle can vary its property because it has moved to another point in the field that could have different characteristics. Therefore this term depends on the motion of the particle, called convection, in areas of the field where there is a non-zero gradient of the considered property

Associated with the Eulerian description is the concept of control volume: volume in the space through which the fluid can flow, therefore it is a geometric entity independent of particles and mass.
Associated with the Lagrangian description is the concept of system: set of matter always composed of the same fluid particles, which can move and interact with the surrounding environment.

Now it is possible to understand how the Eulerian description is the most comfortable both from a theoretical point of view and from a practical point of view, but, besides not providing direct information on the variations of properties of a particle, it is incompatible with all the laws of the motion of a fluid which, like Newton's equations, refer to a "marked" body with its own mass.
It can therefore be seen that, in addition to the kinematic relationship of the two descriptions, there is a need for an equation that links the variations over time of an extensive property (B) in the two descriptions:

$$\frac{\partial B_{SIS}}{\partial t} = \frac{\partial}{\partial t}\int_{SIS} \rho b d\Omega \qquad \frac{\partial B_{VC}}{\partial t} = \frac{\partial}{\partial t}\int_{VC} \rho b d\Omega$$

This equation is provided by the Reynolds transport theorem [9] :

$$\frac{DB_{SIS}}{Dt} = \frac{\partial}{\partial t}\int_{VC} \rho B d\Omega + \int_{SC} \rho b \vec{V} \cdot \vec{n} dS \tag{3.7}$$

with SC control volume's surface, and therefore border, with normal $\vec{n}$ .

### 3.1.3 Dynamics

#### Mass conservation

Since the system is always made up of the same elements, the system's mass variation in time is null. The following equation is obtained through the Reynolds transport theorem:

$$\frac{\partial \rho}{\partial t} + \nabla \cdot (\rho \vec{V}) = 0 \tag{3.8}$$

From which it is possible to understand how, in the case of stationary flow, the quantity of mass entering the control volume must be equal to the mass coming out of it [9] .

**Momentum balance**

Taking advantage of Newton's law $\vec{F} = \frac{\partial m\vec{V}}{\partial t}$, the momentum balance is obtained by equalizing the sum of the external forces acting on the system to the variation of its momentum [9].

- External forces are divided into:
  - Volume forces: $\int_{VC} \rho\vec{a}d\Omega$ ;
  - Surface forces: $\oint_{SC} \underline{\Pi} \cdot \vec{n}dS = \int_{VC} \nabla \cdot \underline{\Pi}d\Omega$
- Variation of the Lagrangian momentum is divided, as usual, into the punctual and convective contribution

Both convective and surface forces terms are worthy of further study.

The first one takes into account the velocity vector property which varies because the particle moves in this field transported by the same velocity vector field. I.e., the particle has three velocity components that take it to an area of space where these components are different which become the new ones possessed by the particle that will then be transported to another area of the space. Therefore, unlike solids, the particle will take on a property that depends on the zone, but the reached zone is, in turn, determined by the direction and the module of the velocity vector. Therefore, each speed component will depend on all the others and not only on its own: this feature is the basis of the turbulence phenomenon and is expressed through the diatonic product $\nabla \cdot (\rho\vec{V} \otimes \vec{V})$, obtained through the material derivative's proof (or equivalently of the Reynolds transport theorem) also rewritable as $\rho(\vec{V} \cdot \vec{\nabla})\vec{V}$ .

The surface forces are described by a tension vector for each surface: $\vec{F_S} = \int_{SC} \vec{t}dS$.

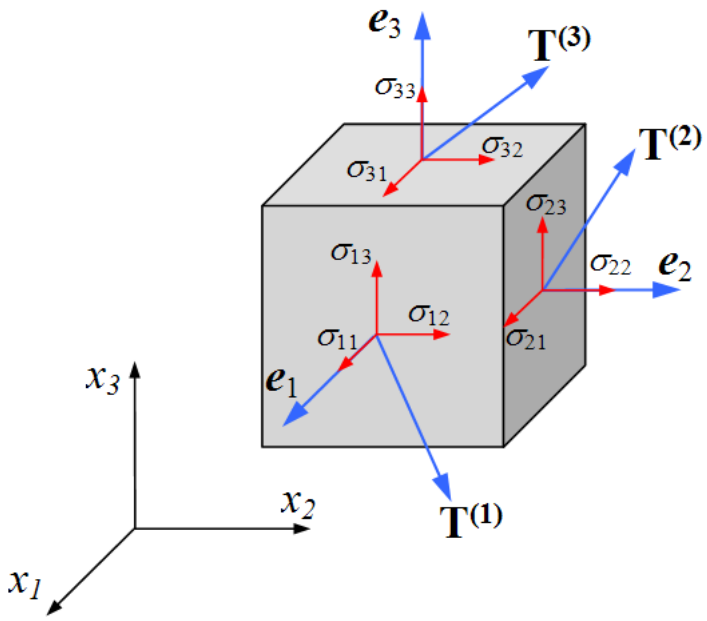


Figure 3.2: Stress components

In turn, the tension vector will have three components and therefore everything can be expressed through a 3x3 tensor: indeed, for each of the three normals that identify each surface we will have that the surface force will have three components, one normal and two of shear:

$$\vec{t} = \underline{\Pi} \cdot \vec{n} \qquad\qquad \vec{F_S} = \int_{VC} \vec{\nabla} \cdot \underline{\Pi} dS$$

A first formulation of the equation of the momentum balance is obtained:

$$\frac{\partial \rho \vec{V}}{\partial t} + \nabla \cdot (\rho \vec{V} \otimes \vec{V} + \underline{\Pi}) = \rho \vec{a} \tag{3.9}$$

If you want to further detail it, you can divide the contribution of the tensor of surface stresses into [2] :

- Forces in inertial conditions
- Forces in dynamic conditions

$$\underline{\Pi} = \underline{\Pi_{hydst}} - \underline{\Pi_{\nu}} \tag{3.10}$$

It is known that in inertial conditions (stillness or uniform motion) there are no tangential efforts, so only normal stresses are present, which do not depend on the direction, but only on the position: that is the pressure. So the three normal stresses must be equal and coincide with the pressure value: $p = \frac{tr(\underline{\Pi})}{3}$ .

For a Newtonian fluid the tensions depend linearly on the speed of deformations, so it can be shown as $\underline{\Pi_{\nu}} = (-\lambda - \frac{2}{3}\mu)(\nabla \cdot \vec{V})\underline{I}$ . Where $\lambda$ is another viscosity

coefficient: $\lambda = -\mu \cdot \dfrac{\nabla\vec{V} + (\nabla\vec{V})^T}{\vec{\nabla}\cdot\vec{V}}$, generally taken equal to $-\dfrac{2}{3}\mu$ to ensure that even for compressible fluids the normal tension coincides with the pressure.

$$\underline{\Pi_{hydst}} = p\underline{I} \qquad (3.11) \qquad\qquad \underline{\Pi_\nu} = \rho\nu[\nabla\vec{V} + (\nabla\vec{V})^T - (\frac{2}{3}\nabla\cdot\vec{V})\underline{I}] \qquad (3.12)$$

Thus, a second, more detailed, expression of the momentum balance was reached:

$$\frac{\partial\rho\vec{V}}{\partial t} + \nabla\cdot(\rho\vec{V}\otimes\vec{V}) + \nabla p = \nabla\cdot\underline{\Pi_\nu} + \rho\vec{a} \qquad (3.13)$$

**Energy conservation**

The energy conservation equation derives from the first principle of thermodynamics, so we need to match the total energy variation of the system (punctual and convective term) to heat and work contributions [2] :

- heat is exchanged only by conduction;
- the work is done both by volume's and external forces

$$\frac{\partial\rho_t}{\partial t} + \nabla\cdot(\rho e_t\vec{V} + \vec{q_a} + \underline{\Pi}) + \rho\vec{a}\cdot\vec{V} = 0 \qquad (3.14)$$

**Navier - Stokes**

In conclusion, the main equations governing the motion of a fluid are 5 (1 vectorial, 2 scalars):

$$\begin{cases} \dfrac{\partial\rho}{\partial t} + \nabla\cdot(\rho\vec{V}) = 0 \\ \dfrac{\partial\rho\vec{V}}{\partial t} + \nabla\cdot(\rho\vec{V}\otimes\vec{V}) + \nabla p = \nabla\cdot\underline{\Pi_\nu} + \rho\vec{a} \\ \dfrac{\partial\rho_t}{\partial t} + \nabla\cdot(\rho e_t\vec{V} + \vec{q_a} + \underline{\Pi}) + \rho\vec{a}\cdot\vec{V} = 0 \end{cases}$$

In general, these 5 equations are all intimately related to each other, and, in addition, they need other equations in order to arrive at the closure of the system: indeed, the unknowns should be 5 (pressure, speed components, temperature), instead in this system they are 15. The value of the parameters, and not of the unknowns present in the system, is obtained by:

- Equation of state of perfect gases: relationship between pressure, density and temperature;
- Thermal flow model equation: conduction heat exchange, as seen before;
- Boundary conditions: it is necessary to know the overall situation, therefore having, for example, a known speed profile;
- Complete model of the viscous stress equation: evaluation of speed gradients

In particular, the value of the dynamic viscosity is very low for the vast majority of fluids, for example at T = 20 °C :

| Fluid | Dynamic viscosity $[Pa \cdot s]$ |
|---|---|
| Air | $18.3 \cdot 10^{-6}$ |
| Water | $10^{-3}$ |
| Petrol | $0.65 \cdot 10^{-3}$ |
| Lubricating oil | 0.11 |
| Asphalt | $10^{5}$ |

Table 3.1: Main dynamic viscosity values

Taking into account the fact that viscous efforts, to be non-negligible, must be in the order of MPa, i.e. reaching values of $10^6$ Pa at least, it is clear that the speed gradients, in a flow that has scale dimensions not insignificant, cannot have such a high vlue as in the case where viscous terms are significant.
Ergo, for the motion not in direct contact with the wall, it can be assumed that the fluid is inviscid, which makes it possible to obtain simpler equations, as will be seen in the next paragraph.

Further simplifications of the system can be performed considering the Mach number, defined as the ratio between the speed of the fluid and the sound's speed in the medium:

$$Ma = \frac{|V|}{|a|} \tag{3.15}$$

Specifically, if $Ma \leq 0.3$ then the fluid can be considered incompressible, since the variations of density and therefore of temperature are very small, such as to be able to consider these quantities as constant [9] . This affects the decoupling of the energy equation, which is no longer connected to the other four, given that there are no heat flows linked to the temperature variation: so, in the case of interest only for the fluid flow, i.e having as an unknown the three components of velocity and fluid pressure, it is useless to solve this scalar equation.

### 3.1.4 Ideal and incompressible fluid

An ideal fluid is an inviscid fluid $\mu = 0$ , while incompressible means that $\rho =$ *costante*. Since an inviscid fluid does not act as a tangential force, the only forces that develop are the weight and the pressure, whose directives both pass through the center of mass of the particle: therefore, in an inviscid fluid the particles which move coming from a region where the motion is irrotational, continuing in their motion they cannot start to rotate [9].

#### Velocity potential

The irrotational motion therefore foresees a vorticity null $\vec{\zeta} = \vec{0}$, where:

$$\vec{\zeta} = \nabla \vec{\times} \vec{V} = 2\vec{\omega} \tag{3.16}$$

Therefore in the two-dimensional case it must be valid:

$$\frac{\partial v}{\partial x} - \frac{\partial u}{\partial y} \tag{3.17}$$

It is identically satisfied, just replace the 3.18 in 3.17:

$$\vec{V} = \vec{\nabla}\phi \tag{3.18}$$

where $\phi$ is the speed potential, and exists only in the case of null vorticity. It is clear that when the potential is known, it is possible to calculate the whole velocity field: this function can be calculated by exploiting the mass conservation equation which becomes, for potential, a Laplace equation [9]. Thus, the potential motion is the irrotational motion of an incompressible inviscid fluid described by the Laplace equation:

$$\nabla^2\phi = 0 \tag{3.19}$$

Laplace equation's major advantage is its linearity, so a linear combination of its solutions is its solution. This allows to obtain solutions for remarkable cases, while for the more complex ones it is sufficient to use the superposition of the effects. In particular the remarkable cases are combined in such a way as to generate a speed field that is always tangent to a body (impermeability condition) and therefore the resulting flow will be the potential flow around that given object.

### 3.1.5 Boundary layer

In potential theory the tangential speed on the body contour is not null: the fluid slides on the contour instead of adhering to it. Ergo, all potential flows, due to non-viscosity, violate the adherence condition and, more generally, do not accurately represent the speed field near the body: this thin zone is precisely called the boundary layer [9] .
However, as long as the viscosity is limited to thin and negligible regions of the motion field, the potential motion still manages to describe correctly:

- The speed field of the undisturbed flow (only if the boundary layer has not separated);
- The pressure field because the thickness of the boundary layer is negligible, and therefore, as will be seen, there is no change in pressure within it

This occurs for aerodynamically "well-started" invested bodies at high Re numbers. The first condition guarantees a negligible thickness of the wake, while the high Re numbers limit the boundary layer to a thin region around the profile. Outside these regions the fluid can be considered as inviscid.

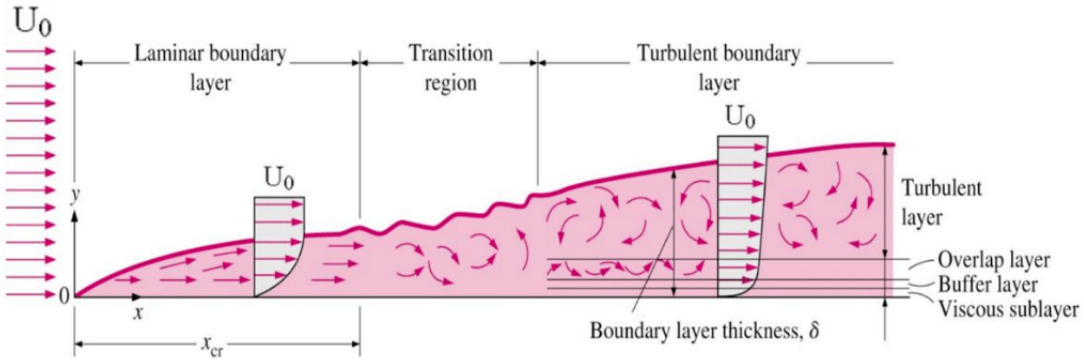


Figure 3.3: Boundary layer

Within the thickness of the boundary layer the speed varies from the undisturbed value to the null value to respect both the conditions at the boundary. For this reason one of its possible definitions is: the thickness of the boundary layer is the distance from the wall where the velocity component parallel to the body has a value of 99% of that of the external current [9].

In the boundary layer the flow can be laminar or turbulent, with considerable differences from the point of view of the velocity profile within its thickness. in fact, the turbulent profiles are flatter, have a higher wall gradient and a greater thickness.

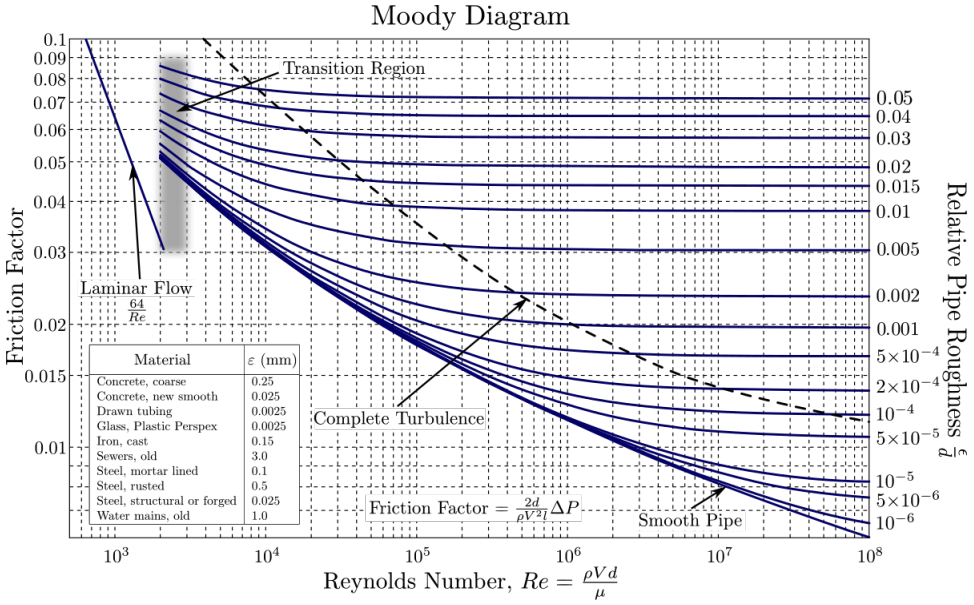


Figure 3.4: Moody diagram

At the leading edge the thickness of the boundary layer is zero, then it grows with the distance, but it always remains much smaller than the characteristic size of the object if the viscosity is low. So the phenomenon's scales in the two directions are completely different (L and $\delta$): in particular, in the direction of the boundary layer's thickness the scale is much smaller so that the gradients are much higher and therefore, despite the low value of the viscosity, they do not make more negligible viscous effects.

As already illustrated, in the boundary layer the viscous terms of Navier-Stokes are not negligible, which is why they must be of the same order as the convective ones. Taking, for convenience,a single convective term and a single viscous term we can estimate the thickness of the boundary layer:

$$u\frac{\partial u}{\partial x} \approx \frac{U^2}{x} \qquad \nu\frac{\partial^2 u}{\partial y^2} \approx \nu\frac{U}{\delta^2}$$

$$\delta \approx \sqrt{\frac{\nu x}{U}} = \frac{x}{\sqrt{Re(x)}} \tag{3.20}$$

Notice how it depends on:

- Body x-coordinate: $\delta$ grows along the flow direction;
- Viscosity: $\delta$ increases with increasing viscosity;
- Undisturbed speed: $\delta$ increases as the speed of the undisturbed flow decreases

Using the dimensionless equations it is possible to prove that:

- In the boundary layer the transverse velocity component is larger than the undisturbed flow's one, but is in any case negligible with respect to the relate longitudinal components;
- $\frac{\partial p}{\partial y} = 0$, which indicates, as anticipated, that the pressure distribution is that calculated with the potential motion: and therefore the pressure in the boundary layer is imposed by the external solution

Consequently, the dimensional equations of the boundary layer motion, also known as Prandtl equations, are:

$$\frac{\partial u}{\partial x} + \frac{\partial v}{\partial y} = 0 \tag{3.21}$$

$$u\frac{\partial u}{\partial x} + v\frac{\partial v}{\partial y} = -\frac{1}{\rho}\frac{dp}{dx} + \nu\frac{\partial^2 u}{\partial y^2} \tag{3.22}$$

with the following boundary conditions:

$$u(x, y = 0) = 0 \tag{3.23}$$

$$v(x, y = 0) = 0 \tag{3.24}$$

$$u(x, y = \infty) = U_e(x) \tag{3.25}$$

$$u(x_0, y) = u_{in}(y) \tag{3.26}$$

where:

- 3.23 represents the adherence condition;

- 3.24 indicates the impermeability condition;
- 3.25 expresses the linked speed profile;
- 3.26 symbolizes the need to know a speed profile in order to calculate the solution

The Prandtl equations are analogous to Navier-Stokes ones, with an important difference: in the boundary layer everything that happens downstream does not influence what happens upstream.
The solution of these equations allows the calculation of the tangential stresses on the body and therefore the aerodynamic resistance due to friction.

While the pressure in the boundary layer is the same as the undisturbed flow, the viscosity is much more relevant and tends to dissipate energy by reducing speed. Thus the pressure gradient greatly influences the resulting force and therefore the motion of the particles.
In particular, the condition $\frac{dp}{dx} = \mu(\frac{\partial^2 u}{\partial y^2})_{y=0}$ indicates the beginning of the boundary layer's separation which leads to velocity vectors near the wall directed in the opposite direction to that of the external current generating a recirculation zone.
The turbulent boundary layer has a greater exchange of momentum, so it goes to energize the weaker layers near the body more effectively, thus delaying the separation of the boundary layer.

### 3.1.6 Turbulence

The treatise carried out so far is valid only for laminar motion.

- In fluid dynamics we talk of laminar flow or laminar regime when the motion of the fluid occurs with the sliding of infinitesimal layers over each other without any type of fluid mixing, even on a microscopic scale. The flow is governed by viscous forces and is constant over time (steady flow).
- In fluid dynamics, a turbulent regime is a fluid motion in which the viscous forces are not sufficient to counteract the inertia forces: the resulting motion of fluid particles takes place chaotically, without following ordered trajectories as in the case of laminar regime.

A turbulent flow differs from a laminar flow because within it there are swirling structures of different size and speed that make the flow unpredictable over time even if the motion remains deterministic. That is, motion is governed by the laws of deterministic chaos: if we were able to know 'exactly' the whole velocity field at a given instant and were able to solve the Navier-Stokes equations we could obtain all the fields of future motion. But if we knew the field with a very small inaccuracy, after a certain time it would make the found solution completely different from the real one.

The difference between the two types of motion is indicated by the Reynolds number (as shown by the homonymous experiment), and in particular by its critical

value (depending on the geometry of the body) which establishes the difference between high and low values:

$$Re = \frac{\rho |V| L}{\mu} = \frac{|V| L}{\nu} \tag{3.27}$$

Equation 3.27 expresses the relationship between inertial forces and viscous forces. In laminar motion the fluid is much more ordered due to the predominance of dissipative phenomena and therefore of viscous forces, so it occurs at low values of the Reynolds number.

The turbulent motion, which occurs therefore for high values of the Reynolds number, is characterized by the presence of vortices, i.e. parts of fluid that whirls around the entire field of motion, contributing to the transport of mass, momentum and energy between the various areas of the field very quickly, so that the turbulent regime involves significant fluctuations in the values of speed, pressure, temperature and, in the case of compressible fluids, also of density.
This conclusion is confirmed if quantities (speed, pressure, density and temperature components) are broken down into a mean time value and into a fluctuating component over time:

$$u(x, y, z, t) = \overline{u}(x, y, z) + u'(x, y, z, t) \tag{3.28}$$

where not only the fluctuating component determines the instantaneous value of the quantity, but also influences, through its presence in the Navier-Stokes equations, also the mean value which is the most interesting quantity in the engineering field.

The process of turbulent motion can be interpreted as a series of vortices, of different dimensions and strength, where the smaller ones are stuck in the larger ones, continuously changing, which give the motion a character of randomness. This makes characteristic of the turbulent phenomenon the presence, in fully developed motion, of a wide spectrum of magnitude scales, both spatial and temporal, in relation to the dimensions of the considered vortices, which are, indeed, of different dimensions due to the continuous fragmentation of larger vortices in smaller vortices. Each vortex can be described by two parameters, its diameter d and its orbital speed $\widehat{u}$ , varying from vortex to vortex; in the hypothesis of stationary, homogeneous and isotropic turbulence, all the vortices of a certain size, i.e. with the same diameter d, behave more or less in the same way and have the same orbital velocity, for which it can be assumed that it is, precisely, function of d.

The range of variation, in space and in time, of speed is linked to the strong non-linearity of the equation of motion for high Re values. The non-linear terms determine, in fact, the spread, through an interaction between the different scale of magnitude, of the kinetic energy of motion from the largest scales, where it is produced, to the smallest ones, where it is dissipated by the viscosity of the fluid; this process is called turbulent energy cascade or cascade of vortices.
The process is stationary and, therefore, the rate of energy transfer from one scale to the next must be the same on all scales, so that no group of vortices belonging to the same scale presents a decrease or increase in its total energy over time. In other

words, the energy production rate on the largest possible scale, which corresponds to a diameter $d_{max}$, is equal to the rate of dissipation on the smallest possible scale, with diameter $d_{min}$ and, therefore, all vortices, both large and small , are always simultaneously present in the turbulent motion. We can therefore now define $\epsilon$ as the energy production / transfer / dissipation rate per unit mass of the fluid, which is dimensionally $m^2\,K^{-3}$; in other words, this parameter represents, per unit of mass and time, both the energy supplied to the turbulent motion, on the largest scale, and the energy transferred from a larger scale to a smaller one, and, finally, the energy dissipated on the smallest scales from viscosity. Furthermore, Kolmogorov's theory makes the hypothesis that the characteristics of the vortices depend only on their diameter d and on the characteristic energy rate of the vortex cascade, i.e. that the orbital velocity depends on d and on $\epsilon$.

Since the small movements take place on a very small time scale, it can be assumed that they are statistically independent from the main motion and from the large-scale turbulence linked to it. In this hypothesis, they depend only on the energy transferred along the vortex cascade and on the viscosity of the fluid. Furthermore, since the kinetic energy of small and medium motions varies according to the characteristics of the average motion, it can be assumed that the behavior on the intermediate scale depends only on the energy transferred from the larger scale, which is then dissipated on the lower scale. This approach forms the basis of the Kolmogorov turbulence equilibrium theory, which is based on the hypothesis that the Reynolds number is so high that the scale, at which the production of turbulent kinetic energy takes place, is quite different from the one at which it has place its dissipation.

## 3.2 Geometry

The geometry imported into the CFD software (Star CCM +) was created using the Catia V5 CAD software. The original CAD file, being the design file of the entire car, included a very complex geometry both for the parts inside the bodywork and for the external parts. The CAD file used for CFD simulations has a simplified geometry, both to reduce the onerousness of the calculation (need for a smaller number of cells, therefore both mesh and faster iterations), and for the convergence of the solution (as with ultra detailed geometry if a mesh is not made so detailed the software fails to understand what happens, running to a very high Reynolds number in those areas that invalidates the convergence of the solution). Therefore, the CAD model was developed to represent the main components that influence the flow, in particular:

- The components residing inside the body have been completely eliminated, as they had no influence from an aerodynamic point of view and weighed down the CAD file;
- The complex geometry components outside the body were:
  - Eliminated, as in the case of electrical power and signal cables or as the pipes for the cooling liquid, or finally as the switches, in that their influence is minimal and their geometry had not yet been defined;

– Simplified, like the suspensions, the pilot, the radiators, the wheels (with a footprint), the electric motors

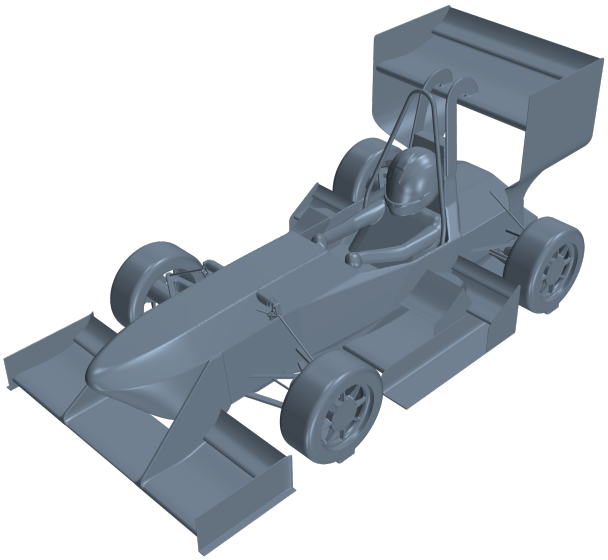

Figure 3.5: Imported CAD

As you can see from the figure 3.5, the elements considered in the geometry are: aerodynamic package, monocoque, damper, suspension, rocker, motors' cooling jacket, pilot, main hoop, supports, wheels with footprint, radiators.
In particular, the rear damper was not inserted since it is located behind the driver's headrest and therefore its influence on aerodynamics is totally null.
As for the pilot, it is a simplified model of the 95th percentile, that is the most probable stature in men.

CFD analyses were conducted using the Galilean relativity principle, i.e. the fixed vehicle and the air in relative motion. To do this, a parallelepiped having the function of a tunnel was made, of sufficient size both to prevent the artificial walls from influencing the solution, and to allow the full development and calculation of the wake, fundamental for the accuracy of the solution.
As the analysed region we used the geometry resulting from the logical operation of subtraction between the the tunnel's one and the car's one, corresponding exactly to the volume of air taken into consideration. Indeed, we are interested in knowing both the motion in this region and the exchanged force values on its contour with the car components.

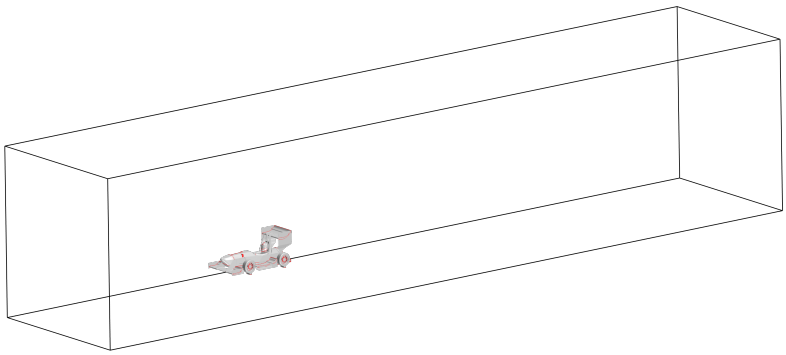

Figure 3.6: CFD wind tunnel domain

According to [22], the dimensions of the gallery are:

- Length: 10 m ahead e 20 m behind, with car's length 1.8 m;
- Width: 6 m from symmetry plane, with half-car's width 0.6 m;
- Height: 6.26 m from ground, with car's height 1.2 m

## 3.3 Physic models

**Three-dimensional**

The CFD simulations carried out are divided into two types:

- Two-dimensional: preliminary analysis exploiting the possibility of testing many different solutions in a short time and being able to understand their potential;
- Three-dimensional: design of the details since, considering all the effects deriving from the three-dimensionality of motion, they lead to very precise solutions, fundamentals both to know the exact values at stake and to perform a correct post-processing, and therefore be able to make the appropriate implementations

**Incompressible and segregated flow**

Starting from the theoretical concepts and equations expressed above, all the physical models to be used in CFD simulations have been established.
First of all, as already mentioned, the average and maximum speeds of the car will be 60 $\frac{\text{km}}{\text{h}}$ e 130 $\frac{\text{km}}{\text{h}}$, corresponding respectively to 16.67 $\frac{\text{m}}{\text{s}}$ e 36.11 $\frac{\text{m}}{\text{s}}$, with the speed of sound in the air at 20 °C equal to 343.8 $\frac{\text{m}}{\text{s}}$, ergo:

$$\overline{Ma} = \frac{16.67}{343.8} = 0.05 << 0.3 \qquad Ma_{max} = \frac{36.11}{343.8} = 0.11 << 0.3$$

The above analysis shows that the air can be modeled as an incompressible fluid, and so the first established physical law is: $\rho = cost$.
The immediate consequence was, therefore, to eliminate, in order to save computational resources, the energy equation, given that the unknown temperature is not useful for the purposes of this analysis, and so the flow is assimilated to a segregated flow.

### Steady flow

Analysis of inertial and viscous forces at medium speed:

$$Re = \frac{1.18 \cdot 16.67 \cdot 2.86}{1.83 \cdot 10^{-5}} = 3074203 \tag{3.29}$$

Leads to consider a definitely turbulent motion. As already anticipated, the knowledge of the instantaneous value of the quantities over time is not an engineering interest, indeed it is interesting to understand the behavior of the car over time and not in a single instant. This explains the particular interest for the mean value over time of the various quantities, which therefore leads to the choice of the steady flow model.

### RANS equations

Replacing the 3.28 in the segregated Navier-Stokes system:

$$\begin{cases} \nabla \cdot \overline{\vec{V}} = 0 \\ \rho(\dfrac{\partial \overline{\vec{V}}}{\partial t} + \overline{\vec{V}} \cdot \nabla \overline{\vec{V}}) = -\nabla \overline{p} + \mu \nabla^2 \overline{\vec{V}} - \nabla \cdot \rho \begin{bmatrix} \overline{u'u'} & \overline{u'v'} & \overline{u'w'} \\ \overline{v'u'} & \overline{v'v'} & \overline{v'w'} \\ \overline{w'u'} & \overline{w'v'} & \overline{w'w'} \end{bmatrix} \end{cases}$$

where the last term is the turbulent stress tensor, also called the Reynolds stress tensor.

These recirculating fluid motions cannot create or destroy mass, but fluid parcels transported by the eddies will carry momentum and energy into and out of the control volume. Figure 3.13 shows that, because of the existence of the velocity gradient, fluctuations with a negative y-velocity will generally bring fluid parcels with a higher x-momentum into the control volume across its top boundary and will also transport control volume fluid to a region of slower moving fluid across the bottom boundary. Similarly, positive yvelocity fluctuations will – on average – transport slower moving fluid into regions of higher velocity. The net result is momentum exchange due to convective transport by the eddies, which causes the faster moving fluid layers to be decelerated and the slower moving layers to be accelerated. Consequently, the fluid layers experience additional turbulent shear stresses, which are known as the Reynolds stresses. In the presence of temperature or concentration gradients, the eddy motions will also generate turbulent heat or species concentration fluxes across the control volume boundaries. This discussion suggests that the equations for momentum and energy should be affected by the appearance of fluctuations [26].

Ergo, this equation is formally similar to the classical Navier-Stokes equation, but it encompass the effects of turbulence in the equations of momentum and energy, while not of continuity one. Indeed, it contains the average time values of the corresponding physical magnitudes of the turbulent field and, moreover, to the second member, there are 3 further terms, which contain, as we have seen, the products of the speed agitation components. These terms represent the contribution of the turbulent phenomenon to the average velocity field and, if multiplied by the density , have the size of tensions and are therefore called Reynolds stresses or turbulent stresses. They produce an effect similar to that of the viscous types' stresses, although it must be remembered that the latter have a physical basis in the viscosity of the fluid, while the turbulent stresses arise from the presence of agitation components in the turbulent motion field. In other words, the turbulent vortices carry different properties of the fluid due to their random three-dimensional motion that add to the fluid's main motion (mean one).

This system, useful for the mean value treatment, takes the name of Reynolds Average Navier Stokes (RANS), and is the model of motion equations that will be implemented in place of Direct Navier Stokes (DNS), containing the real equations, but it is much more computationally expensive and lacking in interest because it is not important to find the value of the fluctuations, but only their effects. However, DNF only has 4 unknowns, while in RANS all 6 mixed products are added, so there is a need for additional equations to make the system determined.

**Turbulence flow**

These equations are provided by the chosen turbulence model (indeed, as obvious, we choose a model of the turbulent regime), where the model is defined as the computational procedure that allows us to quantify the effects of fluctuations.

The $k - \epsilon$ model, widely validated, is a more sophisticated and a general, but also a more costly, description of turbulence which allows the effects of transport of turbulence properties by convection and diffusion and production of destruction of turbulence [26]. The choice fell on this model because it has a low computational cost, less than the more precise RSM model, but at the same time, having two parameters to characterize it, it is much more stable and more easily arrives at the convergence than the Spallart-Allmaras model, as demonstrated by Lewis and Postle [14].

T he turbulent kinetic energy per unit of mass is $k = \frac{1}{2}(\overline{u'^2 + v'^2 + w'^2})$, which gives a direct measure of the intensity of fluctuating speeds, while *epsilon* is the energy dissipation rate. At the base of this model there is an analogy between the viscous stresses and Reynolds ones, that is to put in relation the latter to the deformation's speed of the fluid element, which, as known, is linked to the gradients of the velocity components in the different spatial directions.
We use k and $\epsilon$ to define velocity scale $\theta$ and length scale $l$ representative of the large-scale turbulence as follows:

$$\theta = \frac{k}{2} \qquad\qquad l = \frac{3}{2}\frac{k}{\epsilon}$$

One might question the validity of using the 'small eddy' variable $\epsilon$ to define the 'large eddy' scale. We are allowed to do this because at high Reynolds numbers the rate at which large eddies extract energy from the mean flow is broadly matched to the rate of transfer of energy across the energy spectrum to small, dissipating, eddies if the flow does not change too rapidly.

## 3.4 The finite volume method

### 3.4.1 Mesh

As already illustrated, although the laws of motion are built on the Lagrangian description, in reality they are used through the Eulerian description, because it can be put in practice easily. Ergo, the equations found so far, must be integrated within a control volume, then deriving the finite volume method that is used in CFD simulations.
In this case the control volume cannot be the entire "subtraction" presented previously because the numerical method is able to calculate only what happens on the border of the defined control volume, and this leads to two drawbacks:

- It is not possible to visualize what happens to the flow within this volume;
- The numerical method finds enormous difficulties to calculate the solution because within that whole domain there are phenomena that it is not possible to see with this method and therefore to find the right direction to reach solution, and then is probable to diverge. For example, it could take a road or another one that would lead to the same configuration on the border, but perhaps is due to completely different phenomena inside the volume.

As illustrated, the domain is in turn discretized into smaller volumes. Continuous equations are integrated within them in order to create equations discretized in nodal points. The discretized equation is no longer differential, but becomes algebraic and is modified considering the boundary conditions, where the boundary is the one with the other volumes.
Discretized equations must be set up at each of the nodal points in order to solve a problem. For control volumes that are adjacent to the domain boundaries the general discretized equation is modified to incorporate boundary conditions. The resulting system of linear algebraic equations is then solved to obtain the distribution of a general property at nodal points [26].
Since it is, therefore, a system composed of a finite number of algebraic equations, a numerical method can be implemented that calculates the solution at each nodal point through multiple iterations. Once the system has been solved, the solution is approached at the points between the different nodal points,whose solution is now known, in a linear, parabolic or more advanced manner depending on the degree of precision desired.

This discretization of the domain is called mesh. The volumes can be of different shapes and this implies different characteristics of the mesh: indeed, when

the processor calculates the value of the thermo-fluid dynamic variables of each cell, referred to its center of gravity (nodal point), it does so by involving the values of the centers of gravity of the adjacent cells, which in the case of tetrahedral cells are four while in the case of polyhedral cells there are more, depending on the number of faces composing the polyhedron, having a higher order interpolation function and therefore with a best degree of solution approximation in points between the different nodes.
However, Star CCM + first creates the tetrahedral volume grid, from which it then joins multiple cells of this type to obtain a polyhedron volume grid, so that the number of elements in the second case is smaller than in the first. The fluid volume discretized with this grid contains a lower number of cells than tetrahedral one.
In conclusion, therefore, with the polyhedral mesh you have the disadvantage of having information, as regards speed and pressure, in fewer points than the field, but at the same time the mathematical model is affected by a lower error, as highlighted above. Actually, Star CCM + also features a trimmed mesh that is based on hexahedral cells.
In any case the solution is never exact, due to the presence of a numerical method of resolution; moreover it should not depend on the mesh made, since it is only a fictitious construction to be able to apply the numerical method, but absent in reality. So it was necessary to develop a sensitivity analysis of the solution to varying of the mesh, verifying that as the type and fineness changes, the solution always converges to the same solution.

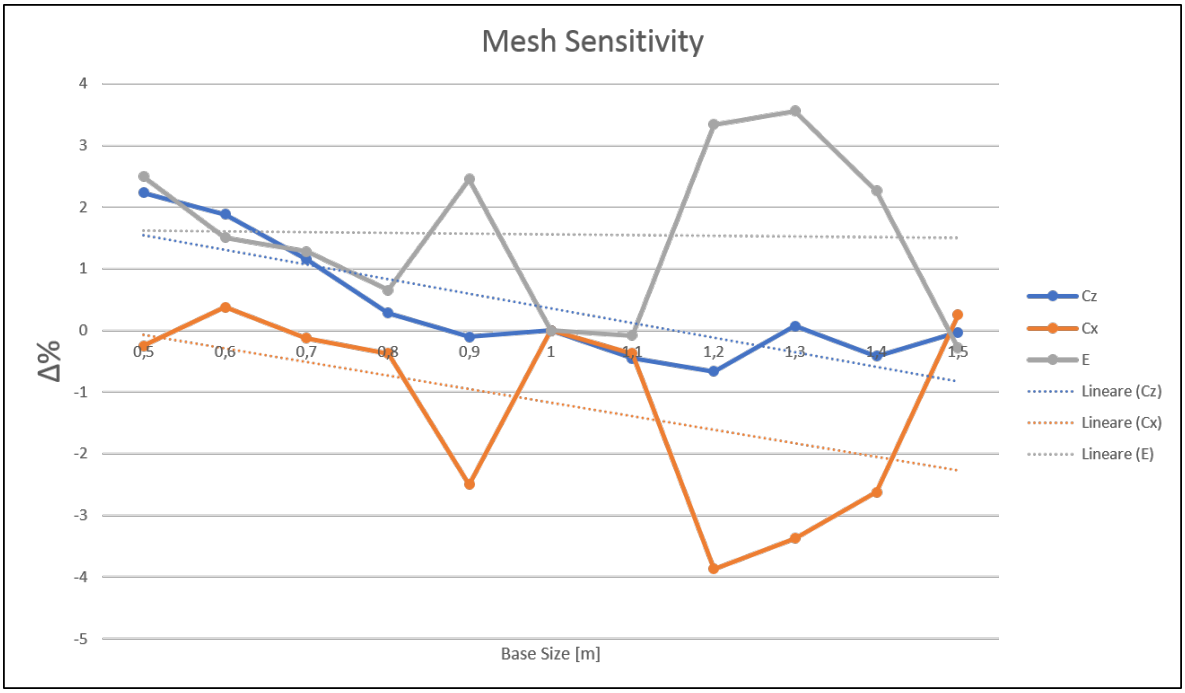


Figure 3.7: Mesh sensitivity

Finally, it was decided to use the polyhedron typology because, as specified, it requires a lower number of cells and therefore a lower computational cost. Depending on the sensitivity analysis performed, the following characteristic values of the general mesh were set:

| Property | Description | Value |
|---|---|---|
| Target Surface Size | Max Dimension | 300 mm |
| Minimum Surface Size | Min Dimension | 1 mm |
| Surface Growth Rate | Dimension Increase | 1.1 |

Table 3.2: Mesh size

Since the minimum size is so low, especially for the areas with more variable geometry, it was decided to impose a greater minimum size for the monocoque, being a more sinuous geometry, equal to 5 mm to reduce the computational cost.
For the same reason, the creation of the prismatic mesh for the boundary layer on every real walls of the tunnel with the exception of the ground was similarly disabled, because ground and flow have the same speed so there are not speed gradients.

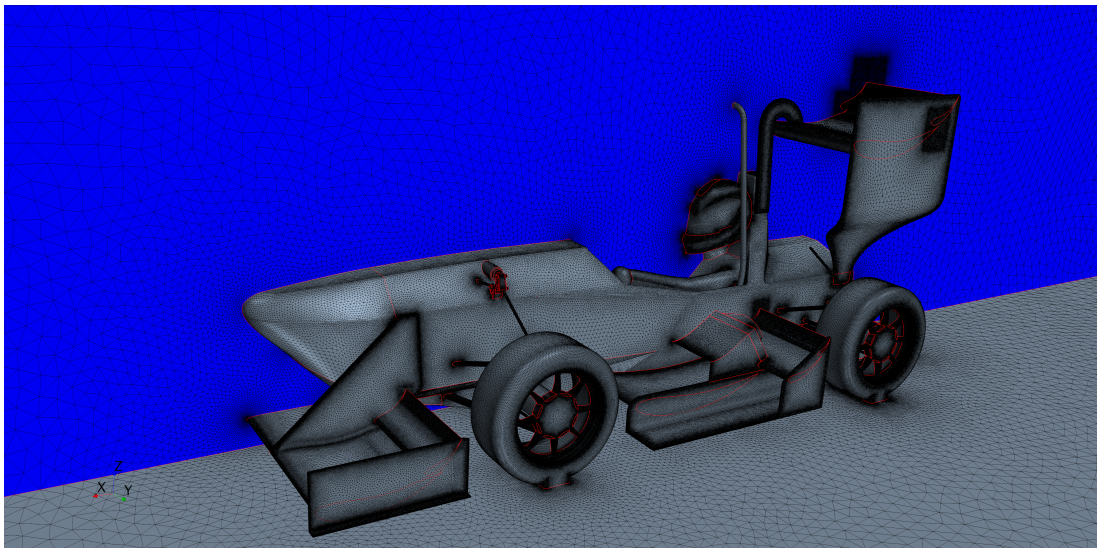

Figure 3.8: Car mesh

As already illustrated, the volumes cannot be the same everywhere, but they must be smaller where the flow is much more variable so that these variations can be calculated in order to both visualize them and prevent the numerical method from diverging.
For this purpose, further refinements of the mesh in the following areas have been defined (the size indicated is the maximum size of the cell in the specific area):

| Area | Value mm |
|---|---|
| Wake | 70 |
| Vehicle | 60 |
| Wings | 40 |
| LE and TE | 2 |
| Undertray | 10 |
| Suspensions | 50 |
| Radiators | 50 |

Table 3.3: Mesh refinement

Since in these areas there are components that significantly alter the flow, and consequently influence it a lot, for example, with the creation of vortices that must be considered.

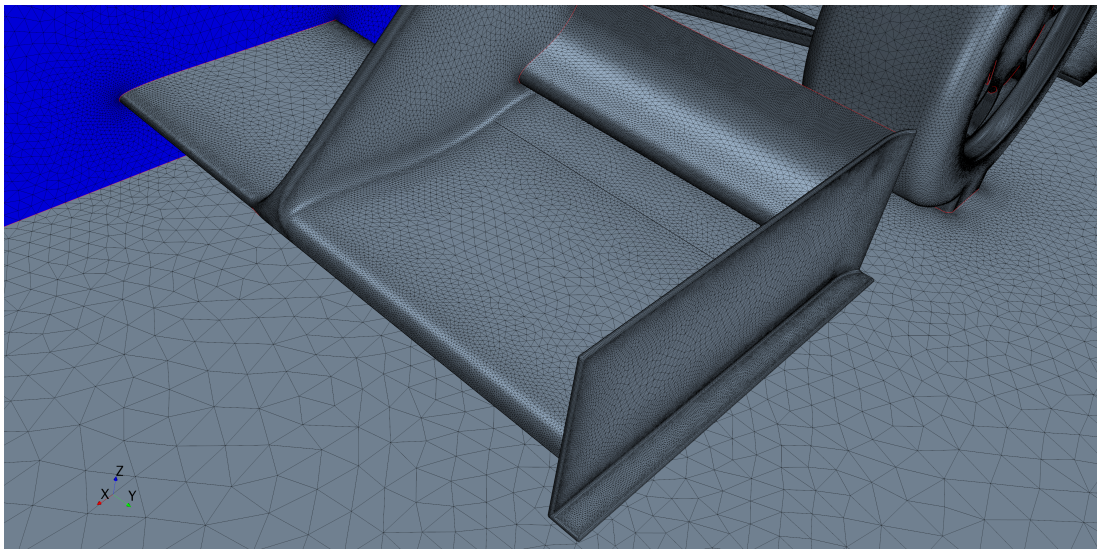


Figure 3.9: Front wing mesh

A very particular area of the flow around a body, as understood, is the boundary layer, so it is evident that, to solve the flow inside it, we must foresee for it a mesh that is further different from the other areas.
In this case, prismatic cells characterized by the following values are used:

| **Property** | **Value** |
|---|---|
| Number of Prism Layers | 15 |
| Near Wall Thickness | 0.1 mm |
| Total Thickness | 7 mm |
| Stretching Factor | 1.2 |

Table 3.4: Prism Layers treatise

It is important to mention that the characteristics of the prism layer are related to the selected wall treatment and consequently to the wall y+ and the turbulence model.

The y+ value is a non-dimensional distance (based on local cell fluid velocity) from the wall to the first mesh node. To use a *wall function approach* for a particular turbulence model with confidence, we need to ensure that our y+ values are within a certain range.

We need to be careful to ensure that our y+ values are not so large that the first node falls outside the boundary layer region. If this happens, then the Wall Functions used by our turbulence model may incorrectly calculate the flow properties at this first calculation point which will introduce errors into our pressure drop and velocity results. The upper range of applicability will vary depending on the flow

physics and the extent of the boundary layer profile.

We use y+ because experimental observation has confirmed that flows of all scales (big or small, fast or slow) tend to demonstrate very similar flow patterns as the flow approaches a wall. So y+ is really used to identify where in the boundary layer profile our first calculation point resides. We can then utilise this y+ number to determine the applicability of near wall turbulence modelling we intend to use, and these should be applicable regardless of internal or external flow conditions. So if we have a y+ $\approx$ 1, we do not need any wall models and instead are resolving the flow all the way to the wall (typically with 10-15 cells within the boundary layer thickness as well as having a Y+ $\approx$ 1, indeed our simulations were made with 15-18 cells within the boundary layer). If we intend to use a coarser mesh and utilise wall functions to capture the near wall velocity profile, we may aim for a y+ between 30 and 300.

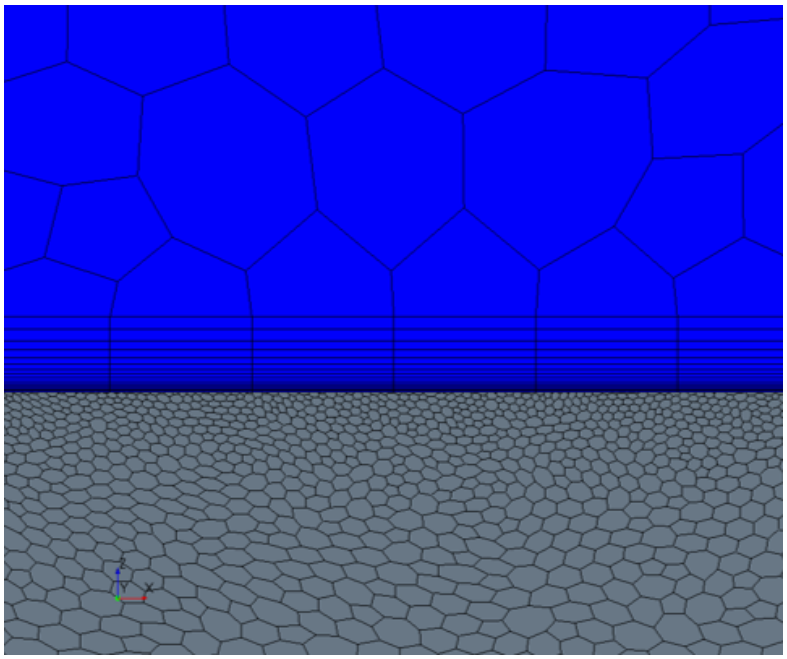

Figure 3.10: Boundary layer mesh

If you have an attached flow, then generally you can use a Wall Function approach, which means a larger initial y+ value, smaller overall mesh count and faster run times. If you expect flow separation and the accurate prediction of the separation point will have an impact on your result, such as the drag or lift forces, then you would be advised to resolve the boundary layer all the way to the wall with a finer mesh. That is, if you are sure that the flow remains attached, it is possible to have a coarser mesh and therefore a lower computational cost by simulating the behaviour of the fluid near the wall through specific functions that already take its influence into account. While, in the case of a separating flow, the behavior is no longer so predictable and it is not possible to use pre-set functions, and therefore it is necessary to refine the mesh.

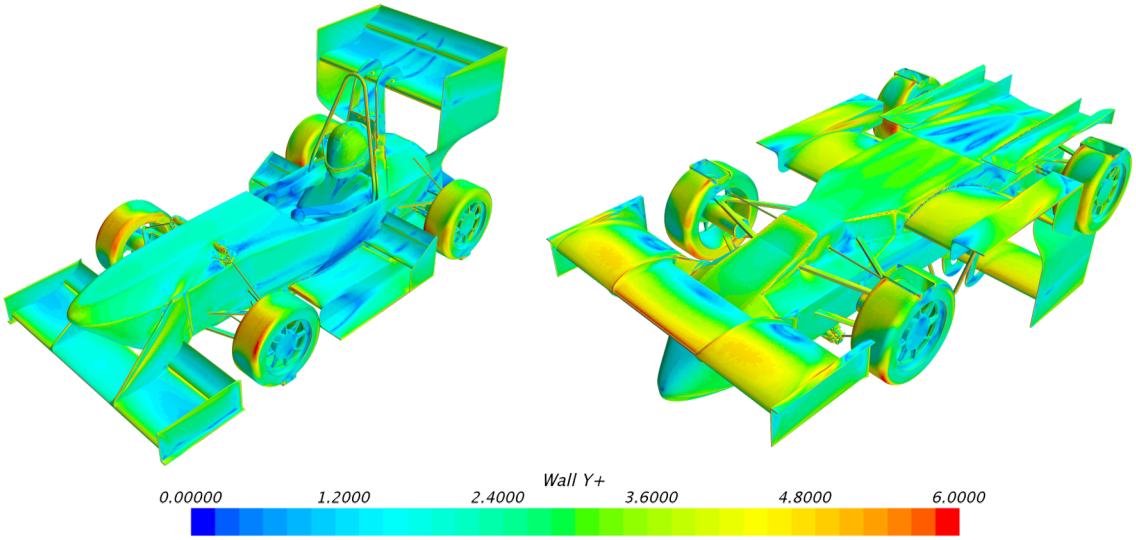


Figure 3.11: Wall y+

In the case of presence of Wall Functions, even y + values that are too low could cause compatibility problems with this model. In addition to the concern about having a mesh with y+ values that are too large, you need to be aware that if the y+ value is too low then the first calculation point will be placed in the viscous sublayer (logarithmic) flow region and the Wall Functions will also be outside their validity (y+ $\approx$ 11).

### 3.4.2 Boundary conditions

As already mentioned the algebraic equations are modified based on the boundary conditions deriving from adjacent cells. When the cell is a frontier cell, it needs external boundary conditions, based on the interacting surface.
In particular:

- Input velocity surface: 60 $\frac{\text{km}}{\text{h}}$, since we are sure that all the particles have the same speed because the principle of Galilean relativity is in force and the flow is undisturbed;
- Output pressure surface: reference pressure (environment), while pressure values are surely uniform, the speed is uncertain due to the presence of wake and vortices;
- Moving ground surface, with the specification of an inviscid wall in order to correctly simulate the ground effect;
- Symmetry plan, because to reduce computational cost the simulation is performed only on half of the car;
- Viscous wall for all car's components, in order to avoid the D'Alembert paradox;
- Inviscid conditions on the remaining walls, since in reality they do not exist and are only created to establish a finished volume of air

### Wheels

The aerodynamic flow inside a formula car is strongly influenced by the rolling of the wheels. For this reason the wheels must be made consistently in the CAD and can be properly implemented in the CFD.

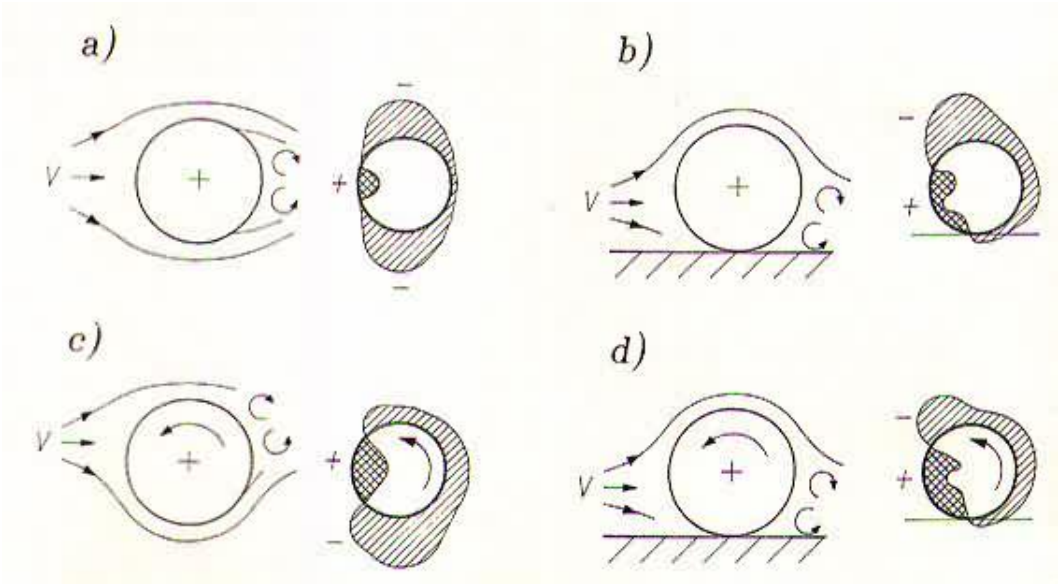


Figure 3.12: Magnus effect

First of all, the contact footprint must be represented because otherwise there would only be a point of contact between the ground and the wheel that would create significant mesh problems.
Finally, the rotation around its own axis must be set with an angular velocity equivalent to the movement of pure rolling at the speed of the center of the hub of 60 $\frac{km}{h}$, corresponding to 70.323488 $\frac{rad}{s}$ .

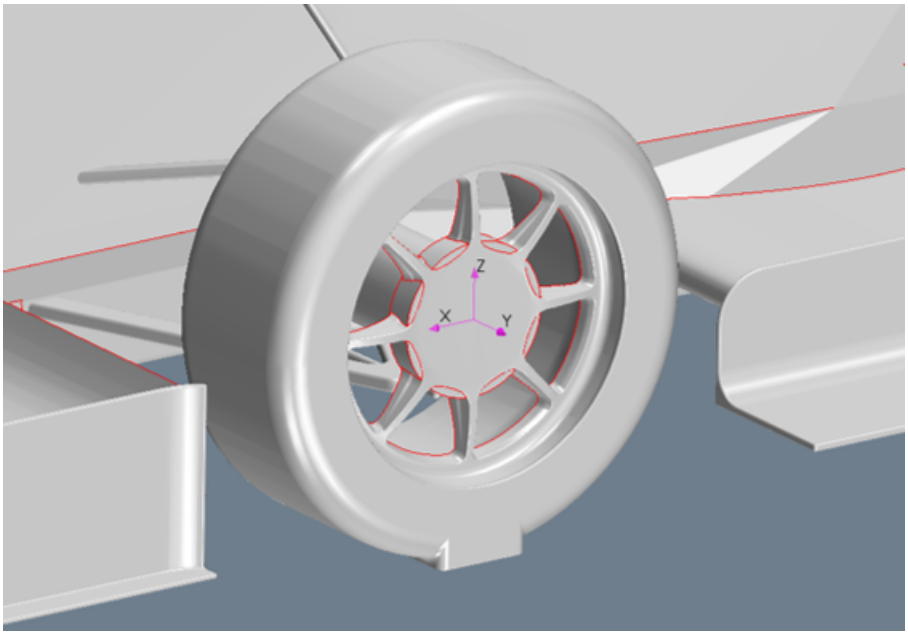


Figure 3.13: Wheels boundary condition

### Radiators

Finally, the effects produced by radiators were also considered, in terms of geometry, material and flow.

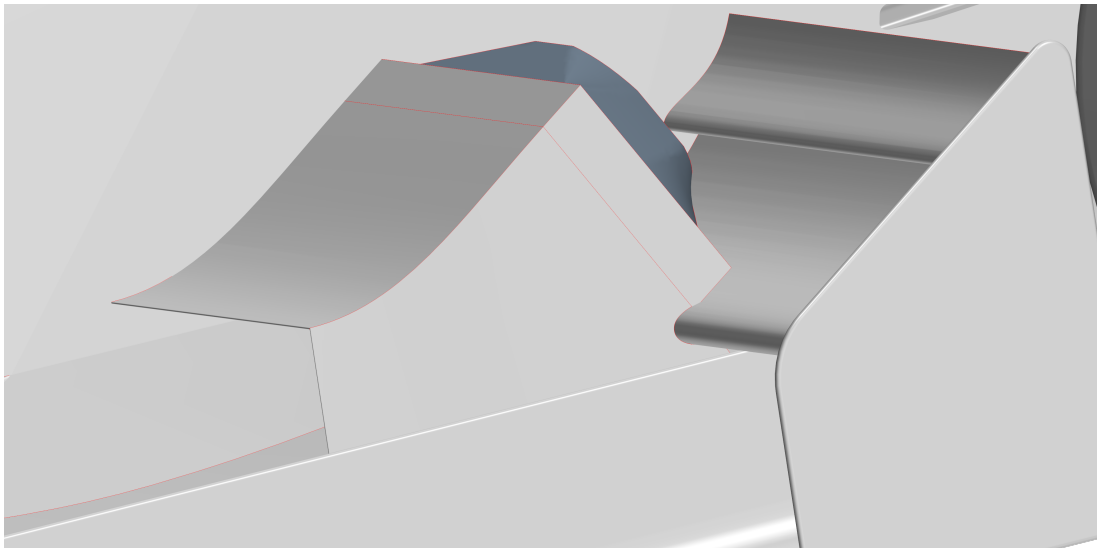

Figure 3.14: Radiator

CFD models are also not suitable to be used as a design tool since considerable amount of computational power and time is required due to the multiple length scales involved in the problem, especially the small-scale geometric details associated with the fins. Although fins introduce a significant complexity for the problem, the repetitive and/or regular structure of the fins enables the porous medium based modeling. By porous modeling, a memory and time efficient computational model can be developed and implemented as an efficient design tool for radiators.
The basic law governing the flow of fluids through porous media is Darcy's Law, which was formulated by the French civil engineer Henry Darcy in 1856 on the basis of his experiments on vertical water filtration through sand beds.

$$Q = \frac{-kA \cdot \Delta p}{\cdot L} \tag{3.30}$$

where A is the passage section, L is the characteristic length, *Deltap* is the pressure drop, $i$ is the dynamic viscosity and $k$ is the permeability.
The complex fluid flow occurring through fins can be introduced into the model through porous parameters. Although the determination of these porous parameters requires a rigorous, detailed computational model with very fine mesh structure especially within the regions mainly responsible for the fluid friction and heat transfer, this modeling can be performed on a representative unit cell due to the repetitive nature of the fins. Once these effects are included through the porous parameters, the mesh structure simplifies dramatically. Besides, the porous modeling does not require any boundary layer meshing since the friction and heat transfer parameters are already included through the porous parameters [5].

$$F = A \cdot \Delta p = -(P_i \cdot |v| + P_v) \cdot v \cdot \Omega \tag{3.31}$$

where we have broken down the coefficient of resistance $P = \frac{}{k}$ $[\frac{\text{kg}}{\text{m}^3\,\text{s}}]$ in its two components: $P_i$ and $P_v$, the first one *porous inertial resistance*, the last one *porous viscosity resistance*:

$$P_i = 150\ \frac{\text{kg}}{\text{m}^4} \qquad\qquad P_v = 500\ \frac{\text{kg}}{\text{m}^3\,\text{s}}$$

These parameters were enclosed in the porosity tensor and in the inertia tensor and were obtained by experimental tests. They must be referred to a planar reference system with the radiator surface, therefore one local coordinates system was created that respected this condition .

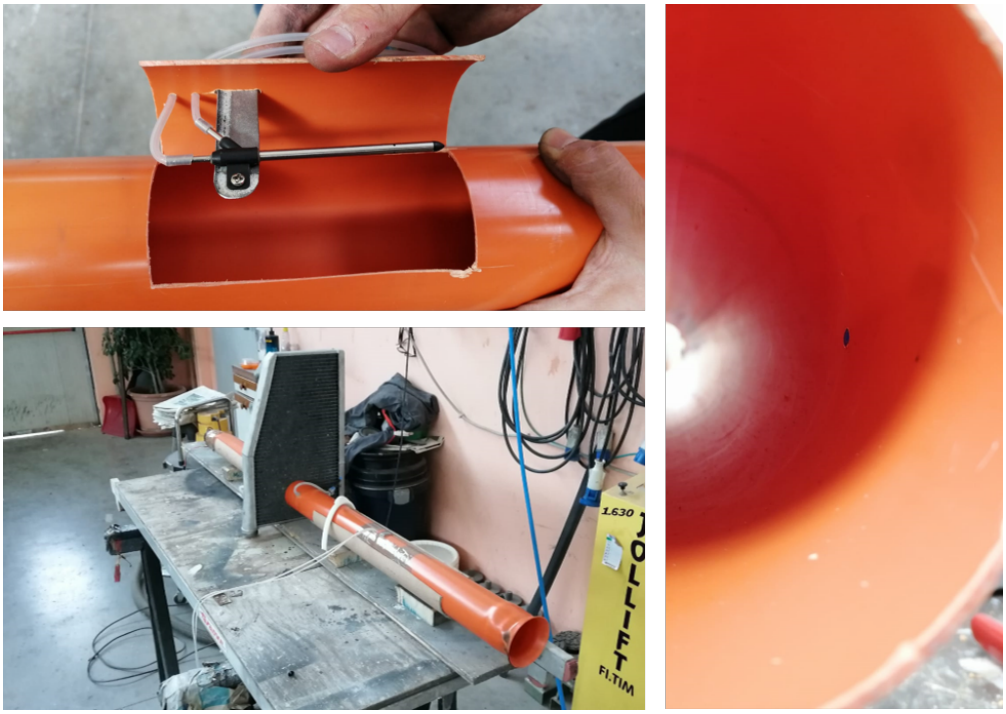


Figure 3.15: Radiators porosity experiment

Furthermore, as anticipated, the radiator has been modelled as a solid of simplified geometry, in this way it has been obtained that the external aerodynamics perceives it as a solid surface. However, in order to simulate the passage of the air flow inside the porous material, in addition to the porosity characteristic of the material and of the region, interfaces have been defined, i.e. sections in which the passage of the air flow is allowed.
One of these sections is the fan interface which is then characterized by the following property *fan interface*: the characteristic polynomial curve is defined which links the flow to the pressure jump and the *rounds per minute* is fixed so as to have established all the possible points of work.

Consequently, in addition to the mesh relative to external aerodynamics, it is necessary to add appropriate meshes both for the radiator and for the conveyor, as well as providing a volume control to take into account the vortices created downstream by the fan.

## 3.5 Other parameters

After checking the y+ values and before performing the mesh again with more expensive settings, assuming that you have not made errors in the setting of the simulation, in the case of non-convergence of the solution, you can try to modify the "under relaxation factor" in order to avoid complete divergence of the solution.

## 3.6 Results

Similar simulations and trends were obtained for all residual simulations

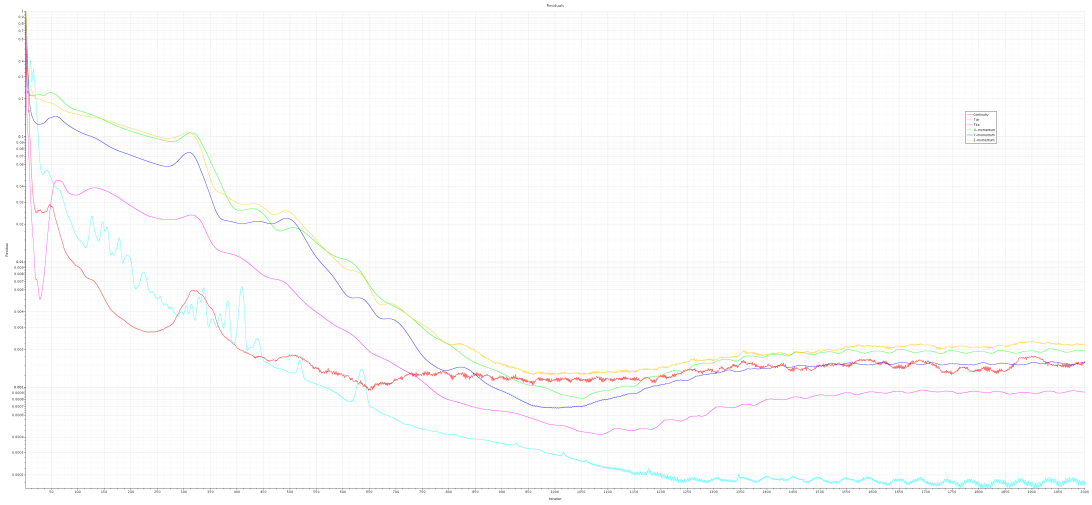

Figure 3.16: Residuals report

Figure 3.17: Downforce report

Figure 3.18: Drag report

It can be seen how the residues are sufficiently low, and how the reports no longer

have a clear tendency, but a long oscillation of such a small amplitude. It means that they are going to convergence, i.e. the figures that vary iteration after iteration are not significant for the interest of this project.

# Chapter 4

# Overall design

## 4.1 Load distribution

All the macroscopic choices made during the design phase favoured the achievement of the objectives of the overall aerodynamic package for the 2019 season:

$$C_z \approx 4 \qquad\qquad E \approx 4$$

As already mentioned above, it is not only important to reach certain values of downforce and efficiency but also to obtain an excellent balance. Indeed, according to Van Valkenburg [25], downforce stability is one of the greatest importance because of the high forces available and the fact that they change drastically with speed. Further, we are witnessing a change in balance even with the pitching, both because the front wing is much more sensitive to the change in height from the ground than the rear wing due to the ground effect, and because it increases the upwash of the front wing which therefore damages the rear wing flow.

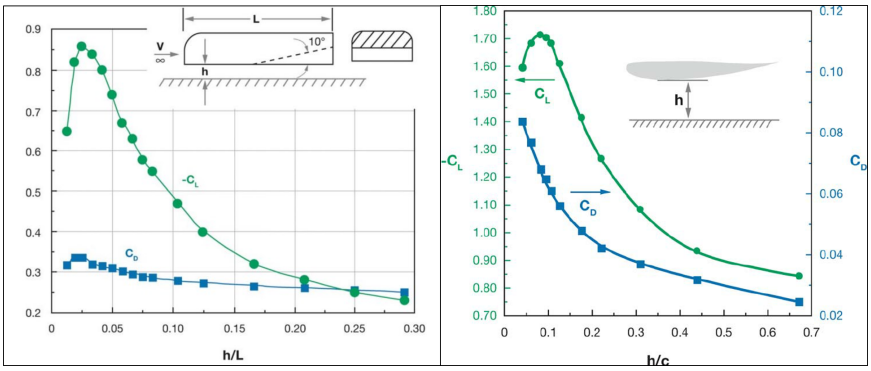


Figure 4.1: Ground effect

To carry out a preliminary analysis on how to distribute the forces, not having the definitive data available, it was assumed that sidepods and the undertray (included the diffuser) generated a downforce close to the center of gravity of the car so that they did not influence the aerodynamic balance of the vehicle in any way. Therefore these two elements were the first to be designed, because they had the sole objective of maximizing downforce, limiting the value of aerodynamic resistance, without any constraint regarding the balance of the car: overall it was obtained

$C_z = 1.66$ e $C_x = 0.37$ .

So, the sum of the vertical loads of the two wings should indicatively reach the value of $C_z = 2.3$, containing the drag within $C_x = 0.63$ . Moreover, to guarantee an excellent balance the $C_z$ had to be equally divided between both elements, because, due to the regulation's constraints, they have about the same longitudinal distance from the center of gravity of the vehicle.
According to the research of [18], it was noticed how the aerodynamic resistance of a single-seater is mainly due to the rear wing, with the front one giving a minimum contribution even at high angles of incidence. This happens for various reasons:

- The front wing exploits the ground effect, so it generates an increase in downforce with a minimum increase in resistance;
- The front wing works with the totally clean flow, as it is the most advanced element of the car;
- The front wing must produce at its trailing edge a flow that is as clean as possible so as not to compromise the work of the aerodynamic components that follow it, and so must work at high efficiency.

Therefore, we first designed the rear wing in order to be able to generate the maximum possible downforce, almost completely saturating the available drag deriving from the battery capacity studies. Only later, the front wing was designed with the aim of providing that amount of missing downforce to reach the target, remaining below the imposed drag threshold, but above all generating a downforce as similar as possible to the rear wing's one.

Ergo, the flowchart followed during the design was the following:

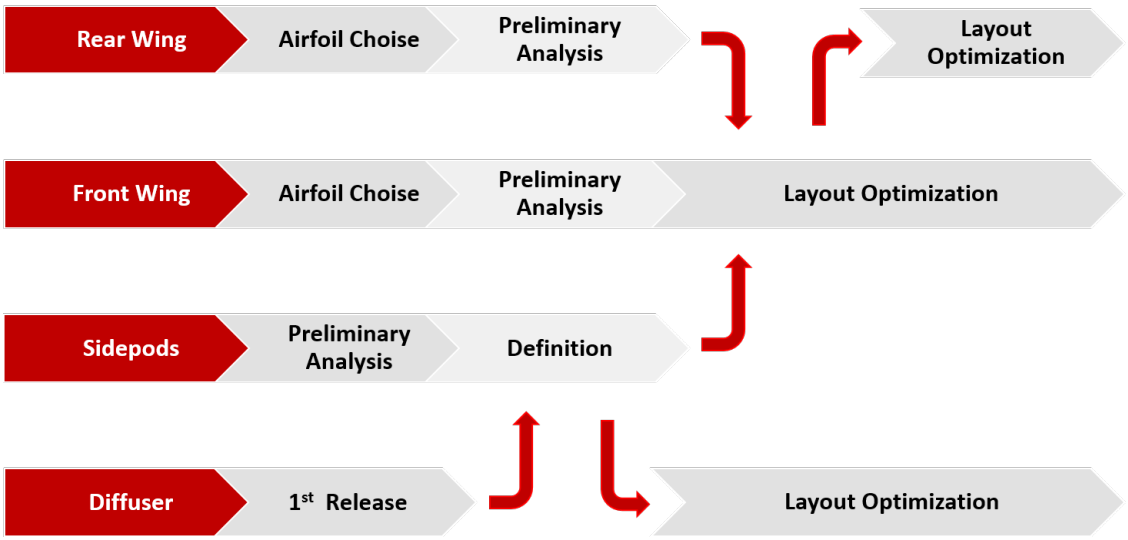


Figure 4.2: Overall workflow

Since the performances obtained from the rear wing have been $C_z = 1.02$ e $C_x = 0.31$ , with downforce slightly lower than the optimal calculated value of

$C_z = \frac{2.3}{2} = 1.15$, the best option was to recover part of the downforce by exploiting the front wing even in spite of a little loss of perfect balancing, obtaining the following overall results:

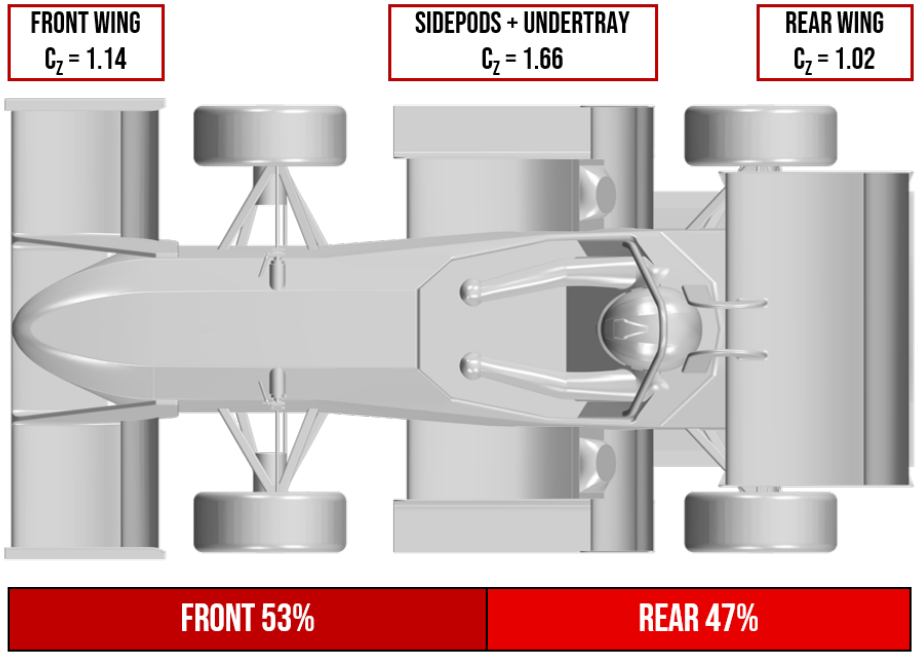


Figure 4.3: Aerodynamic balance

In addition to downforce generation, paying close attention to balancing, other needs had to be taken into account when designing the front wing

- Ensure a sufficient reach to the car's undertray;
- Generate the cleanest possible flow at the trailing edge so that sidepods and undertray work optimally;
- Evaluate the upwash phenomenon to avoid damaging the rear wing's job;
- Remove the flow from the wheels to avoid the phenomenon of squirting, without compromising the work of the other aerodynamic elements;
- Also consider the cooling system, even if not yet designed

## 4.2 Aerofoils

### 4.2.1 2D theory

The purpose of a wing profile is to generate a vertical force which in the case of the automotive must be directed towards the ground. Through the Kutta-Joukowsky theorem it is shown that this force is generated, around a body of any shape, only if a circulation is generated around it: $\Gamma \neq 0$.
Circulation is a measure of the effect of the tangential velocity distribution on the

body contour and therefore of the pressure difference between upper camber and lower camber:

$$\Gamma = \oint_c \vec{v} \cdot \vec{dl} \tag{4.1}$$

For a thin body, which has angles of incidence such as not to behave like a tapered body, the viscous effects, with the exception of the area of the boundary layer, can be neglected [9].

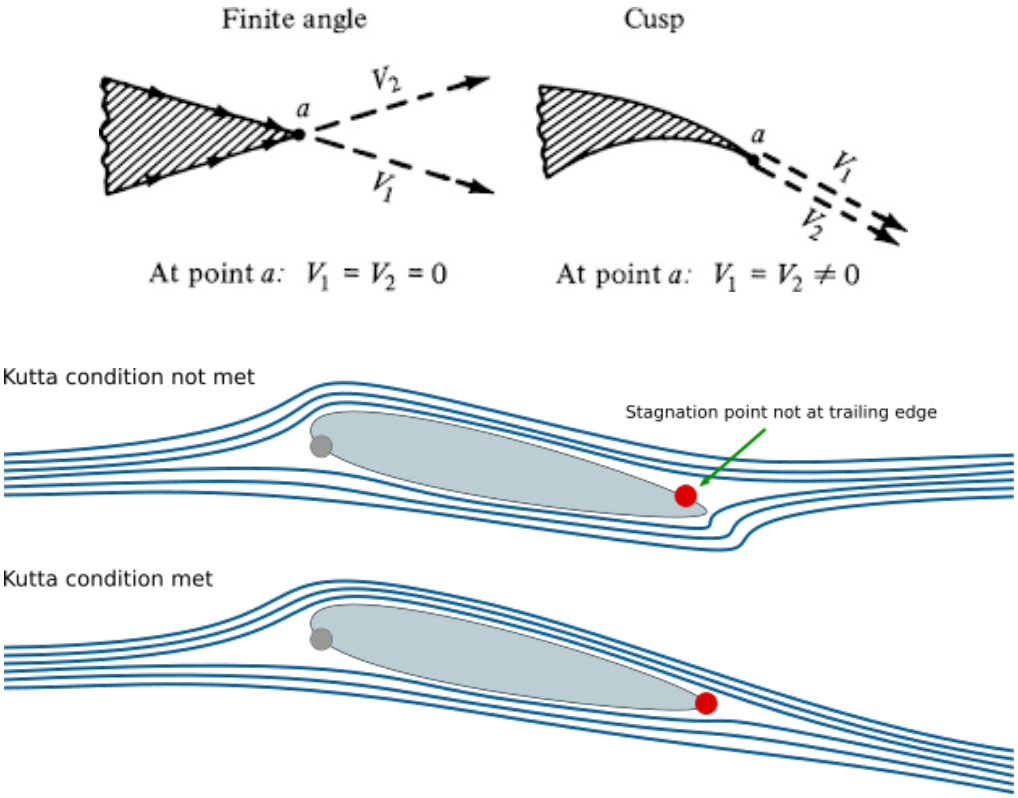


Figure 4.4: Kutta hypotesis

Taking advantage of the Kutta hypothesis, we will choose the value of the circulation, since there are infinite ones that satisfy the Laplace equation, which will guarantee the coincidence of the stagnation points of this theoretical model with those experimentally verified: therefore, actually, the Kutta hypothesis allows to consider the influence of viscous effects while theoretically treating an ideal fluid. In particular, the Kutta hypothesis provides that, at the trailing edge, both velocity vector, coming from upper camber and lower camber, are identical. Indeed, Kelvin's theorem states that in a inviscid, incompressible fluid, with conservative mass forces:

$$\frac{D\Gamma}{Dt} = 0 \tag{4.2}$$

As a consequence, every irrotational motion is maintained over time and therefore could not generate any non-zero circulation, thus arriving at the paradox of D'Alembert who states: *"A body hit by a potential flow will not exchange forces with it, neither lift nor drag"*.

As for resistance it is possible to understand how, in the two-dimensional case, it is composed by:

- Friction resistance: caused by tangential stresses due to fluid viscosity;
- Shape resistance: caused by the asymmetry of the potential flow lines due to growth and to the eventual separation of the boundary layer, where viscous stresses predominate

As for downforce's treatise, we must follow an analogous reasoning to that of the Kutta hypothesis, i.e. the treatment at potential flow is maintained since, for tapered bodies, the viscous effects are negligible, but modifications will be introduced that allow to take into account their influence.
In particular, at the start the viscous stresses on the trailing edge, due to the high speed gradients, are not negligible and will generate the so-called starting vortex. In order to maintain the flow overall irrotational, this vortex, which remains fixed at the starting point, must be balanced by vortices along the profile that simulate the same effects as the one introduced by the boundary layer, which is the rotational heart of the flow. These vortices are punctual (infinitesimals), so they are singularities that do not affect the potential flow, but cause a circulation that is not null and produces the downforce. Similarly to the start, upon stopping, a homonymous vortex will be generated which will entirely compensate the starting one, thus cancelling the vortices distributed along the profile.

It should be remembered that, although the tangency equations are applied to points geometrically belonging to the contour of the profile, the velocity and pressure trends obtained by them are to be attributed to fluid particles belonging to the edge between the boundary layer and the potential flow. However, if the thickness of the boundary layer is limited, the error committed is negligible. Hence the need to work with rather high Reynolds numbers since the greater the Reynolds, the lower the thickness of the boundary layer. Further, the limited thickness allows to neglect the viscosity and to hypothesize the fluid as inviscid and irrotational.

Defining $\gamma$ as $\Gamma = \int_a^b \gamma ds$ , it can be shown that [9]:

$$\frac{1}{2\pi V_\infty} \int_0^c \frac{\gamma(\xi) d\xi}{x - \xi} = \alpha - \frac{dz(x)}{dx} \tag{4.3}$$

Known as the fundamental equation of thin profile theory. It shows how downforce depends on the shape of the profile $\frac{dz(x)}{dx}$ or, better, from the shape of the mean camber line since the integration is done on this curve, and from the angle of incidence $\alpha$ with respect to the undisturbed flow.

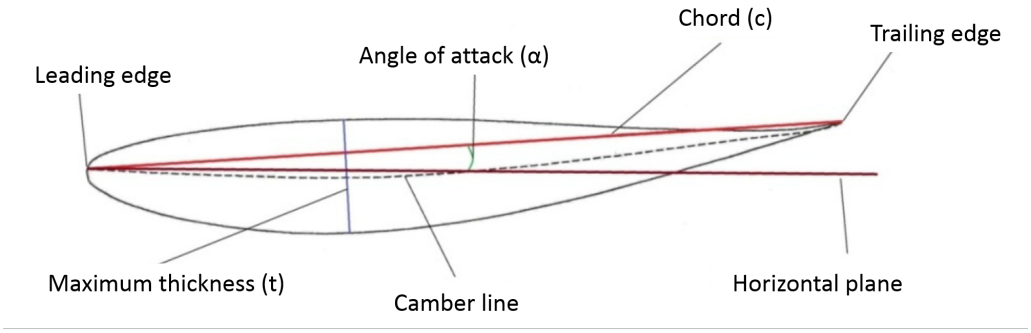


Figure 4.5: Single aerofoil nomenclature

The variation of the camber line, compared to its horizontal configuration (symmetrical profile), determines the translation of the characteristic ($C_{every}$ , $\alpha$) curves upwards or downwards, thus increasing the downforce values, with the same incidence.
As the thickness of the profile increases so the downforce's maximum decreases, but there is a more delayed separation.

### 4.2.2 Selection

Given the similar load to be realized, always containing the resistance, it was decided to use the same profiles for both the rear and the front wing.
In particular given the value of $C_z \approx 2.3$ overall to be achieved it was understood that a two-profile configuration was sufficient in order to optimally contain the drag values, costs and production complexity.

Indeed, the addition of a flap in the appropriate position generates the increase in area and in camber of the wing without modifying the main's incidence angle of attack, with a consequent increase in downforce (translates the characteristic curve upwards).
As far as size and positioning are concerned, the texts give advice that must be verified with CFD analysis; the length of flap's chord must be between 25% and 30% of the main element one; you get up to 40% in the case of wings to produce high downforce. The fundamental elements to consider are the vertical distance and the longitudinal overlap that are created between the trailing edge of the main aerofoil and the leading edge of the flap: the aeronautical texts say that it is worth having a gap between 1% and 2% of the chord length and an overlap between 1% and 4% [3]. However, experimental tests often give different results, so it is necessary to find the best configuration through CFD simulations [27].

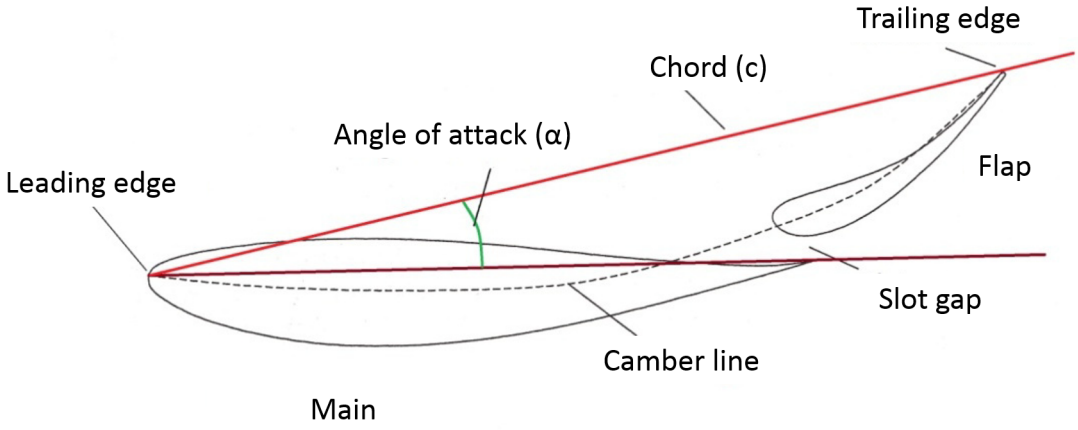


Figure 4.6: Main and flap nomenclature

Furthermore, as stated by Katz [12], the addition of more elements delays the separation and increases the downforce, obviously increasing also the drag. The basic principle behind the multi-element design is that aerofoil camber can be increased far more than with a single element aerofoil. Additional benefits include energizing the boundary layer, and favourable interaction between the wing elements, resulting in a gain in the combined lift. Indeed, the presence of the rear flap allows to keep the flow more attached to the lower area of the main element, since part of the upper flow is accelerated by the passage through the slot and that allows it to have a pressure gradient more favourable at the trailing edge of main aerofoil. In this way it is possible to increase the angle of attack (overall: $\alpha_{main} + \alpha_{flap}$) without having flow separation and therefore having more downforce.So the flap must be close enough to create a convergent section that accelerates the flow, but also far enough to let the flow pass and to not be affected by the wake generated by the main element.

Aerofoils to be used were chosen from those belonging to the Benzing class, a category usually used in motorsport. From the catalogue those with the most interesting features for our objectives were taken, the polar and efficiency curves were built:

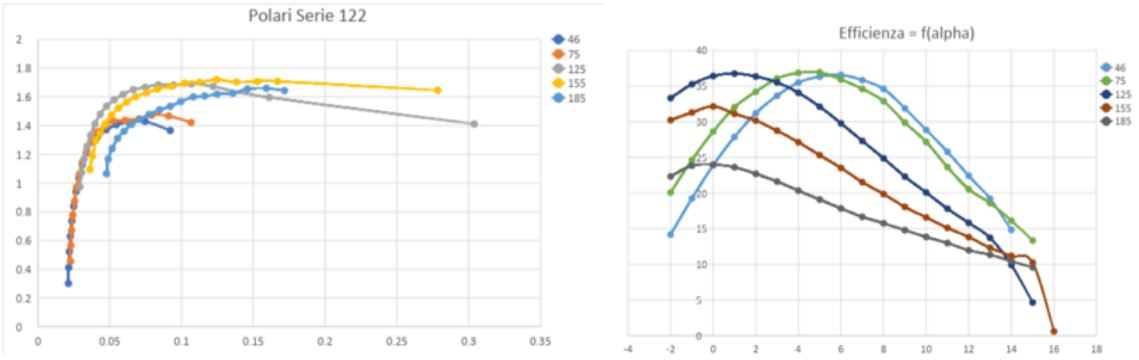


Figure 4.7: Characteristic curves

They were obtained by using a two-dimensional CFD analysis on Star CCM +, whose aerofoil import process and angle of incidence variation was automated

through a macro written in Java (attached in the appendix).

Having therefore to study a configuration with only one flap, taking advantage of the amount of single aerofoils available from the catalogue, different pairs were organized following the criteria indicated below:

- Aerofoils with greater downforce coefficient have been selected as main: since the main must have a less incident position, and, despite this, it must still be able to generate downforce. In fact, with a low incidence it is possible to minimize the separation and therefore the vortices generated allowing also a closer positioning of the flap, without damaging its job because of not clean air, and therefore being able to optimize the size and shape of the slot;
- Aerofoils with lower drag coefficient have been chosen as flaps: since the flap must have a more incident position, so there is no problem of generating downforce, but an excessive increase in drag must be avoided and separation must be delayed

The potential of each couple was evaluated through a two-dimensional CFD simulation on Star CCM + managed automatically by another Siemens software: Heeds MDO. The latter is an optimization software to which the unconstrained parameters have been supplied so that it can vary to arrive at the optimal configuration:

| **Dimension** | **Reference 1** | **Reference 2** |
|---|---|---|
| Angle of incidence | Main | Ground |
| Angle of incidence | Flap | Ground |
| X-gap | Main | Flap |
| Z-gap | Main | Flap |

Table 4.1: DoF

The following parameters were set a priori were:

- Main and flap chords: through a compromise taking into consideration the regulation constraints and the proportions indicated above. Moreover, an attempt was made to maintain a certain distance between the profile and the wheel, to avoid that the high pressure of the stagnation point could cause an enormous adverse pressure gradient which would have considerably accentuated the boundary layer separation. Obtaining in this way, respectively, 300 mm and 150 mm;
- Ground clearance: not completely determined, because an analysis on the ground effect is necessary, but to a first approximation it has been set at 400 mm from the ground, so as to respect the rule and to avoid damage during the pitching movement. In any case, these simulations were carried out to evaluate the potential of the profiles in general, therefore without implementing the ground effect;
- Wingspan: even this dimension was not precisely determined, but in first approximation it turned out to be equal to 450 (1200) mm, since you don't

want to go beyond the outermost section of the wheels to avoid the risk of incurring penalties during competitions due to contact with the cones. In this way an aspect ratio of 1 (2.66) was obtained which is not far from the usual values present in motorsport [12]. Indeed, it would be better to have it as high as possible in order to approach the infinite wing's condition and therefore the two-dimensional flow, but for questions of dimensions and constraints of regulation in the field of motorsport only limited AR values can be obtained

The optimal configurations of the most promising couples have produced these values:

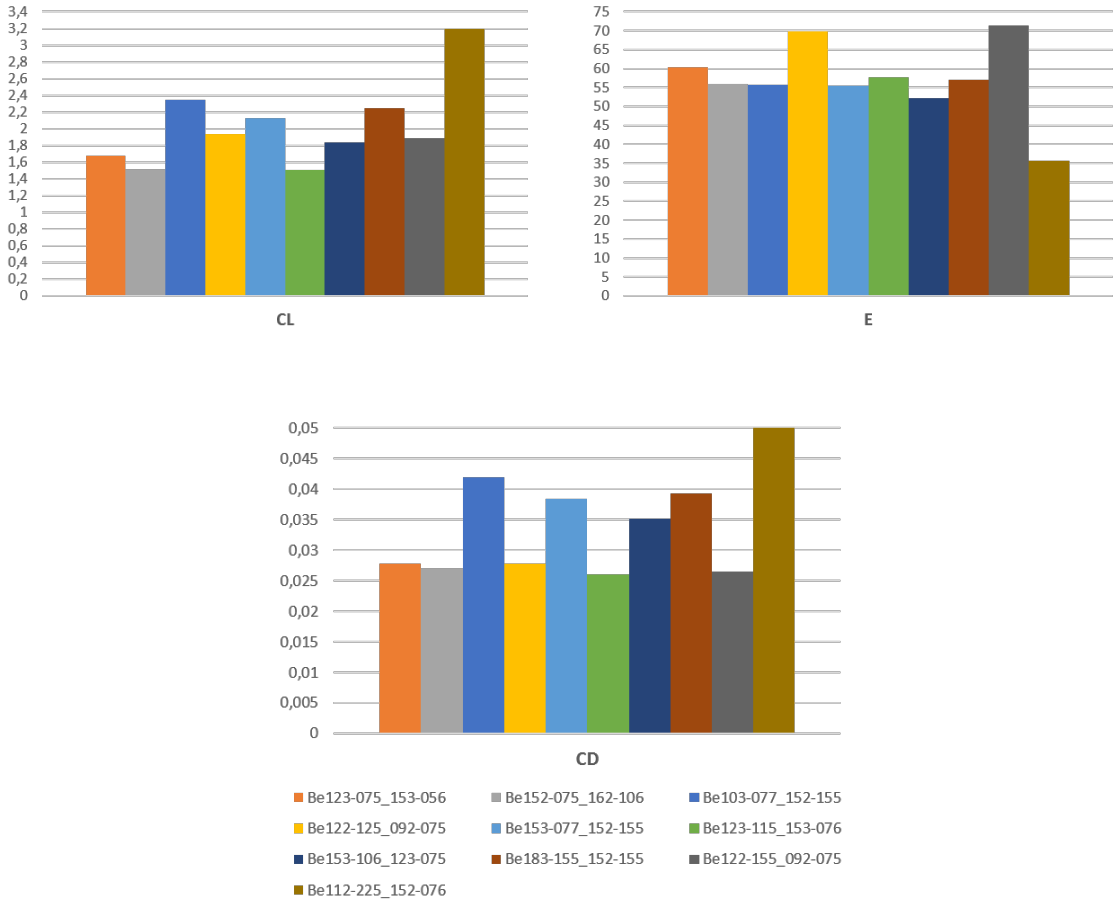


Figure 4.8: Aerodynamic values of 2D configurations

To compare such different results we chose to create a performance index:

$$PI = E_{coeff} + C_{L_{coeff}} \tag{4.4}$$

where

$$E_{coeff} = \frac{E}{E_{max}} \tag{4.5}$$

$$C_{L_{coeff}} = \frac{C_{L_{max}}}{C_L} \tag{4.6}$$

This index is constructed in this way

$$PI = \frac{C_L}{C_{Lmax}} \cdot \frac{C_{Dmax}}{C_D} + \frac{C_L}{C_{Lmax}}$$

because the main objective, as mentioned, is efficiency and it could be pursued in only two ways:

- High downforce and low drag;
- Low downforce and very low resistance

Because two-aerofoil configuration has intrinsically low aerodynamic resistance. To reach $C_z = 2.63$ overall for the two wings, it is necessary to take the first option and therefore favour higher values of downforce than to lower values of drag.

The following results were obtained:

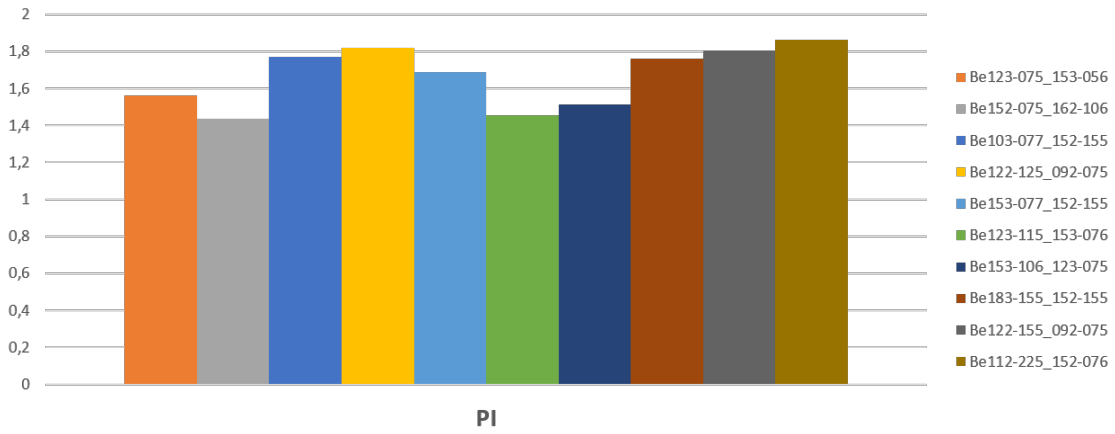


Figure 4.9: PI

Therefore all the design of the front wing was made using:

| **Role** | **Aerofoil** |
|---|---|
| Main | Benzing 112-225 |
| Flap | Benzing 152-076 |

Table 4.2: Definitive aerofoils

# Chapter 5

# Front wing design

## 5.1 Methodology

The front wing design was, as above described, aimed at achieving all the objectives set so far. After choosing the aerofoils to be used, illustrated in the previous chapter, efforts were focused on the following areas:

- Search for the best three-dimensional configuration of main and flap selected;
- Choice and positioning of a third aerofoil: the central part of main element;
- Evaluation of strakes' influence;
- Endplates shape and size design

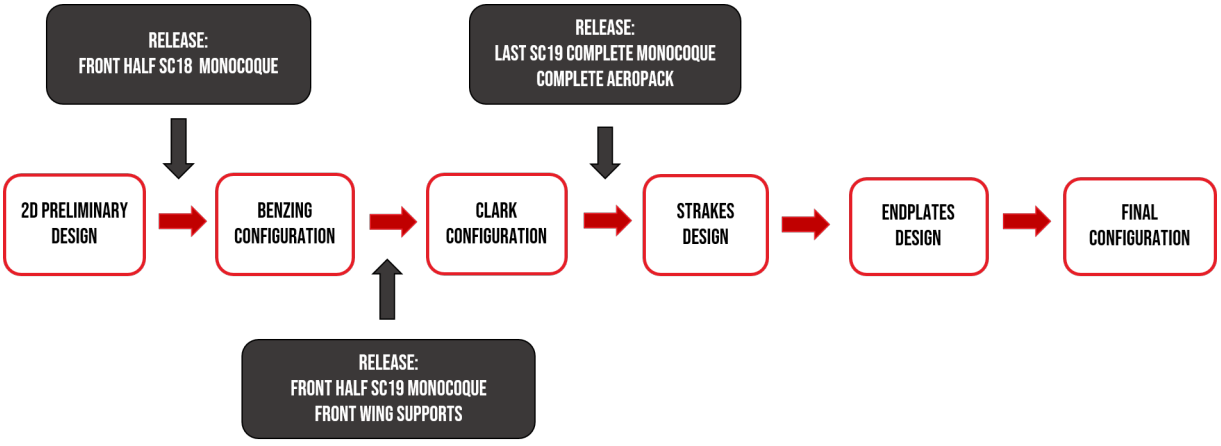


Figure 5.1: Front wing workflow

The work was always carried out focusing on the overall performance of the vehicle and not on individual components' performance: following this approach, the insulation of the undertray, the work of the sidepods, the upwash on the rear wing and only later also influence on the cooling system were taken into account in the various design choices.

## 5.2 Main and flap configurations

### 5.2.1 3D theory

The two-dimensional theory illustrated in the previous chapter adequately reflects what happens in reality, with the exception of some phenomena due to the three-dimensionality of the flow.

In particular, the phenomenon of upwash and downwash is generated, characterized by a secondary whirling motion that produces a component of speed, vertically directed, which combines with the undisturbed current to produce the aerodynamic force on the wing.

Indeed, since the pressure at the extremity of the wing is the ambient pressure, the pressure of the upper camber, which for what has been said must be less than the one of the lower camber, is diminishing moving from the root towards the extremity; in the meantime the pressure of of the lower camber increases moving in similar way. This difference in pressure between the root and the extremity causes a secondary motion of the flow, attracted by the zones with less pressure (configuration with minimum energy always sought in nature): therefore a movement will occur from the extremity towards the root for the upper camber, and vice versa for the lower camber.
Moreover, the air of the lower camber tends to circumvent the extremity, attracted by the depression of the upper camber, causing a whirling motion, which propagates downstream of the wing, of greater intensity at the extremities and lower intensity at the root.

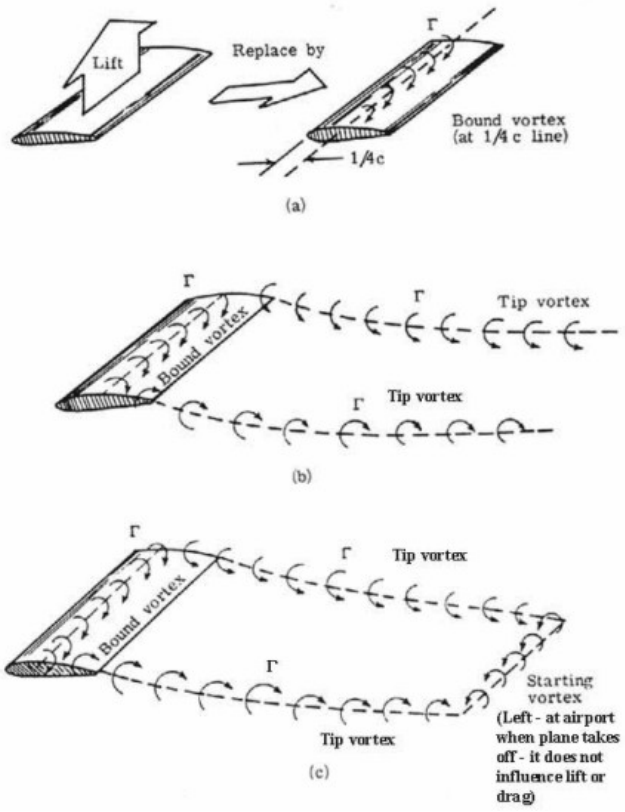


Figure 5.2: Tip vortex and stating vortex

This phenomenon is theoretically described by a vortex filament (three-dimensional extension of the point vortex), called adherent vortex, which, starting from the root reaches the end, by the Helmotz theorem, bends of $\pi$ rad and continues in the longitudinal direction: this filament takes the name of free vortex. Further, the adherent vortex loses its intensity moving towards the extremity because it leaves a longitudinal vortex filament for each section. This loss of vortex filameent intensity also translates into a reduction of the circulation, and therefore of the downforce, section by section [9].
This model therefore represents the main phenomena of three-dimensional flow:

- Extremity free vortices (counter-rotating);

- Longitudinal axis vortices along the entire airfoil, but with considerably lower intensity
- Variation of downforce from the root to the extremity

These vortices, moving from upper camber to lower camber outside the aerofoil's wingspan, cause within aerofoil's wingspan a component of velocity exactly directed in the opposite direction, therefore, in the case of automotive applications, upwards. In each point, the module of this speed is consistent with the value of the adherent vortex in the respective section, so it will be higher towards the aerofil's extremity.

### Induced Resistance

This vertical speed, called induced speed, is added to the speed of the undisturbed flow, modifying the direction of the flow that hits the aerofoil and varying the effective angle of incidence with respect to the angle of geometric incidence, section by section (to have the same optimal incidence the wing is done spoon-shaped, warping it alongside the wingspan).

Moreover, from the theory of potential flux (which precisely evaluates only the downforce), it is known that this aerodynamic force is orthogonal to the velocity of the flow that hits the object. This implies that in each section the downforce will be inclined by the angle of induced incidence with respect to the previous direction. Therefore it will not be purely vertical, but will have only one component in that direction in addition to an horizontal component. Hence, this three-dimensional phenomenon not only causes a reduction in the downforce, but also gives rise to a component of aerodynamic resistance even from the potential flow: the induced resistance.

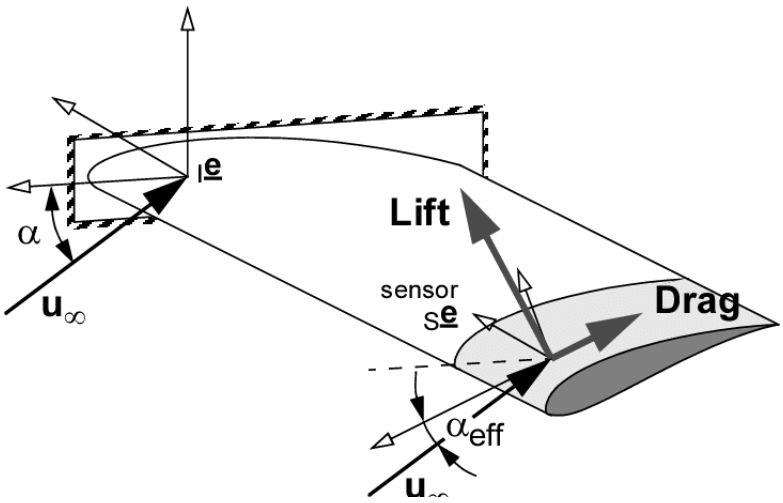


Figure 5.3: Induced resistance

All this is summarized [9] in the following formula, called the carrier line equation, which is valid for each section and in which the unknown is Γ:

$$\frac{\Gamma(y_0)}{\pi V_\infty c(y_0)} + \frac{1}{4\pi V_\infty} \cdot \int_{-\frac{b}{2}}^{+\frac{b}{2}} \frac{(\frac{d\Gamma}{dy})dy}{y_0 - y} = \alpha(y_0) - \alpha_{L=0}(y_0) \tag{5.1}$$

### 5.2.2 Benzing Aerofoils

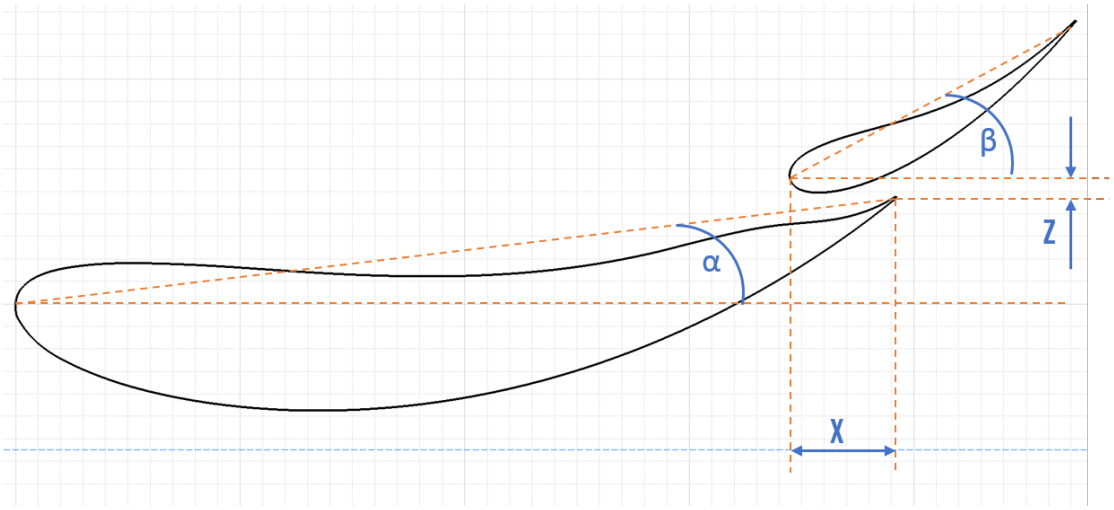


Figure 5.4: Benzing DoF

The analyzes carried out in the previous chapter were preliminary analyzes valid for different aerodynamic assemblies. As for the front wing, further preliminary two-dimensional analyses were required, again performed with Heeds' MDO optimization software, for three reasons:

- Implementation the ground effect in the simulation, in order to evaluate its influence and choose the optimal configuration based on its effects;
- Starting from the configuration used for the previous PI calculation, to restrict the parameter variation fields so as to investigate the maximum PI point in more depth around this configuration;
- To consider within the simulation both the influence of the nose and of the rolling of the wheel, as can be seen in the figure 5.5

So, starting from this two-dimensional optimal configuration (REF in table 5.1), 3D simulations have been carried out, so as to take into account also the three-dimensional effects described above, by varying the usual independent parameters.

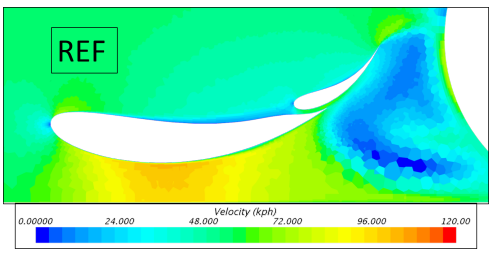

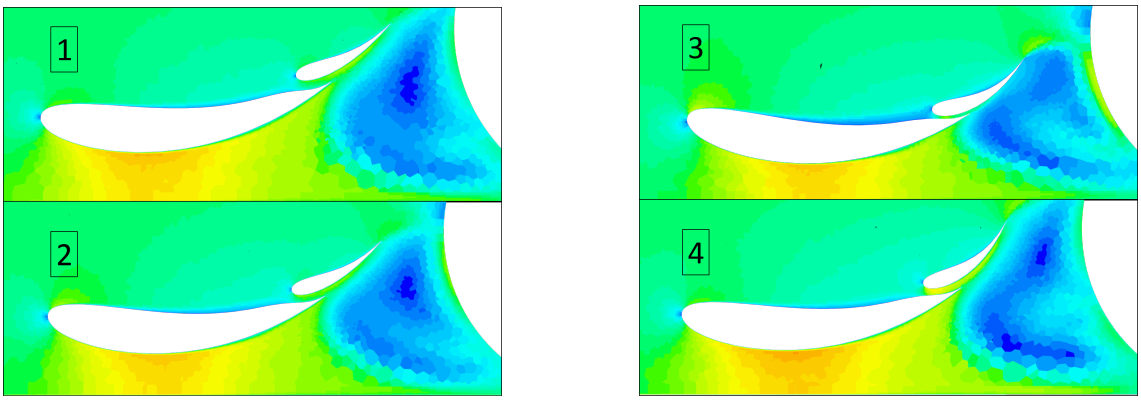


Figure 5.5: Benzing configurations

In the reference configuration it can be seen that there is a detachment both on the lower camber and on the upper camber of the main aerofoil, and that the latter is not significantly reduced by the dimensions of the slot. Furthermore the flap is located near the turbulence zone of the wheel, but, despite this, the aerodynamic values are good.
In an attempt to reduce the separation on the lower camber of the main and to optimize the slot so that the one on the upper camber is also reduced, in *1* the incidence of main was increased and the one of the flap was reduced. Since the first target has been reached, but not the second, it has been decided to return the main to minor incidences.
In *2*, indeed, the incidence of the main is reduced and the detachment on the lower camber of the main is absent, while the one on the upper camber continues to be present. To help the flow, one could opt for changing the slot in the opposite way to what has been done so far, therefore reducing the incidence of the main and increasing the flap incidence, in addition to overlapping them more.
However, by reducing the angle, the detachment on the lower camber of the main aerofoil also occurs again, as can be seen in *3*. Therefore, an incidence value is chosen among those tested in *1* and *2* which gave excellent results from this point of view, while maintaining the same overlap as in *3*, since the previous ones had not worked. Furthermore, the incidence of the flap is increased up to the height limits of the regulation, both to have higher downforce values and to keep it outside the wheel turbulence. So in *4* we can see:

- The fluid does not separate on the lower camber of the main;
- The slot is optimized producing an acceleration that energizes the fluid delaying the separation on the flap and reducing the pressure gradient on the trailing edge of the main and therefore delaying the separation also there;
- Main and flap have the maximum possible incidence, thus guaranteeing much higher downforce values;
- The flap is outside the turbulent area caused by the rolling of the wheel

Being the slot optimized and the incidence of the two profiles limited by the maximum height established by the regulation, this configuration is certainly the one with maximum downforce, as can be seen from the figure 5.6. Indeed, by designing

a wing with multiple slots the designer never knows how to orient and accelerate the flows, but proceeds by trial and correction according to various experiences, in particular as regards the slot sizing, which can have different distances and optimal shapes, proceeds even by varying the aerofoils' incidence in consideration [3].

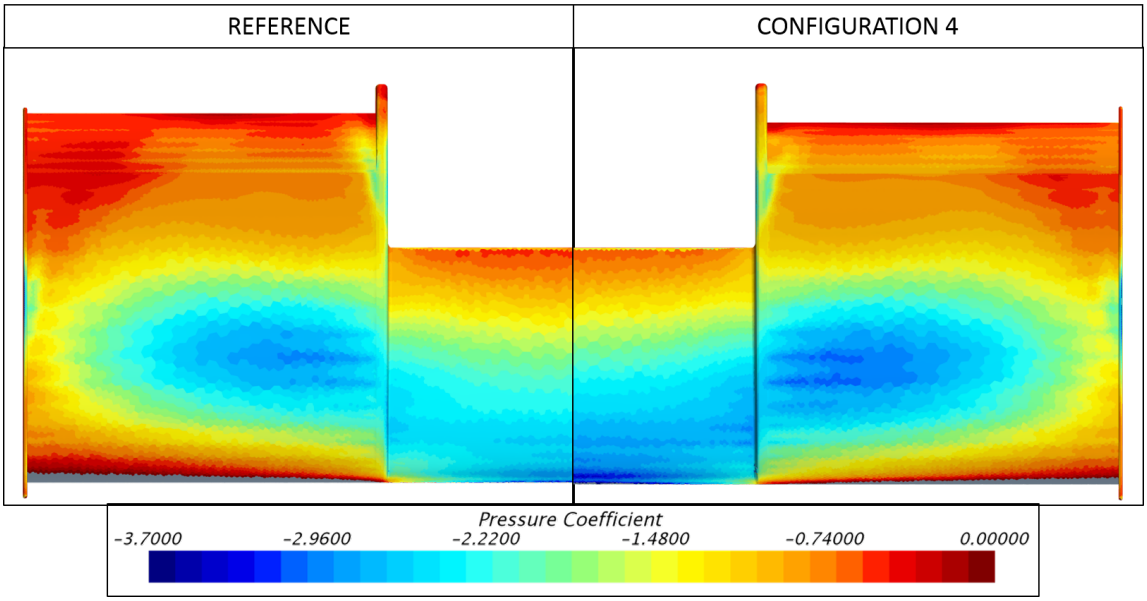


Figure 5.6: Reference and the best Benzing configurations

Indeed, compared to the configuration chosen on Heeds, it has a greater depression under all the main, as well as under the entire flap; furthermore, the pressure gradient varies less abruptly on both trailing edges, a symptom of postponed separation.

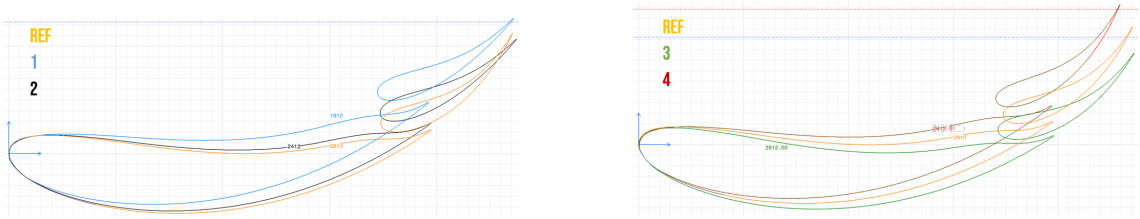


Figure 5.7: Overlapping Benzing configurations

| **Configuration** | $\alpha$ [°] | $\beta$ [°] | **x** mm | **z** mm | $\Delta C_z$ [%] | $\Delta C_x$ [%] | $\Delta E$ [%] |
|---|---|---|---|---|---|---|---|
| REF | 4 | 35 | -51 | 1.5 | - | - | - |
| 1 | 8 | 25 | -51 | 3.5 | -2.6 | -14.0 | +13.0 |
| 2 | 5 | 25 | -51 | 3.5 | -9.0 | -22.4 | +17.5 |
| 3 | 2 | 30 | -57 | 1.5 | -14.0 | -22.0 | +10.5 |
| 4 | 6.5 | 38 | -57 | 1.5 | +10.5 | +18.0 | -6.0 |

Table 5.1: 3D Benzing configurations' values

As can be noted that the three-dimensional flow brings variations with respect to the preliminary 2D analyzes: indeed, the performances are very different in quantitative terms. However, this influence is always present for all the configurations, and

therefore at the end of the day the configuration number *4*, the definitive one, does not differ much, in terms of free parameters' values, from the *reference* one which was the optimum in two-dimensional analysis. This demonstrates the goodness of the performed 2D simulations.
Since, as already mentioned, the previous design choices have all been taken in the direction of efficiency and low drag philosophy, with the choice of profiles and their configuration we try to reach the expected downforce values. Therefore, the configuration *4* was evaluated as the best one, being the only one that guarantees sufficient downforce value and being compliant with respect to the height limitations imposed by the regulation (maximum angle on incidence allowable).

As above described, a parametric analysis of all degrees of freedom was not carried out for reasons of time. However, based on an appropriate post-processing, the individual effects of each parameter were evaluated and, by varying them simultaneously, the optimal configuration of the profiles, shown in figure 5.8, has been quickly found.

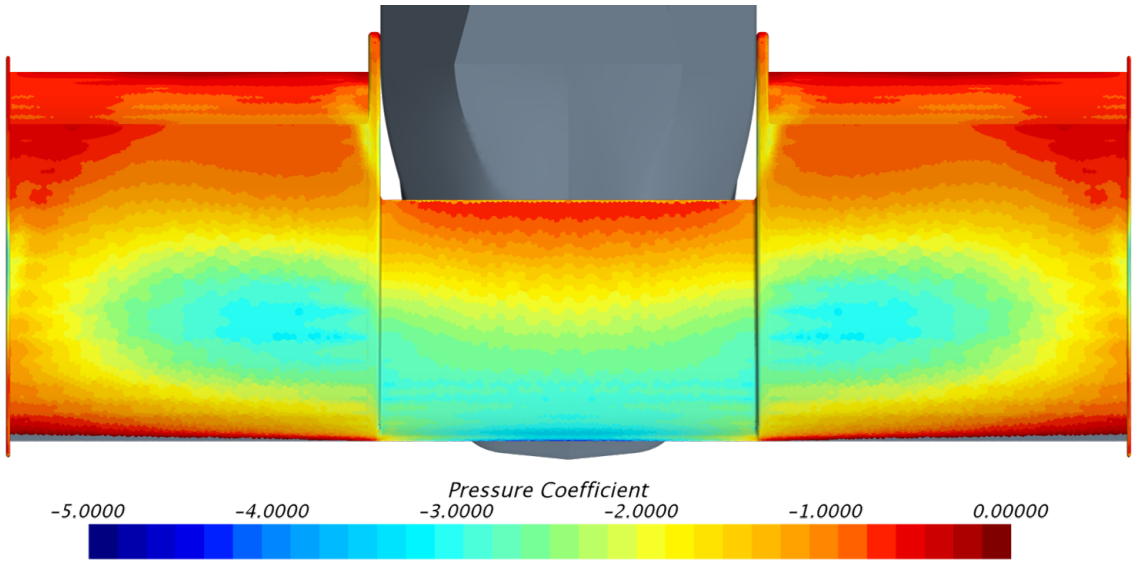


Figure 5.8: Pressure coefficient of temporary front wing

Several details are evident from the figure:

- Absolute value of $C_p$ is excellent for the set objectives;
- The separation zone, indicated by a high pressure gradient, is very limited for both aerofoils;
- Secondary motion is present, displayed by the pressure gradients that are noticed between the root and the extremity;
- The endplates allow to have a different pressure from the environment even on the extremity, as we will see later

### 5.2.3 Clark Aerofoil

As can be seen from the figure 5.8 the main is not composed only by the chosen Benzing aerofoil, but in the central zone there is a Clark aerofoil which has the particular characteristic of having:

- Flat lower camber: so as not to hinder the air passage towards the undertray, which is the primary objective for this zone;
- Curved upper camber: so as to generate in any case downforce, even if its leading function is not that, and also exploit the ground effect

In a qualitative way, by only knowing the aerodynamic laws without performing simulations, the Clark vertical position poses the following problems:

| Position | Description | Result |
|---|---|---|
| Almost to the ground | Occlude passage section<br>Stall: lower passage section | Negative |
| Low | Occlude passage section<br>Accentuated ground effect | Negative |
| Half-height | Occlude partially passage section<br>Ground Effect | Positive |
| High | Free passage section<br>Moderate ground effect | Positive |
| Near nose | Free passage section<br>Modest ground effect<br>Stall: upper passage section | Negative |

Table 5.2: Clark options

Based on the table 5.2, we decide to investigate only the two areas that we know to be more interesting. In particular, we try to privilege the work of the undertray, therefore trying to guarantee a greater air flow rather than maximizing the downforce of the front wing looking for a greater ground effect.

However, despite the smaller size chord than the Benzing ones and equal to 200 mm, it can be seen in the figure 5.9 on the left as the immediate proximity of the nose causes an early separation and the ground effect is less significant, indeed:

- The distance from the nose guarantees a more gradual deviation of the flow due to the compliance with the Kutta condition (in fact the fluid from the upper camber should go upwards, but then bend to follow the nose), which therefore is not forced to separate for bending . Furthermore, the flow above the trailing edge is faster, so the pressure is lower, thus ensuring a lower adverse pressure gradient, delaying the separation;
- The ground effect causes the increase of the upper camber's speed, making the flow more energized and therefore more able to counteract the adverse pressure gradient, thus delaying the detachment

As a result, Clark is positioned at the highest possible point which does not generate a marked separation due to the presence of the nose. This condition is depicted in the right side of image 5.9.

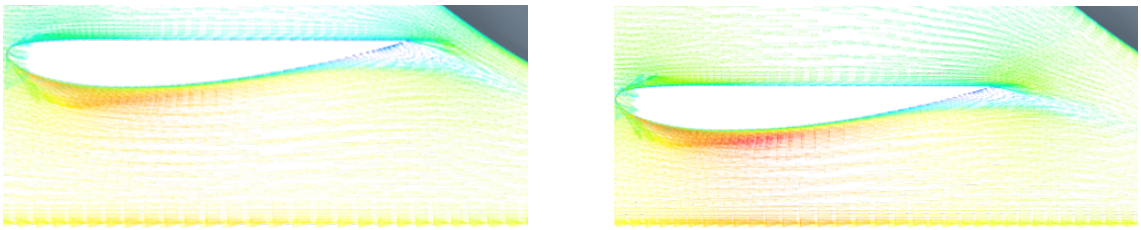

Figure 5.9: Clark positions

From the comparison it can be seen how, in addition to the lower separation that makes the whole aerodynamic package work better, there is also an increase in the downforce of the single front wing, due to the ground effect, to the detriment of a lower mass flow towards the undertray due to the reduction of the passage section, despite the greater speed of the current.

## 5.3 Strakes

Strakes are vertical elements which run underneath the wing - and work to both align the flow and produce vortices which are beneficial to the flow downstream - especially the front wheel wake.
It guides low pressure air, speeding it up or bending it. They also create vortices. The placement of them is very important, for front, global and rear downforce, as well as tire wake. They may also have the effect of speeding up the airflow a bit, while bending air away from the tire.
Strakes may be longitudinal straight, but latitudinally they may be bent over their complete length. Important to know is that the first strake should be positioned right next to the inner edge of the tire. At the back end of the bent part of the strake, it creates a strong vortex at the tip, shielding airflow. The airflow that it is shielding is meant for the splitter and undertray, making this a very critical solution. Without it, the rotating tire would send more turbulent air into that region, robbing the undertray and splitter of downforce.
Air between the strakes and the underside of the wing tends to stagnate, which creates drag. Creating a vortex in front of the stagnated air re-energizes the air there and speeds it up. They prevent marbles or other dirt from clogging up the slots in between the elements, which would also lead to downforce loss.
These strakes prevent diagonal secondary motion, flow under the wing. If the flow goes diagonally, when it comes over the top edge, it will be misaligned with the flow over the top. This will create vortices and will be bad for anything behind and outside of it. The target is to have parallel flow between top and bottom for better efficiency.

The influence of the strakes was assessed both in terms of:

- Flow cleaning, as they tend to straighten it, reducing swirling;

- Flow direction, as the fluid is forced to lap onto the strakes:
  - To sidepods: in order to make them work with the straightest and cleanest possible, and, perhaps, even accelerated, flow;
  - Far from undertray: in an attempt to prevent the outside air from being attracted by the depression destroying the undertray and diffuser work;
  - Behind the front wheel: in order to make this area assume an appropriate motion that is instead in complete turbulence due to the wake of the wheel
- Energy compartmentalization, since, being a physical barrier, they prevent the exchange of momentum between the areas of fluid that divide. This determines the risk that if an area, in itself is already critical in terms of energy with the risk of fluid separation, it is isolated, as it no longer receives motion from the adjacent areas, it does not have enough energy to remain attached to the aerofoil and , separating itself, irreparably damages the aerodynamics of the front wing and more

**Optimization criteria**

In order to correctly evaluate the validity of a solution in presence of strakes, the design process was not limited to a comparison between a configuration without them and one that presented them. Indeed, an optimization process of the solution with the strakes was followed, varying all the possible parameters, and only at the end was the comparison implemented. In this way we were sure to compare both optimal solutions of the two options.
The degrees of freedom for choosing the type of strakes are:

- Number;
- y-positioning;
- x-length;
- z-height;
- Flat or curved shape

### 5.3.1 Number and positioning

First of all, the number of strakes by the configuration was decided. A high number of strakes ensures a greater ability to clean and to direct the flow, together with a range of possibilities to manage it more widely, due to the higher number of editable elements. However, the solution with four flaps was excluded a priori, as it was considered impossible not to cause the fluid separation due to the compartmentalization, an intuition justified by the feedbacks obtained later.

Indeed, it is necessary to avoid isolating those areas that have low wall shear stress, and to prevent them, if they no longer receive an exchange of momentum, from separating.

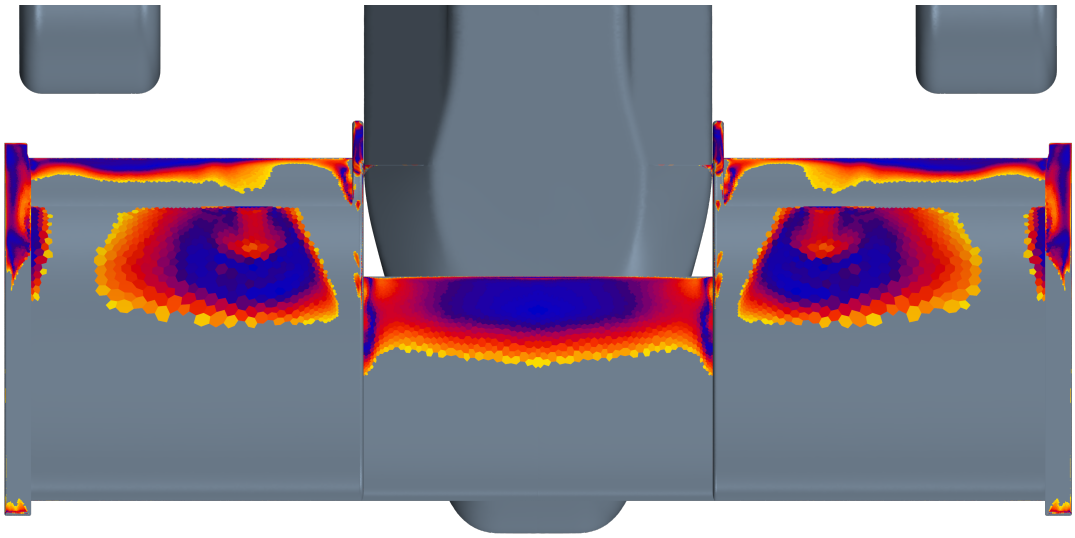

Figure 5.10: Areas a priori critical for separation

As can be seen from the image 5.10, this area on the main is rather extensive, so using three strakes a part of it could certainly be isolated, compromising the quality of the flow. Indeed, the right sides of the two following figures demonstrates what has just been said.

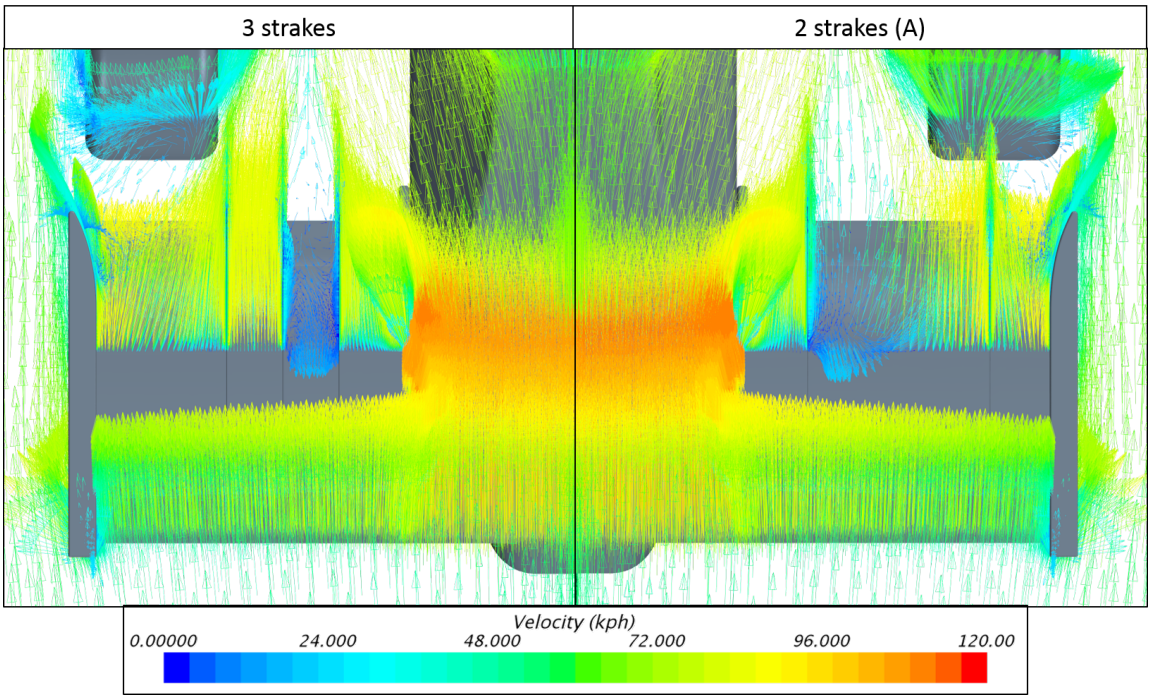


Figure 5.11: Airflow separation: strakes quantity

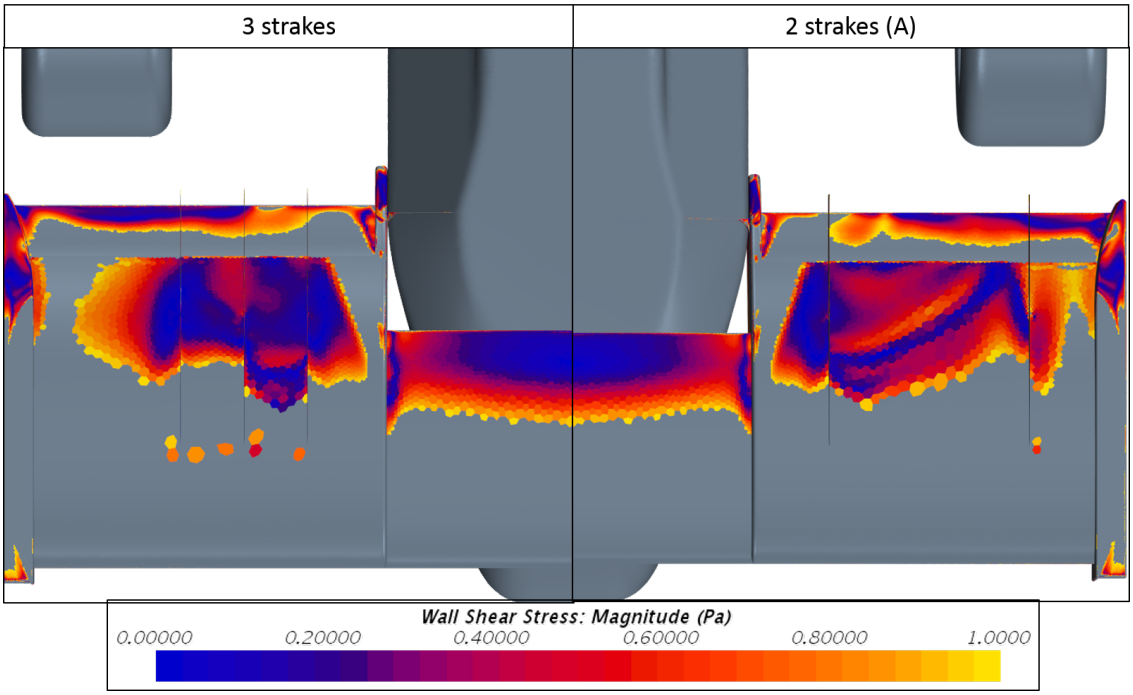


Figure 5.12: WSS decrease: strakes quantity

The three-strakes configuration has no potential as this quantity is too high since it always tends to isolate energetically too little areas. Whereby the flow no longer receiving the energy necessary to remain adherent to the profile separates compromising the work of all aerodynamic components.
This justifies the a priori abolition of the four-strakes configuration, and legitimates the attempt to find a solution that foresees only two.

Generally speaking, the two-strakes configuration has more chances of being valid since the compartmentalised areas are more extensive and therefore there are higher chances that the low-energy zones will not be isolated from those with greater momentum.
However, as noted in the two previous figures, this does not imply that separation does not occur, similarly to the previous case.
In particular, if you are going to isolate the critical areas illustrated by 5.10, fluid separation will be a necessary consequence, while otherwise there will be an increase in performance, as the following images show.

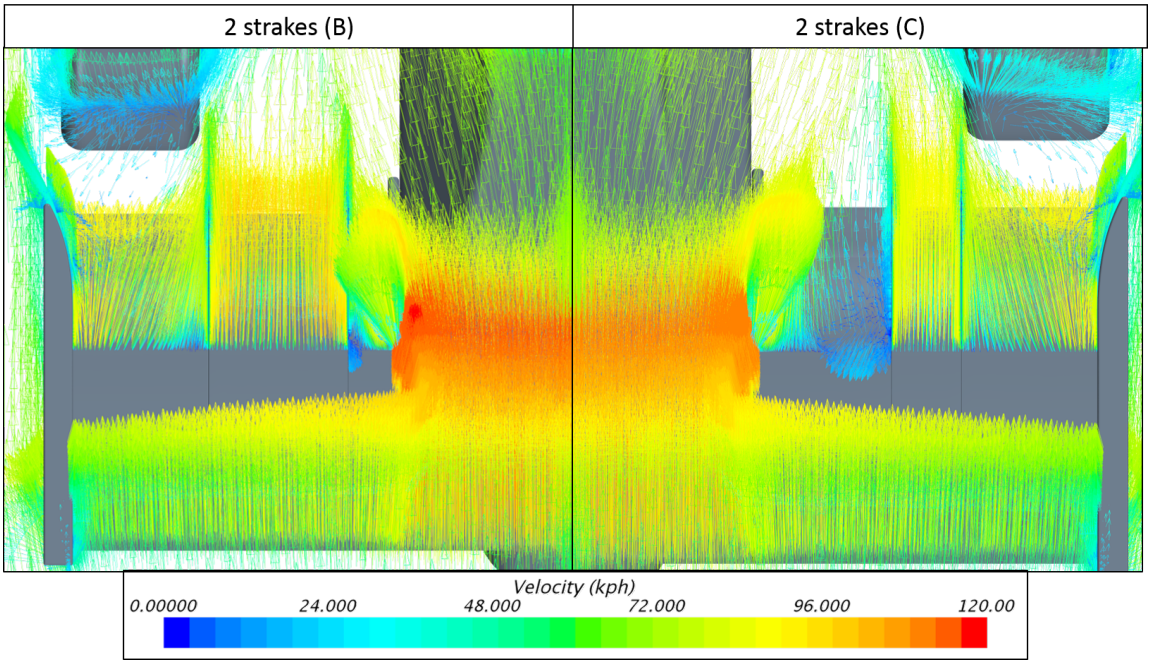


Figure 5.13: Energized vs isolated airflow: strakes quantity

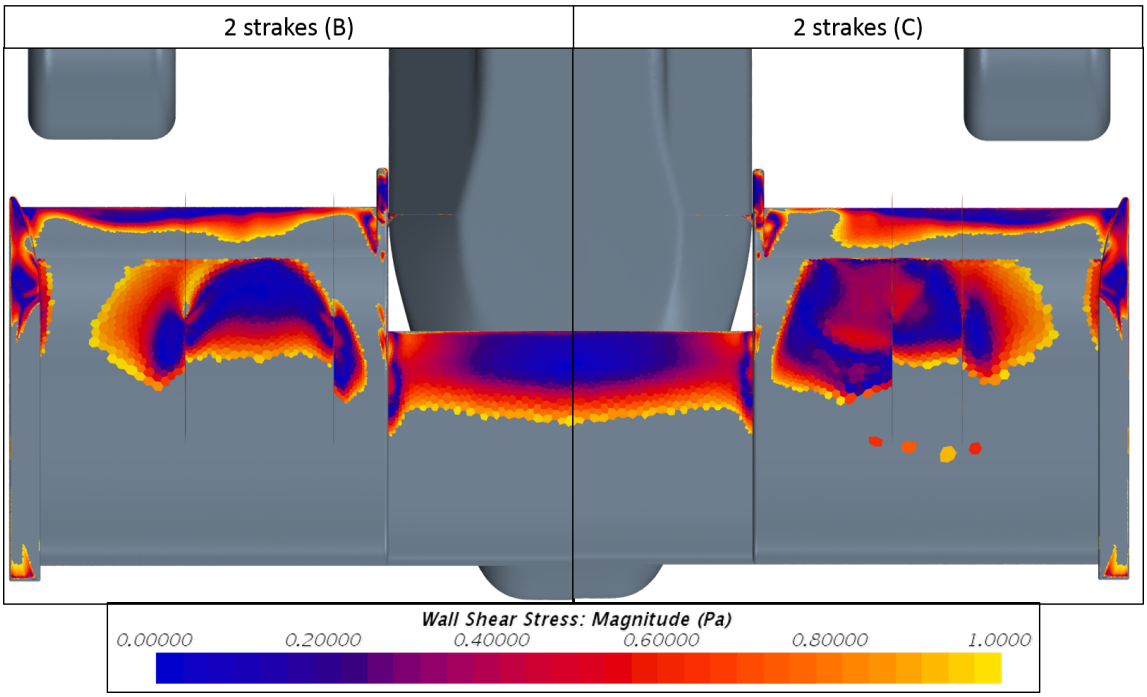


Figure 5.14: WSS increase: strakes quantity

Figures show that the configuration on the left side presents a clear improvement in the wall shear stress compared to 5.10. This is due to the fact that isolated areas provide higher energy flow next to areas with more critical flow, so, forced by strakes to exchange momentum only with them, they helps the airflow to remain more attached to the aerofoil.
Consequently, by analysing the various flow behaviours, an ideal positioning of the configuration with two strakes was obtained.

### 5.3.2 Length

Once the strakes number has been choosen and optimally positioned, simulations have been performed to vary their length (represented by the parameter R). The expected changes are the following:

- Deeper direction towards the sidepods;
- Better undertray insulation;
- Greater cleanliness of flows;

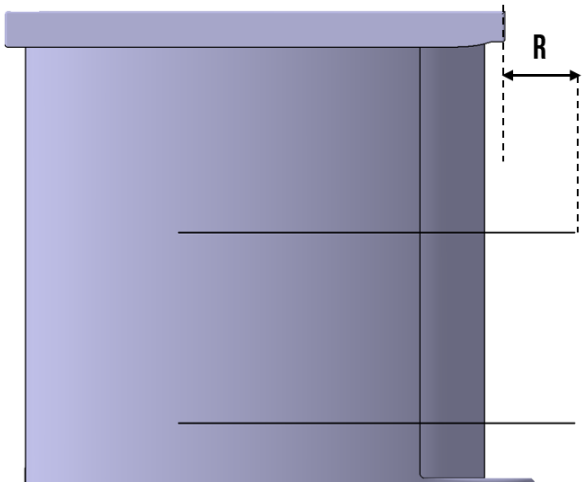


Figure 5.15: R DoF

As can be seen from the following images, with oversized length strakes a better celaning of the flow towards the sidepods is reached, increasing their performance. However, there are no improvements either for the undertray or for the wake of the wheel.

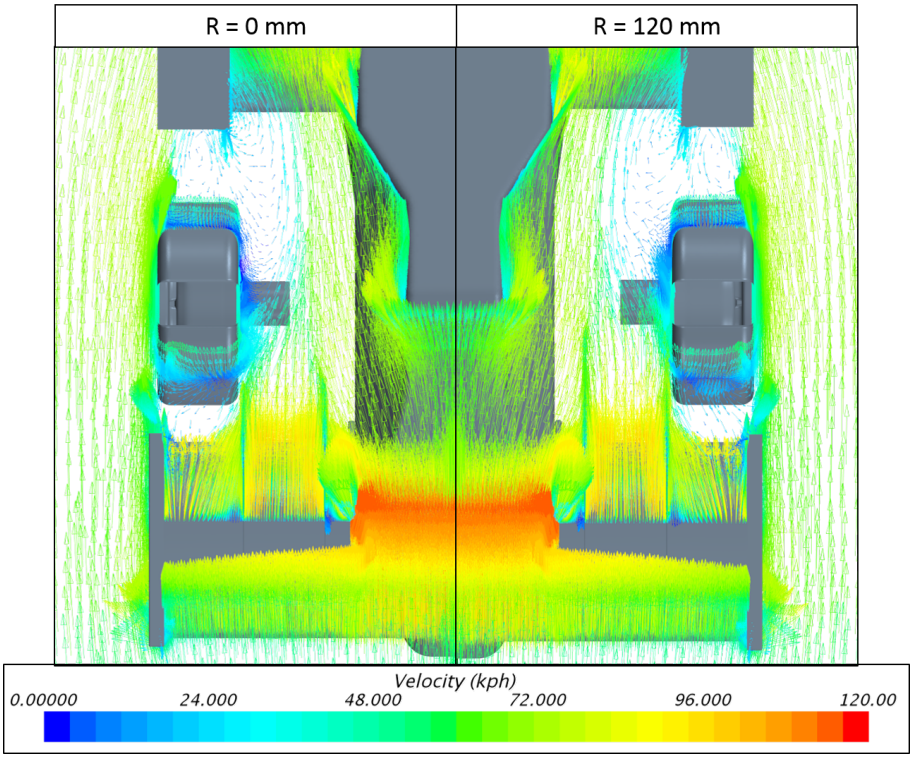


Figure 5.16: Cleaned airflow: R

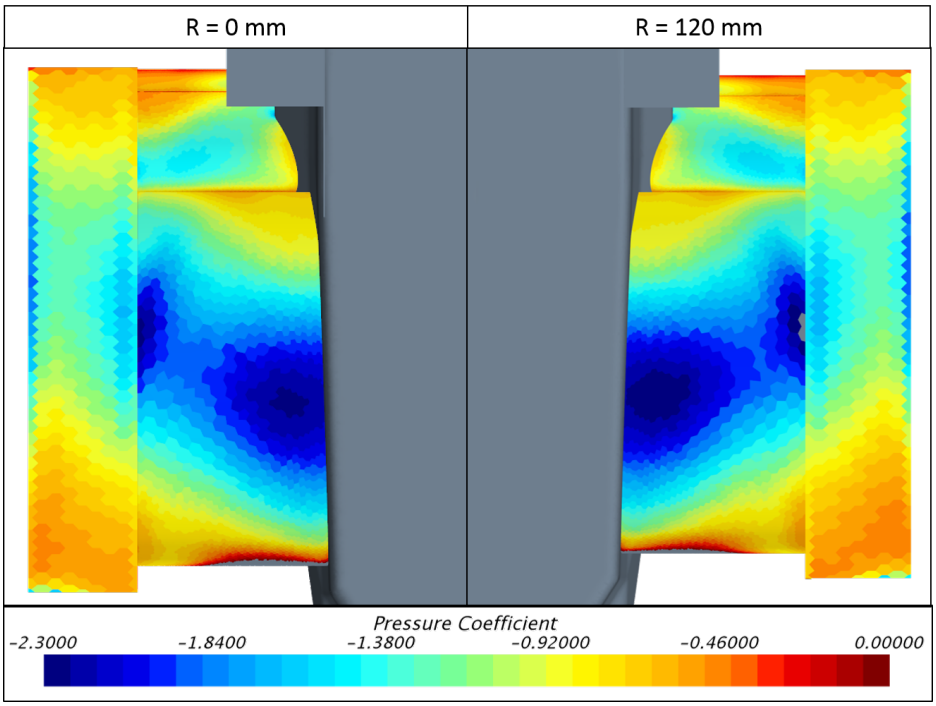


Figure 5.17: Sidepods enhancement: R

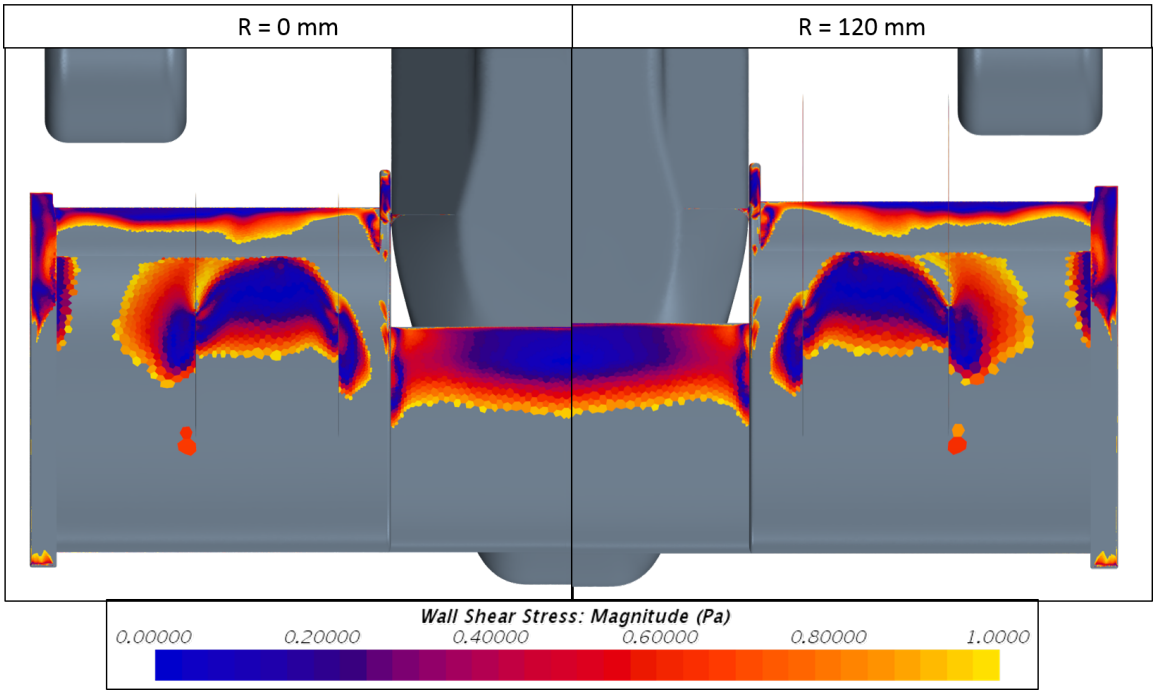


Figure 5.18: WSS improvement: R

There is a slight increase in the performance of the front wing, which is also due to the greater cleanliness of the surrounding flow.

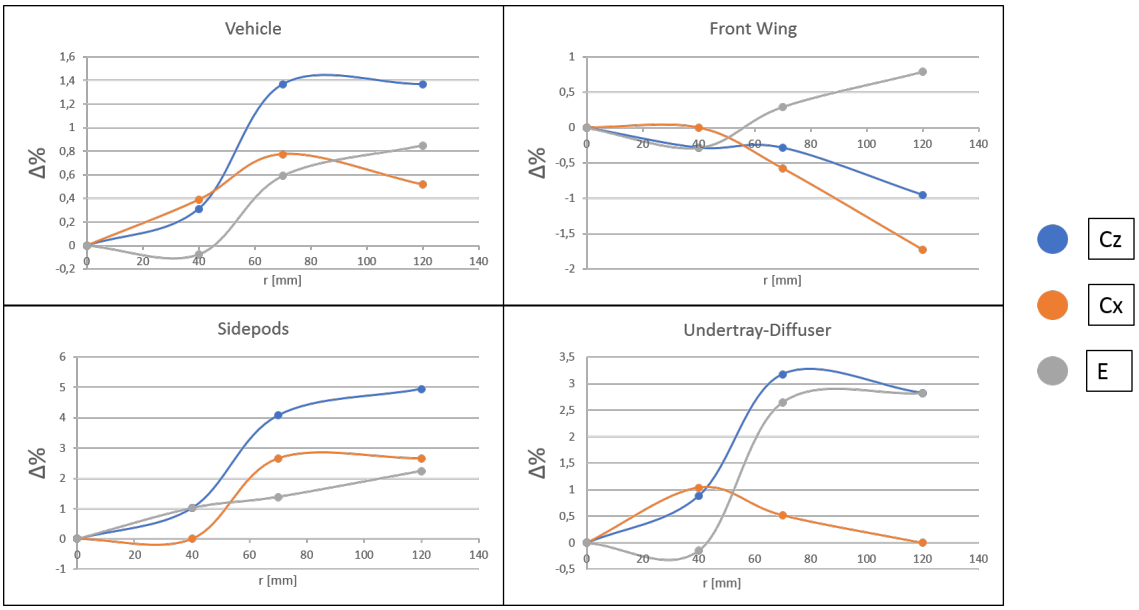


Figure 5.19: R DoF results

However, since there were no significant differences in terms of flow analysis, the choice was made using the numerical values just shown and privileging the overall vehicle performance.

It can be seen how, to vary the length, the downforce stabilizes overall, while the efficiency continues to increase. However, the longer length solution is not chosen because the performance improvement made is not such as to justify the drawbacks:

- It presents accentuated structural problems, as it is made up of only carbon plies, with the total absence of core, so it has a very low bending stiffness that could lead to large oscillations due to aerodynamic forces. These disturbances, in addition to not respecting the design conditions, could even be harmful in terms of performance;
- It causes interference with the wheel, as it risks being in the area that could be occupied by the wheel when steering, or in any case where the cooling pipes and electric power cables are located.

So the chosen configuration is $R = 70$ mm.

### 5.3.3 Height

Moving on to the analysis of the HEIGHT parameter's influence, in particular it was decided to increase its value for the following reasons:

- To search for Greater flow control;
- To limit the structural problems described above

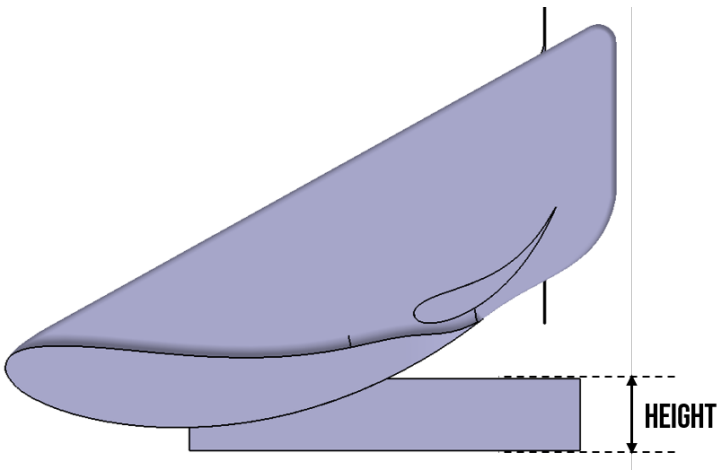


Figure 5.20: Height DoF

One can guess how, following this path, the problem of separation caused by the compartmentalization of energy, already solved, can recur. Indeed, the increase in streakes' height causes the isolation of the trailing edge, which by construction has minor wall shear stress, which could cause a fluid separation that cannot be improved precisely because of the greater predisposition of this area to such phenomenon.

Indeed, in the following figures you can see how the area that, isolated by the strakes, improved its flow, presents a further increase in its performance, while the other sections find a marked separation.

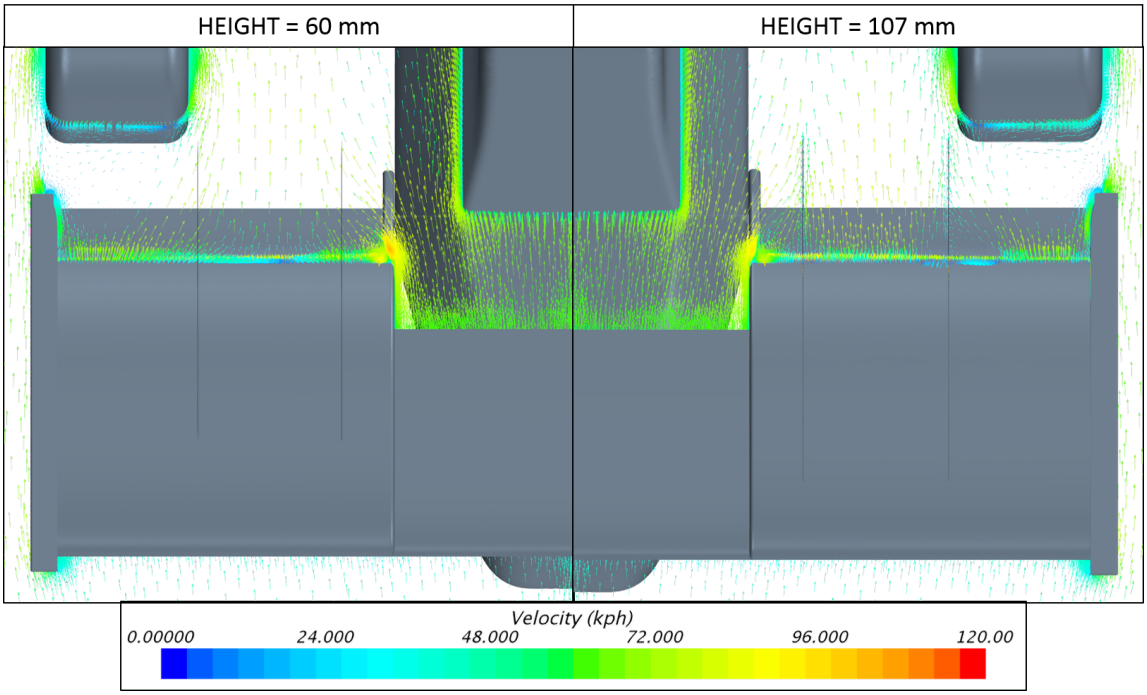


Figure 5.21: Separation increase: height

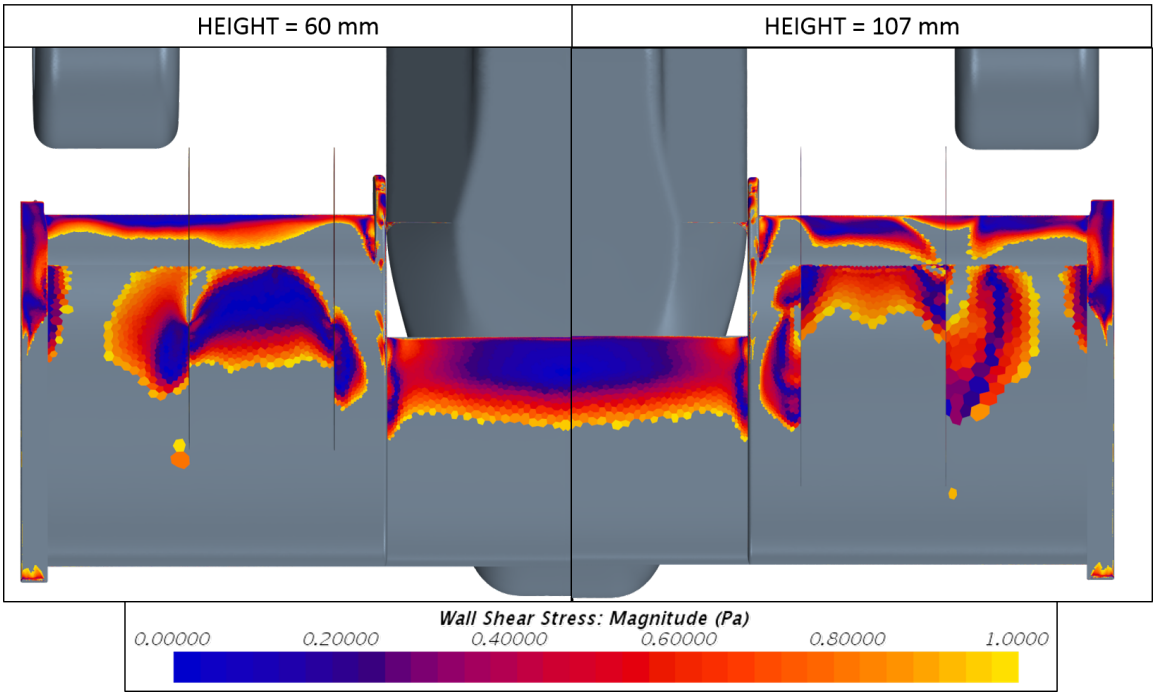


Figure 5.22: WSS worsening: height

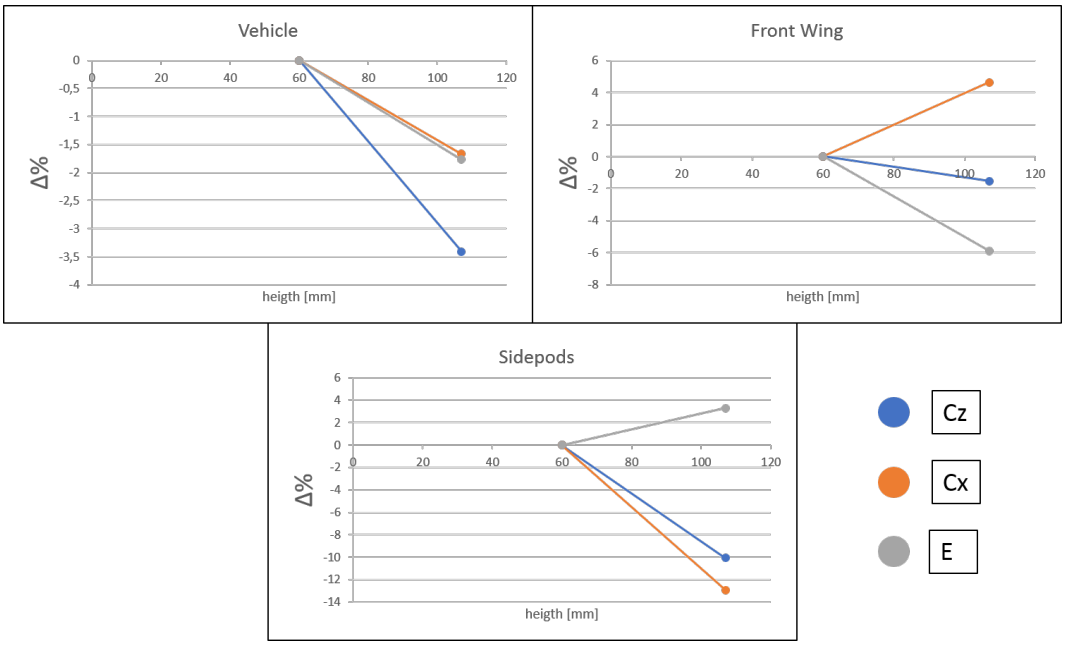


Figure 5.23: Height DoF results

Results meet expectations: the work of the front wing deteriorates from all points of view due to the considerable detachment, while the subsequent components, and therefore the entire vehicle, suffer with dirty flow and lower speed (also due to of greater friction resistance), so that all aerodynamic quantities collapse.
Moreover, it was not even possible to increase the strakes' height nor move them downwards to avoid compartmentalizing the trailing edge, because they were already in correspondence with the minimum ground clearance allowed by the regulation.

For these reasons, we chose the strakes with the smallest height achievable, which coincides with those tested in all previous simulations: $HEIGHT = 60$ mm, both for reasons of effectiveness (too small does nothing) and for structural reasons, as explained above.

### 5.3.4 Shape

The last parameter to be established is the aerial projection shape of each of the two strakes. The curved geometry was tested with the aim of:

- Bending the fluid and then try to reduce the wake of the wheel
- Creating whirlwinds that isolate the undertray

Initially we tried to bend both strakes so as to maximize the two effects.
It can be seen how the internal strake actually succeeds in the purpose of considerably reducing the wake of the wheel, causing the fluid to curve.

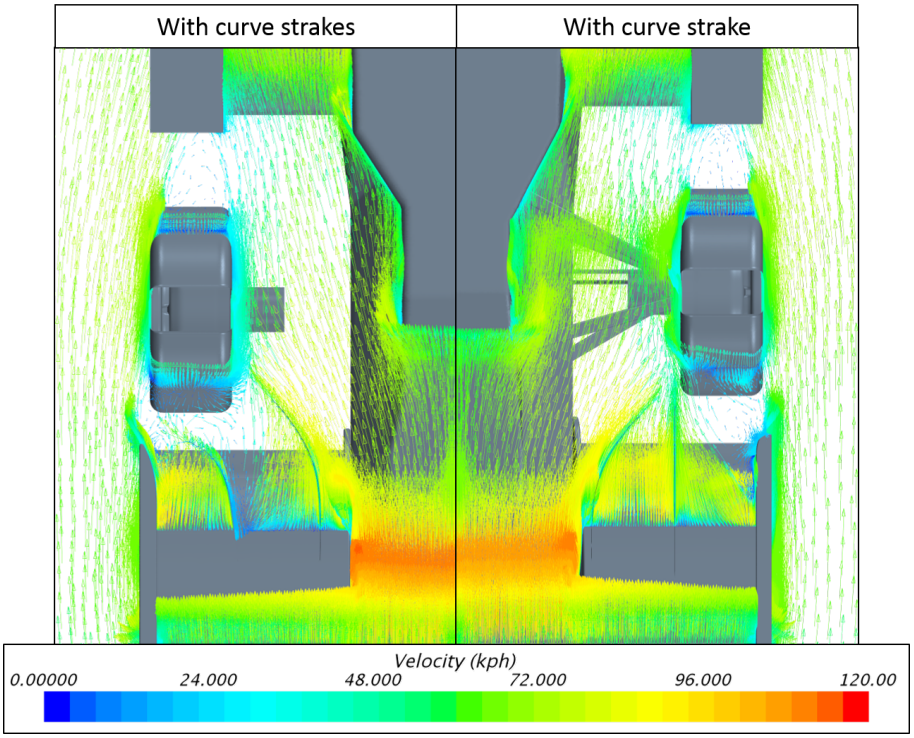


Figure 5.24: 2 or 1 curved strakes

However, the external strake, although partially able to direct the flow outside (outwash), causes an important separation for two reasons:

- A divergent duct is formed which therefore increases the adverse pressure gradient, making this area more critical;
- The turbulence deriving from the rolling of the wheel is directed in the area weakened energetically by the divergent duct

Moreover, the generated vortices, not being sufficiently strong and having no space available for controlling them, do not lead to an increase in the performance of the undertray, but, actually, having a longitudinal axis, they could irreparably damage the work of downstream components.

To continue to guarantee the reduction of the wake of the wheel and avoid the creation of a divergent duct, as in the case analysed, it was decided to give a curved geometry only to the internal strake. In this way, indeed, a convergent duct is generated which increases the air speed even further below the front wing, increasing its downforce. However, the vortices generated by the curved strip not only increase its resistance, but are also attracted, not having enough strength to divert them, from the undertray depression, compromising its work.
As a result, the sidepods work at much lower speeds so their interaction with the fluid is weaker in all respects, thus also causing a cleaner flow around the rear wing.

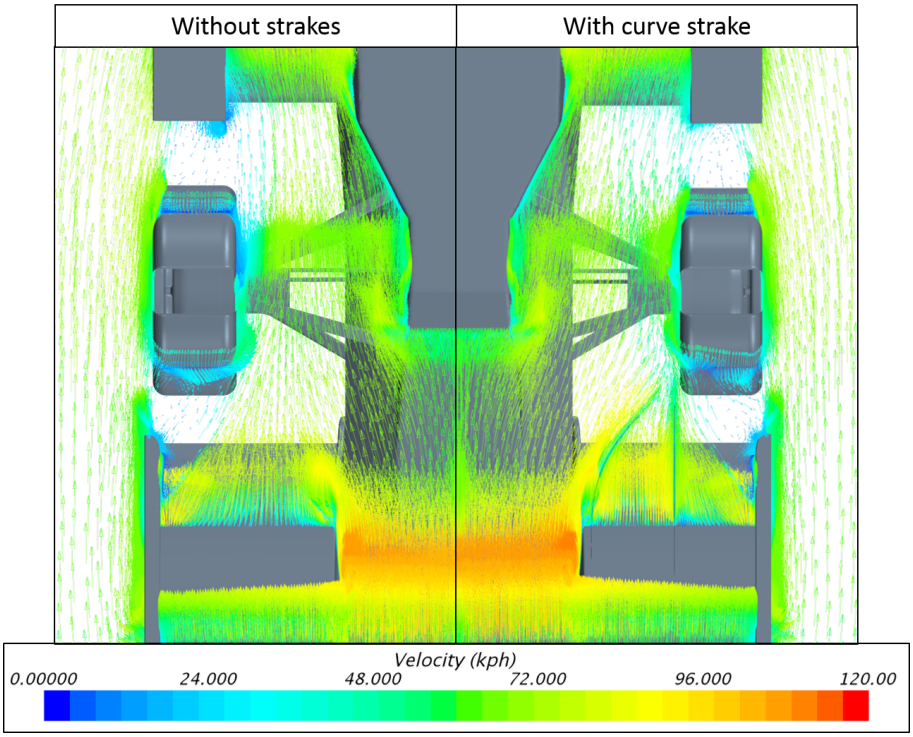


Figure 5.25: 1 curved strake

However, implementing such a strakes configuration the performance increase, in numerical terms, is really limited.

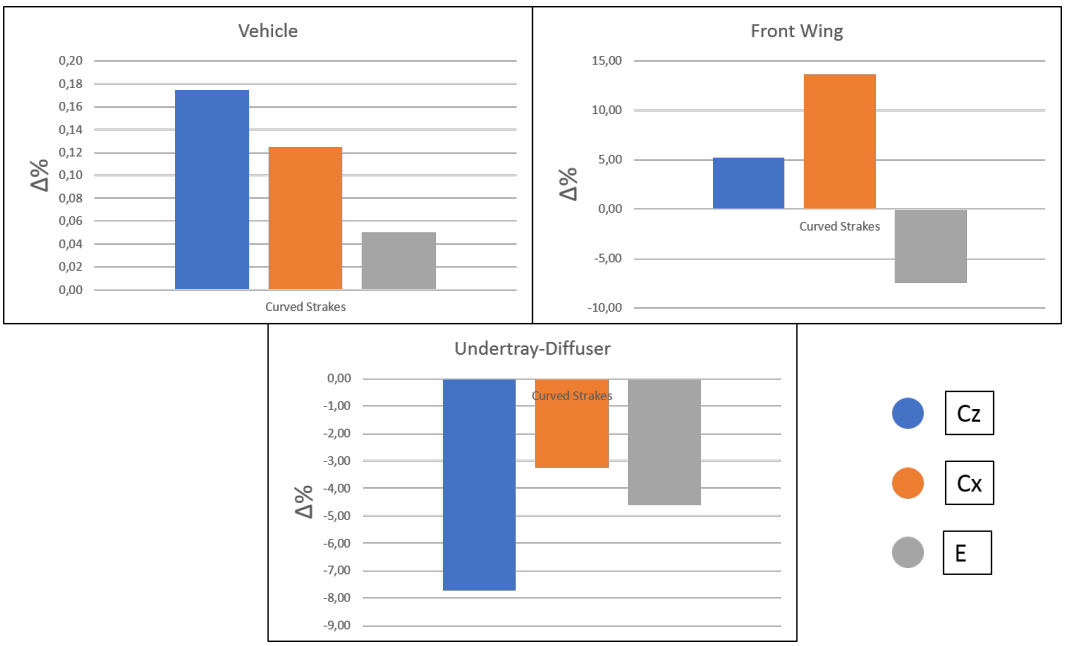


Figure 5.26: Shape DoF Results

Furthermore, a structural problem would arise: indeed for a curved strake it is accentuated since the aerodynamic forces could not only cause oscillations, but also statically deform the aerial projection shape and thus compromise the design configuration. These issues suggest that the best achievable configuration is that, analysed above, with flat strakes.

### 5.3.5 Effect

Having reached the strakes configuration with the maximum potential, it was decided to compare it with the strake-less configuration in order to evaluate the impact on flow control and on the resulting aerodynamic values.

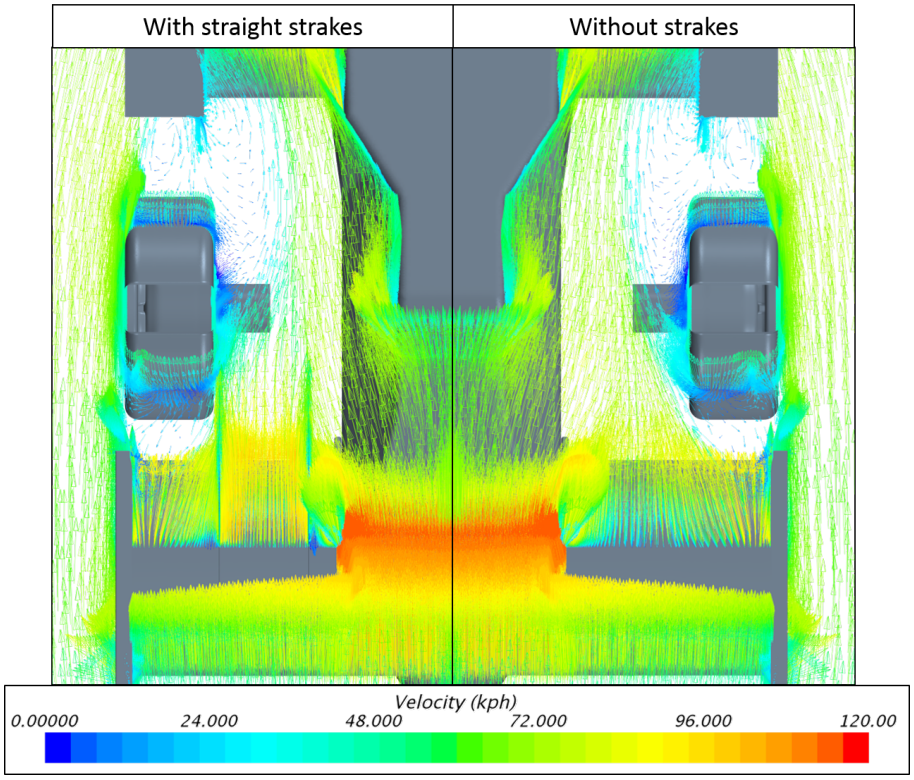


Figure 5.27: Airflow: strakes presence

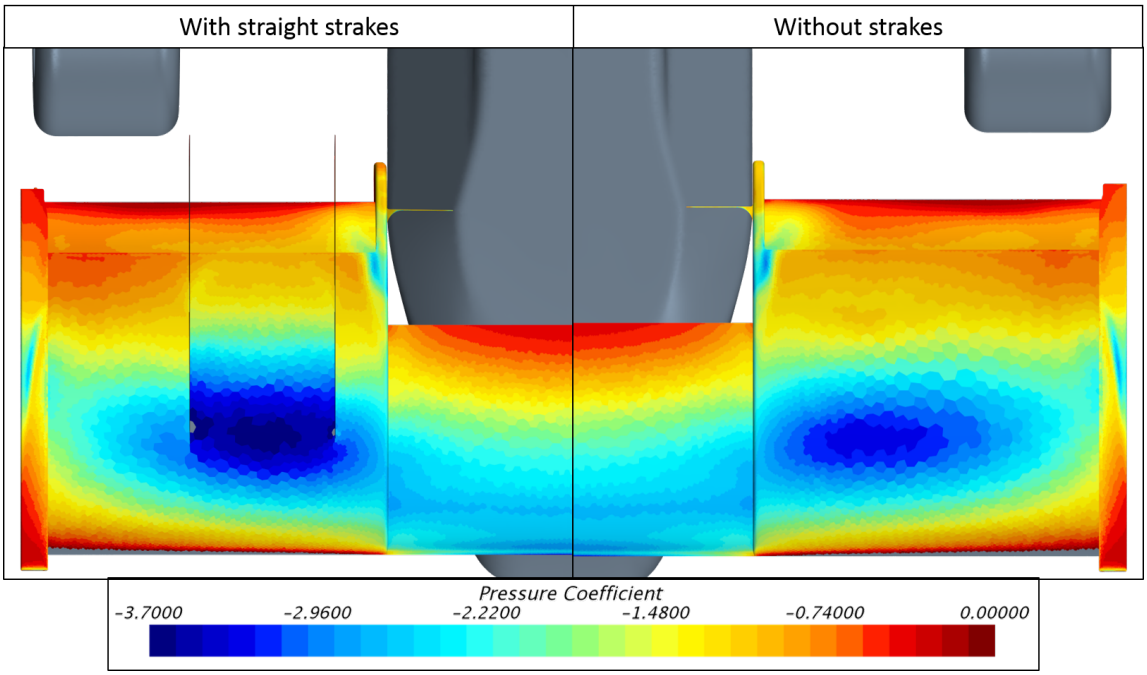


Figure 5.28: Pressure coefficient improvemente: strakes presence

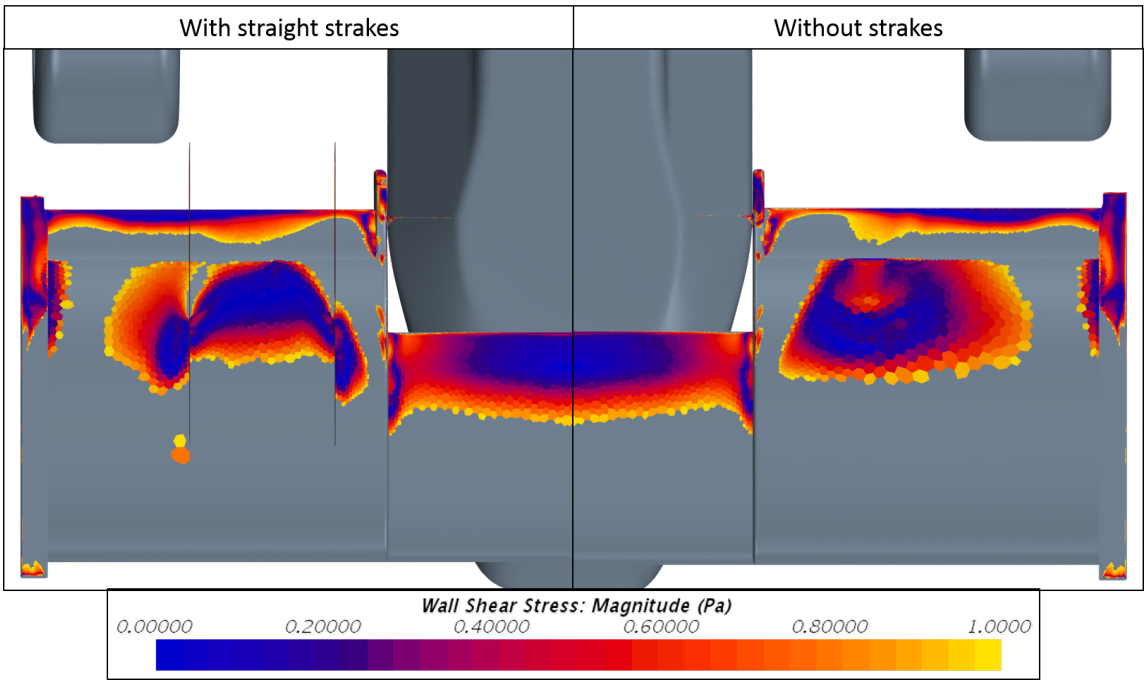


Figure 5.29: WSS enhancement: strakes presence

From the images you can see how:

- The wake of the wheel is not significantly changed;
- The flow below the mainplane is different, in particular it is accelerated and with less separation (also due to the better partitioning of the energy) thus guaranteeing greater performance;

- The flow below the flap remains approximately unchanged;
- The flow to sidepods is unchanged;
- The flow towards the undertray is more contrasted, indeed the greater isolation of the fluid translates into an increase in its performance

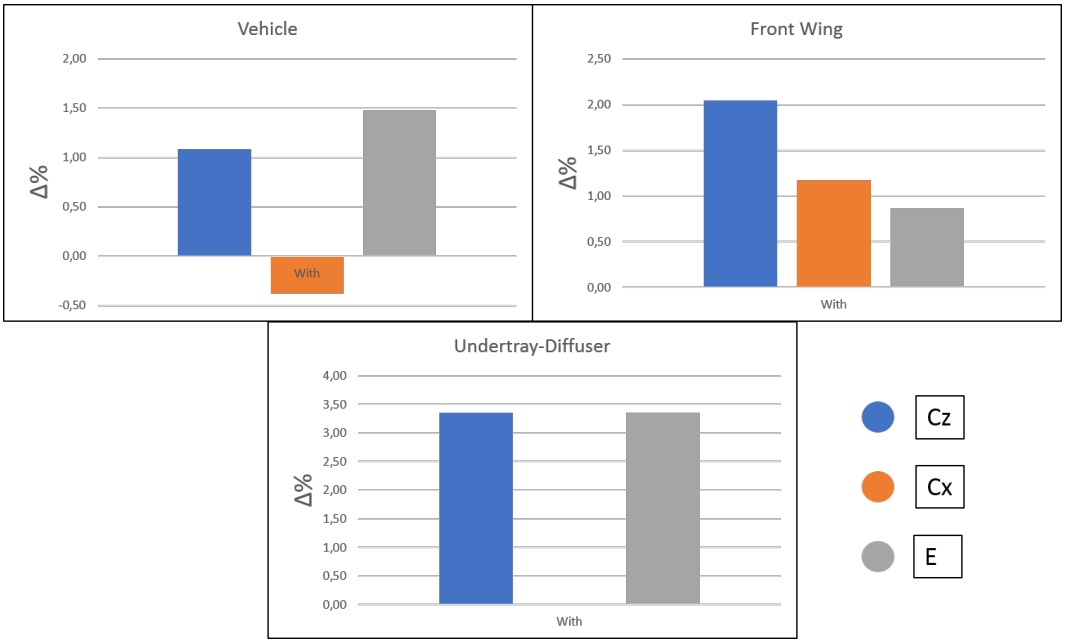


Figure 5.30: Presence DoF results

However, the advantages obtained are not sufficient to justify a greater waste of money, which can be invested elsewhere, and issues that cannot be neglected during production, as well as the already expressed structural problems. Therefore the final choice was to discard the configuration with strakes.

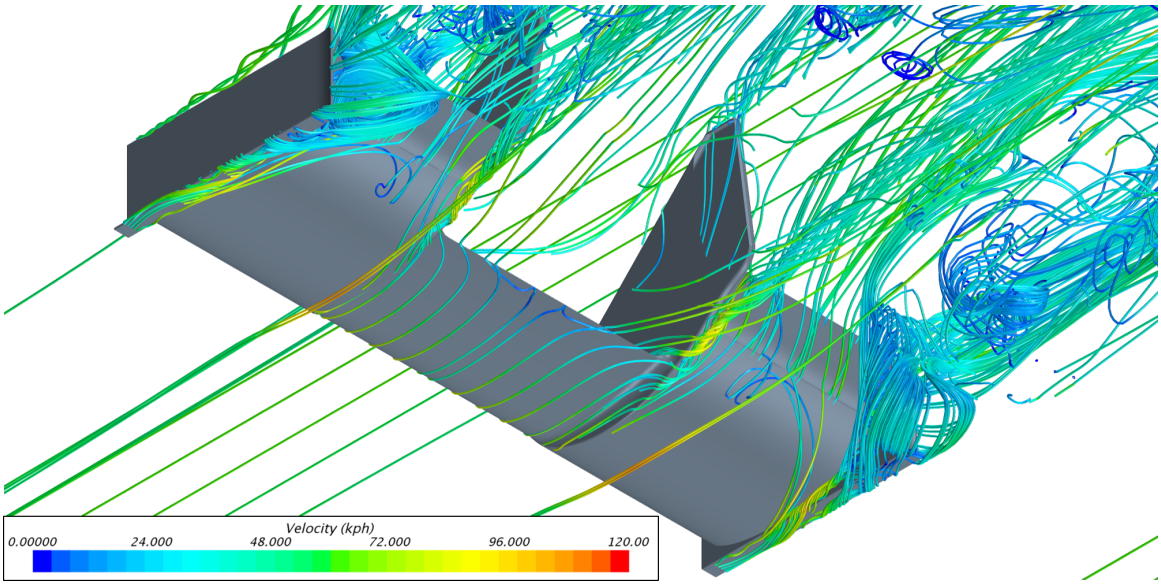


Figure 5.31: Front wing's streamlines

## 5.4 Endplates

Endplates are necessary in order to limit the vortices of extremities, introducing a physical barrier to the passage of air from the lower camber to the upper camber due to the different pressure.

These vortices are responsible for the induced resistance and, therefore, for the longitudinal counter-rotating vortices which are the most damaging both in terms of the component's drag, and in terms of cleanliness of the flow that interacts with the downstream components. Furthermore, by reducing the phenomenon of induced quantities, they also allow an increase in downforce, compared to the profile alone. Basically, the endplates increase the effective wing Aspect Ratio, bringing the wing closer to the two-dimensional case, following the Hoerner formula:

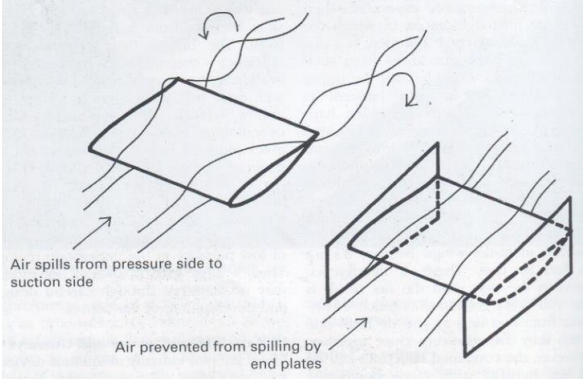


$$AR_{effective} = AR_{actual} \cdot (1 + 1.9 \cdot \frac{h}{b}) \tag{5.2}$$

where $b$ is the wingspan and $h$ the height of the endplate, while the measured aspect ratio is $\frac{b}{c}$, with $c$ symbolizing the chord of the airfoil.

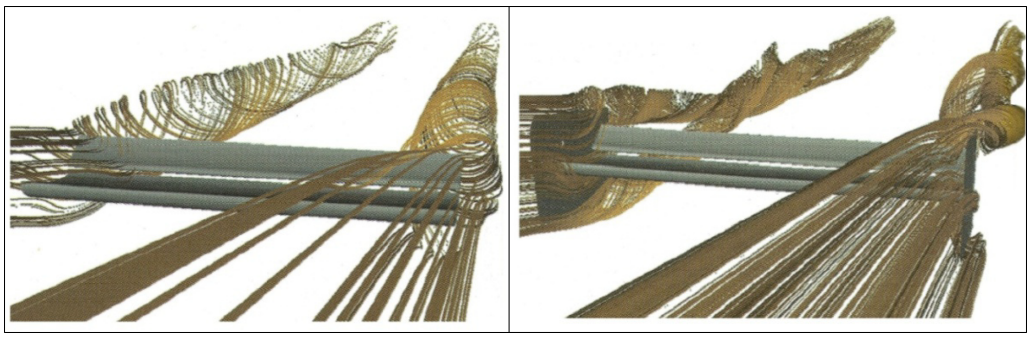

Figure 5.32: Endplates effect

At the same time, endplates can also perform other functions, such as:

- To direct the flow in motion to avoid the impact with the wheel;
- To create downforce using the ground effect, obviously only for parts with a limited ground clearance;
- To generate exploitable vortices

As known, endplates were born as a barrier with the aim of avoiding the migration of the flow from the lower camber to the upper camber and therefore maintaining the pressure difference. In order to grant the downforce and to avoid vortices that cause a resistance increase, they should, in principle, be as great as possible in order

to increase the aspect ratio of the wing.
However, there are contraindications to the excessive increase in the endplates' size:

- Increased viscous friction and therefore friction aerodynamic resistance;
- Rules are generally more restrictive on the dimensions of front wing ones rather than rear wing ones;
- Yaw: in the event of a side wind or car's yaw motion, endplates that are more extended at the front rather than at the rear would cause a center of pressure closer to the front axle with a consequent reduction in vehicle stability

**Optimization criteria**

Given the enormous surface of the rear wing endplates and given their negligible resistance, we have tried to maximize the surface based on the regulation constraints, opting for rectangular shape in lateral projection. In detail:

- the height imposed by regulation is: 250 mm;
- The thickness is the minimum possible for mounting issues (inserts): 5 mm

The remaining degrees of freedom for defining the complete geometry and dimensions of the endplates are:

- Shape of the footplate;
- Length and curvature of the rectangular surface;
- Presence of a vortex generator profile;
- Presence of the headplate

Some of the main parameters are shown in the figure:

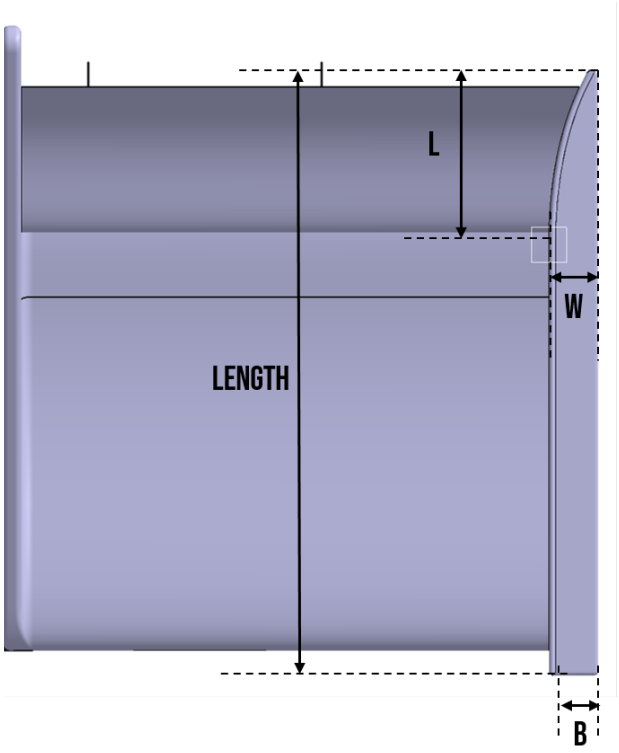


Figure 5.33: Endplates DoF

### 5.4.1 Footplate

The footplate is the orthogonal surface (characterized by B and W in figure 5.33) perpendicular to the endplate which prevents the vertical surface from being circumvented by the induced vortex.
For this component two forms have been studied: a curve and a flat one, whose specific purposes, besides those already mentioned, are respectively to generate vortices and clean the flows, granting the ground effect.

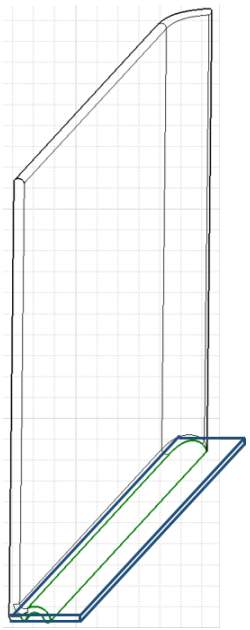

Figure 5.34: Footplate shapes

The curved shape, based on the figure 5.36, generates vortices that more than isolate the main's upper camber, as seen in figure 5.35:

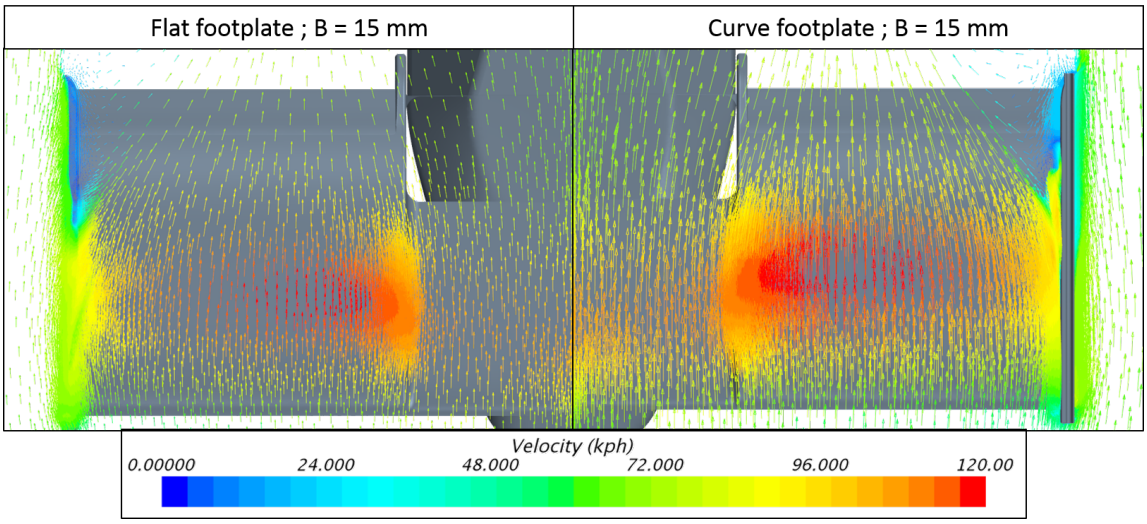


Figure 5.35: Airflow: flat vs curved footplate

This isolation causes an increase in downforce due to two main effects:

- Increase in the ground effect: more performing depression zone;
- Reduction of the induced vortex: area of downforce more extended from the root towards the end

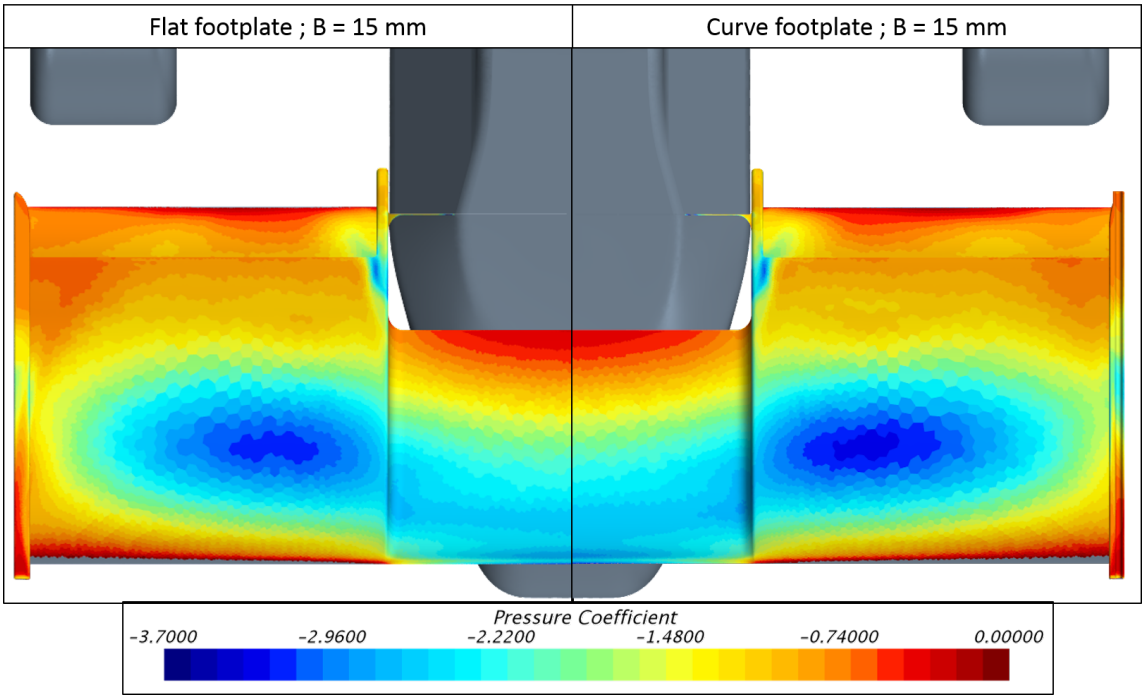


Figure 5.36: Pressure coefficient: flat vs curved footplate

However, the generated vortices damage the flow that hits the sidepods, not being sufficiently energized and adequately controlled, due respectively to the low speed of the car and the little longitudinal space available.

Therefore, when the curved shape was discarded, the surface of the footplate was investigated, with the same y-extension as the front wing. Indeed, as stated by [18], there is a 3.6% increase in downforce compared to the configuration without footplate, with a footplate extension equal to 1.6% of the chord size.

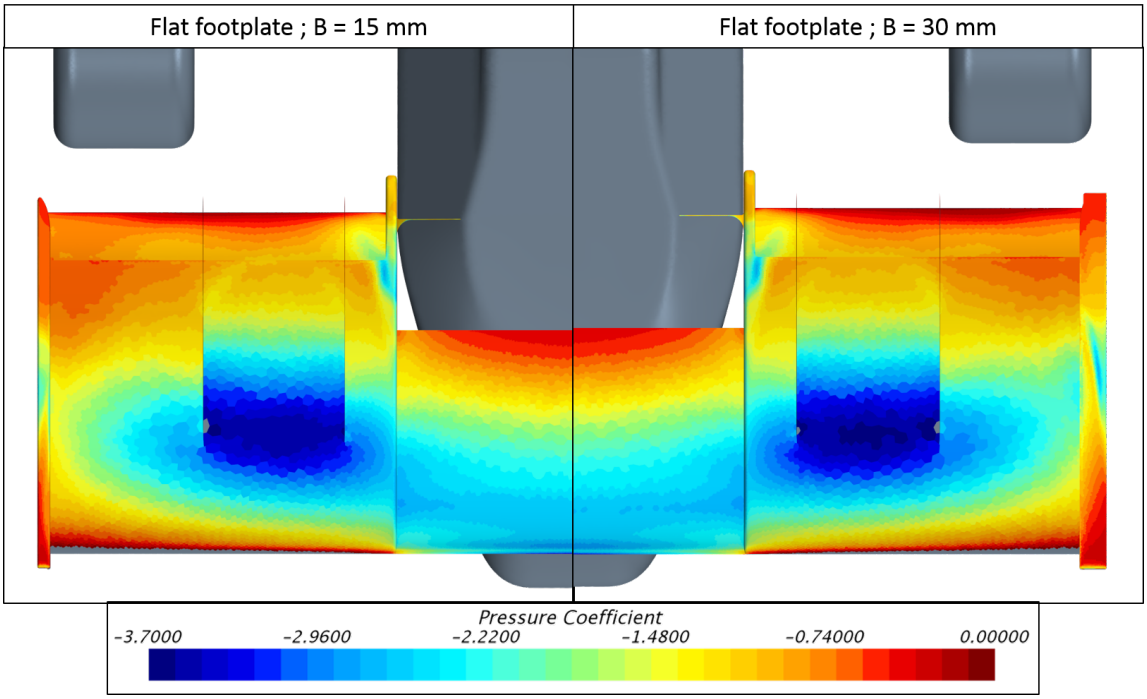


Figure 5.37: Pressure coefficient: footplate extension

Indeed, in figure 5.37 it is possible to notice how the depression area is more extended towards the extremity: this is a symptom of a reduction of the induced vortex, just as happened for the curved footplate.
This phenomenon is also displayed in figure 5.38, where it is clearly shown that the velocity vectors do not all go down anymore, due to a major obstacle, although they are attracted by the depression of the aerofoil's upper camber.

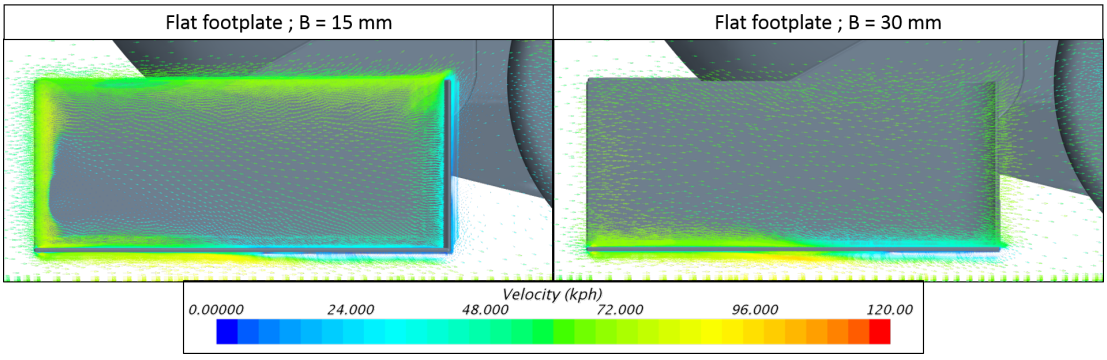


Figure 5.38: Airflow: footplate extension

It can be seen that a transverse dimension $b = 30$ mm guarantees an increase in downforce despite the decrease in surface area of the Benzing aerofoils, due to the reduction in the induced vortex and therefore to the increase in the pressure drop between upper camber and lower camber.

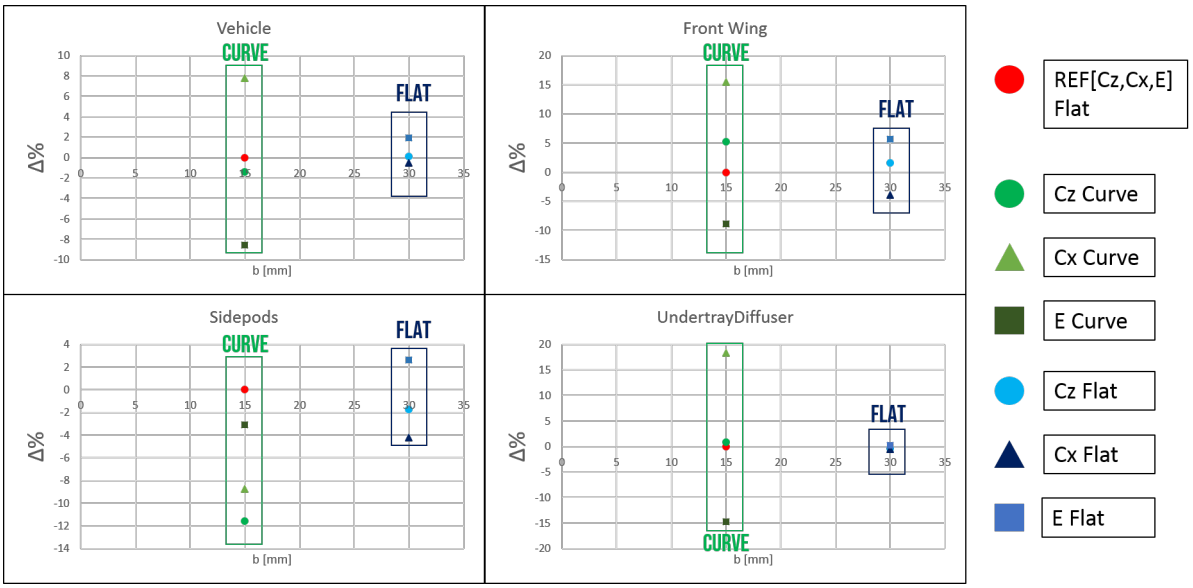


Figure 5.39: Footplate shape DoF results

Everything happens exactly as with the curved footplate, although without vortices generation, avoiding to compromise the work of the subsequent aerodynamic appendices, but with greater flows cleanliness and ground effect.

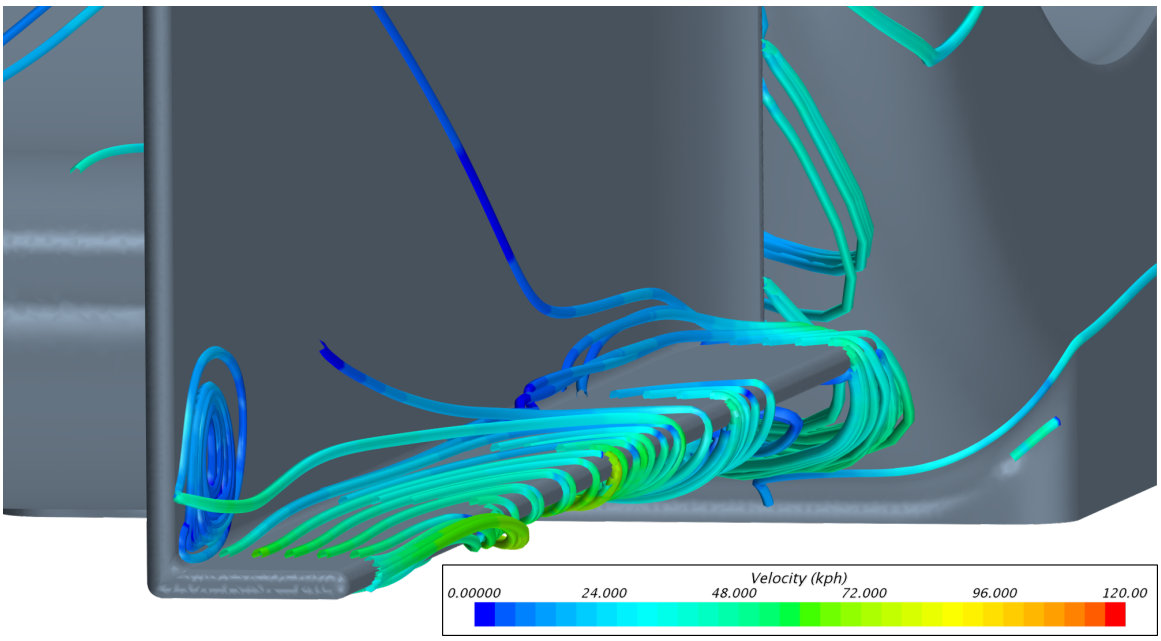


Figure 5.40: Footplate's streamlines

### 5.4.2 Length

In an attempt to better isolate the undertray from the inflow of air from the outside and to increase the surface extension, an increase in the endplate's length beyond the minimum length, necessary to avoid the formation of vortices at the ends of the Benzing profiles, was considered.
However, has been noted that this occlusion attempt, rather than hindering the flow

towards the undertray, forces the air coming from the Benzing to continue towards the wheel. Hence, the airflow directed towards wheel's stagnation point, suffers an increase in the pressure gradient, as seen in 5.41 and therefore an earlier separation.

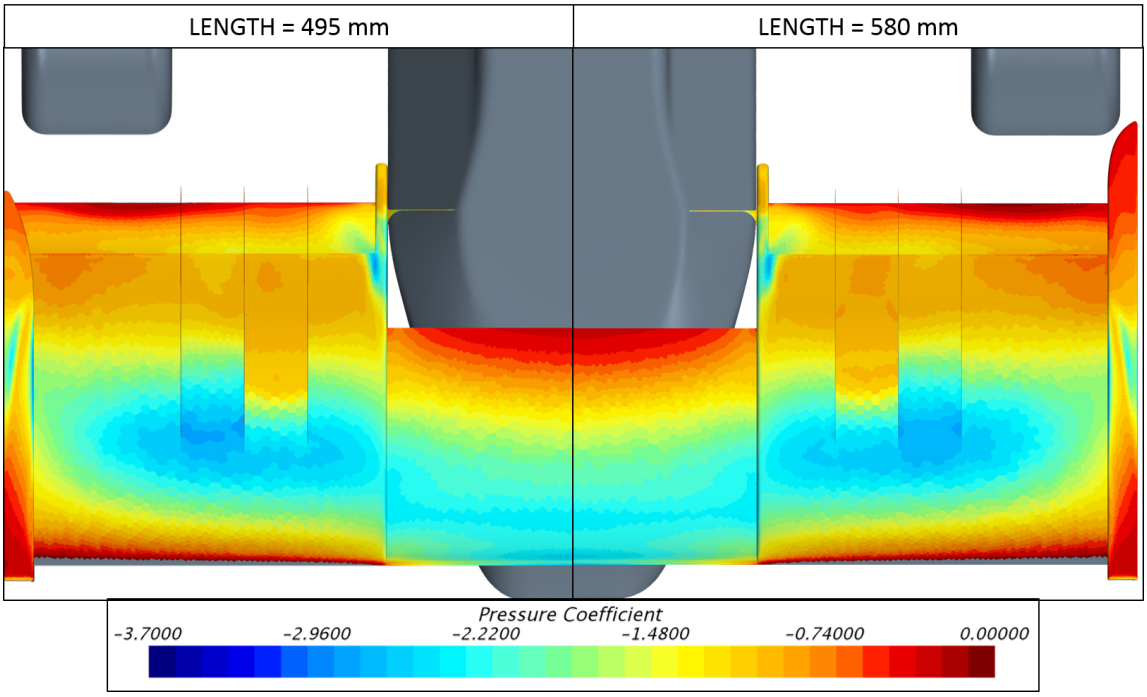


Figure 5.41: Pressure coefficient: length

Furthermore, the vortices resulting from the rolling of the wheel are bound to go towards the front wing, further favouring detachment, which causes a reduction even in the performance even of downstream elements.

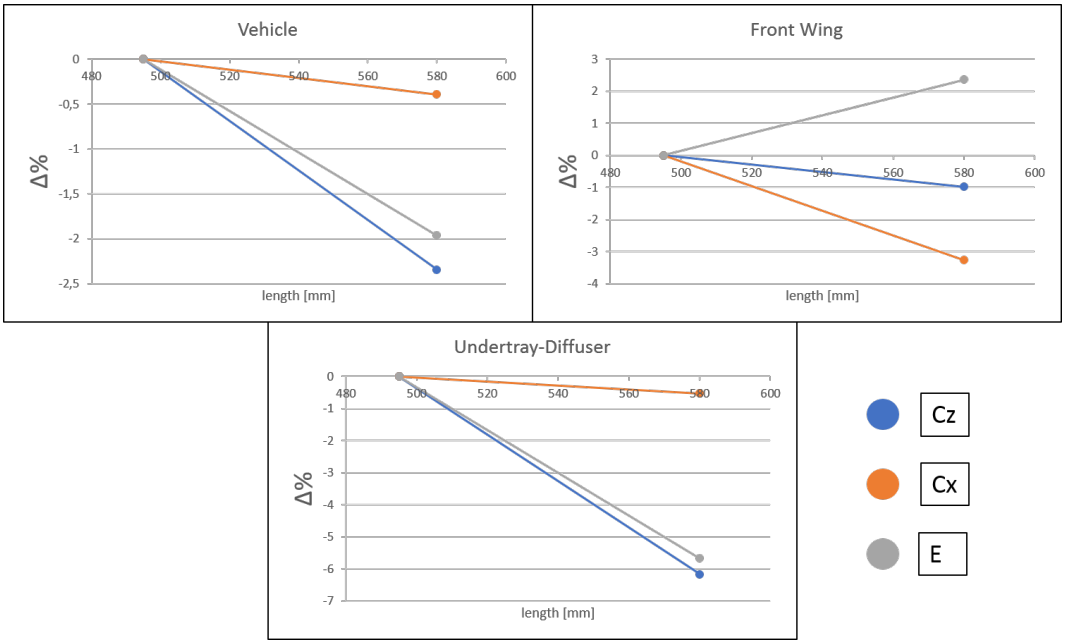


Figure 5.42: Length DoF results

Consequently, the minimum possible length was chosen: $LENGTH = 475$ mm.

### 5.4.3 Curvature

The curvature of the endplate has been studied to generate the phenomenon of outwash, in order to limit the negative influence of the wheel.
However, not having much space and strength to govern the flow, the complete outwash is not possible. The flow, after having turned around the wheel, will tend to return to the sidepod, as can be seen in the two following figures:

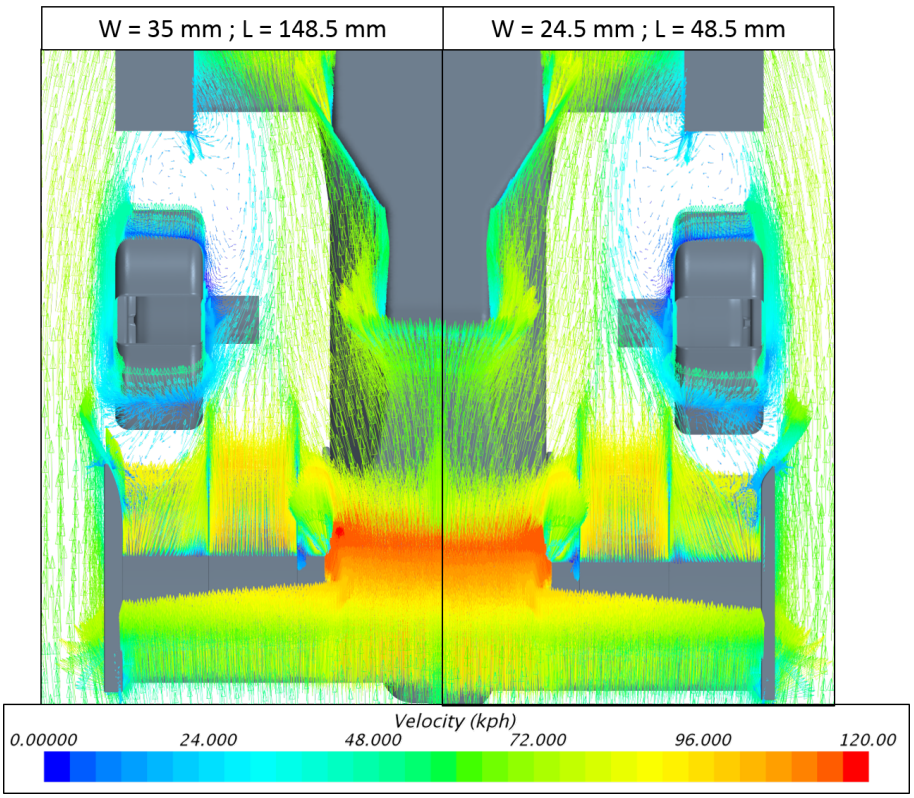


Figure 5.43: Airflow: curvature

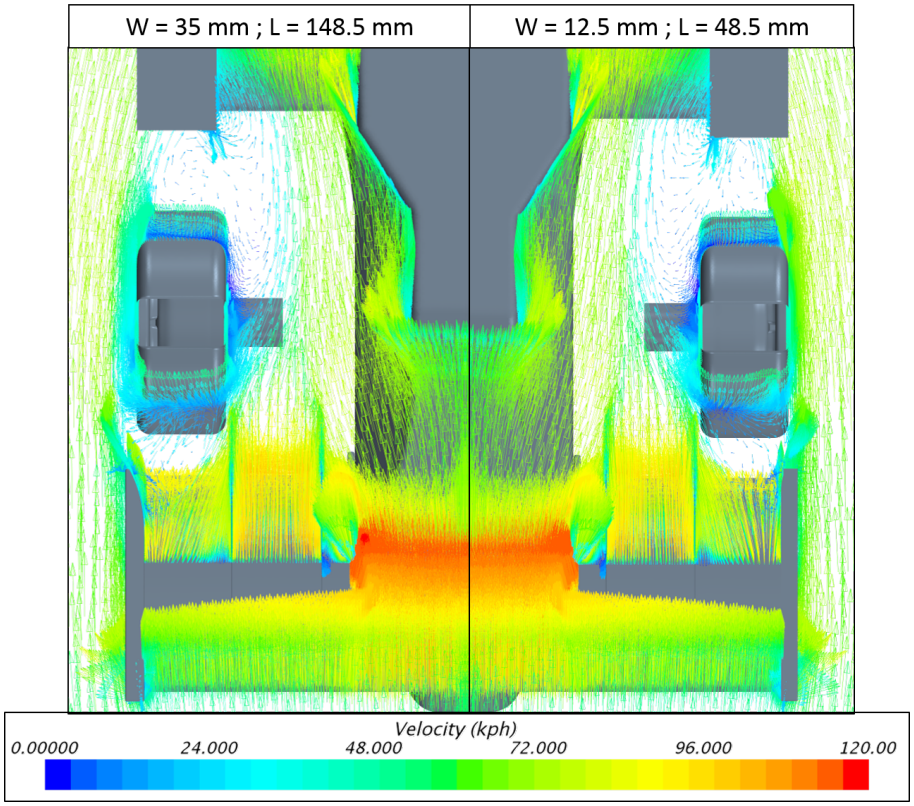


Figure 5.44: Outwash: curvature

Figures show that:

- A limited curvature does not succeed in diverting the flow which is therefore irremediably disturbed by the rolling of the wheel, making all the following components work worse;
- An accentuated curvature causes like a collision with the fluid that therefore loses energy and, although it avoids the wheel, decreases its speed, negatively affecting the downforce produced by the sidepods

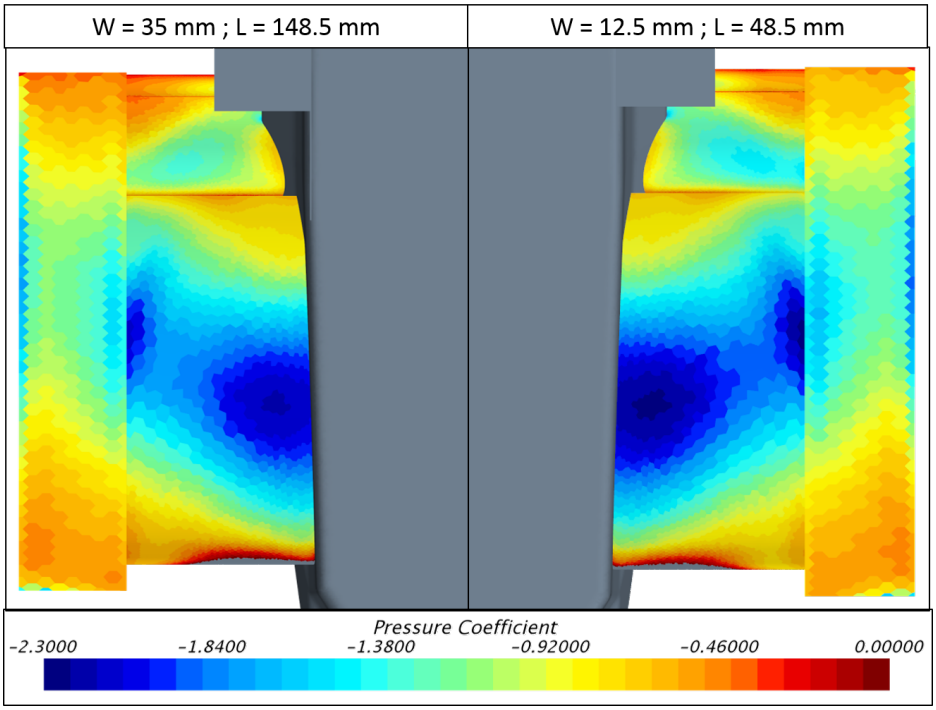


Figure 5.45: Sidepods improvement: curvature

The corresponding numerical values are shown in figure 5.46.

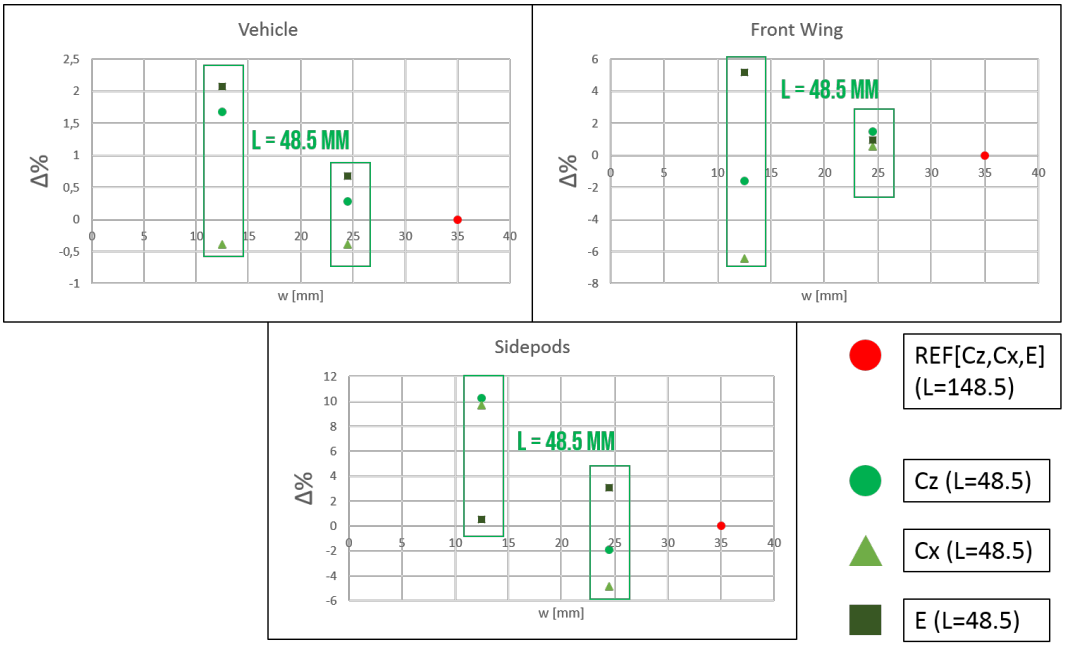


Figure 5.46: Curvature DoF results

So the right compromise, which allows the flow to avoid the wheel without slowing down, corresponds to the following parameters: $L = 48.5$ mm and $w = 12.5$ mm, as shown in the graphics 5.46 .

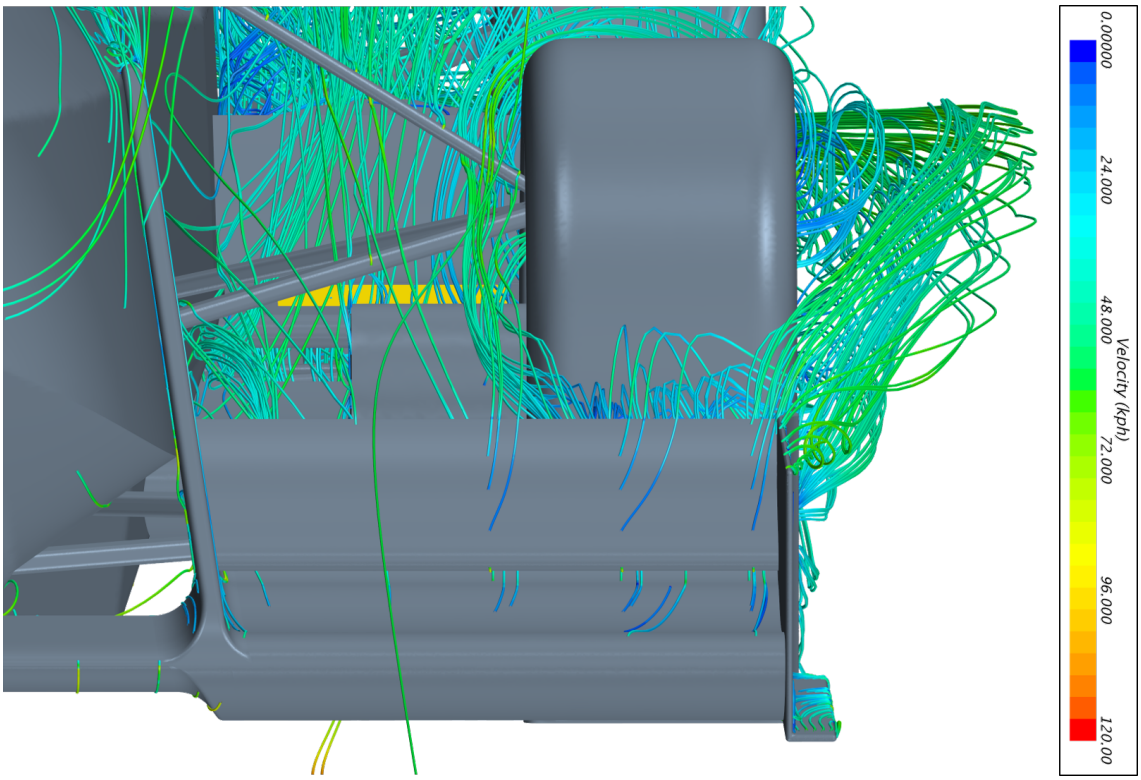


Figure 5.47: Endplate's streamlines

### 5.4.4 Vortex generator

In an attempt to create vortices that could be appropriately controlled with the aim of favouring the phenomenon of outwash in order to remove the air flow from the disturbance of the wheel, a vortex generator profile was optimized.
The front wing generates two vortices, one called the outwash and the other one, called the inwash. The outwash vortices direct air around the aerodynamically inefficient tires, reducing their drag, while the inwash vortices prevent the disturbed wake from the tires from moving to the rear wing.

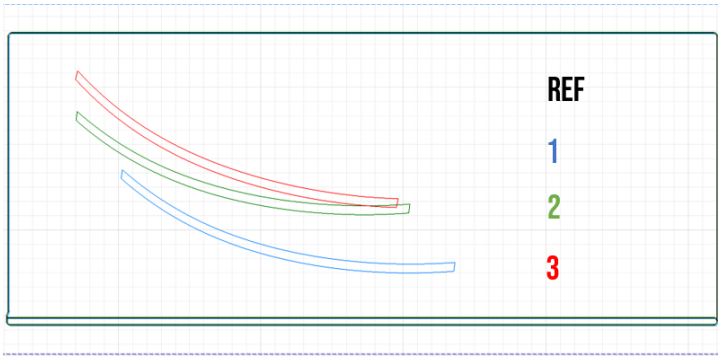


Figure 5.48: Vortex generator DoF

In particular, the results were tested by varying two parameters: the incidence and height position of this profile, comparing them with the configuration where

VG is missing.
With regard to the front wing, graphs 5.50 and figure 5.49 indicate that:

- The height greatly influences the ground effect created between the profile and the footplate: indeed there is a noticeable difference of downforce and efficiency between configuration *1* and *2*;
- The incidence increases, as with an aerofoil, both the downforce and the drag, as shown comparing configuration *2* and *3*

However, the overall loss of performance of the car shows that the vortices generated are harmful to all downstream aerodynamic components, since they make them work in dirty and even slowed air. This depends on two main factors: the lack of sufficient speed to have adequately energized vortices and the absence of space to be able to manage them, which involve an uncontrollable aerodynamic flow (also due to the excessive computational cost to be incurred in order to analyse and control them).

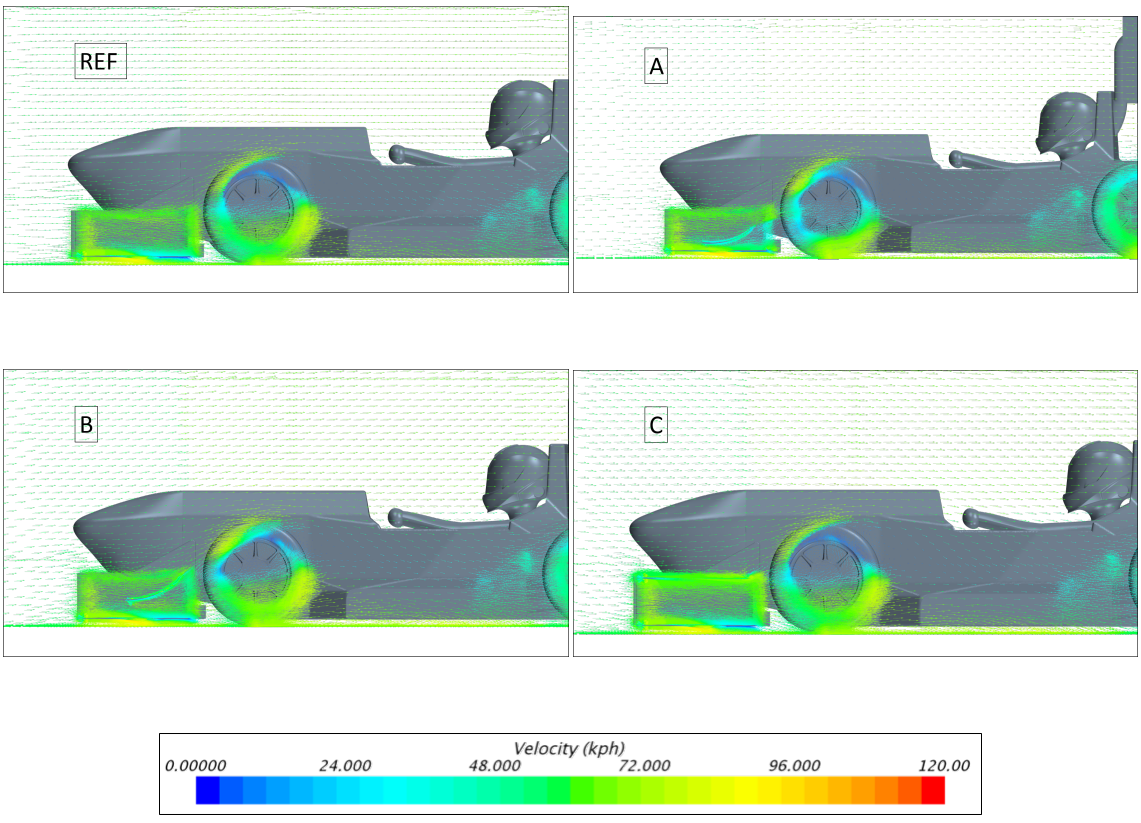


Figure 5.49: Airflow: vortex generator

Ergo, from the comparison with the configuration where VG is missing, it can be deduced that the latter is the most performing configuration.

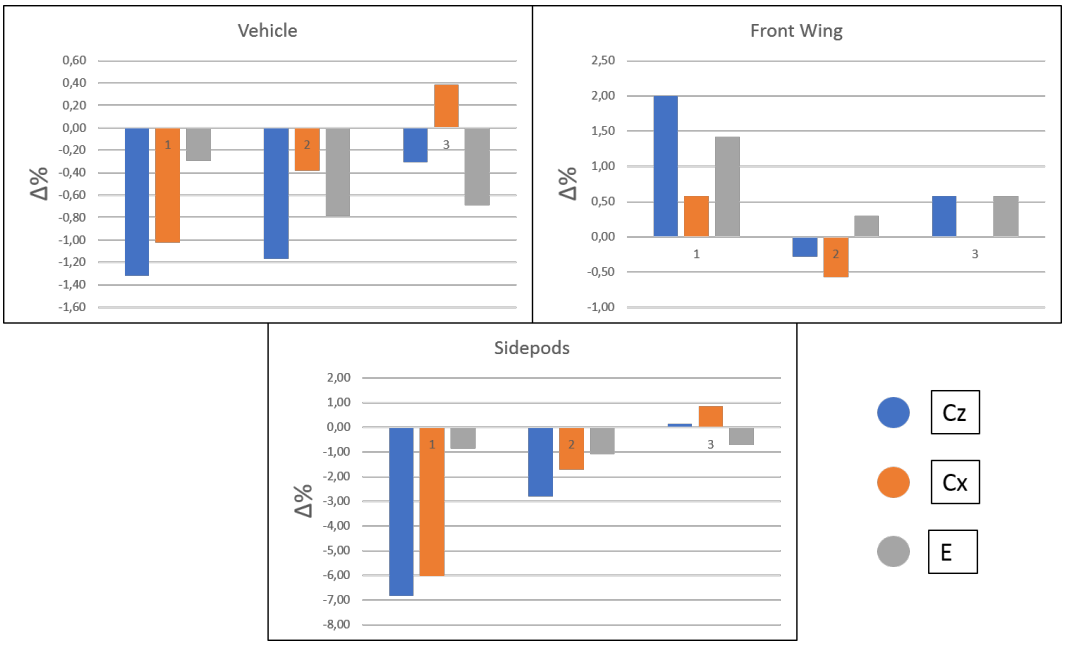


Figure 5.50: Vortex Generator DoF results

### 5.4.5 Headplate

The *C* configuration depicted in figure 5.49 shows an headplate, which was introduced to clean the flows, without affecting the work of the front wing, and to avoid the induced vortices more.
Actually, it is noted that it cleans the flows, but directs them towards the wheel, so that by sending clean flows to the wheel, the damage caused by its rolling is increased, because there are less vortices counter-rotating with respect to ones generated by the wheels.

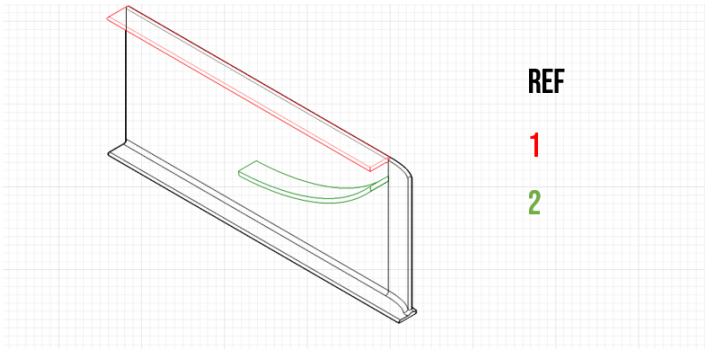


Figure 5.51: Headplate DoF

Indeed, from the comparison between the solution with only the vortex generator profile and the one where both of them are missing, it can be seen that the headplate does not affect the work of the front wing, but also that, it slows down the flow making the overall aerodynamic values worse, due to friction and because it directs it directly to the stagnation point of the wheel.

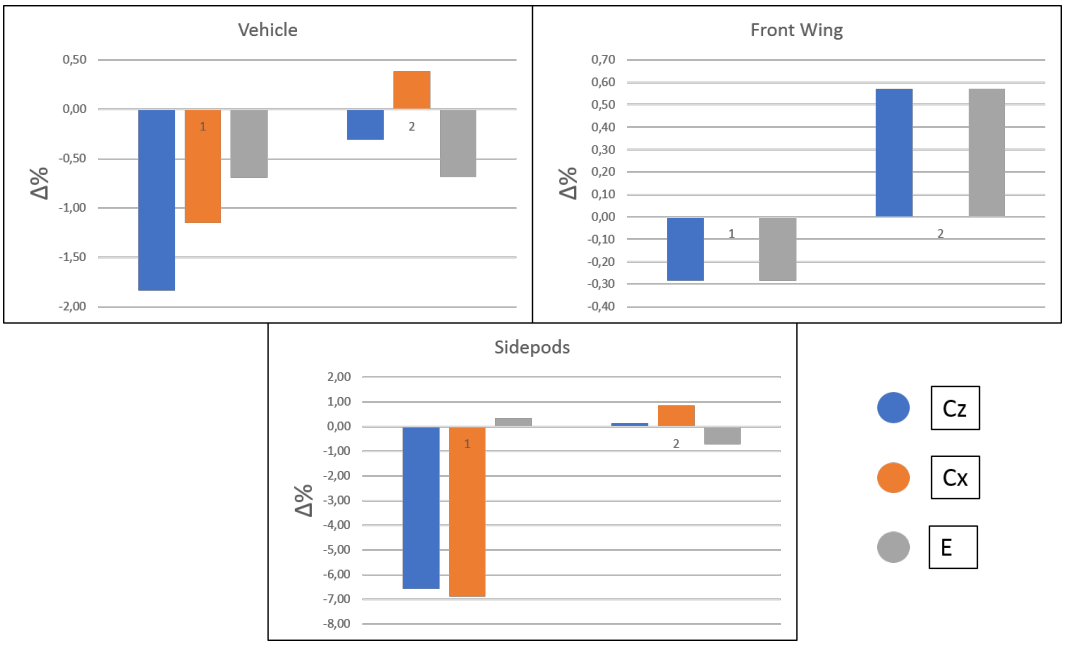


Figure 5.52: Headplate DoF results

In conclusion, the final shape of the endplates is characterized by the parameters seen above and is devoid of both the headplate and the vortex generator profile as they worsen the aerodynamic performance of the vehicle.

## 5.5 Front wing: the final project

With the definition of all the geometries and sizes of the components of the front wing, the fluid dynamics design phase can be considered concluded.
The final results both in numerical terms and in terms of fluid behavior are the following.

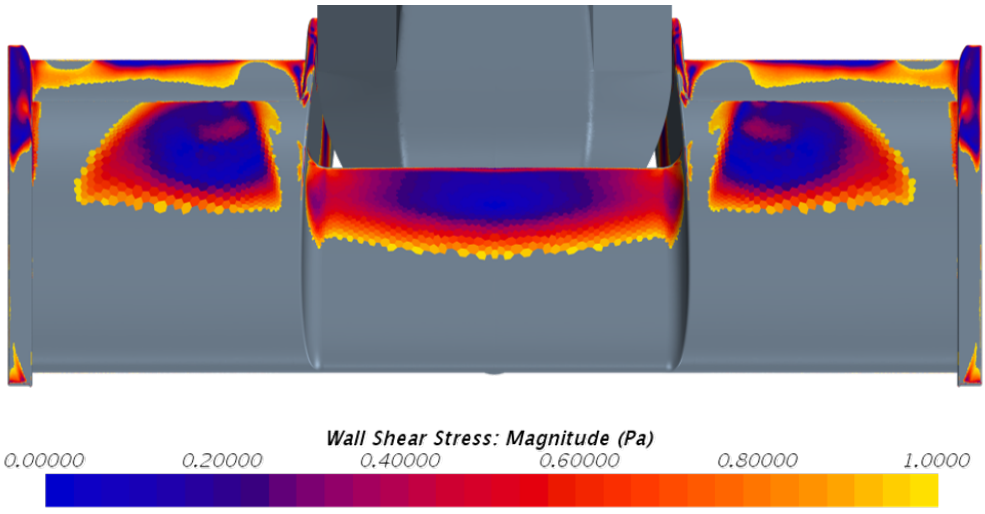


Figure 5.53: Final WSS

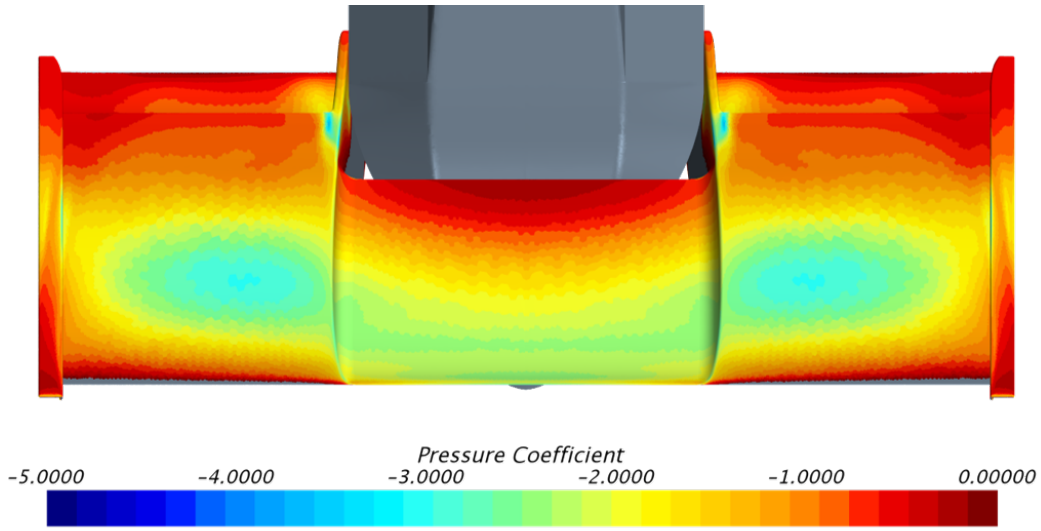


Figure 5.54: Final pressure coefficient

The behavior of the fluid is consistent with the described theoretical dissertation and with the design choices made. Indeed it is possible to note:

- Depression towards the root of the aerfoils, more accentuated on the Benzing than on the Clark due to the different aerfoils' camber;
- Benzing area with low wall shear stress, but where the fluid does not separate because it receives energy from the surrounding areas;
- Area on the Clark with low walls hear stress in which the flow separates, but very small compared to the configuration with the aerofoil next to the nose;
- Endplates that actually manage to maintain a depression, and therefore a pressure difference, even under the aerofoil extremity and under the footplate itself;
- Flap that does not separate early and that delays the detachment of the main thanks to the optimization of the slot

The numerical values obtained (table 5.3), on which a sensitivity analysis was performed as the speed changed (figure 5.55), are consistent with the objectives set at the beginning for an optimal performance of the entire aerodynamic package, even at the expense of a lower performance of the individual component.

| | $C_z$ | $C_x$ | E |
|---|---|---|---|
| Front Wing | 1.14 | 0.19 | 6.00 |
| Overall SC19 | 3.82 | 0.87 | 4.20 |

Table 5.3: Final aerodynamic values

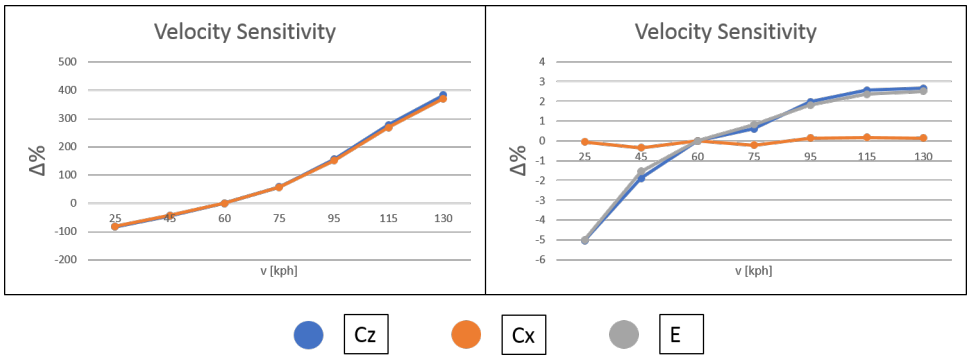


Figure 5.55: Velocity sensitivity

Indeed, the front wing is characterized by a high efficiency precisely because it must guarantee the cleanest flow possible downstream to make the rest of the aerodynamic package work in optimal conditions, since its downforce can be amplified by exploiting the ground effect and the totally clean air that invests it.

The above is demonstrated by a CFD analysis performed on the entire car missing the front wing.

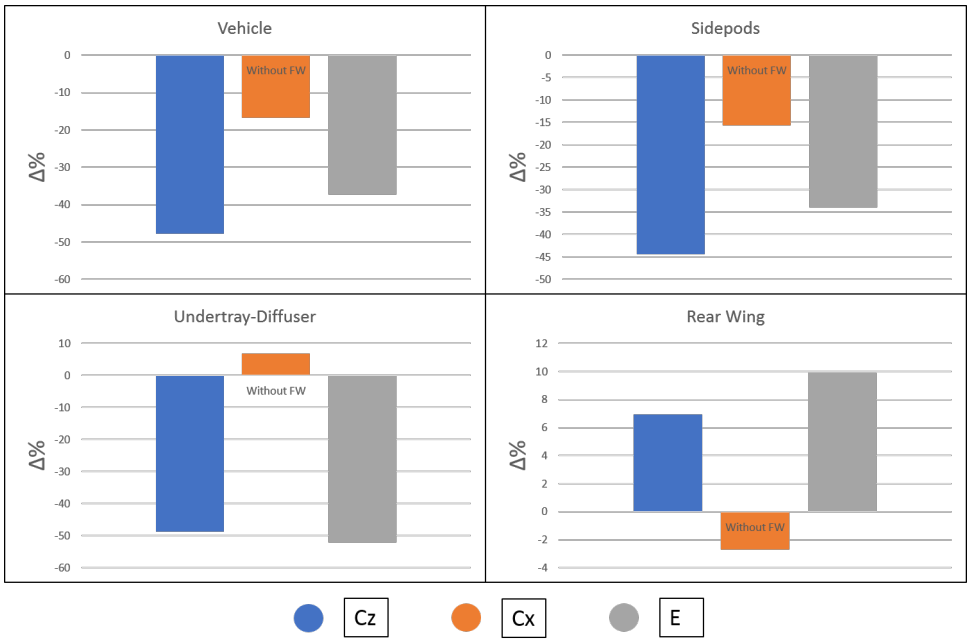


Figure 5.56: Front wing effect

Indeed, it is noted that the performance of the sidepods have significantly deteriorated as the flow that invests them is totally distracted by the rolling of the wheel, which, indeed, is not avoided by any device. Furthermore, the undertray's performance also collapses as flows are not controlled for the purpose of isolating it. The only aerodynamic element that improves its performance is the rear wing because it is no longer affected by the disturbance caused by the front wing upwash. However, the drastic drop in undertray and sidepods performance combined with the absence of front wing contribution cause a sharp reduction in the aerodynamic performance of the vehicle.

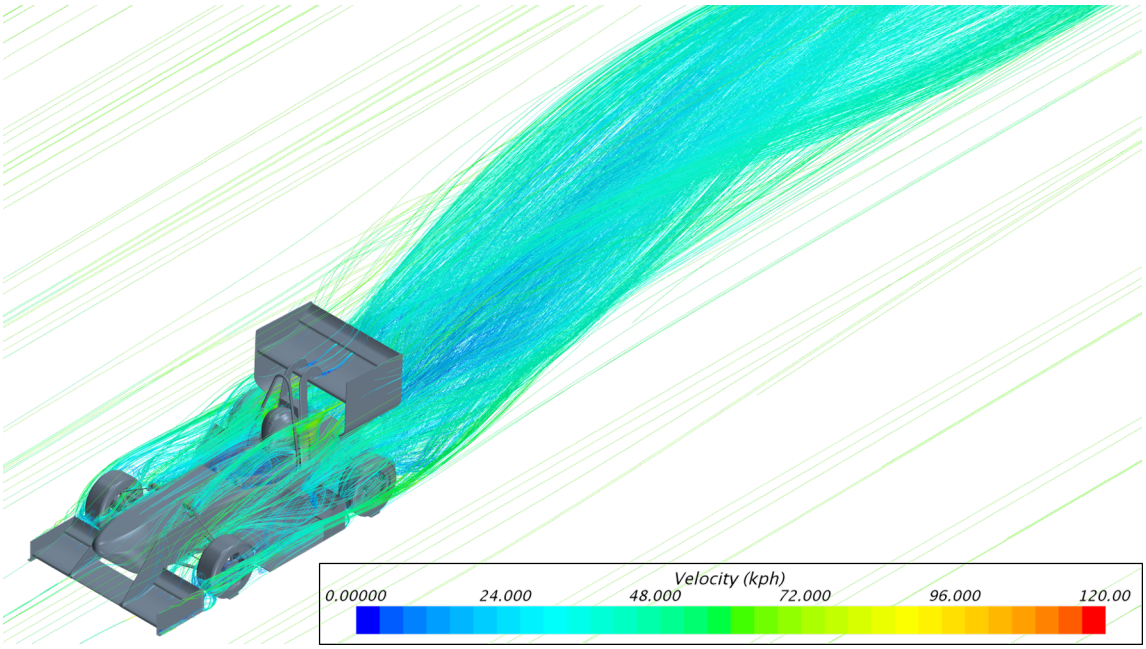


Figure 5.57: SC19's streamlines

Moreover, the same front wing has been optimized to work not alone, but with the entire car: indeed, although alone it generates a greater downforce, the overall front wing performance deteriorates due to a lowering of efficiency. This shows that the carried out design took into account the global integration of the various components of the vehicle and not the work of the individual components as if they acted alone.

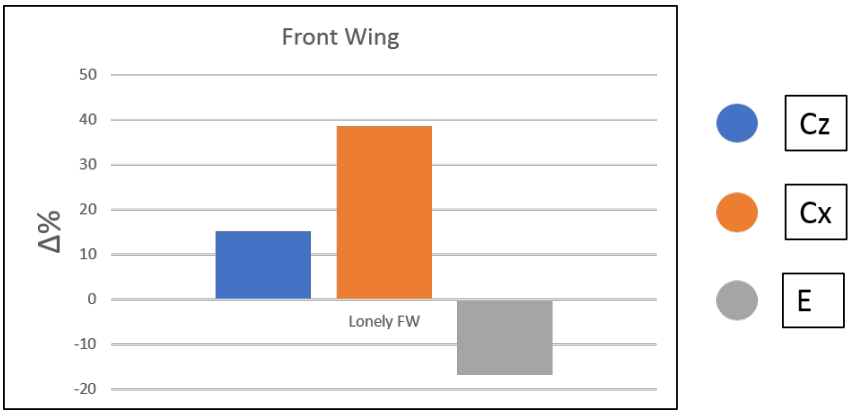


Figure 5.58: Performance of lonely front wing

A final analysis was carried out to evaluate the type of connection of the front wing to the monocoque. It was opted for full supports, since they guaranteed greater structural rigidity than the hollow ones, which, on the other hand, did not bring advantages neither from the weight's point of view, being the aerodynamic package very light, neither from the aerodynamic point of view as seen from figure 5.59.

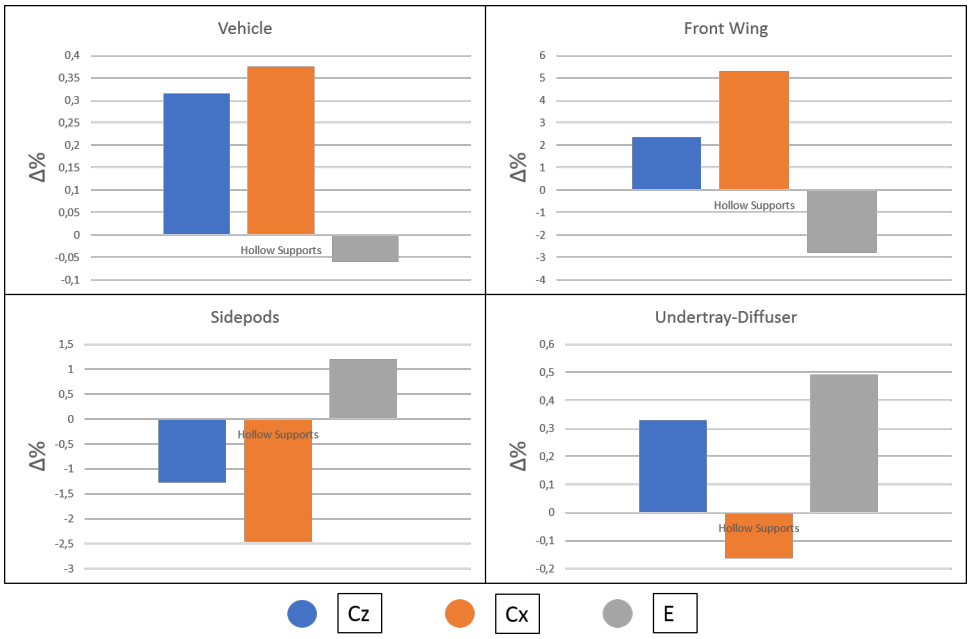


Figure 5.59: Hollow supports

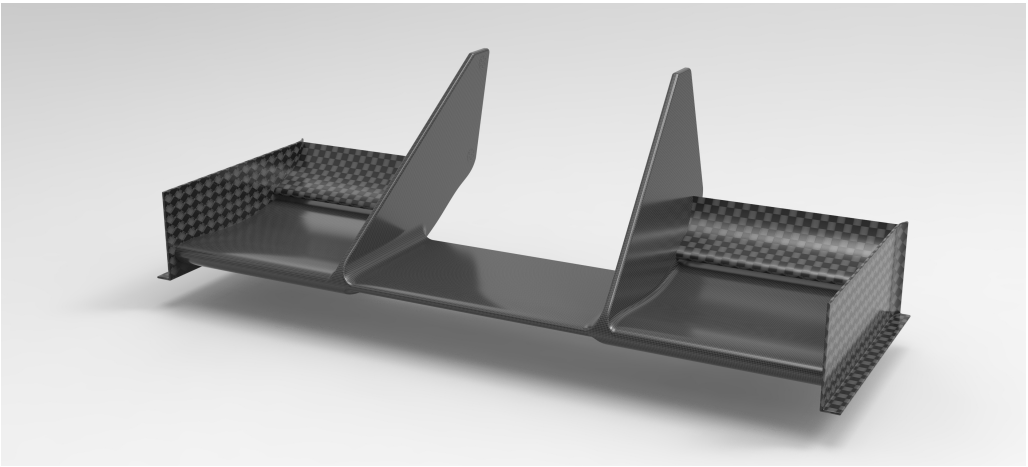

Figure 5.60: Front wing rendering

# Chapter 6

# Production

## 6.1 Materials

### 6.1.1 Options

The factor that more than any other characterizes aeronautical constructions is weight.

#### Reticular structure

In the first "attempts" the main need was to fly and the aerodynamic requirements were often left in the background; this was also due to the low flight speeds of the epoch.

In that situation bamboo was often used. This natural "tube" offered good characteristics of lightness and strength and, above all, ease of processing. Once selected the canes of adequate diameter, they could be used naturally, simply by cutting them to the desired length. Once the bamboo elements were cut, they were connected with sheet metal tiny plot (very often brass). The resulting structures, of reticular type, were stiffened and "put in shape" with metal cables.
The reticular structure (still used today for metal trusses and bridges) has the advantage of be simple to calculate and build. Its elements are classified as struts if they resist to compression stresses or tie-rods if they resist to tensile stresses.

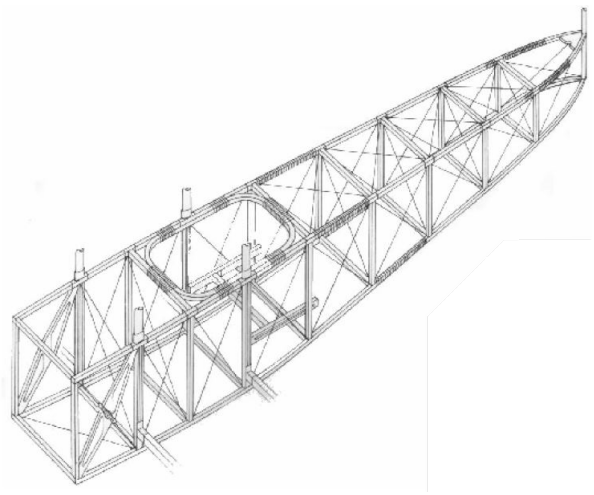

Figure 6.1: Reticular

The low power available had already highlighted the need for lighter materials and the first aerodynamic needs required "shapeable" materials. The answer to these needs was found in ash and fir wood. With these woods it was possible to profile wing and fuselage uprights and meet the needs of thicker wings and obtain better aerodynamic characteristics.

### Shell structure

In the shell structure all stresses are supported by the outer shell and not by an internal supporting structure, with obvious aerodynamic and weight advantages; disadvantage, not to be underestimated, is a major constructive difficulty.

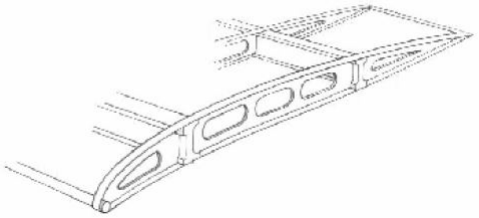

Figure 6.2: Shell

The wing construction poses a series of different problems, such as not to make the pure shell construction applicable. The wing covering resists tension well but not compression, unless not adequately supported by reinforcements. As for the wing a structure made up by one or more spars (different section) and a series of ribs connected to them was used (and it is still used with the appropriate changes). Often the ribs were a wooden truss or a shaped wood with lightening. Even in this case the whole structure was stiffen by an adequate number of cables metal.

Thus, the wooden structure of the aircraft was converted in a metallic one but little have been done for the design of the new structures.. The drawback that persists in the reticular structure - regardless of the materials used- is given by the need to make everything aerodynamic. It is therefore necessary to build a support for the covering (not working), either the metallic or canvas ones. Obviously, this structure and the covering are additional weights that do not participate in the stiffness of the structure; a structure with a working covering gave the same internal volume as a fuselage with a reticular structure with a 35% savings in the cross section area, all this for the benefit of reduced aerodynamic drag and weight.

The increasing use of metallic materials (steel and aluminium alloys) led to the general adoption of half-shell structures, first in a wood-metal combination and, subsequently, all in metal. Basically, this technique consists of employing some strength and shape frames designed to give the fuselage its transverse shape and to grant a metallic covering stiffened by battens, fastened to the frames, able to withstand compression stresses. In the wings, frames were replaced by ribs; the wing's carrier element remained the longitudinal member.

### Geodetic structure

The geodetic structure essentially consists of a basket-shaped light alloy lattice, covered with canvas. This type of structure is very resistant and able to withstand considerable stresses without damage.

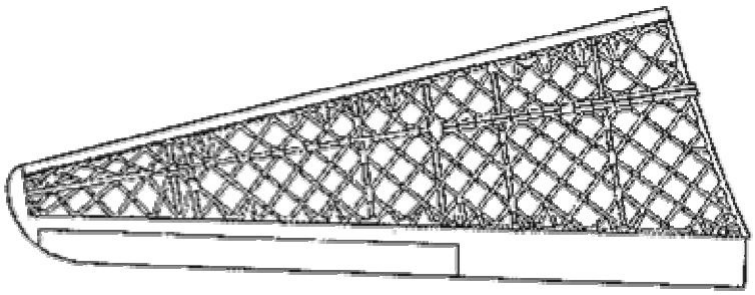

Figure 6.3: Geodetic

The geodetic structure allows to build refined fuselages, with large internal space e wings of strong elongation, without ribs. On the other hand the construction is more complicated than conventional facilities.

#### Chemical milling

Chemical milling consists in consuming with a weak acid sheet (of a suitable thickness) areas that are not isolated by special paint, until they reach the desired thickness, sizes and shape. This production process allows to perform precise manufacturing, gradually reducing the thickness and avoiding abrupt changes in section. Mechanical milling of large panels allows to get from a single block various stiffening elements, the ribs and the openings that are part of the element being processed.

#### Composite materials

Since the early 1970s composite materials were introduced also for structural elements. Until then, fibrous materials drowned in resins were used in non-structural details such as pulleys, careening, various panels.
Carbon and boron fibers were used for the construction of honeycomb used for moving surfaces. Since then the search for new ones "plastic" materials (composites of Kevlar, Nomex, etc.) led to drastically reduce the weights of structural elements (spars, covering) maintaining the resistance in fields of all safety.

From the metal point of view aluminium-lithium alloys are successfully being tested in place of traditional alloys (aluminium - copper, aluminium - zinc, aluminium - magnesium) and the use of titanium alloys is widespread.

### 6.1.2 Composites

A composite material (also called a composition material or shortened to composite which is the common name) is a material made from two or more constituent materials with significantly different physical or chemical properties that, when combined, produce a material with characteristics different from the individual components [19]. The individual components remain separate and distinct within the finished structure. The new material may be preferred for many reasons: common examples include materials which are stronger, lighter, or less expensive when compared to traditional materials.
A typical composite material is a system of materials composing of two or more

materials (mixed and bonded) on a macroscopic scale. For example, cement is made up of cement, sand, stones, and water. If the composition occurs on a microscopic scale (molecular level), the new material is then called an alloy for metals or a polymer for plastics. Generally, a composite material is composed of reinforcement (fibers, particles, flakes, and/or fillers) embedded in a matrix (polymers, metals, or ceramics). The matrix holds the reinforcement to form the desired shape while the reinforcement improves the overall mechanical properties of the matrix. When designed properly, the new combined material exhibits better strength than would each individual material [19].

Fiberglass, when combined with a plastic polymer creates an incredibly strong structure that is also lightweight. Engineers soon realized other benefits of composites beyond being lightweight and strong. It was discovered that fiberglass composites were transparent to radio frequencies [19].

In the 1970s the composites industry began to mature. Better plastic resins and improved reinforcing fibers were developed. Kevlar, this fiber has become the standard in armour due to its high tenacity. Carbon fibers was also developed around this time; it has since been replacing metal as the new material of choice. In contrast to metallic alloys, each material retains its separate chemical, physical, and mechanical properties. The two constituents are a reinforcement and a matrix.

Composite materials are commonly classified at following two distinct levels [19]:

- The first level of classification is usually made with respect to the matrix constituent. The major composite classes include Organic Matrix Composites (OMCs), Metal Matrix Composites (MMCs) and Ceramic Matrix Composites (CMCs). The term organic matrix composite is generally assumed to include two classes of composites, namely Polymer Matrix Composites (PMCs) and carbon matrix composites commonly referred to as carbon-carbon composites.
- The second level of classification refers to the reinforcement form - fibre reinforced composites, laminar composites and particulate composites. Fibre Reinforced composites (FRP) can be further divided into those containing discontinuous or continuous fibres.
  - Fibre Reinforced Composites are composed of fibres embedded in matrix material. Such a composite is considered to be a discontinuous fibre or short fibre composite if its properties vary with fibre length. On the other hand, when the length of the fibre is such that any further increase in length does not further increase, the elastic modulus of the composite, the composite is considered to be continuous fibre reinforced. Fibres are small in diameter and when pushed axially, they bend easily although they have very good tensile properties. These fibres must be supported to keep individual fibres from bending and buckling;
  - Laminar Composites are composed of layers of materials held together by matrix. Sandwich structures fall under this category;
  - Particulate Composites are composed of particles distributed or embedded in a matrix body. The particles may be flakes or in powder form.

Concrete and wood particle boards are examples of this category

The most basic fabrication method for thermoset composites is hand layup, which typically consists of laying dry fabric layers, or "plies," or prepreg plies, by hand onto a tool to form a laminate stack. Resin is applied to the dry plies after layup is complete (e.g., by means of resin infusion).
Several curing methods are available. The most basic is simply to allow cure to occur at room temperature. Cure can be accelerated, however, by applying heat, typically with an oven, and pressure, by means of a vacuum. Many high-performance thermoset parts require heat and high consolidation pressure to cure — conditions that require the use of an autoclave.

In particular, there are the following advantages over metals:

| **Advantage** | **Description** |
|---|---|
| Light Weight | Also compared to woods |
| High Strength | In a specific direction |
| Strength Related to Weight | As designed for specific direction |
| Corrosion Resistance | Resist damage from the weather |
| High-Impact Strength | Absorb impacts |
| Design Flexibility | Molded into complicated shapes |
| Part Consolidation | Single piece replace an entire assembly |
| Dimensional Stability | When they are hot or cool, wet or dry |
| Nonconductive | Possibility to make some composites conductive |
| Nonmagnetic | Lack of magnetic interference |
| Radar Transparent | Radar signals pass right through |
| Low Thermal Conductivity | Good insulators |
| Durable | Long life and need little maintenance |

Table 6.1: Composite vs metal

### 6.1.3 Selection

As already mentioned, the advantage of exploiting aerodynamics to generate downforce is that of having an increase in vertical load that is greater than the increase in drag and inertial mass growth. In order not to compromise this gain, the aerodynamic package must be as light as possible but able to withstand the stresses it has to bear.
In particular, since the higher tensions develop on the surface, it is necessary that in these areas the material has high mechanical properties. Furthermore, the further away (from neutral axis) is the surface, the greater the stresses it can withstand, so it is advisable to space out the plies as much as possible by inserting, as a core, a very light material with minimal mechanical properties inside.
As a result, the elements of the aerodynamic package have the following structure:

- Plies, on the surface, in carbon fiber: they have the purpose of supporting all the load. The virtue of carbon fiber is its high stiffness and load resistance despite its enormous lightness;

- Core in rohacell: it is light and cheap and suitable to be a filler between plies, as the core is not subject to significant stresses

| **Material** | **E** [MPa] | $\sigma_R$ [MPa] | $\sigma_{sn}$ [MPa] | **G** [MPa] | $\rho$ $[\frac{kg}{m^3}]$ |
|---|---|---|---|---|---|
| Rohacell | 36 | 1 | 0.4 | 13 | 32 |

Table 6.2: Rohacell properties

The diffuser and its lateral channels have instead a Kevlar honeycomb core, which has the same peculiarities as the rohacell but can be thinner and therefore more suited for the geometry of the diffuser channels.

The core thickness depends on the geometry studied by CAD, so not so much from a structural analysis as from an aerodynamic analysis. As regards the number of plies number chosen and CFRP typology used, reference is made only to the FEM analysis carried out to verify the stiffness both in terms of performance and in terms of regulation. In particular, from these analyses, it was decided to apply on each aerodynamic elements two CFRP plies, but of different types depending on the different structural function performed:

- Textreme, non-pre-impregnated CFRP, with a greater quantity of hypoxy resin, therefore with less rigidity of the structure. Used for less stressed parts;
- M46J, pre-impregnated CFRP, with a greater quantity of fiber, therefore with greater structure stiffness. Used for the most stressed parts

| **Material** | **Type** | **E** GPa | $\sigma_R$ MPa | $\sigma_{sn}$ MPa | **G** MPa | $\rho$ $[\frac{kg}{m^3}]$ | **Th** [mm] | **Matrix** |
|---|---|---|---|---|---|---|---|---|
| Textreme | - | 60000 | 1100 | 800 | 7000 | 1400 | 0.1 | 50% Resin |
| M46J | Pre | 110000 | 680 | 440 | 12500 | 1400 | 0.22 | 40% Resin |

Table 6.3: CFRP properties

Aerodynamic elements have very complex geometries, so it is impossible and deleterious to produce each appendix as a single block (you would only have one configuration and if you break it you should rebuild the whole component). Consequently, in addition to having to establish a sufficiently stiff and resistant connection between the body and the aerodynamic components, it is necessary to carry out the same connection also between the individual elements of each of them. In particular, in order to realize this type of junctions, it was decided to use a threaded connection, as it is simple, economical, easy to produce and removable. It is, therefore, composed of a through-hole and a threaded-hole.
Since both of them would reside in the rohacell, which has no great mechanical properties as previously specified, it has been decided to insert more resistant inserts and to laminate them together with the CFRP so that it was the latter, and not the rohacell , to bear their stress:

- Threaded inserts: less resistant and machined with laser cutting;

- Perforated inserts: CFRP more resistant and processed with water cutting

It can be seen that even in this choice, as in that of the screws, lightness has been privileged: indeed the choice of aluminium is to be seen precisely in this perspective since, due to its fragility, it is not possible to make a CFRP thread since with wear it would crumble excessively. CFRP relies on the axial strength of the fibers and also the weave, which transmits the load to be shared by other fibers. The crest of the thread, unless specifically moulded or laid-up that way, is just going to be a peak that is disjointed from the other fibers and relies largely on the strength of the matrix.

For reasons of comfort, all the screws used correspond to the ISO M5 standard, and consequently the inserts are sized accordingly. In particular, both of them have a wider surface in order to better distribute the force exerted by the threaded connection: those in CFRP to avoid penetration of the screw head (flaring head); those in aluminium to avoid the sinking of the insert itself inside of the friable rohacell due to high pressures.

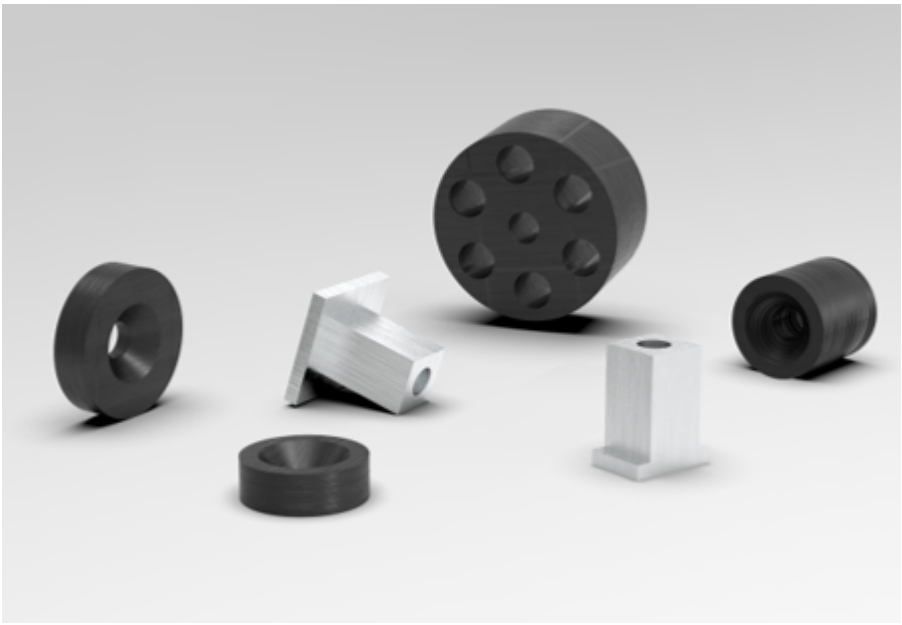

Figure 6.4: Inserts rendering

## 6.2 Process

After making the choices described above, we moved on to the actual manufacturing phase. The production process was characterized by the following main phases:

| Phase | Producing | Details |
|---|---|---|
| Moulds | Milling | WB/Pesca |
| Core | Double milling | Rohacell |
| Inserts | Gluing | Al/C in rohacell |
| Laminate | Lamination | CFRP |
| Vacuum | Suction | Vacuum bag |
| Blank | Mould opening | Awl |
| Element | Assembly | Screws |

Table 6.4: Production process

The different phases will be described in detail in the next paragraphs.

### 6.2.1 Moulds

The moulds are the negative of the external shape of the component to be produced, and represent the external surface on which the carbon fiber plies will be laid. Two different materials are used, both resins:

- WB: high density mixed resin with wood, suitable for the lamination and cure of M46J CFRP as it resists in the oven at high temperatures;
- Pesca: low density and high porosity resin, it is used for TEXTREME carbon, which polymerizes at environmental temperature, and therefore has lower performance, but is cheaper

The surface roughness of the component can significantly influence the flow, leading to separation even in areas where the CFD results provided good fluid behaviour. Therefore, for the production we chose to use the double mould so as to guarantee excellent surface finish on both surfaces of the aerodynamic appendix, except for diffuser and endplates where, due to a compromise between economic issues and aerodynamic performance, the external surface was privileged in the case of endplates and the lower one in case of the diffuser.

The mould of the various elements was obtained by milling, and in the case of complex geometries it was separated into different parts by providing, on each one, suitable accommodation for centering pins so as to be able to subsequently recompose and maintain the original geometry even in depression.

With a view to resources saving, both in terms of the volume of material used and the number of jobs performed and also the time spent, attention was paid to the following issues:

- Recycling of resins' block already used through appropriate bonding, planing and grouting;

Figure 6.5: Moulds recycling

- Moulds size reduction, optimizing the volume and shape of the external surfaces;
- Use of the same mould for symmetrical components both with respect to a plane or with respect to a point

Before using the moulds, we had to properly treat them:

- Roughing and finishing, repeatedly using sandpaper with ever-increasing grain values (increasing grain fineness): 320, 600 and 800 respectively. In this way, at the beginning more material is removed, making the surface, which was studded with imperfections due to milling, uniform; finally, the roughness is reduced to an optimal value so that the element would be tighter with tolerance, but also to prepare it for the shutters passages. This treatment is similar for both the WB and for Pesca and the passages of the sandpaper must be done with circular motions in order to guarantee a uniformity of the entire treated surface;
- Correction of defects, putting plaster in correspondence with the defects deriving from milling or from a bad roughing so as to bring the mould back into an excess material condition. In this way it is possible to proceed again with the previous point and so iteratively until the mould is free of defects. Also this process is similar for the two resins, obviously with the use of two different types of plaster;
- Shutter, more than one coat of this substance is passed, which has the purpose of reducing as much as possible the roughness of the mould with the sole

objective of avoiding the absorption by the material of the subsequent release agent coats;

agent: several coats of this liquid are deposited, which accumulates, in the absence of surface porosity, above the mould, creating a layer that will separate the CFRP polymerized resin from the mould, thus facilitating the mould's opening

These last two treatments are applied only in the case of the WB, since the Pesca is so porous that the shutter is not able to prevent the absorption of the release agent. In this case, gluing prevention is carried out precisely during lamination, through the interposition of an anti-adhesive film: the FEP.

### 6.2.2 Rohacell

The rohacell components of each element too were obtained by milling. However, in this case it was a double milling: the first one on one side with the material bound to a table; the second one on the other side with the material bound in the mould of the already milled surface. Unlike moulds, the rohacell produced by the milling machine is the definitive component so it must also contain the appropriate holes for inserting aluminium or CFRP inserts.

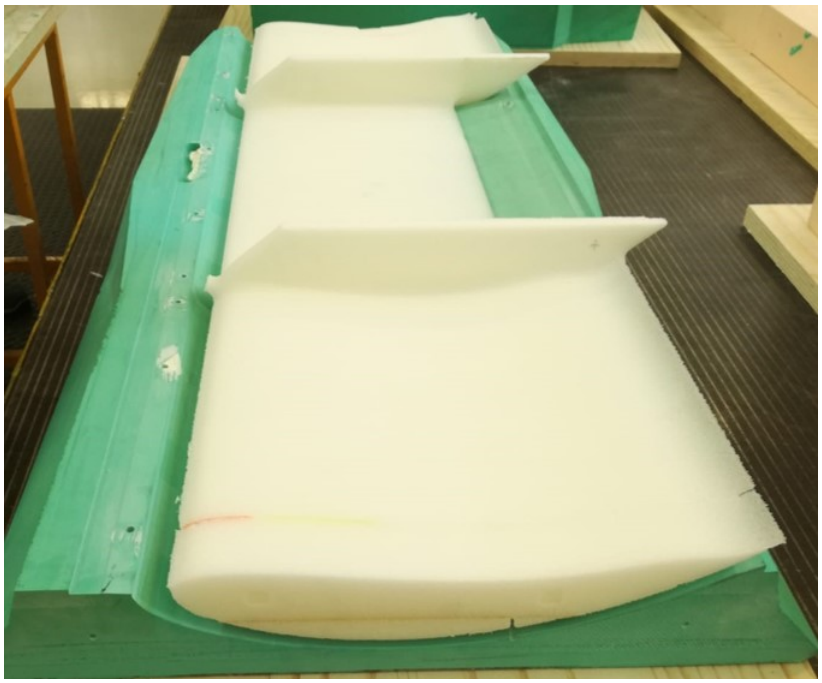

Figure 6.6: Rohacell

The rohacell constitutes the internal surface on which the carbon fiber plies will be positioned and then pressed, so that, although it must not guarantee a surface roughness of any kind, it must also avoid containing macroscopic defects, otherwise geometry errors occur on the final element.
For these reasons, it is necessary to correct any material deficiencies by inserting a foam that expands at room temperature. Just this last property implies the fact that it must be inserted only immediately before the lamination so that it expands, guaranteeing the right internal pressure, during the polymerization process.

**Inserts**

Inserts must also be inserted in the appropriate accommodation before lamination. To improve the fixing, an abundant quantity of glue is used and, as regards the aluminium inserts, they are abraded so as to improve the cohesion between the different materials.

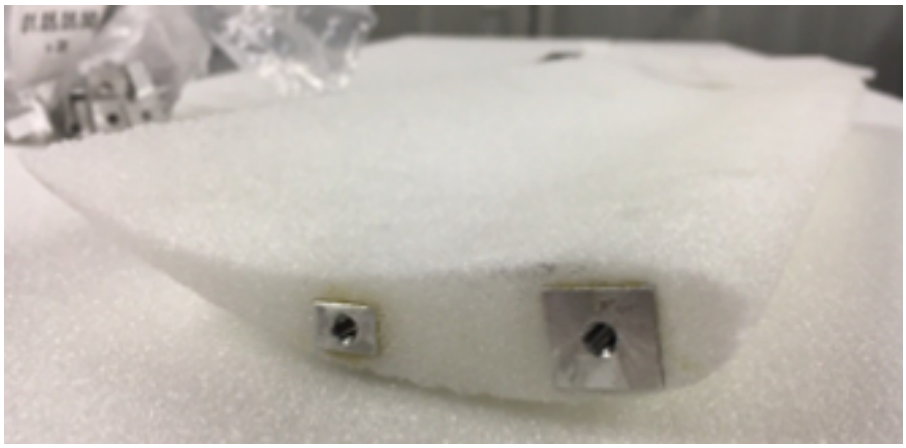

Figure 6.7: Inserts

Similarly, the centering pins must be inserted into the moulds, previously treated with the release agent in order to facilitate extraction during the mould opening and to prevent the polymerized resin from sticking them to the material.

### 6.2.3 Lamination

Once moulds and rohacells are available, we proceed with the first step of lamination: cutting the shaped plies. CFRP plies are cut with a safety margin with respect to the component size and taking into account, already at this stage, the different orientation of the fibers in the various layers in order to optimize resistance, coherently with what has been analysed in FEM simulations.
For Textreme, the resin that will polymerize at room temperature is also prepared, with an appropriate dosage between glue and hardener, and also the FEP films that will be inserted between the mould and the carbon plies will be prepared.

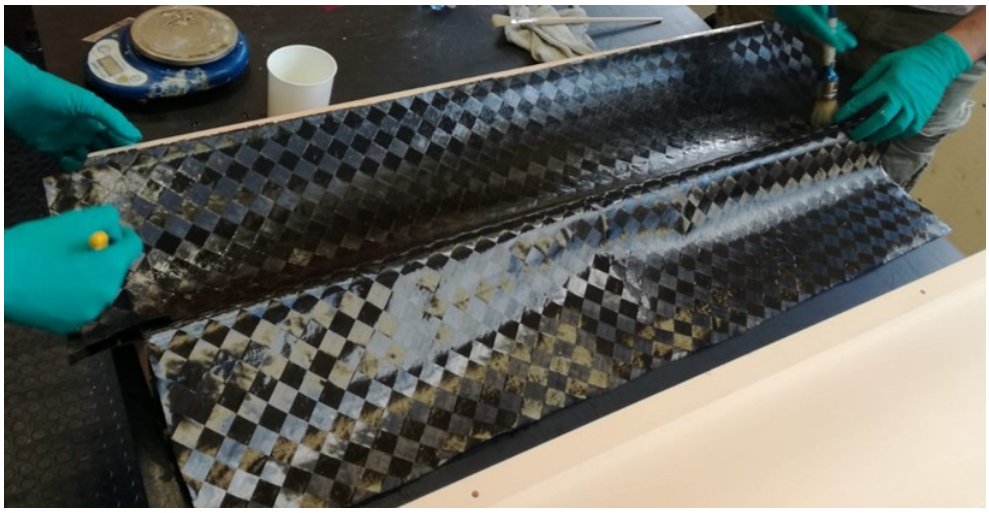

Figure 6.8: Textreme

The plies are positioned inside the mould in a precise manner, avoiding imperfections, and soaked in resin in the case of the textreme.

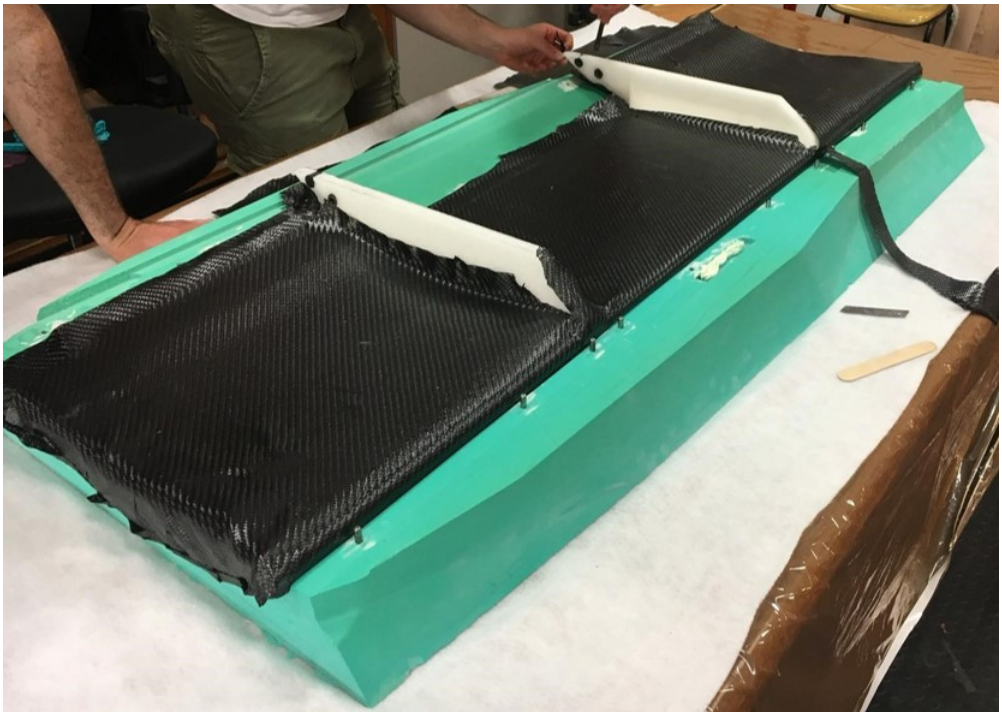

Figure 6.9: M46J

Following the positioning of the rohacell element above them, plies are similarly closed, avoiding imperfections, and pressed by the closing of the mould above.

Figure 6.10: Closing moulds

The uncovered carbon fiber parts are meticulously covered by a FEP film to prevent the cured resin from sticking to the outside material.

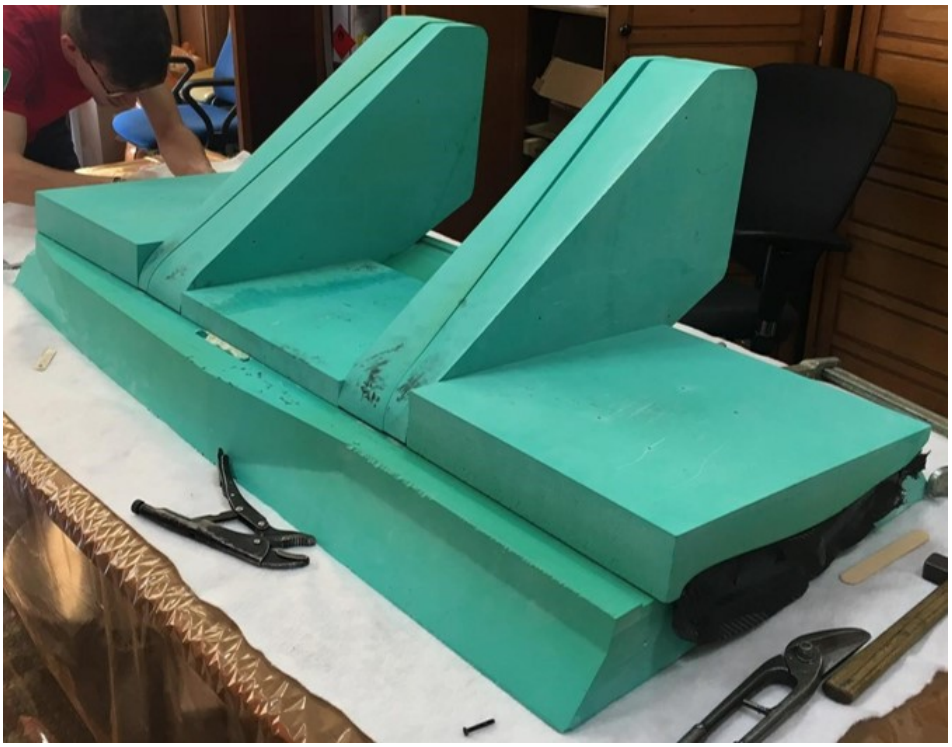

Figure 6.11: Closed moulds

### 6.2.4 Cure

Everything is wrapped in a aerator sheet in order to facilitate the passage of air and to cover the mould's sharp edges that could damage the vacuum bag. Once inserted inside the vacuum bag, this is closed through the arrangement of a butyl strip, having first inserted half of the valve body. By completely re-assembling the valve and positioning it on the aerator, it is possible to proceed with air suction.

The purpose of the vacuum bag is to push, thanks to the .depression generated, evenly over all surfaces, so it must be positioned so that it does not break and can apply pressure at all points of the mould.

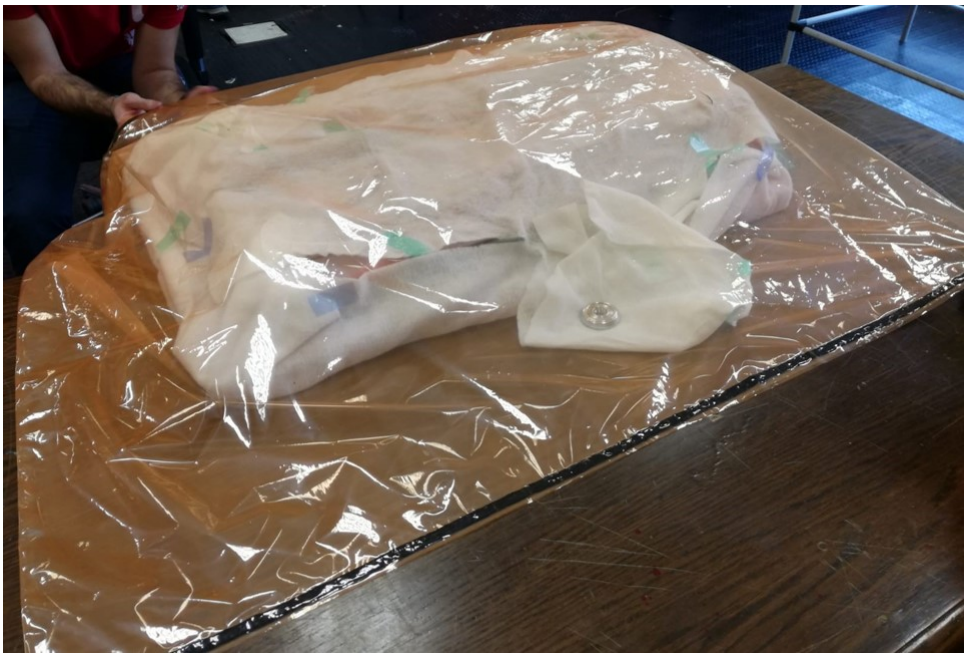

Figure 6.12: Vacuum bag

This operation is necessary for both types of carbon since neither hyperbaric chambers nor autoclaves are available. In fact, the polymerization of the textreme takes place in a standard environment, the polymerization of the M46J in an oven at 135 °C, but in both cases at ambient pressure.

Figure 6.13: Cure

### 6.2.5 Moulds opening and assembly

Figure 6.14: Opening moulds

Once the polymerization process has been completed according to the indications enclosed by the supplier, the moulds are opened with appropriate awls.

Figure 6.15: Opened moulds

Finally, further actions must be implemented:

- Correction of macroscopic defects;
- Surface roughness refinement;
- Verifying dimensional and geometric tolerances;
- Controlling assembly correctness;
- Threaded connection preparation;
- Controlling and assuring compliance with the regulation;
- Preparation for painting

Figure 6.16: Raw product

After having properly assembled the various elements, the various minimal splits in the assembly are sealed with American tape.

# Chapter 7

# Validation

## 7.1 Wind tunnel testing

### 7.1.1 Theoretical concepts

Wind tunnel testing is based on the aforementioned principle of Galilean relativity, which states that: *the dynamic actions exercised on a body in translational motion in the fluid (first at rest) are the same as those produced on an immobile body hit by an air flow at the same speed* [3].
A further important concept is the dynamic similarity, the phenomenon that occurs when fluid flows among bodies with different sizes are analogous. This is true only if the geometries of the two bodies differ only by a scale factor and the unidimensional motion field with respect to the undisturbed speed is unchanged: in this case both the geometric similarity and the kinematic similitude are valid.
So the dynamic similarity is verified if the fluid is at the same conditions, if the motion field is proportional and if it is proportional (in equal measure, but with the opposite direction) the characteristic dimension, too.

Wind tunnels are composed by several ducts of different sections, within which air flows generated by several large fans circulate at the selected speed and density.
An effusion, or convergent, serves to progressively accelerate the flow of incoming air and special filters or networks reduce turbulence. At the exit, the flow is decelerated by a diffuser, or divergent, while at the center is the test room, where the body under examination is installed and connected to a scale, for measuring the forces.

The most used wind tunnel layouts include:

- Open circuit gallery;

- Closed circuit gallery;
- Closed test room;
- Open or semi-open test room

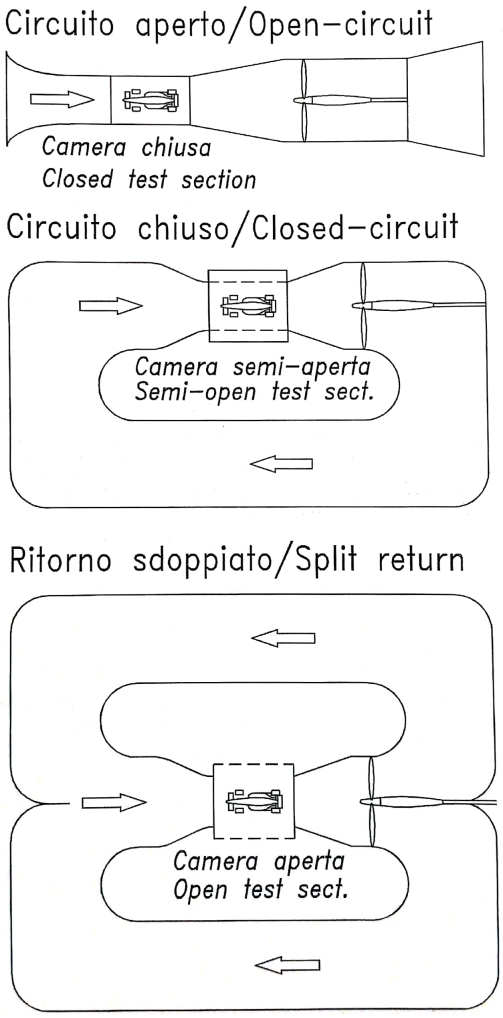


Figure 7.1: Wind tunnel typologies

In the first case (open circuit gallery) the construction is very simple because the air is taken from the atmosphere and re-introduced into the environment after passing through the test chamber. However, the efficiency, given by the ratio between the dynamic pressure and the power of the engine, is very low since the fan must supply the entire kinetic energy of the jet.
In the second case (closed circuit gallery), the efficiency greatly improves, both in the case of a single return duct and a split one, since the fan takes care of supplying only the pressure drops of the duct. In this way, also the current becomes independent from the atmospheric conditions making the air conditions, therefore, easily adjustable.
The closed test room has walls with rectilinear generators which therefore force the flow to deviate to obtain tangency: this causes an influence on the motion around the body that causes a slight overestimation of the aerodynamic actions in play. Similarly, although the open room provides a layer of stagnant air, having a section larger than that of the jet, the measurements, although more precise, are still affected by an error due to the fact that the air near the walls will never be perfectly at rest as it happens on track.

The wind tunnel is designed to best reproduce the range of motion around the body under examination. To this end, during wind tunnel setup the aerodynamic blocking of the fluid vein is minimized, through experimental analyses, by the body itself until it will be negligible, thus avoiding the major source of error.
Other two main issues regard:

- The possibility of testing the body in its entirety precisely because in the subsonic motion even the upstream components are influenced by those downstream;
- The rotation of the wheels and the relative motion of the ground for the correct simulation of the boundary layer, since, on the track, the ground does

not generate a boundary layer in the absence of side wind, while in the wind tunnel there is relative motion between the air flow and the ground that causes the presence of a boundary layer with thickness dependent on speed

The first problem concerns the structure of the wind tunnel only in terms of absolute dimensions and flexibility in the regulation of its devices for adapting them to different bodies.
The second one requires, in the most equipped systems, not only the presence of belts in movement both for the wheels and for the ground, but also a suction system of the boundary layer placed immediately before the body under examination.

### 7.1.2 Description

**Fiat Research Centre**

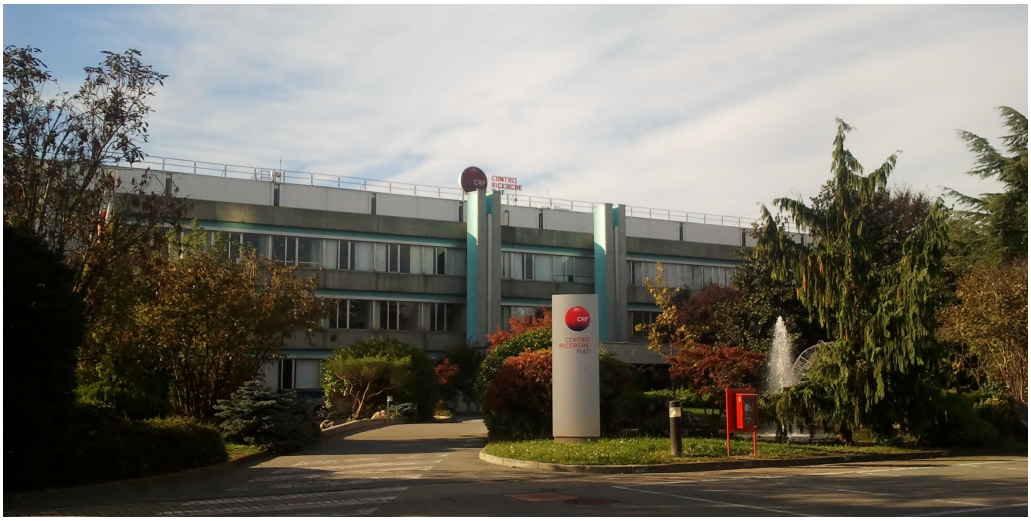

Figure 7.2: CRF - Fiat Research Centre

The wind tunnel of the AeroThermal department of the Fiat Research Center in Orbassano (TO) was used to validate the aerodynamic package of the car.
The birth dates back to 1978 when the S.p.a. Fiat Research Center was established, with Ugo Lucio Businario the first Chief Executive Officer. The prototype of the XI / 23 electric car was completed, and the Total Energy Module (TOTEM) was created, the first cogenerator for the autonomous production of energy with biogas supply.
Later it dealt with, among other things:

- Inertia motogenerator;
- Laser welding;
- Non-gravity fluid behavior, in collaboration with NASA;
- Electromagnetic compatibility tests;
- Tests for noise and vibrations;

- Hydrogen and electric supply

The main office is located in Orbassano (Turin). Smaller locations, dedicated to specific activities and themes, are located in Turin, inside the Mirafiori plant, in Pomigliano d'Arco (NA), in the Magneti Marelli plant in Bologna, in Melfi (PZ), in Valenzano (BA) and in Trento.

The CRF mission has three main objectives:

- The development of innovative powertrains, vehicle systems, materials, methodologies and processes to improve the competitiveness of FCA products;
- Representing FCA in the areas of collaborative research at European and national level, participating in pre-competitive research projects and promoting the development of a network of contacts and partnerships at international level;
- Support FCA in enhancing its intangible capital

**Wind Gallery and Aerothermal**


In particular, the Wind Gallery and Aerothermal department has:

- Scale Model Wind Tunnel;
- Aerodynamic and Aeroacoustic Full Scale Wind Tunnel;
- Climatic Wind Tunnels (Hot and Cold);

It is therefore characterized by the following main activities:

- Aerodynamic coefficients evaluation on max 1:2.5 scale;
- Aerodynamic coefficients evaluation on 1:1 car models, prototypes and production cars;
- Aerodynamic noise: external noise evaluation and inside passenger compartment (shape and infiltration);
- Sun roof buffeting;
- Flow field measurements;
- Spider and cabrio cars comfort evaluation;
- Cooling performance (ATB index), intercooler and condenser;
- Underbody and underhood temperature (air and components);
- Temperature (electric and electronic components , oil, drive-line);

- De-frosting and de-fogging;
- Passenger compartment thermal transient (warm-up and cool-down);
- HVAC manual and automatic regulation;
- Water test (intake system, front and rear lamp)

Figure 7.3: CRF wind tunnel

### 7.1.3 Instrumentation

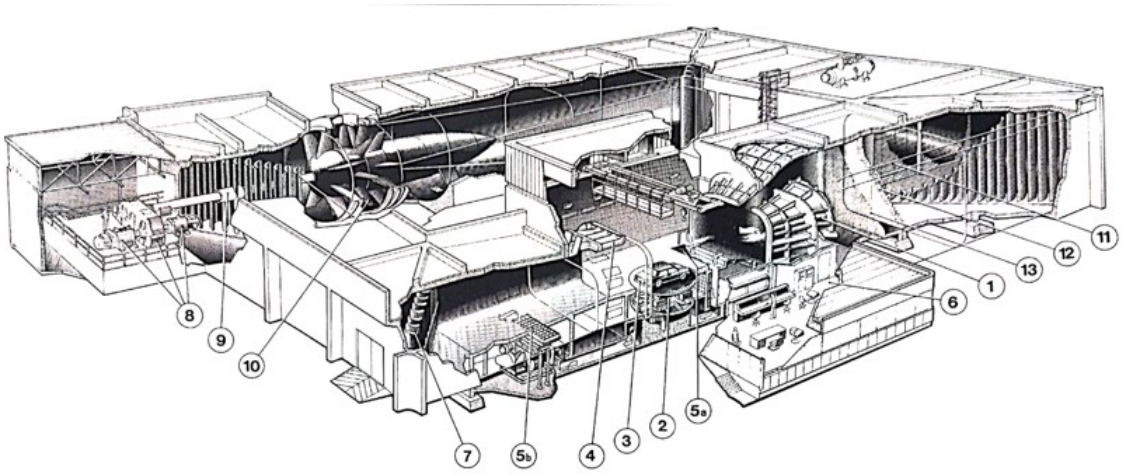


Galleria del vento Fiat.
1) effusore;
2) bilancia;
3 veicolo 1:1;
4) diffusore;
5) controllo dello strato-limite;
a: aspirazione;
b: re-immissione della corrente;
6) sala di comando;
7) «gomito» ad alette deflettici;
8) gruppo propulsore;
9) albero del ventilatore;
10) ventilatore;
11) scambiatore di calore;
12) rettificatore dei filetti d'aria a nido d'api;
13) rete di turbolenza.

*Fiat wind tunnel.*
*1) nozzle;*
*2) balance;*
*3) 1:1 vehicle;*
*4) diffuser;*
*5) boundary-layer control;*
*a: suction;*
*b: re-inlet;*
*6) control room;*
*7) corner with vanes;*
*8) propulsion unit;*
*9) propeller shaft;*
*10) fan;*
*11) heat exchanger;*
*12) flow straightener;*
*13) turbulence screen.*

Figure 7.4: CRF wind tunnel scheme

The plant of the Full Scale Wind Tunnel consists of a closed circuit gallery, in a rectangular plan equal to 37 m x 62 m, equipped with an air renewal system and with a fan in the opposite position to the semi-open test room of a size equal to 16x12x10.5 [m] (length/width/height). The fan has 10 variable pitch blades with a diameter of 9 m and is driven by an electric motor with 1800 kW.
To obtain the values of aerodynamic coefficients with a tolerance of 1 thousandth the air can be sent with a variable speed from 40 $\frac{km}{h}$ to 215 $\frac{km}{h}$. This last speed can be reached only through a suitable reduction of the rectangular section of the nozzle to 22 $m^2$, with respect to original 31 $m^2$, which guarantee a contraction ratio $4 \div 1$. The vehicle is secured by jacks, whose position can be adjusted in all the three Cartesian directions:

- x: it could vary from 360 mm to the maximum size depending on the wheelbase of the vehicle: indeed both of them must be inside the wheels at a minimum distance of 400 mm. So in the case of the SC19, which has a wheelbase of 1525 mm, the maximum pitch is 725 mm;
- y: 1200 mm $\div$ 1850 mm;

- z: the jacks are regulated by steps by steps equal to 0.1 mm and they also have a "floating" operating mode in which they are free to move vertically

In particular, these jacks and the clamps that connects them to the car have the purpose of supporting the longitudinal and lateral forces expressed during the test. The vertical force will be contrasted by the restraint on which the four wheels rest, which can also be suitably set in rotation by moving belts, adjustable in track (1200 mm ÷ 1850 mm) and in wheelbase (360 mm ÷ 2520 mm), in order to correctly simulate the turbulence they created, up to 250 $\frac{km}{h}$.
All these forces are measured by a 6-component electro-mechanical scale, which contains the entire test platform and is fully computerized: indeed, the values are then processed and transmitted to the display and storage system.

With the aim of achieving a correct simulation of the ground effect, there is a moving ground, which is immediately preceded by two systems of aspiration of the boundary layer, that reduce it to lower values than 5.5 mm.

The platform on which the car is bound can rotate around the z axis with a resolution equal to 0.1° thus simulating yaw dynamic. Furthermore, there is a mechanical shroud equipped with pressure intakes that can move allowing a vehicle wake mapping. Finally, the entire room is constantly monitored by cameras and sensors which are controlled by the adjacent operating room which communicates with the test room through a door and a glass window.
Other technical features of this wind tunnel are:

- Pressure probes (static, Pitot, 5 holes) up to 64 channels and 3D hot wire anemometer;
- Stereo PIV anemometer;
- Test room and corners treatment to reduce background noise;
- Microphones and beamforming for noise evaluation;
- Turbulence factor equal to 1.08 (0.1% intensity)

### 7.1.4 Preparations

During the days preceding the test it was necessary to take certain precautions:

- To design and produce clamps to tie the vehicle to the jacks;
- To create a dummy to simulate the presence of the pilot, thus respecting the safety constraints;
- To produce stiff suspensions so that the balance remains unchanged even if subjected to aerodynamic forces

In order to impact as little as possible on the car, it was decided to design clamps that would anchor to the already existing holes for the harness connections. Furthermore, an attempt was made to study a form that could influence the aerodynamics

of the single-seater as little as possible.
Through laser cutting, a V-shaped geometry was then created with two steel plates, with a thickness equal to 4 mm each, overlapped by point welding so as to have a thickness such as to guarantee sufficient bending stiffness.

Figure 7.5: Clamps

It has been possible to realize such a long structure, without having bending problems, since these clamps, being connected to floating jacks, do not have to bear any load along the vertical axis, but only along the longitudinal and transversal ones.

In order to correctly and easily position the dummy inside the cockpit, the mannequin used has no legs, but only head, arms and bust. In particular, arms, shoulders and helmet have been positioned faithfully with respect to the carried out CFD simulations. Everything has been assured by belts and fillers, so that it could withstand even very strong winds.


Figure 7.6: Dummy

The stiff suspensions have been obtained by turned steel and are composed of an internally threaded cylinder. In this way, the height of the car and the load

balancing on the different wheels can be adjusted not only through push-rods, but also through these components.

Figure 7.7: Stiff suspensions

Finally, inside the body the LV battery was positioned so as to be able to activate the radiator fans, also implemented in the CFD simulation. In contrast, the HV battery was not inserted as there was no need to have the traction part active.

Before entering the test room, the following operations were performed on the vehicle:

- Adjustment of ground clearance and weight balance;
- Convergence regulation;
- LV battery recharge and connection;
- assembly of the clamps;
- Removal of the battery pack air ducts, respecting the simulated CFDs;
- Closing of all the cracks through the application of the American tape;
- Positioning and binding of the dummy inside the cockpit, in compliance with the carried out CFD simulations

Inside the test room, on the other hand, the wheel moving belts were adjusted and the clamps fixed to the floating jacks, so as to hold the car in place.

Figure 7.8: Test room

### 7.1.5 Tests and results

The characteristics of the tests are the following:

| Config. | F ht [mm] | R ht [mm] | V start [$\frac{km}{h}$] | V stop [$\frac{km}{h}$] | V step [$\frac{km}{h}$] | Yaw start | Yaw stop | Yaw step | Note |
|---|---|---|---|---|---|---|---|---|---|
| Std | 30 | 30 | 40 | 100 | 10 | 0° | 0° | 0° | Fan |
| Std | 30 | 30 | 80 | 80 | 0 | 0° | 2° | 0.5° | - |
| Std | 30 | 30 | 80 | 80 | 0 | 2° | 10° | 2° | - |
| Std | 30 | 30 | 80 | 80 | 0 | 10° | 15° | 2.5° | - |
| Acc | 30 | 30 | 80 | 80 | 0 | 0° | 0° | 0° | Fan |
| Ptc | 20 | 45 | 80 | 80 | 0 | 0° | 0° | 0° | - |
| Std | 30 | 30 | 80 | 80 | 0 | 0° | 0° | 0° | Fan Wires |

Table 7.1: Tests

The tests were carried out with variable temperature and pressure between 25 °C ÷ 27 °C e 100200 Pa ÷ 100500 Pa respectively, and in each case the moving ground (WSU) and the rotation of the wheels (MB) were implemented.

#### CFD validation

The validation of the implemented CFD model was carried out through a standard configuration test at set speed in symmetrical flow conditions.
As the main test, the radiator fans were kept on to reflect the CFD simulation.

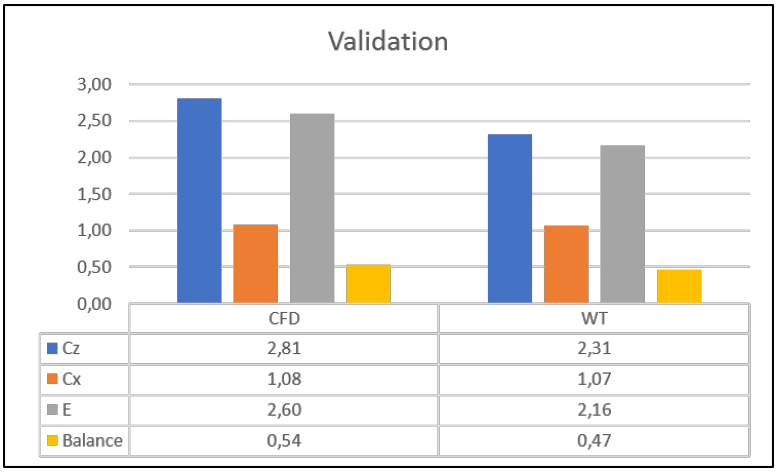


Figure 7.9: Validation

These results indicate that the CFD model is excellent, perfectly reflecting reality. In fact, $C_x$ is really similar to the CFD one, and as for the $C_z$ and the balancing, despite the presence of a slight error, the measure coincides with the expectations. Indeed, this slight deviation is perfectly justifiable:

- Downforce:
  - It is affected by the imperfection of the construction and of the assembly of the various components;

  - It is affected by the greater geometric complexity of the car, compared to the CAD geometry used;
  - It suffers from damages caused in an accident during the tests, in which the undertray and the front wing, expecially, were damaged;
  - It is affected by the reduced size of the moving ground

- Balance:
  - It suffers from the greatest damage suffered by the front wing during the accident, therefore with the center of pressure moving towards the rear axle;
  - It is affected by the approximation with which it was assumed that the center of pressure of sidepods and undertray coincides with the center of gravity of the car

In order to validate the CFD simulation model, the values obtained in the wind tunnel were compared with a more computational expensive simulation, apt to reproduce reality as closely as possible, in all the smallest details:

- CAD with many more detail elements and more complex and adherent geometries;
- CAD appropriately modified in order to take into account all assembly errors;

These reasons explain the difference in aerodynamic values between the design simulation and the specific validation simulation. However, although the values are different, these measures do not affect the characteristics of each design choice, as they are constant disturbances, regardless of the aerodynamic components designed.

### Speed sensitivity

The quality and reliability of CFDs and wind tunnel tests have been verified by varying the flow velocity.

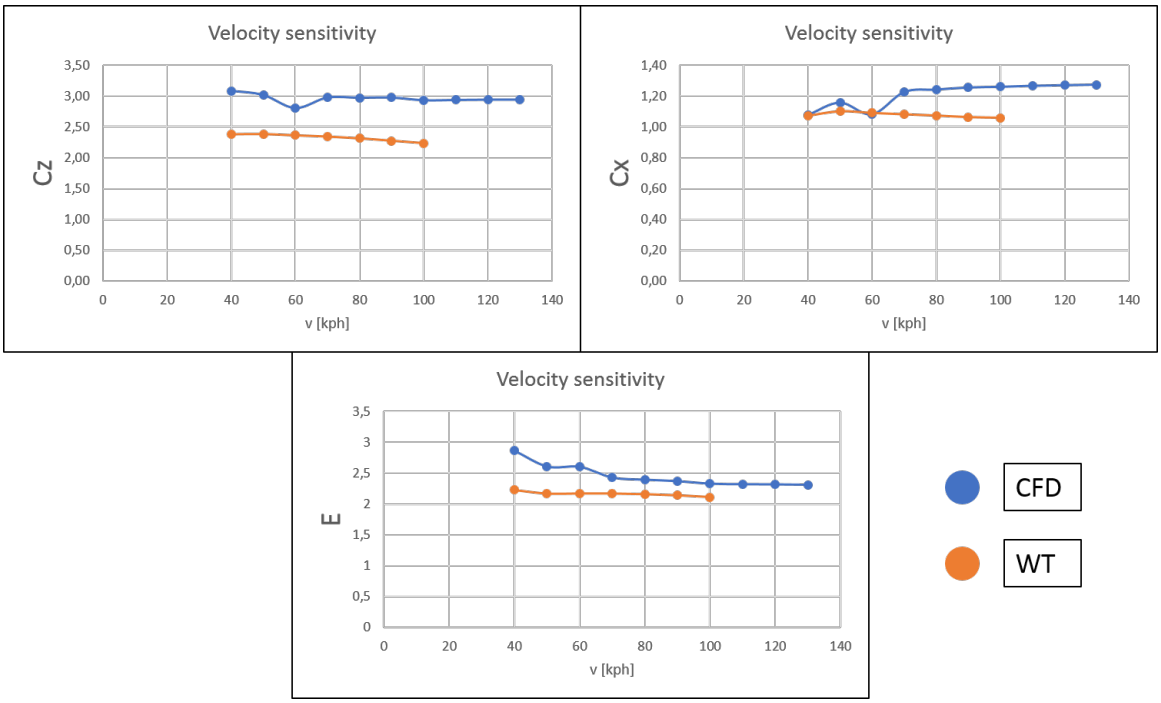


Figure 7.10: Velocity Sensitivity SC19

The results obtained are excellent, as the aerodynamic coefficients, according to theory, remain constant as the speed changes.
It can be seen that the only slightly different value corresponds to the speed at which the CFDs were performed: indeed in this simulation the results are more precise, since the mesh has been optimized precisely in these conditions.

### Fans impact

The radiator fans dispose of a very high flow rate and direct it both towards the rear axle of the car and upwards. Therefore they interact with both the undertray and the rear wing.

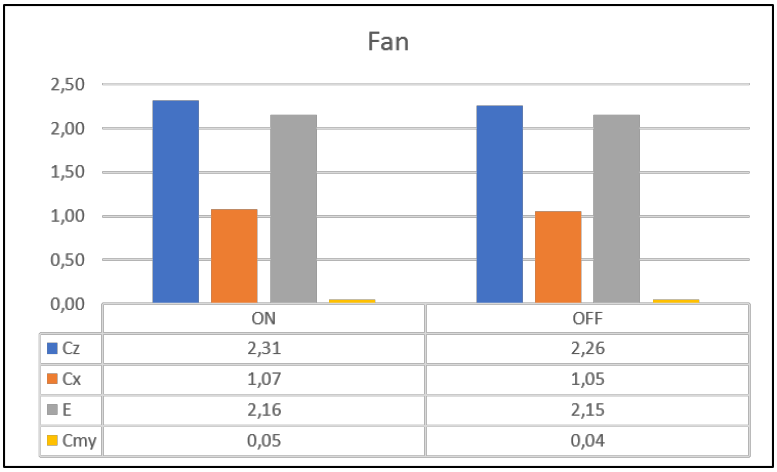


Figure 7.11: Fans impact

Indeed, it is noted that this flow distorts the work of the aerodynamic components

by lowering the aerodynamic performance, and, as expected, only on the rear axle, as shown by the reduction of the $C_{my}$.

### Yaw and Pitch

After evaluating the accuracy and the reliability of the CFD model, we searched for useful data to understand the dynamic behaviour of the car.
In particular, in order to have a more precise aerodynamic model, in order to be able to implement more efficient vehicle dynamics controls, it was also decided to evaluate the behaviour at different angles of yaw and in the pitch configuration corresponding to the maximum braking.

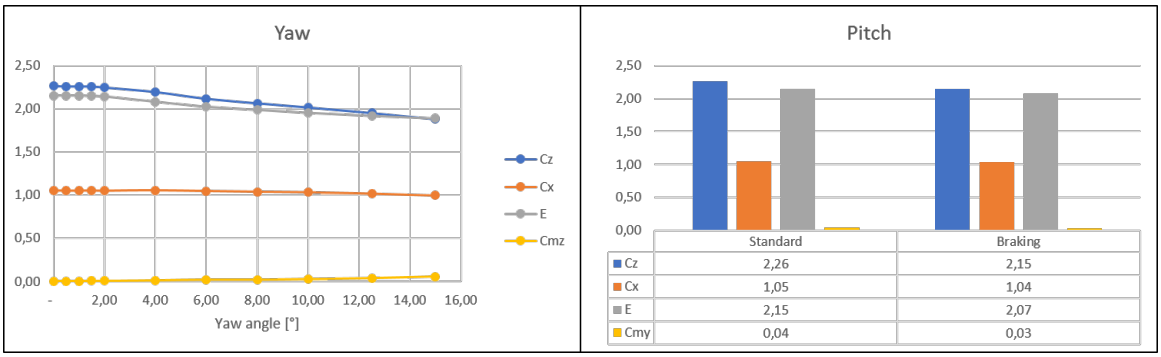


Figure 7.12: Yaw and pitch

As expected, outside the project conditions the aerodynamic performance decreases in both cases.
Moreover, both in the condition of yaw and in that of pitch, the rear axle worsens more: indeed, an increase of $C_{mz}$ and a reduction of $C_{my}$ are shown, respectively.

### Acceleration configuration

In order to have data also for this typical configuration in acceleration event, drag reduction with less incident flap was also tested.

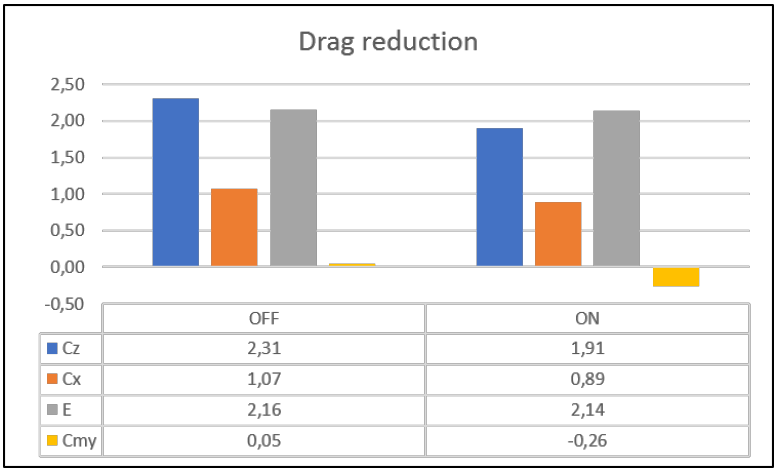


Figure 7.13: Acceleration configuration

substantially constant efficiency can be noticed, thus a proportional reduction of both the downforce and the drag. Of course, all these changes occur on the rear axle with a consequent reduction of the $C_{my}$, which actually becomes negative.

### Flow visualization

Finally, the configuration implemented in CFD was tested again for the dual purpose of:

- Evaluating the reproducibility of the same identical settings after having repeatedly modified them;
- Applying woolen threads in order to visualize the streamlines

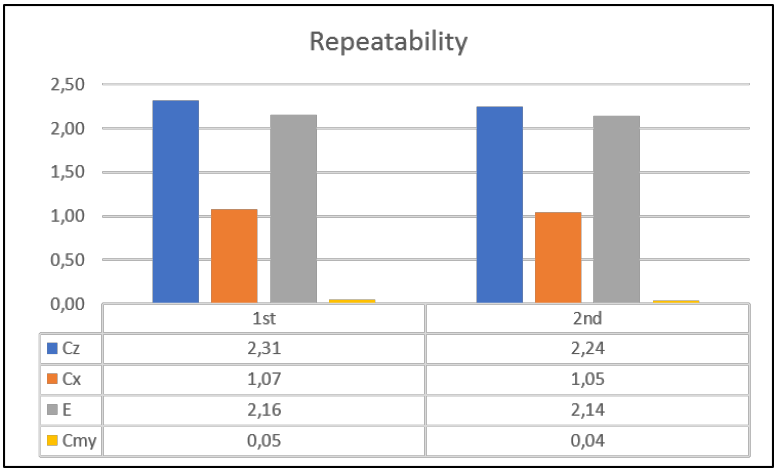


Figure 7.14: Repeatability

First, we notice how the reproduction of the same settings is not exact, but they are however very similar to the original. This denotes a remarkable security in the correlation between the desired set-up, corresponding to the design data, and the actual set-up with which the car takes part in the races.


Figure 7.15: Woolen threads

Finally, there is a complete correspondence between the streamline images of the CFD simulations and those displayed in the wind tunnel by means of woolen threads.
In particular, the main points of interest are:

- Great work of the TE of the flap: the threads are well stretched in the direction of the flow;
- Excellent slot performance: the wires stay close to the main;
- Clean air flow to the undertray: the wires on the clark are not subject to whirling;
- Presence of the vortex at extremities despite the presence of endplates and footplates: the wire circumnavigates the footplate attracted by the depression below the front wing;
- Whirlwind of the wheel and propagation of the end vortex: unpredictable turbulent phenomenon, witnessed by the continuous variability of the position of the woolen thread

All these observations have already been noted, and partially resolved, during the design phase, as witnessed above, demonstrating the excellent correlation between the results of the CFD simulation and those of the wind tunnel tests.

# Chapter 8

# Conclusions and future developments

## 8.1 Technical results

During the design phase of the front wing and, more generally, of the whole aerodynamic package, the predetermined forces and efficiency values have been obtained for a minimum lap time:

$$C_z \approx 4 \qquad\qquad E \approx 4$$

and an excellent balance was assured, with a load distribution between front and rear axles equal to 53% / 47%.

Furthermore, using as a core the rohacell, a very light material as well as using as plies the CFRP, a stiff and resistant but also very lightweight material, it was possible to obtain a very light aerodynamic package which therefore contributed little to the inertial mass of the vehicle and so much to the vertical load generated. Indeed, its total weight is 10 kg, that is equal to 4% of the total mass of the vehicle including the driver, guaranteeing an increase in the vertical load equal to 23%, at the speed of 60 $\frac{\text{km}}{\text{h}}$, i.e. the average speed obtained during a Formula Student event.

Finally, after preparation of clamps, dummy, stiff suspensions, moving ground and rolling wheels, wind tunnel tests were performed with varying speeds, yaw, pitch, drag reduction system, so as to validate the CFD model, as well as to obtain additional data on the car. Moreover, the streamlines were visualized thanks to the woolen thread method.
Both the aerodynamic values and the streamline are very similar to the ones shown during the design phase, demonstrating the excellent correlation between the results of the CFD simulation and those of the wind tunnel tests.

## 8.2 Events results

During the 2019 Formula Student season, Squadra Corse and its SC19 participated in 3 Formula SAE events, the maximum allowed by the budget , but it also qualified

in other races, like FSUK. Results obtained, overall and in static and dynamic events, are the following:

| | **FSItaly** | **FSCzech** | **FSSpain** |
|---|---|---|---|
| **Overall** | **1** (801.9) | **6** (488.4) | **14** (399.4) |
| Business | 17 (48.7) | 6 (65.0) | 12 (68.9) |
| Design | 2 (138.6) | 2 (145.0) | 16 (86.0) |
| Cost | 2 (96.0) | 2 (94.0) | 4 (91.0) |
| Acceleration | 3 (96.2) | 4 (70.3) | 7 (59.7) |
| Skidpad | 2 (47.5) | 5 (40.1) | 14 (42.3) |
| Autocross | - | 3 (74.0) | 7 (51.5) |
| Endurance | 1 (275) | - | - |
| Efficiency | 1 (100) | - | - |

Table 8.1: 2019 Results

Unfortunately, the SC19 could not express its full potential due to the imperfect reliability of a too young car. Indeed, given the production delays, very few pre-seasonal tests have been carried out and this has led to unforeseen accidents that prevented an excellent placement, having caused the loss of many points. Furthermore, to avoid such accidents, due to the lack of pre-seasonal tests, and to guarantee a greater safety margin, the car's performance has been voluntarily reduced.

Despite this, a historical result was achieved: first place in the home race in Varano de' Melegari. Indeed, it was the first victory of an Italian team in the full electric category and the first victory of our team after many years. Furthermore, in the other two competitions excellent results were achieved, underlining the goodness of the project and its enormous potential.

**Overall Results**
**Class 1E - Official Results**

| Place | Car No. | Team Name | University | Cost Score | Presentation Score | Design Score | Acceleration Score | Skid Pad Score | Autocross Score | Endurance Score | Efficiency Score | Penalties | Total Score |
|---|---|---|---|---|---|---|---|---|---|---|---|---|---|
| 1 | 146 | Squadra Corse PoliTo | Politecnico di Torino | 95,960 | 48,670 | 138,542 | 96,286 | 47,482 | 0 | **275** | **100** | 0 | 801,940 |
| 2 | 159 | Superior engineering | University of Ljubljana | 72,352 | 49,867 | 103,125 | 83,944 | 41,204 | 92,543 | 251,446 | 88,126 | 0 | 782,607 |
| 3 | 121 | Aristotle University Racing Team Electric - Aristurtle | Aristotle University of Thessaloniki | 90,070 | **75** | 83,333 | 83,874 | 39,912 | 75,366 | 172,212 | 88,855 | 40 | 668,623 |
| 4 | 124 | FS Team Tallinn | Tallinn University of Technology | 84,340 | 64,229 | **150** | 97,745 | **75** | **125** | 5 | 0 | 10 | 591,314 |
| 5 | 198 | Metropolia Motorsport | Metropolia University of Applied Sciences | 81,982 | 60,239 | 116,667 | **100** | 46,797 | 91,376 | 2 | 0 | 0 | 499,061 |
| 6 | 114 | BME Formula Racing Team | TU BUDAPEST | 66,647 | 36,303 | 126,042 | 0 | 0 | 69,367 | 67,480 | 81,723 | 60 | 387,562 |
| 7 | 185 | Race UP Electric | Università di Padova | 84,946 | 59,840 | 107,292 | 49,559 | 32,355 | 25,934 | 0 | 0 | 0 | 359,926 |
| 8 | 126 | E-Motion Rennteam Aalen | Hochschule Aalen | **100** | 41,888 | 115,625 | 0 | 0 | 32,840 | 2 | 0 | 0 | 292,353 |
| 9 | 191 | Blue Flash Mobility Concepts | HAWK Göttingen | 90,070 | 67,021 | 125 | 0 | 0 | 0 | 4 | 0 | 0 | 286,091 |
| 10 | 122 | Formula Electric Belgium | KU Leuven & Thomas More | 72,107 | 54,654 | 123,958 | 0 | 0 | 9,451 | 0 | 0 | 0 | 260,171 |
| 11 | 194 | E.Stall | UAS Esslingen | 79,217 | 45,479 | 127,083 | 0 | 0 | 0 | 8 | 0 | 0 | 259,779 |
| 12 | 179 | e-Tech Racing | Escola d'Enginyeria Barcelona Est (UPC) | 63,473 | 55,053 | 121,875 | 0 | 0 | 0 | 0 | 0 | 0 | 240,401 |
| 13 | 129 | HofSpannung Motorsport | University of Applied Sciences Hof | 61,404 | 73,404 | 79,167 | 4,5 | 0 | 0 | 8 | 0 | 0 | 226,475 |
| 14 | 171 | KTH Formula Student | KTH Royal Institute of Technology | 66,306 | 61,436 | 92,708 | 0 | 0 | 0 | 0 | 0 | 0 | 220,451 |
| 15 | 188 | UniPR Racing Team | Università di Parma | 63,181 | 42,287 | 101,042 | 0 | 0 | 0 | 0 | 0 | 0 | 206,510 |
| 16 | 153 | Speeding Scientists Siegen | University of Siegen | 31,683 | 52,261 | 93,750 | 0 | 0 | 64,305 | 0 | 0 | 50 | 191,999 |
| 17 | 172 | Bremergy | University of Bremen | 71,211 | 49,468 | 82,292 | 0 | 0 | 6,5 | 16 | 0 | 50 | 175,471 |
| 18 | 140 | E-Team Duisburg-Essen | University of Duisburg-Essen | 29,636 | 55,452 | 80,208 | 0 | 0 | 0 | 0 | 0 | 0 | 165,296 |
| 19 | 128 | Herkules Racing Team | University of Kassel | 50,557 | 42,287 | 86,458 | 0 | 0 | 0 | 0 | 0 | 20 | 159,303 |
| 20 | 175 | Team Spark | University of Iceland | 28,895 | 59,840 | 67,708 | 15,148 | 3,5 | 0 | 0 | 0 | 20 | 155,092 |
| 21 | 101 | CURE Mannheim | DHBW Mannheim | 50,229 | 54,255 | 0,000 | 8,175 | 7,784 | 14,520 | 19 | 0 | 0 | 153,963 |
| 22 | 116 | UniNa Corse E-Team | Università di Napoli Federico II | 49,410 | 46,676 | 55,208 | 0 | 0 | 0 | 0 | 0 | 0 | 151,294 |
| 23 | 155 | BGRe - Ben Gurion Racing Electric | Ben-Gurion University of the Negev | 0 | 40,691 | 108,333 | 0 | 0 | 0 | 0 | 0 | 0 | 149,025 |
| 24 | 176 | eForce FEE Prague Formula | Czech Technical University in Prague | 45,643 | 36,702 | 126,042 | 0 | 0 | 0 | 0 | 0 | 60 | 148,387 |
| 25 | 190 | STUBA Green Team | Slovak University of Technology | 69,817 | 34,309 | 90,625 | 0 | 0 | 6,5 | 0 | 0 | 100 | 101,251 |
| 26 | 184 | Proton Dynamic | Warsaw University of Technology | 0 | 52,660 | 29,167 | 0 | 0 | 0 | 0 | 0 | 100 | 0 |

Figure 8.1: FSItaly 2019 overall results

## 8.3 Improvements planned for 2020 season

### 8.3.1 Front wing

Based on the analyzes carried out for the 2019 season, taking into account positive and negative results, weaknesses and strengths, and exploiting the acquired experience, possible areas for improvement were identified with regard to the performance provided by the front wing:

- Take more care of synergies between the nose and clark, filling a last season gap du to shortage of human and time resources.;
- Optimization of the aerofoils for ground effect (the previous analysis made it possible to identify the best configuration so it is possible to restrict the range of variation of DoF parameters and give Heeds the possibility to modify also the geometry especially of the main);
- evaluation of the possibility to increase the downforce by adding a second flap with half wingspan;
- Studies and analyses on the possibility to reduce weight and frictional resistance by using thinner supports (but both these sizes are already negligible);
- More in-depth studies on vortices

Of course, all the above possible improvements must be evaluated as part of the whole project of the 2020 Formula Student car, carefully considering interactions among the different elements and assuring global coherence and consistency.

### 8.3.2 Aeropack

In order both to generate and to control vortices in particular those generated by th front wing, a series of appropriate aerodynamic appendices should be introduced. As for example these appendices might in turn generate further vortices, it is clear how any front wing development is strictly dependent on those on the rest of the rest of the aerodynamic package and viceversa. In particular, other developments might be the following:

- The use of radiators to accentuate the ground effect;
- The evaluation of a rake asset;
- Further improvement of aerodynamic balance;
- Rear wing's main twist

Instead, we advice against the following:

- To further reduce the front wing's height to try to maximize the ground effect, because pitch dynamics would lead to an impact with the asphalt and then to an inevitable damage;

- To implement the Gurney flaps, given the car's low drag philosophy, since they do too much aerodynamic resistance;

In conclusion, it should always be kept in mind that, in any case, all aerodynamic choices must be shared within the whole team in order to have a common orientation to the project, creating and exploiting positive synergies and limiting negative interactions, in order to reach a reasoned balance of the different needs and to obtain an optimal performance.

# Appendix

*Java listing of the Star-CCM+ macro to execute a multiple number of simulations as the profiles and their incidence vary.*

```
1  // STAR-CCM+ macro: star_macro_2D.java
2  // Written by STAR-CCM+ 13.02.011
3  package macro;
4
5  import java.util.*;
6
7  import star.common.*;
8  import star.base.neo.*;
9  import star.segregatedflow.*;
10 import star.material.*;
11 import star.keturb.*;
12 import star.resurfacer.*;
13 import star.turbulence.*;
14 import star.prismmesher.*;
15 import star.vis.*;
16 import star.flow.*;
17 import star.metrics.*;
18 import star.meshing.*;
19
20 public class star_macro_2D extends StarMacro {
21
22   public void execute() {
23     execute0();
24   }
25
26   private void execute0() {
27
28     Simulation simulation_0 =
29       getActiveSimulation();
30
31     SubtractPartsOperation subtractPartsOperation_0 =
32       ((SubtractPartsOperation) simulation_0.get(MeshOperationManager.
           class).getObject("Subtract"));
33
34     subtractPartsOperation_0.execute();
35
36     Scene scene_3 =
37       simulation_0.getSceneManager().getScene("Geometry Scene 1");
38
39     CurrentView currentView_2 =
40       scene_3.getCurrentView();
41
42     currentView_2.setInput(new DoubleVector(new double[]
         {0.2878366495673801, -0.019085723946409575,
```

```
        0.029627096636660966}), new DoubleVector(new double[]
        {0.2878366495673801, -0.019085723946409575, 9.883356911561867})
        , new DoubleVector(new double[] {0.0, 1.0, 0.0}),
        11.181346072812522, 0);
43
44      currentView_2.setInput(new DoubleVector(new double[]
        {0.3079111148804509, -0.04166949742361442,
        0.02961611084849647}), new DoubleVector(new double[]
        {0.3079111148804509, -0.04166949742361442, 5.266478190287123}),
         new DoubleVector(new double[] {0.0, 1.0, 0.0}),
        11.181346072812522, 0);
45
46      currentView_2.setInput(new DoubleVector(new double[]
        {0.2589604494536927, -0.019525148778176144,
        0.02828238377519643}), new DoubleVector(new double[]
        {0.2589604494536927, -0.019525148778176144,
        3.1220881753960543}), new DoubleVector(new double[] {0.0, 1.0,
        0.0}), 11.181346072812522, 0);
47
48      currentView_2.setInput(new DoubleVector(new double[]
        {0.21904418542099627, -0.01333124573861982,
        0.028355676592945578}), new DoubleVector(new double[]
        {0.21904418542099627, -0.01333124573861982,
        1.8558472093400185}), new DoubleVector(new double[] {0.0, 1.0,
        0.0}), 11.181346072812522, 0);
49
50      currentView_2.setInput(new DoubleVector(new double[]
        {0.2457563751571597, -0.01747624069767966,
        0.028316507476521036}), new DoubleVector(new double[]
        {0.2457563751571597, -0.01747624069767966, 2.7032228281926654})
        , new DoubleVector(new double[] {0.0, 1.0, 0.0}),
        11.181346072812522, 0);
51
52      currentView_2.setInput(new DoubleVector(new double[]
        {0.45240720962346986, -0.04954274949417605,
        0.028013369766856755}), new DoubleVector(new double[]
        {0.45240720962346986, -0.04954274949417605, 9.258689844258265})
        , new DoubleVector(new double[] {0.0, 1.0, 0.0}),
        11.181346072812522, 0);
53
54      currentView_2.setInput(new DoubleVector(new double[]
        {0.5135004083875113, -0.059022728612734186,
        0.027923739595626884}), new DoubleVector(new double[]
        {0.5135004083875113, -0.059022728612734186,
        11.196714679424874}), new DoubleVector(new double[] {0.0, 1.0,
        0.0}), 11.181346072812522, 0);
55
56      currentView_2.setInput(new DoubleVector(new double[]
        {0.7851000594980584, -0.10116750206092248,
        0.027525255278394667}), new DoubleVector(new double[]
        {0.7851000594980584, -0.10116750206092248, 19.81251610615649}),
         new DoubleVector(new double[] {0.0, 1.0, 0.0}),
        11.181346072812522, 0);
57
58      PhysicsContinuum physicsContinuum_0 =
59        simulation_0.getContinuumManager().createContinuum(
            PhysicsContinuum.class);
60
```

```
61      physicsContinuum_0.enable(TwoDimensionalModel.class);
62
63      physicsContinuum_0.enable(SteadyModel.class);
64
65      physicsContinuum_0.enable(SingleComponentGasModel.class);
66
67      physicsContinuum_0.enable(SegregatedFlowModel.class);
68
69      physicsContinuum_0.enable(ConstantDensityModel.class);
70
71      physicsContinuum_0.enable(TurbulentModel.class);
72
73      physicsContinuum_0.enable(RansTurbulenceModel.class);
74
75      physicsContinuum_0.enable(KEpsilonTurbulence.class);
76
77      physicsContinuum_0.enable(RkeTwoLayerTurbModel.class);
78
79      physicsContinuum_0.enable(KeTwoLayerAllYplusWallTreatment.class);
80
81      physicsContinuum_0.enable(CellQualityRemediationModel.class);
82
83      VelocityProfile velocityProfile_0 =
84        physicsContinuum_0.getInitialConditions().get(VelocityProfile.
            class);
85
86      Units units_1 =
87        ((Units) simulation_0.getUnitsManager().getObject("kph"));
88
89      velocityProfile_0.getMethod(ConstantVectorProfileMethod.class).
          getQuantity().setUnits(units_1);
90
91      velocityProfile_0.getMethod(ConstantVectorProfileMethod.class).
          getQuantity().setComponents(60.0, 0.0, 0.0);
92
93      MeshOperationPart meshOperationPart_0 =
94        ((MeshOperationPart) simulation_0.get(SimulationPartManager.class
            ).getPart("Subtract"));
95
96      PrepareFor2dOperation prepareFor2dOperation_0 =
97        (PrepareFor2dOperation) simulation_0.get(MeshOperationManager.
            class).createPrepareFor2dOperation(new NeoObjectVector(new
            Object[] {meshOperationPart_0}));
98
99      prepareFor2dOperation_0.execute();
100
101     currentView_2.setInput(new DoubleVector(new double[]
          {0.2147709226279642, -0.00796657761526148,
          0.048497314646360756}), new DoubleVector(new double[]
          {0.2147709226279642, -0.00796657761526148, 3.0086205554979824})
          , new DoubleVector(new double[] {0.0, 1.0, 0.0}),
          11.181346072812522, 0);
102
103     currentView_2.setInput(new DoubleVector(new double[]
          {0.18974771868176157, 0.00454502435783983,
          0.04917543635179755}), new DoubleVector(new double[]
          {0.18974771868176157, 0.00454502435783983, 1.7970358405446822})
          , new DoubleVector(new double[] {0.0, 1.0, 0.0}),
```

```
        11.181346072812522, 0);
104
105     currentView_2.setInput(new DoubleVector(new double[]
            {0.17497176698356842, 0.011933000206936422,
            0.04915425760516512}), new DoubleVector(new double[]
            {0.17497176698356842, 0.011933000206936422,
            1.0816071822119082}), new DoubleVector(new double[] {0.0, 1.0,
            0.0}), 11.181346072812522, 0);
106
107     currentView_2.setInput(new DoubleVector(new double[]
            {0.2144544147840927, -0.007808323693325671,
            0.049107946377842104}), new DoubleVector(new double[]
            {0.2144544147840927, -0.007808323693325671, 2.993295736716898})
            , new DoubleVector(new double[] {0.0, 1.0, 0.0}),
            11.181346072812522, 0);
108
109     currentView_2.setInput(new DoubleVector(new double[]
            {0.29700232368360596, -0.04908227814308225,
            0.04901109639716861}), new DoubleVector(new double[]
            {0.29700232368360596, -0.04908227814308225, 6.990137423697799})
            , new DoubleVector(new double[] {0.0, 1.0, 0.0}),
            11.181346072812522, 0);
110
111     Region region_0 =
112       simulation_0.getRegionManager().createEmptyRegion();
113
114     region_0.setPresentationName("Aria");
115
116     Boundary boundary_0 =
117       region_0.getBoundaryManager().getBoundary("Default");
118
119     region_0.getBoundaryManager().removeBoundaries(new NeoObjectVector(
            new Object[] {boundary_0}));
120
121     FeatureCurve featureCurve_0 =
122       ((FeatureCurve) region_0.getFeatureCurveManager().getObject("
            Default"));
123
124     region_0.getFeatureCurveManager().removeObjects(featureCurve_0);
125
126     FeatureCurve featureCurve_1 =
127       region_0.getFeatureCurveManager().createEmptyFeatureCurveWithName
            ("Feature_Curve");
128
129     simulation_0.getRegionManager().newRegionsFromParts(new
            NeoObjectVector(new Object[] {meshOperationPart_0}), "OneRegion
            ", region_0, "OneBoundaryPerPartSurface", null, "
            OneFeatureCurve", featureCurve_1, RegionManager.
            CreateInterfaceMode.BOUNDARY);
130
131     Boundary boundary_1 =
132       region_0.getBoundaryManager().getBoundary("Subtract.Galleria.
            Inlet");
133
134     InletBoundary inletBoundary_0 =
135       ((InletBoundary) simulation_0.get(ConditionTypeManager.class).get
            (InletBoundary.class));
136
```

```
137     boundary_1.setBoundaryType(inletBoundary_0);
138
139     Boundary boundary_2 =
140       region_0.getBoundaryManager().getBoundary("Subtract.Galleria.
              Outlet");
141
142     PressureBoundary pressureBoundary_0 =
143       ((PressureBoundary) simulation_0.get(ConditionTypeManager.class).
              get(PressureBoundary.class));
144
145     boundary_2.setBoundaryType(pressureBoundary_0);
146
147     VelocityMagnitudeProfile velocityMagnitudeProfile_0 =
148       boundary_1.getValues().get(VelocityMagnitudeProfile.class);
149
150     velocityMagnitudeProfile_0.getMethod(ConstantScalarProfileMethod.
          class).getQuantity().setUnits(units_1);
151
152     velocityMagnitudeProfile_0.getMethod(ConstantScalarProfileMethod.
          class).getQuantity().setValue(60.0);
153
154     Boundary boundary_3 =
155       region_0.getBoundaryManager().getBoundary("Subtract.Galleria.
              Wall1");
156
157     boundary_3.getConditions().get(WallShearStressOption.class).
          setSelected(WallShearStressOption.Type.SLIP);
158
159     Boundary boundary_4 =
160       region_0.getBoundaryManager().getBoundary("Subtract.Galleria.
              Wall4");
161
162     boundary_4.getConditions().get(WallShearStressOption.class).
          setSelected(WallShearStressOption.Type.SLIP);
163
164     AutoMeshOperation2d autoMeshOperation2d_0 =
165       simulation_0.get(MeshOperationManager.class).
              createAutoMeshOperation2d(new StringVector(new String[] {"
              star.twodmesher.DualAutoMesher2d", "star.prismmesher.
              PrismAutoMesher"}), new NeoObjectVector(new Object[] {
              meshOperationPart_0}));
166
167     PartsTargetSurfaceSize partsTargetSurfaceSize_0 =
168       autoMeshOperation2d_0.getDefaultValues().get(
              PartsTargetSurfaceSize.class);
169
170     partsTargetSurfaceSize_0.getRelativeSizeScalar().setValue(30.0);
171
172     PartsMinimumSurfaceSize partsMinimumSurfaceSize_0 =
173       autoMeshOperation2d_0.getDefaultValues().get(
              PartsMinimumSurfaceSize.class);
174
175     partsMinimumSurfaceSize_0.getRelativeSizeScalar().setValue(0.001);
176
177     SurfaceProximity surfaceProximity_0 =
178       autoMeshOperation2d_0.getDefaultValues().get(SurfaceProximity.
              class);
179
```

```
180     surfaceProximity_0.setNumPointsInGap(4.0);
181
182     SurfaceGrowthRate surfaceGrowthRate_0 =
183       autoMeshOperation2d_0.getDefaultValues().get(SurfaceGrowthRate.
              class);
184
185     surfaceGrowthRate_0.getGrowthRateScalar().setValue(1.08);
186
187     NumPrismLayers numPrismLayers_0 =
188       autoMeshOperation2d_0.getDefaultValues().get(NumPrismLayers.class
              );
189
190     IntegerValue integerValue_0 =
191       numPrismLayers_0.getNumLayersValue();
192
193     integerValue_0.getQuantity().setValue(18.0);
194
195     PrismLayerStretching prismLayerStretching_0 =
196       autoMeshOperation2d_0.getDefaultValues().get(PrismLayerStretching
              .class);
197
198     prismLayerStretching_0.getStretchingQuantity().setValue(1.4);
199
200     PrismThickness prismThickness_0 =
201       autoMeshOperation2d_0.getDefaultValues().get(PrismThickness.class
              );
202
203     prismThickness_0.getRelativeSizeScalar().setValue(0.5);
204
205     SurfaceCustomMeshControl surfaceCustomMeshControl_0 =
206       autoMeshOperation2d_0.getCustomMeshControls().
              createSurfaceControl();
207
208     surfaceCustomMeshControl_0.getGeometryObjects().setQuery(null);
209
210     PartSurface partSurface_6 =
211       ((PartSurface) meshOperationPart_0.getPartSurfaceManager().
              getPartSurface("Galleria.Inlet"));
212
213     PartSurface partSurface_7 =
214       ((PartSurface) meshOperationPart_0.getPartSurfaceManager().
              getPartSurface("Galleria.Outlet"));
215
216     PartSurface partSurface_8 =
217       ((PartSurface) meshOperationPart_0.getPartSurfaceManager().
              getPartSurface("Galleria.Wall1"));
218
219     PartSurface partSurface_9 =
220       ((PartSurface) meshOperationPart_0.getPartSurfaceManager().
              getPartSurface("Galleria.Wall2"));
221
222     PartSurface partSurface_10 =
223       ((PartSurface) meshOperationPart_0.getPartSurfaceManager().
              getPartSurface("Galleria.Wall4"));
224
225     surfaceCustomMeshControl_0.getGeometryObjects().setObjects(
          partSurface_6, partSurface_7, partSurface_8, partSurface_9,
          partSurface_10);
```

```
226
227         PartsCustomizePrismMesh partsCustomizePrismMesh_0 =
228           surfaceCustomMeshControl_0.getCustomConditions().get(
                  PartsCustomizePrismMesh.class);
229
230         partsCustomizePrismMesh_0.getCustomPrismOptions().setSelected(
                PartsCustomPrismsOption.Type.DISABLE);
231
232         autoMeshOperation2d_0.execute();
233       }
234     }
```

*Matlab listing for the post processing of two-dimensional simulations and the construction of the aerfoils' characteristic curves.*

```
%% POST PROCESSING PROFILI 2D

close all
clear
clc

it = 550; % numero iterazioni su stra ccm+
coeff = 1; %numero coefficienti nel file .csv
prof = 26; % numero profili complessivi da analizzare
alfa = -2:1:15;%campo di variazione dell'angolo di attacco
alfa = alfa.';
a=length(alfa);
CD = zeros(a,prof);
CL = CD;
eff = CD;
ww = 2; %numero di elementi gi  processati
w = ww+1; %nella macro l'indice parte da zero, in matlab da 1
wcorr = 0; % poich nella nomenclatura della macro non sono stati inseriti quelli gi processati
                %(la nomenclatura parte da 0); se ci fossero stati

%% Eventuali dati gi post processare

CD(:,1:ww) = 10*[           0.0032     0.003023888;
          0.0034          0.003003458;
     0.003610068     0.00310031;
     0.003806831     0.003242742;
       0.0040253     0.003463523;
     0.004259229     0.003708123;
     0.004535322     0.004037569;
     0.004839606     0.004406824;
     0.00517582      0.004868204;
     0.005552234     0.005396007;
     0.005970098     0.006029425;
     0.006454886     0.00680256;
     0.007009575     0.007668353;
     0.007634842     0.008581224;
     0.008358755     0.009994847;
     0.009232335       0.0113343;
       0.01032468      0.01280206;
       0.01176767      0.01455028]; %dati gi processati come vettori colonna
CL(:,1:ww) = 10*[  0.097           0.09308329;
              0.098      0.1051111;
     0.09955439      0.1148972;
       0.107791      0.1235702;
       0.1156542     0.1313765;
       0.1227804     0.1383196;
       0.1299672     0.1446721;
       0.1368408     0.1494677;
       0.1429844     0.1537408;
       0.1489093     0.1571046;
       0.1544373       0.159777;
       0.1598267     0.1612479;
       0.164783      0.1612295;
```

```
54  ␣␣␣␣␣0.1691636␣␣␣␣␣0.1653782;
55  ␣␣␣␣␣0.1727854␣␣␣␣␣0.1591065;
56  ␣␣␣␣␣0.1753633␣␣␣␣␣0.1568723;
57  ␣␣␣␣␣0.1765177␣␣␣␣␣0.1536851;
58  ␣␣␣␣␣0.1745723␣␣␣␣␣0.1513177];␣%inseriti␣tutti␣in␣una␣matrice␣(al␣
        variare␣di␣alfa)
59  eff(:,1:ww)␣=␣CL(:,1:ww)./CD(:,1:ww);
60
61
62  ww1=ww;␣%per␣la␣nomenclatura
63
64  for␣k=1:ww
65
66  ␣␣␣␣pcd=polyfit(alfa,CD(:,k),3);
67  ␣␣␣␣Pcd=pcd(1)*alfa.^3+pcd(2)*alfa.^2+pcd(3)*alfa+pcd(4);␣%+pcd(5)*alfa
        +pcd(6);
68
69  ␣␣␣␣pcl=polyfit(alfa,CL(:,k),3);
70  ␣␣␣␣Pcl=pcl(1)*alfa.^3+pcl(2)*alfa.^2+pcl(3)*alfa+pcl(4);␣%+pcl(5)*alfa
        +pcl(6);
71
72  ␣␣␣␣peff=polyfit(alfa,eff(:,k),3);
73  ␣␣␣␣Peff=peff(1)*alfa.^3+peff(2)*alfa.^2+peff(3)*alfa+peff(4);␣%+peff
        (5)*alfa+peff(6);
74
75
76  ␣␣␣␣%figure(k)
77  ␣␣␣␣%grid␣on
78  ␣␣␣␣%plot(alfa,Pcd,'red');
79  ␣␣␣␣%xlabel('alfa');
80  ␣␣␣␣%ylabel('CD');
81  ␣␣␣␣%title(strcat(ww1,'␣CD'));
82  ␣␣␣␣%figure(k+prof)
83  ␣␣␣␣%grid␣on
84  ␣␣␣␣%plot(alfa,Pcl,'green');
85  ␣␣␣␣%xlabel('alfa');
86  ␣␣␣␣%ylabel('CL');
87  ␣␣␣␣%title(strcat(ww1,'␣CL'));
88  ␣␣␣␣%figure(k+2*prof)
89  ␣␣␣␣%grid␣on
90  ␣␣␣␣%plot(alfa,Peff,'blue');
91  ␣␣␣␣%xlabel('alfa');
92  ␣␣␣␣%ylabel('eff');
93  ␣␣␣␣%title(strcat(ww1,'␣␣eff'));
94
95
96  ␣␣␣␣␣figure(1)
97  ␣␣␣␣grid␣on
98  ␣␣␣␣plot(alfa,Pcd);
99  ␣␣␣␣xlabel('alfa');
100 ␣␣␣␣ylabel('CD');
101 ␣␣␣␣title('103CD');
102 ␣␣␣␣hold␣on
103 ␣␣␣␣legend('077','115')
104
105 ␣␣␣␣figure(2)
106 ␣␣␣␣grid␣on
107 ␣␣␣␣plot(alfa,Pcl);
```

```
108 ____xlabel('alfa');
109 ____ylabel('CL');
110 ____title('103CL');
111 ____hold on
112 ____legend('077','115')
113 
114 
115 ____figure(3)
116 ____grid on
117 ____plot(alfa,Peff);
118 ____xlabel('alfa');
119 ____ylabel('eff');
120 ____title('103 eff');
121 ____hold on
122 ____legend('077','115')
123 
124 ____figure(19)
125 ____grid on
126 ____plot(Pcd,Pcl);
127 ____xlabel('CD');
128 ____ylabel('CL');
129 ____title('103 polare');
130 ____hold on
131 ____legend('077','115')
132 
133 ____ww1=ww1+1;
134 end
135 
136 %% Dati da post processare
137 
138 for j=w:prof  % j iniziale diprende da quanti sono i dati gi  post
        processati
139 ____for i=1:a
140 ________nom1 = num2str(wcorr);
141 ________nom2 =  num2str(alfa(i));
142 ________cd = strcat(nom1,'CD',nom2,'.csv');
143 ________cl = strcat(nom1,'CL',nom2,'.csv');
144 
145 ________CD(i,j)= csvread(cd,it,coeff,[it coeff it coeff]); %la prima
        riga nel csv   un'intestazione
146         CD(i,j)= CD(i,j)*10;
147         CL(i,j)= csvread(cl,it,coeff,[it coeff it coeff]); %tuttavia
                essa ha indice 0 (it-iesima=riga i-esima)
148         CL(i,j)= CL(i,j)*10;
149         eff(i,j)= CL(i,j)/CD(i,j); %efficienza
150 
151     end
152 
153     pcd=polyfit(alfa,CD(:,j),3);
154     Pcd=pcd(1)*alfa.^3+pcd(2)*alfa.^2+pcd(3)*alfa+pcd(4); %+pcd(5)*alfa
            +pcd(6);
155 
156     pcl=polyfit(alfa,CL(:,j),3);
157     Pcl=pcl(1)*alfa.^3+pcl(2)*alfa.^2+pcl(3)*alfa+pcl(4); %+pcl(5)*alfa
            +pcl(6);
158 
159     peff=polyfit(alfa,eff(:,j),3);
160     Peff=peff(1)*alfa.^3+peff(2)*alfa.^2+peff(3)*alfa+peff(4); %*alfa
```

```
        .^2+peff(5)*alfa+peff(6);
161
162     %figure(j)
163     %grid on
164     %plot(alfa,Pcd,'red');
165     %xlabel('alfa');
166     %%ylabel('CD');
167     %title(strcat(nom1,' CD'));
168     %figure(j+prof)
169     %grid on
170     %plot(alfa,Pcl,'green');
171     %xlabel('alfa');
172     %ylabel('CL');
173     %title(strcat(nom1,' CL'));
174     %figure(j+2*prof)
175     %grid on
176     %plot(alfa,Peff,'blue');
177     %xlabel('alfa');
178     %ylabel('eff');
179     %title(strcat(nom1,' eff'));
180
181     %PROFILI 123
182     if j>=3 && j<=4
183
184     figure(4)
185     grid on
186     plot(alfa,Pcd);
187     xlabel('alfa');
188     ylabel('CD');
189     title('123CD');
190     hold on
191     legend('077','115')
192
193     figure(5)
194     grid on
195     plot(alfa,Pcl);
196     xlabel('alfa');
197     ylabel('CL');
198     title('123CL');
199     hold on
200     legend('077','115')
201
202
203     figure(6)
204     grid on
205     plot(alfa,Peff);
206     xlabel('alfa');
207     ylabel('eff');
208     title('123eff');
209     hold on
210     legend('077','115')
211
212     figure(20)
213     grid on
214     plot(Pcd,Pcl);
215     xlabel('CD');
216     ylabel('CL');
217     title('123polare');
```

```
218     hold on
219     legend('077','115')
220
221
222     %PROFILI 124
223     elseif j==5
224
225     figure(7)
226     grid on
227     plot(alfa,Pcd);
228     xlabel('alfa');
229     ylabel('CD');
230     title('124CD');
231     hold on
232
233     figure(8)
234     grid on
235     plot(alfa,Pcl);
236     xlabel('alfa');
237     ylabel('CL');
238     title('124CL');
239     hold on
240
241
242     figure(9)
243     grid on
244     plot(alfa,Peff);
245     xlabel('alfa');
246     ylabel('eff');
247     title('124eff');
248     hold on
249
250     figure(21)
251     grid on
252     plot(Pcd,Pcl);
253     xlabel('CD');
254     ylabel('CL');
255     title('124polare');
256     hold on
257
258     %PROFILI 153
259     elseif j>=6 && j<=13
260
261     figure(10)
262     grid on
263     plot(alfa,Pcd);
264     xlabel('alfa');
265     ylabel('CD');
266     title('153CD');
267     hold on
268     legend('056','076','077','106','115','126','156','176')
269
270     figure(11)
271     grid on
272     plot(alfa,Pcl);
273     xlabel('alfa');
274     ylabel('CL');
275     title('153CL');
```

```
276     hold on
277     legend('056','076','077','106','115','126','156','176')
278
279     figure(12)
280     grid on
281     plot(alfa,Peff);
282     xlabel('alfa');
283     ylabel('eff');
284     title('153eff');
285     hold on
286     legend('056','076','077','106','115','126','156','176')
287
288     figure(22)
289     grid on
290     plot(Pcd,Pcl);
291     xlabel('CD');
292     ylabel('CL');
293     title('153polare');
294     hold on
295     legend('056','076','077','106','115','126','156','176')
296
297     %PROFILI 154
298     elseif j==14
299
300     figure(13)
301     grid on
302     plot(alfa,Pcd);
303     xlabel('alfa');
304     ylabel('CD');
305     title('154CD');
306     hold on
307
308
309     figure(14)
310     grid on
311     plot(alfa,Pcl);
312     xlabel('alfa');
313     ylabel('CL');
314     title('154CL');
315     hold on
316
317
318     figure(15)
319     grid on
320     plot(alfa,Peff);
321     xlabel('alfa');
322     ylabel('eff');
323     title('154eff');
324     hold on
325
326     figure(23)
327     grid on
328     plot(Pcd,Pcl);
329     xlabel('CD');
330     ylabel('CL');
331     title('154polare');
332     hold on
333
```

```
334
335     %PROFILI 183
336     else
337
338     figure(16)
339     grid on
340     plot(alfa,Pcd);
341     xlabel('alfa');
342     ylabel('CD');
343     title('183CD');
344     hold on
345     legend('055','056','075','076','105','106','125','126','155','156',
            '175','176')
346
347
348     figure(17)
349     grid on
350     plot(alfa,Pcl);
351     xlabel('alfa');
352     ylabel('CL');
353     title('183CL');
354     hold on
355     legend('055','056','075','076','105','106','125','126','155','156',
            '175','176')
356
357     figure(18)
358     grid on
359     plot(alfa,Peff);
360     xlabel('alfa');
361     ylabel('eff');
362     title('183eff');
363     hold on
364     legend('055','056','075','076','105','106','125','126','155','156',
            '175','176')
365
366     figure(24)
367     grid on
368     plot(Pcd,Pcl);
369     xlabel('CD');
370     ylabel('CL');
371     title('183polare');
372     hold on
373     legend('055','056','075','076','105','106','125','126','155','156',
            '175','176')
374
375
376     end
377
378
379
380     wcorr = wcorr+1; %nomenclatura della macro
381 end
```

# Bibliography


[1] S. R. Ahmed and W. H. Hucho, *Aerodynamics of Road Vehicle*, Butterworth Heinemann, 1987.

[2] Asinari and Chiavazzo, *Selected lectures on engineering thermodynamics*.

[3] E. Benzing, *Ali*, Nada, 2012.

[4] L. Casi, *Progetto e costruzione del telaio di vettura f.sae: parte posteriore*.

[5] B. Cetin, K. Guler, and M. H. Aksel, *Computational modeling of vehicle radiators using porous medium approach*.

[6] H. Dahlberg, *Aerodynamic development of formula student race car*.

[7] P. Doddegowda, A. L. Bychkovsky, and A. R. George, *Use of computational fluid dynamics for the design of formula sae race car aerodynamics*.

[8] F. S. Germany, *Formula student rules 2019*.

[9] G. Graziani, *Aerodinamica*, Università La Sapienza, 2010.

[10] S. Gupta and K. Saxena, *Aerodynamics analysis of a formula sae racecar*.

[11] D. Karnopp, *Vehicle Stability*, Marcel Dekker, 2004.

[12] J. Katz, *Race Car Aerodynamics*, Bentley Publisher, 1995.

[13] J. Katz and A. Plotkin, *Low-Speed Aerodynamics*, Cambridge University Press, 2001.

[14] Lewis and Postle, *Cfd validation for external aerodynamics, european automotive cfd conference, 2003*.

[15] M. Luci, *Effetti aerodinamici nelle vetture di formula 1*.

[16] L. Maoggi and A. Spagnolo, *Studio aerodinamico con metodologia c.f.d. di un veicolo formula sae*.

[17] S. McBeath, *Tracking devices*.

[18] ——, *Competition Car Aerodynamics*, Veloce, 2015.

[19] R. R. Nagavally, *Composite materials - history, types, fabrication techniques, advantages, and applications*.

[20] I. Oxyzoglou and I. Nerantzis, *Weight optimization of a f1 composite front wing.*

[21] S. Pescaglia, *Sviluppo di un metodo a pannelli per la valutazione delle caratteristiche aerodinamiche di profili alari.*

[22] P. Soliman, A. Schommer, and M. Martins, *Formula sae aerodynamics: Design process with focus on drivability.*

[23] J.-J. Tan, P. Myler, and W.-A. Tan, *Investigation and analysis on racing car front wings.*

[24] D. Tassetto, *Acquisizione dei carichi aerodinamici della vettura formula s.a.e. mg 13.18.*

[25] P. V. Valkenburgh, *Race car engineering and mechanics*, HPBooks, 2000.

[26] Versteeg and Malalasekera, *An Introduction to Computational Fluid Dynamics*, Pearson Education Limited, 2007.

[27] N. Villa, *Progettazione di un kit aerodinamico per una vettura da formula student.*

[28] S. Wordley and J. Saunders, *Aerodynamics for formula sae: A numerical, wind tunnel and on-track study.*

[29] ——, *Aerodynamics for formula sae: Initial design and performance prediction.*